# *Conjugated materials containing dithienometalloles*

*Joshua Paul Green*

Submitted in partial fulfilment of the requirements for the degree of

Doctor of Philosophy in Physics

Imperial College London

September 2016

# *Declaration*

The work presented herein was carried out at the Chemistry Department of Imperial College London between October 2012 and September 2016 under the supervision of Professor Martin Heeney. Except where otherwise stated, all work was performed by me.

Joshua P. Green, September 2016

# *Contributions*

This work would not have been possible without the people below, to whom I send my whole-hearted thanks.

The organic field effect transistors discussed in Chapters 2 and 4 were prepared and tested by Dr. Yang Han at Imperial College London. Organic photovoltaic devices (Chapter 3) were tested by Dr. Hyojung Cha and Dr. Pabitra Tuladhar at Imperial College London. The X-ray diffraction measurements in Chapter 2 were carried out by Rebecca Kilmurray at Imperial College London. Photoelectron spectroscopy in air measurements were carried out by Adam Creamer at CSIRO (Melbourne, Australia).

Finally, I would like to thank Sam Cryer, Dr. Abby Casey, and Dr. Zhuping Fei for providing starting materials and polymers used in Chapters 2, 3, and 4, respectively. Additional thanks must go to Haojie Dai for his help with the work discussed in Chapter 5 during his time as my student in his Master's year.

# *Copyright Declaration*

The copyright of this thesis rests with the author and is made available under a Creative Commons Attribution Non-Commercial No Derivatives licence. Researchers are free to copy, distribute or transmit the thesis on the condition that they attribute it, that they do not use it for commercial purposes and that they do not alter, transform or build upon it. For any reuse or redistribution, researchers must make clear to others the licence terms of this work.

***I – Acknowledgements***

I would first like to thank Professor Martin Heeney for his advice and support over the course of this project – without his support and dedication this PhD would have been infinitely more difficult. The help and guidance he provided me while I pursued my goal of producing the first arsole-containing conjugated polymers was absolutely invaluable, and it has been a pleasure working for him over the past five years.

This research would not have been possible without the help of my various collaborators, including Dr. Yang Han, Dr. Hyojung Cha, and Dr. Pabitra Tuladhar who helped with devices, as well as Pascal Cachelin, Rebecca Kilmurray, and Adam Creamer, who performed various measurements on my behalf. I would also like to thank all current and past members of the Heeney and McCulloch groups for their help, advice, and support during my PhD, and for making the lab an enjoyable place to work: Zhuping Fei, Yang Han, Hongliang Zhong, Thomas McCarthy-Ward, Jonathan Marshall, Chin Pang Yau, George Barnes, Abby Casey, Pierre Boufflet, Jess Shaw, Rolf Andernach, Adam Creamer, Iain Andrews, Simeng Wang, Haojie Dai, Brett Baatz, Shengyu Cong, Thomas Hodsden, Adam Marsh, Tingman Wu, Hugo Bronstein, Jenny Donaghey, Christian Nielsen, Bob Schroeder, David James, Iain Meager, Sarah Holliday, Dan Beatrup, Mike Hurhangee, Sam Cryer, Cameron Jellett, Mark Little, Andy Wadsworth, Alex Giovannitti, and Maud Jenart. I was also lucky enough to join the Plastic Electronics Doctoral Training Centre when I first arrived at Imperial College, and I would like to extend my thanks to all the staff and students from that group, in particular those in Cohort 3.

Finally, I would like to thank my friends and family for their love and support both before and during this PhD – in particular my parents. You have been absolutely essential for keeping me sane over the last four years, and I could not have done this without you.

***II – Abstract***

The development of new semiconducting conjugated polymers has been an important aspect of plastic electronics research since the early days of the field, as it allows the optoelectronic properties to be tuned for various applications. Dithienometalloles, which consist of a 2,2'-bithiophene fused with a bridging heteroatom, have been an important class of monomers for some time. The heteroatom serves an important role, both in holding the bithiophene unit rigidly coplanar and also in tuning the energetics of the system. In addition, these moieties often possess alkyl chains located on the bridging heteroatom that serve to confer solubility and processability to the final polymers.

In this thesis we report the synthesis and properties of a number of dithienometallole-containing polymers, in which the necessary solubilising groups have been moved from the bridging heteroatom to the adjacent thiophene backbone of the dithienometallole. This enabled the preparation of novel, soluble arsole-containing conjugated polymers. These dithienoarsole-containing materials were used in both organic field effect transistors and organic photovoltaic devices, showing promising performances as well as significantly improved air stability over their phosphorus-containing analogues. The effect of changing the bridging heteroatom in dithienometalloles was also studied by comparing the optoelectronic properties and device performances of polymers with carbonyl, silicon, germanium, and nitrogen bridging groups. Finally, dithienopyrrole-based sensors were developed that showed substantial colour changes on exposure to basic solutions, as well as potential for use as readily dopable materials for electronic applications.

## *III – Table of contents*

I – Acknowledgements ..... v
II – Abstract ..... vi
III – Table of contents ..... vii
IV – List of publications ..... xi
V – Abbreviations ..... xii

**Chapter 1 – Introduction ..... 1**
1.1 – Organic electronics: a history ..... 2
1.2 – Semiconducting polymers ..... 3
1.2.1 – Operating principles ..... 3
1.3 – Designing conjugated polymeric systems ..... 6
1.3.1 – General structure-properties relationships ..... 6
1.3.2 – Advantages of bridging ring systems ..... 10
1.3.3 – Dithienometalloles and naming heterocyclic compounds ..... 12
1.3.4 – Heavy-atom effects ..... 14
1.4 – Polymerisation reactions ..... 16
1.5 – Organic field effect transistors ..... 18
1.5.1 – Basics and device architectures ..... 19
1.5.2 – Operating principles and device characteristics ..... 19
1.6 – Organic photovoltaics ..... 23
1.6.1 – Operating principles ..... 24
1.6.2 – Bulk heterojunction solar cells ..... 27
1.6.3 – Device characteristics ..... 29
1.7 – Scope of the thesis ..... 31
1.8 – References ..... 32

**Chapter 2 – Arsoles in Organic Field Effect Transistors ..... 37**
2.1 – Introduction ..... 38
2.2 – Synthesis of dithienoarsole monomers ..... 39
2.2.1 – Preparation of dithienoarsole ..... 39
2.2.2 – Bromination of dithienoarsole ..... 41
2.2.2.1 – Oxidation of dibromo-dithienoarsole ..... 42
2.2.3 – Stannylation of dithienoarsole ..... 46
2.3 – Polymerization with vinylene ..... 46
2.3.1 – Optical properties ..... 48

2.3.2 – Physical properties ..... 48
2.3.3 – Electronic properties ..... 51
2.3.4 – OFET performance ..... 54
2.4 – Polymerization with bithiophene ..... 56
2.4.1 – Synthesis of dithienophosphole analogue ..... 56
2.4.2 – Coordination with transition metal catalysts ..... 56
2.4.3 – Polymerization reactions ..... 61
2.4.4 – Optical properties ..... 62
2.4.5 – Physical properties ..... 63
2.4.6 – Electronic properties ..... 67
2.4.7 – OFET performance ..... 69
2.5 – Polymerization with benzodithiophene ..... 71
2.5.1 – Optical properties ..... 72
2.5.2 – Physical properties ..... 73
2.5.3 – Electronic properties ..... 74
2.5.4 – OFET performance ..... 76
2.6 – Dithienoarsole lone pair modification ..... 77
2.7 – Ongoing dithiazoloarsole work ..... 80
2.7.1 – Synthesis of dithiazoloarsole ..... 81
2.7.2 – Crystal structure ..... 81
2.8 – Conclusions ..... 86
2.9 – Experimental ..... 87
2.10 – References ..... 100

**Chapter 3 – Conjugated polymers for Use in Organic Solar Cells ..... 104**
3.1 – Introduction ..... 105
3.2 – Photovoltaic performance of PDTAsBDT ..... 106
3.3 – 2D-Benzodithiophene-based polymers ..... 109
3.3.1 – Polymerizations with 2D-benzodithiophenes ..... 110
3.3.2 – Optical properties ..... 111
3.3.3 – Physical and electronic properties ..... 112
3.4 – OPV performance ..... 117
3.5 – Donor-acceptor polymers for OPV materials ..... 124
3.6 – Synthesis of dicyanobenzotriazole monomer ..... 126
3.7 – Polymerisation with benzodithiophene derivatives ..... 127
3.7.1 – Optical properties ..... 128

3.7.2 – Physical and electronic properties ..... 130
3.8 – OPV performance ..... 133
3.8.1 – Ethylhexyl polymer ..... 133
3.8.2 – Butyloctyl polymer ..... 135
3.9 – Conclusions ..... 138
3.10 – Experimental ..... 139
3.11 – References ..... 144

**Chapter 4 – Effect of the Dithienometallole Bridging Group on OFET Properties ..... 147**
4.1 – Introduction ..... 148
4.2 – Synthesis of dithienopyrrole monomers ..... 149
4.2.1 – Preparation of dithienopyrrole ..... 149
4.2.2 – Bromination of dithienopyrrole ..... 150
4.2.3 – Stannylation of dithienopyrrole ..... 150
4.2.4 – Polymerizations with thienothiophene ..... 151
4.2.4.1 – Polymerization via direct heteroarylation with 2,6-dibromothieno[3,2-b]thiophene ..... 151
4.2.4.2 – Polymerization via Stille coupling with 2,6-bis(trimethylstannyl)-thieno[3,2-b]thiophene ..... 153
4.2.4.3 – Polymerization via Stille coupling with 2,6-dibromothieno[3,2-b]thiophene ..... 154
4.3 – Comparison with other dithienometallole-thienothiophene polymers ..... 154
4.3.1 – Computational calculations ..... 156
4.3.2 – Optical properties ..... 162
4.3.3 – Electronic properties ..... 164
4.3.4 – OFET performance ..... 166
4.4 – Conclusions ..... 169
4.5 – Experimental ..... 170
4.6 – References ..... 174

**Chapter 5 – Dithienopyrrole-containing molecules as sensors ..... 176**
5.1 – Introduction ..... 177
5.2 – Attempted synthesis of NH-dithienopyrrole ..... 179
5.2.1 – Synthesis of N-benzyldithienopyrroles ..... 180
5.2.1.1 – Attempted deprotection ..... 181
5.3 – Coupling of N-benzyldithienopyrroles with bithiophene ..... 182

5.3.1 – Deprotection ..... 184
5.4 – Screening potential analytes ..... 186
5.5 – Method of action ..... 188
5.5.1 – Calculation of dissociation constant ..... 191
5.6 – Effects of varying analyte structure ..... 195
5.6.1 – Anion variation ..... 195
5.6.2 – Cation variation ..... 196
5.7 – Polymer-based system ..... 200
5.7.1 – Stannylation of N-benzyldithienopyrroles ..... 201
5.7.2 – Polymerization ..... 201
5.7.3 – Deprotection ..... 202
5.8 – Sensing using polymer ..... 203
5.8.1 – Optical properties ..... 204
5.8.2 – Deprotonation with TBAF ..... 206
5.9 – Conclusions ..... 209
5.10 – Experimental ..... 210
5.11 – References ..... 216

**Chapter 6 – Conclusions ..... 220**
Appendix A – Polymer $^{1}$H NMRs ..... 224
Appendix B – CV of blank FTO-coated glass ..... 230
Appendix C – Crystallographic information ..... 231
Appendix D – Publications ..... 234

### *IV – List of Publications*

The following publications have been produced during the course of this PhD, and copies of the manuscripts are provided in **Appendix D**:

1. An Air-Stable Semiconducting Polymer Containing Dithieno[3,2-b :2′,3′-d]arsole. **J. P. Green**, Y. Han, R. Kilmurray, M. A. McLachlan, T. D. Anthopoulos, M. Heeney, *Angew. Chem. Int. Ed.* **2016**, *55*, 7148.

2. Optical Acetone Vapor Sensors Based on Chiral Nematic Liquid Crystals and Reactive Chiral Dopants. P. Cachelin, **J. P. Green**, T. Peijs, M.Heeney, C. W. M. Bastiaansen, *Adv. Optical Mater.* **2016**, *4*, 592.

Other work discussed in the thesis is also currently being prepared for publication.

## *V – Abbreviations*

| | |
|---|---|
| BDT | Benzo[1,2-*b*:4,5-*b*']dithiophene |
| BHJ | Bulk heterojunction |
| BINAP | 2,2'-Bis(diphenylphosphino)-1,1'-binaphthyl |
| BOC | tert-Butoxycarbonyl |
| $Bu_4NPF_6$ | Tetrabutylammonium hexafluorophosphate |
| CB | Chlorobenzene |
| CPDT | Cyclopenta[2,1-*b*:3,4-*b'*]dithiophene |
| CuSCN | Copper(I) thiocyanate |
| CV | Cyclic voltammetry |
| Đ | Polydispersity index |
| D-A | Donor-acceptor |
| DBU | 1,8-Diazabicycloundec-7-ene |
| DCB | Dichlorobenzene |
| DCBTz | 2-(2-Butyloctyl)-4,7-di(2-thienyl)-2H-benzo[*d*][1,2,3]triazole-5,6-dicarbonitrile |
| DCM | Dichloromethane |
| DFT | Density functional theory |
| DMAc | Dimethylacetamide |
| DMSO | Dimethyl sulfoxide |
| DSC | Differential scanning calorimetry |
| DTAs | Dithieno[3,2-*b*:2',3'-*d*]arsole |
| DTBTz | Dithienyl-benzotriazole |
| DTP | Dithieno[3,2-*b*:2',3'-*d*]pyrrole |
| DTPh | Dithieno[3,2-*b*:2',3'-*d*]phosphole |
| DTT | Dithieno[3,2-*b*:2',3'-*d*]thiophene |
| EI | Electron ionisation |
| ES | Electrospray |
| ESI | Electrospray ionisation |
| FET | Field effect transistor |
| FF | Fill factor |
| FTO | Fluorine-doped indium tin oxide |
| GCMS | Gas chromatography mass spectrometry |
| GPC | Gel permeation chromatography |
| HOMA | Harmonic oscillator measure of aromaticity |
| HOMHED | Harmonic oscillator model of heterocyclic electron delocalization |
| HOMO | Highest occupied molecular orbital |
| HRMS | High resolution mass spectrometry |
| HTL | Hole transport layer |
| $I_D$ | Drain current |
| $I_{off}$ | OFF current |
| $I_{on}$ | ON current |
| ITO | Indium tin oxide |
| $J_{sc}$ | Short circuit current |
| LDA | Lithium diisopropylamine |
| LUMO | Lowest unoccupied molecular orbital |
| MALDI-TOF | Matrix-assisted laser desorption/ionization-time-of-flight |

| | |
|---|---|
| *m*-CPBA | meta-Chloroperoxybenzoic acid |
| $M_n$ | Number average molecular weight |
| $M_w$ | Weight average molecular weight |
| NBS | *N*-Bromosuccinimide |
| *n*BuLi | *n*-Butyllithium |
| NMR | Nuclear magnetic resonance |
| ODT | 1,8-Octanedithiol |
| OFET | Organic field effect transistor |
| OLED | Organic light emitting diode |
| OPV | Organic photovoltaic device |
| OSC | Organic semiconductor |
| P3HT | Poly (3-hexylthiophene) |
| $P(o\text{-tol})_3$ | Tri(*o*-tolyl)phosphine |
| $PC_{61}BM$ | Phenyl-C61-butyric acid methyl ester |
| $PC_{71}BM$ | Phenyl-C71-butyric acid methyl ester |
| PCE | Power conversion efficiency |
| PCPDTBT | Poly[2,6-(4,4-bis-(2-alkyl)-4H-cyclopenta[2,1-*b*;3,4-*b*′]dithiophene)-alt-4,7(2,1,3-benzothiadiazole)] |
| $Pd(OAc)_2$ | Palladium acetate |
| $Pd(PPh_3)_4$ | Tetrakis(triphenylphosphine)palladium(0) |
| $Pd_2(dba)_3$ | Tris(dibenzylideneacetone)dipalladium(0) |
| PEDOT:PSS | Poly(3,4-ethylenedioxy)thiophene/poly(styrene sulfonate) |
| PESA | Photoelectronspectroscopy in air |
| PFBT | Pentafluorobenzene thiol |
| $PPh_3$ | Triphenylphosphine |
| RFID | Radio frequency identification |
| RT | Room temperature |
| SAM | Self-assembled monolayer |
| TBAF | Tetrabutylammonium fluoride |
| TCB | 1,2,4-Trichlorobenzene |
| TD-DFT | Time-dependent density function theory |
| TFA | Trifluoroacetic acid |
| $T_G$ | Glass transition temperature |
| THF | Tetrahydrofuran |
| TLC | Thin layer chromatography |
| TMEDA | *N,N,N′,N′*-Tetramethylethylenediamine |
| TMSCl | Trimethylsilyl chloride |
| UV-vis | Ultraviolet-visible |
| $V_D$ | Drain voltage |
| $V_G$ | Gate voltage |
| $V_T$ | Threshold voltage |
| XRD | X-ray diffraction |
| $\lambda_{max}$ | Absorption maximum |

"Your scientists were so preoccupied with whether or not they *could* that they didn't stop to think if they *should*."

Dr. Ian Malcolm
*Jurassic Park*

# *Chapter 1*

# *Introduction*

### *1.1 – Organic electronics: a history*

Polymeric materials have been used by humans since before recorded history in the form of naturally occurring polymers such as wood, bone, and other fibrous matter. However, polymer science as a field did not truly begin until the 20th century, when a number of discoveries and concepts that are familiar today began to take shape, including Hermann Staudinger's work on macromolecular theory, which won him the Nobel Prize in Chemistry in 1953, and the successes of nylon and Bakelite, two of the first synthetic polymers to see widespread commercial applications.[1] Although plastics saw an explosion in uses across a huge variety of applications, until the late 1970's they were considered to be insulating materials that were uninteresting from an electronics perspective. This changed when Alan G. MacDiarmid, Hideki Shirakawa, and Alan J. Heeger discovered that an unsaturated polymer, polyacetylene, could be doped with halogens to induce electrical conductivity – work that would earn them the Nobel Prize in Chemistry in 2000 and give birth to the field of plastic electronics.[2,3]

Over the next few decades, developments in both doping strategies and materials design led to a substantial expansion of the area, broadening it from the original research regarding plastics with metallic conductivities to cover a range of materials based on similar materials design principles, i.e., the use of alternating double and single bonds to create a π-conjugated network.[4] The huge variety of chemical structures that can be accessed through this relatively simple design principle, especially once elements beyond carbon and hydrogen are included in the materials, means that conjugated organic materials have a large range of applications, including in organic light emitting diodes, organic field effect transistors (OFETs), organic photovoltaic devices (OPVs), photodetectors, sensors, and bioelectronics.[5–8] Although the field of organic electronics also includes small molecule analogues such as pentacene, this thesis focuses almost exclusively on the development of new semiconducting polymers, and thus only concepts relevant to these materials are discussed below.

### *1.2 – Semiconducting polymers*

Organic semiconducting polymers have a number of unique advantages over both traditional inorganic semiconductors and molecular organic semiconductors. Compared to small organic molecules, conjugated polymers generally form much more uniform thin films and have more consistent morphologies due to their smaller domain sizes, which also enables isotropic charge transport. The favourable solution viscosities of polymeric materials also makes them suitable for high-throughput printing, while the versatility of the backbone structures allows both physical and optoelectronic properties to be tuned as required. Whilst conjugated polymers are unlikely to replace traditional inorganic materials such as silicon in many applications, the advantages detailed above as well as factors such as their relatively lower cost and high absorption coefficients mean they have the potential to play a role in prospective disruptive technologies across several fields.

#### *1.2.1 – Operating principles*

The primary components of semiconducting polymers are the same as those of traditional insulating polymers such as polystyrene, with the majority of the conjugated backbones consisting of carbon, hydrogen, and a select few other elements. However, the key difference is the aforementioned π-conjugated backbone. In non-conjugated hydrocarbon polymers such as polyethylene (**Figure 1.1a**), the backbone is composed primarily of tetrahedral $sp^3$-hybridised carbon atoms that are covalently bonded to each other via σ-bonds. The highly localised nature of the electrons in these systems makes them excellent insulators (**Figure 1.2a**). On the other hand, the carbons in conjugated polymers like polyacetylene (**Figure 1.1b**) are instead $sp^2$-hybridised, meaning that they can form both σ-bonds and π-bonds, resulting in a trigonal planar structure with the carbons and hydrogens all in the plane and a single p-orbital out-of-plane. This leads to the characteristic alternating single-double bonds seen in all conjugated polymers.

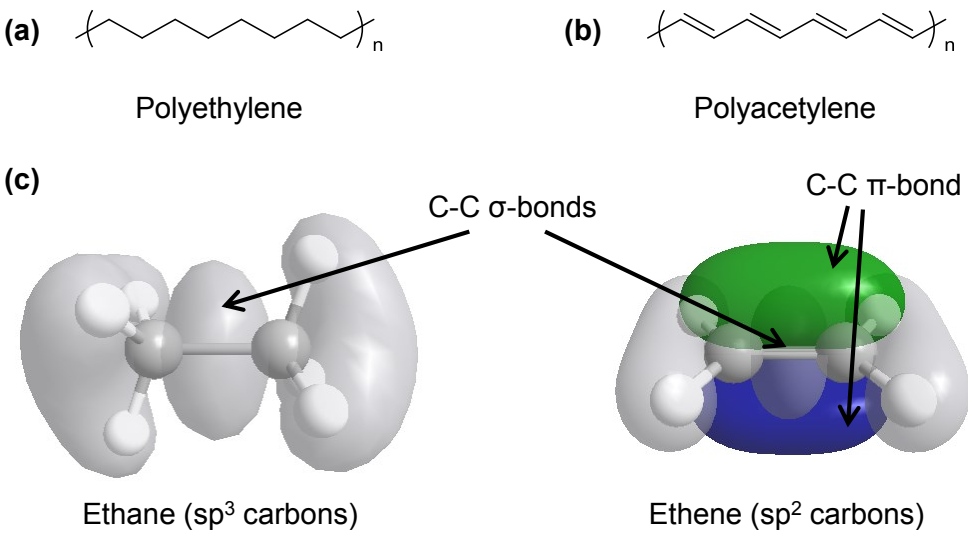



**Figure 1.1: Structures of (a) polyethylene and (b) polyacetylene. (c) Hybridised orbitals of carbon in ethane (left) and ethene (right), with carbon-carbon bonding orbitals highlighted**

Whilst exciting an electron from a bonding σ-orbital (as in polyethylene) to its equivalent anti-bonding orbital requires a large amount of energy due to the substantial energy gap between the two, the higher energies of the π-bonds in polyacetylene mean that their equivalent anti-bonding orbitals are found at much lower energies, reducing the energy gap between the highest occupied molecular orbital (HOMO) and the lowest unoccupied molecular orbital (LUMO) of materials that contain π-bonds. In fact, it was originally believed that the carbon-carbon bonds in polyacetylene would all be the same length due to the presence of degenerate π-orbitals similar to those in benzene, giving polyacetylene a unit cell consisting of a single carbon and hydrogen with only one π-electron (**Figure 1.2b**). This would result in the molecule having fully delocalised π-electrons and a band gap of zero, and hence it would behave as a 1D-metal, showing metallic-type conductivity along individual chains.[9] However, there is in fact an inherent instability in 1D metals, first theorised by Rudolf Peierls in the 1950's.[10] Instead of all the C-C bonds being the same lengths, carbons in polyacetylene move closer together into pairs, leaving larger gaps between pairs, with electron density also redistributing to place more π-orbital density between carbons that are closer together. The result is that a gap opens up between the HOMO and the LUMO, which is an anti-bonding orbital wherein π-electron density is localised on the longer bonds and reduced on the shorter. The HOMO is analogous to the

valence band in traditional inorganic semiconductors, while the LUMO plays the role of the conduction band.

The so-called Peierls distortion occurs because the energetic stabilisation provided by shortening half of the bonds more than offsets the destabilisation caused by lengthening the others, resulting in a lower HOMO level. This net energetic stabilisation results in a structure that is very similar to the alternating double and single bonds commonly used to represent polyacetylene, and doubles the size of the unit cell from a single carbon-hydrogen moiety to a (-CH=CH-) unit (**Figures 1.2b and c**). In conjugated polymers, the HOMO-LUMO band gap ($E_g$) is typically between 1–3 eV, resulting in the semiconducting properties of these materials.

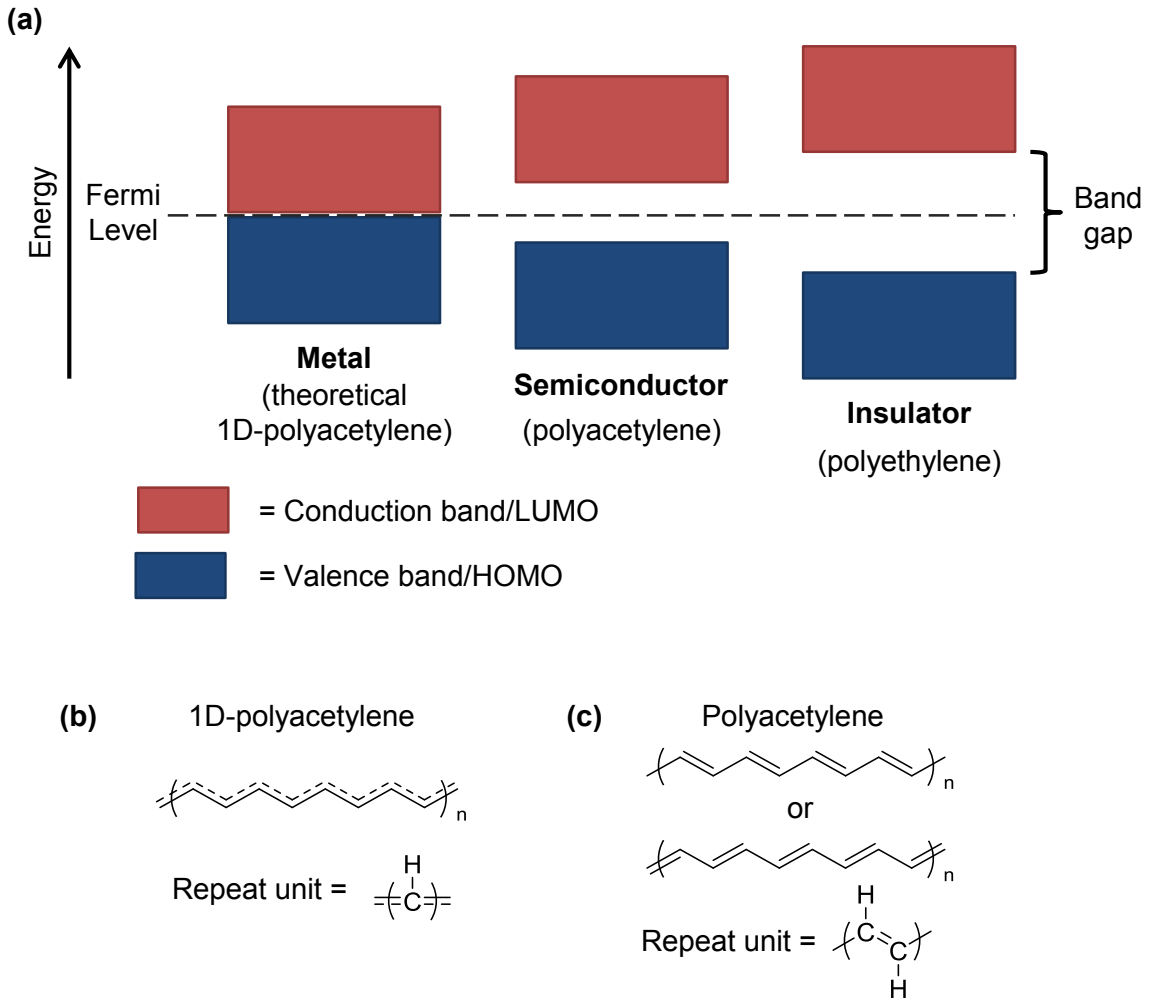



**Figure 1.2: (a) Change from metallic to insulating material as band gap increases, with examples of each. Structures and repeat units of (b) theoretical 1D-polyacetylene, and (c) actual polyacetylene**

Whilst the structural differences between the HOMO and LUMO of polyacetylene induced by the Peierls distortion are minimal, resulting in a small energy gap material, much greater changes are seen between the structures of the frontier molecular orbitals of other conjugated polymers. For example, the phenylic (HOMO) structure of poly(*p*-phenylene) favours keeping π-electron density within individual rings, while the quinoidal (LUMO) structure disrupts the aromaticity of individual rings and is therefore high in energy, resulting in a large band gap (**Figure 1.3**).

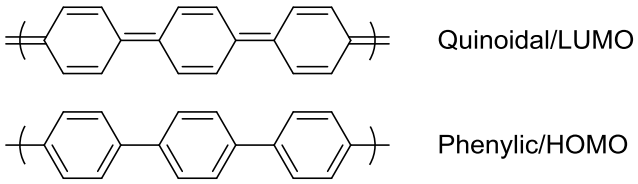



**Figure 1.3: Schematic diagrams of the phenylic and quinoidal structures of poly(*p*-phenylene), where double bonds represent higher π-electron density**

### *1.3 – Designing conjugated polymeric systems*

As mentioned previously, it is possible to tune both the energy levels and macroscopic properties of conjugated polymers through careful design of the repeat units. For example, most conjugated polymers require some form of alkyl side chains on the repeat unit to ensure solubility and therefore processability; however, the position and structure of these side chains can have a substantial impact on the solubility, morphology, and even energy level of the resulting polymer.[11,12] Thus, it is important to be aware of the impact that changing the structure of the repeat unit can have on the final polymer. Whilst the qualities that are desirable for a polymer to be used for one application may not be the same as those required for another, there are some broad rules that can be taken into account when designing a semiconducting polymer.

#### *1.3.1 – General structure-properties relationships*

One of the simplest yet most important things to consider is the degree of electron delocalisation along the polymer backbone, commonly referred to as the effective conjugation

length. This has a substantial impact on the HOMO-LUMO energy gap – indeed, this is one of the key characteristics that separates semiconducting polymers from small molecules. The conjugation length is determined by the degree of orbital overlap within and between monomeric units, and one of the primary factors that influences this is the number of repeat units in the polymer, with higher molecular weights leading to lower $E_g$. The overlap of more repeat units allows a greater number of orbitals to hybridise, decreasing the HOMO and LUMO gap. As discussed above, this does not continue indefinitely, but saturates due to the Peierls distortion. The point of which no further changes to the band gap can be detected is called the maximum effective conjugation length. Studies on oligomeric species have shown this generally occurs between 10–20 repeat units, depending on the exact monomer, although small changes have been observed up to a 96mer in thiophene species.[13,14] Note that although the effective conjugation length can saturate quite quickly, molecular weight effects are still seen in a number of electronic devices due to factors such as polymer entanglement and crystallisation at higher molecular weights.[15]

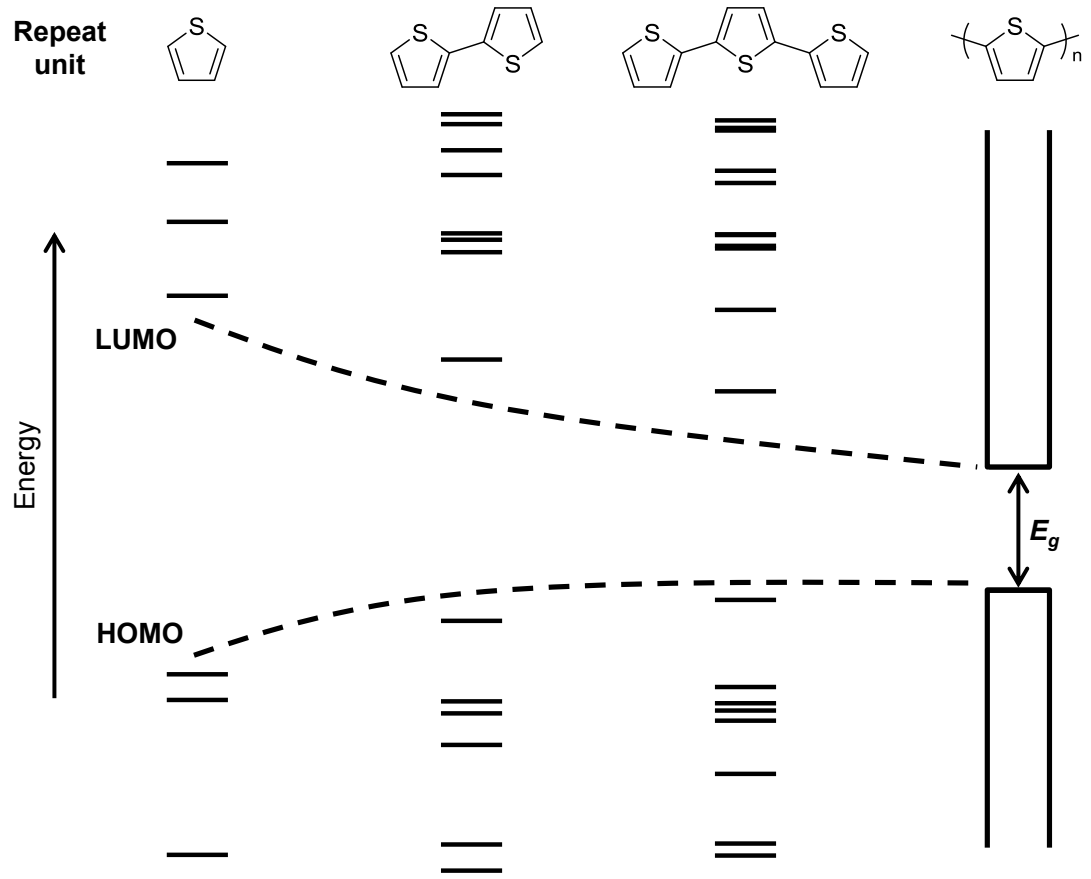



**Figure 1.5: Evolution of the electronic structure of thiophene as the number of repeat units is increased from one to three to 'infinite'. Energy levels of thiophene, bithiophene, and terthiophene calculated using Gaussian 09 at the B3LYP level of theory with the 6-31G* basis set. Energy levels of polythiophene taken from the work of Salzner et al.**[16]

Beyond increasing the molecular weight, there are a number of other common methods of tuning the energy levels of conjugated polymers. For example, stabilisation of quinoidal form of a monomer is an effective approach to lowering $E_g$. This occurs because stabilising the quinoidal resonance structure (and in turn destabilising the aromatic resonance structure) reduces the bond length alteration in the polymer backbone, pushing the HOMO and LUMO closer together. The result is a higher HOMO energy and lower LUMO energy, which can significantly decrease the band gap.[17] Thought of another way, this causes the bonds between the monomer units to become shorter due to the adoption of more double-bond character, whilst other bonds in the ring become longer, reducing the bond length alteration caused by the Peirels distortion and decreasing the band gap as the polymer chain becomes closer to the theoretical electronic

structure of a 1D metal.[18] A commonly cited example of this quinoidal amplification is the modification of polythiophene to poly(isothianaphthene) by fusing a benzene ring to the 3,4 bond of thiophene. As only the thiophene ring or the benzene ring can be aromatic in a given resonance structure (**Figure 1.6**) and a greater energetic stabilisation is provided by benzene being aromatic, the backbone chain (going through the thiophene rings) favours its quinoidal form, resulting in polymers with low band gaps of ~1 eV.[19]

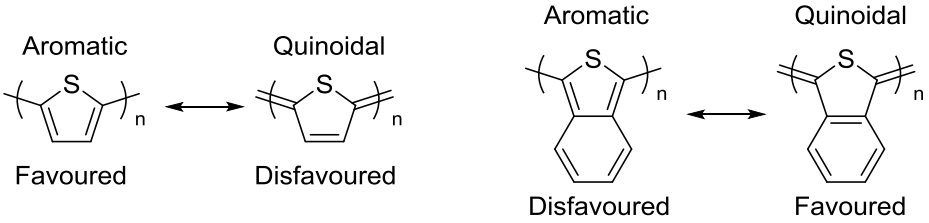



**Figure 1.6: Aromatic and quinoidal resonance structures of polythiophene (left) and poly(isothianaphthene) (right)**

Whilst it is clearly important to consider the impact of quinoidal resonance structures on the band gaps of conjugated polymers, other strategies can also be employed to tune the properties of conjugated polymers. For example, another related method of reducing the band gap of a conjugated polymer is to use an alternating donor-acceptor (D-A) system, wherein alternating electron donating and electron accepting moieties are copolymerised.[20,21] In such systems, hybridization of the molecular orbitals of the two monomers leads to a higher HOMO and lower LUMO level on the polymer backbone, with the HOMO being closer to that of the donor and the LUMO on that of the acceptor, as shown in **Figure 1.7**.[22,23] This allows the HOMO and LUMO to be tuned relatively independently by altering their respective monomers, which can be of great benefit as some device properties are affected more by one than the other. These D-A polymers have been used to great effect in organic electronics, particularly for OPV devices as their narrow band gaps can result in excellent light absorption capabilities.[12]

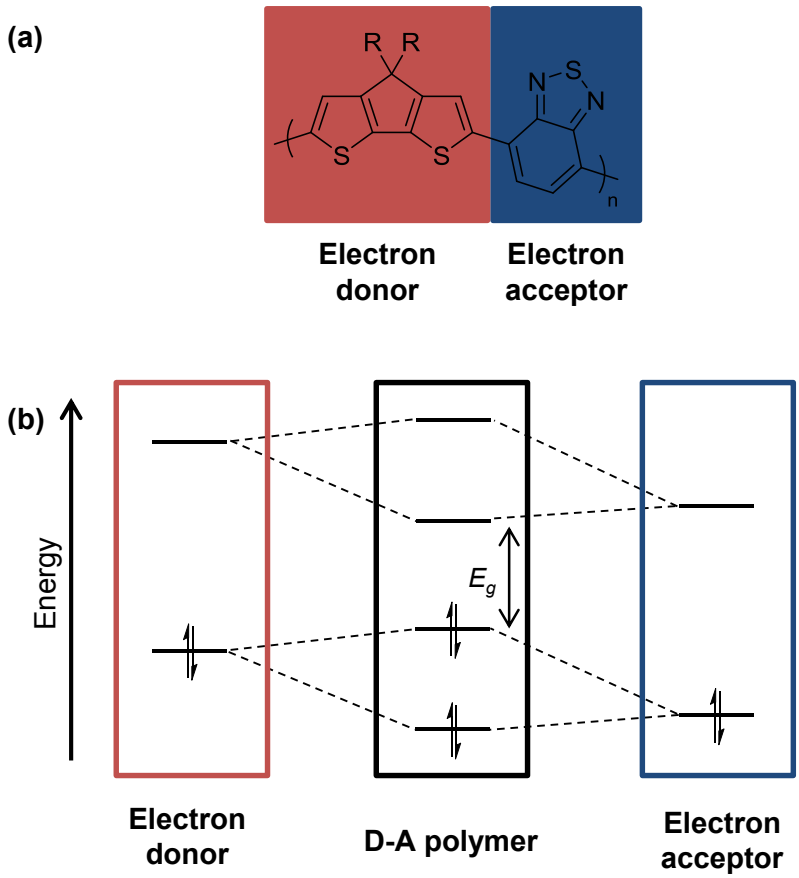



**Figure 1.7: (a) Structure of a common donor-acceptor polymer, PCPDTBT. (b) Hybridisation of frontier molecular orbitals to lower the band gap in donor-acceptor polymers**

### *1.3.2 – Advantages of bridging ring systems*

A common structural feature that is heavily featured in this thesis is the extension of conjugation by restricting rotation between adjacent ring systems, which is commonly performed using by either fusing aromatic rings together, as is the case with thieno[3,2-*b*]thiophene, or by using a bridging atom to increase coplanarity, as can be seen in molecules such as fluorene (**Figure 1.8**). Both of these strategies increase the planarity of the polymer backbone, ensuring effective conjugation and enhancing π-π stacking between polymer chains. This can be beneficial for some applications, as π-π stacking can lead to improved intermolecular charge transport amongst other things. However, this can come at the expense of solubility, which can limit the processability of the material. Therefore, tuning the degree of planarity and interchain stacking is highly important when trying to design conjugated polymers for specific applications.

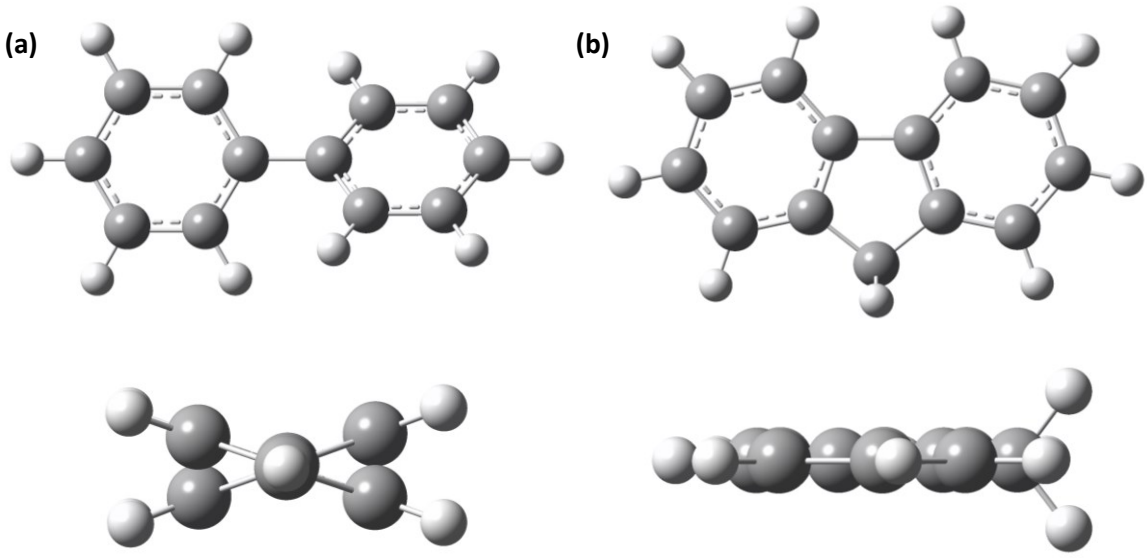



**Figure 1.8: Top down and axial views of (a) 1,1'-biphenyl and (b) fluorene as calculated using Gaussian 09 at the B3LYP level of theory with the 6-31G* basis set**

Using bridging atoms instead of ring fusion has additional advantages that can make it a sensible choice in many situations. As previously mentioned, combining two rings through a bridging ring can substantially reduce the torsion between adjacent rings – the dihedral angle between the two benzene rings in 1,1'-biphenyl is ~38°, while it is 0° in the C-bridged analogue, fluorene (**Figure 1.8**). In addition the bridging atom itself will influence the electronic properties of the aromatic system by either inductive or mesomeric effects, as well as potentially serving as a convenient point of attachment for side chains, with the choice of side chains being capable of altering the solubility of the final polymer as well as its solid-state morphology.

### *1.3.3 – Dithienometalloles and naming heterocyclic compounds*

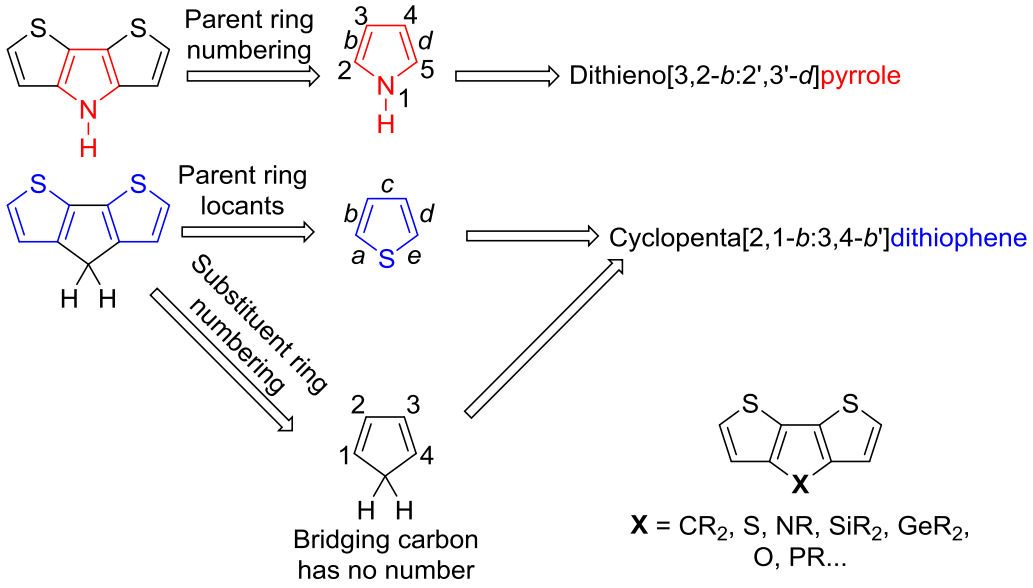



**Figure 1.9: Structures and systematic names of dithieno[3,2-*b*:2',3'-*d*]pyrrole and cyclopenta[2,1-*b*:3,4-*b*']dithiophene. Bottom right: general structure of dithienometalloles**

Systematic naming and numbering of heteroaromatic rings involves a complex system of rules for determining the priorities of heteroatoms and ring systems, which are used to assign "parent" and "substituent" rings. A brief overview of the rules that are relevant to this thesis is provided here, but a more comprehensive review of the subject has recently been published by Rasmussen and can be referred to for more detail.[24] Heterocycles are always given priority over all-carbon rings, and are named according the Hantzsch-Widman rules regarding ring size and saturation. Heteroatoms are assigned priorities that decrease as group number decreases, and then decrease as atomic number increases within a given group, such that all atoms in Group 16 have a higher priority than those in Group 15, whilst within Group 15 the priority follows the trend N > P > As > Sb. To determine the parent ring system when multiple heterocycles are fused together, rings containing nitrogen are given highest priority, and in the absence of a nitrogen-containing ring the same rules as described above are applied to determine the highest priority heterocycle. After the parent ring system has been determined, the other substituents are assigned names using their accepted fusion prefixes: for example, "thiophene" becomes "thienyl". Atoms in the parent ring are then numbered using the standard rules, and fusion

positions are identified via a letter representing the two-atom bond that is the point of fusion (e.g., the bond between atoms 1 and 2 is identified by the fusion locant "*a*". This is most easily understood by using an example such as the dithienopyrrole compound shown in **Figure 1.9**. The pyrrole ring has the highest priority as it contains nitrogen, and is thus the parent ring system. In order to show that two separate thiophene rings are fused to this pyrrole, the prefix "di-" is used before the term "thieno", thus giving the name "dithienopyrrole". A bracketed descriptor is then inserted between the substituents and the parent to identify the points of fusion, with the two fusion locants being separated by a colon. As the substituents are identical, the first is described using unprimed numbers, while the second is described using primed numbers. Fusion locants are based on the numbering used for the first ring, i.e., the unprimed numbers. This gives the final name of "dithieno[2,3-*b*:3',2'-*d*]pyrrole". If two identical "parents" are identified as in cyclopentadithiophene, where the parents are the two identical thiophene rings, the fusion numbering is derived from the substituent ring (and is thus unprimed), while the locant letters identify the parent rings (and are thus primed as necessary as there are two of them). This gives the cyclopentadithiophene system shown in **Figure 1.9** the systematic name "cyclopenta[2,1-*b*:3,4-*b*']dithiophene".

Note that in this thesis, phosphorus- and arsenic-containing ring systems are named in the same manner as their nitrogen-containing analogues, treating the pnictogenic ring as the parent despite these heteroatoms having lower priority than the sulfur-containing rings. This is in line with naming of such compounds in the literature, as it both simplifies the nomenclature and highlights the ring of interest in these compounds.[24]

One of the first and most common bridged moieties investigated was cyclopenta[2,1-*b*:3,4-*b*']dithiophene (CPDT), in which two adjacent thiophene rings are bridged by an $sp^3$-hybridised carbon atom. The application of this molecule to plastic electronics was pioneered by Zotti et al., who produced alkylated CPDT homopolymers as early as 1994, although they did not investigate them in any devices.[25] Brabec and co-workers later showed that when combined

with a suitable electron accepting unit such as benzothiadiazole, CPDT was capable of OPV device performances that were exemplary for their time.[26,27] The Brabec group were also the first to replace the bridging carbon with a heteroatom, in their case silicon, in order to produce a dithienometallole (**Figure 1.9**).[28] Since this report, a large variety of dithienometalloles have been investigated, all of which have different advantages and disadvantages. For example, the use of sulfur as a heteroatom yields dithieno[3,2-*b*:2',3'-*d*]thiophene (DTT), which has increased stability over CPDT but cannot be functionalised at the bridging site due to the valence of the sulfur atom.[29,30] Replacing the bridging sulfur with a nitrogen atom to produce dithieno[3,2-*b*:2',3'-*d*]pyrrole (DTP) has been shown to allow the incorporation of the positive attributes of both DTT and CPDT, i.e., increased stability and the potential for alkylation, respectively. Other bridging groups all have their own characteristics, allowing various degrees of alkylation, the addition of other functional groups, or simply more finely tuned energy levels. The most common elements found in dithienometalloles are sulfur, nitrogen, and silicon, but heavier elements are also being investigated due to the interesting properties they can confer to conjugated polymers.

### *1.3.4 – Heavy-atom effects*

There has been significant progress in the field of incorporating heavier elements (i.e., those in period 3 and below) into heterocycles in conjugated organic polymers over the last 10–15 years.[31,32] Although the qualities imparted by the inclusion of these elements can vary, they are all of interest as they show the potential to fine-tune polymer properties as well as enabling the investigation of new materials with unique characteristics.[33] Heavier elements that have been used as bridging atoms in 5-membered bridging rings include silicon, germanium, and phosphorus, yielding siloles,[34] germoles,[35] and phospholes,[36] respectively. In addition, selenium and tellurium have been used by several groups to replace sulfur in thiophene rings, leading to significant interest in selenophenes and tellurophenes.[37,38]

The specific category of heavy-atom-containing heterocycles relevant to this thesis consists of dithienometalloles with group 14 and 15 elements acting as bridging groups, as shown in **Figure 1.9**. In the previously mentioned Brabec paper on dithienosiloles, the group found that the longer C-Si bond reduced the steric interference of the side chains in the π-π stacking between polymer chains, enhancing the crystallinity of the polymer compared to the CPDT-containing analogue, which led to a noticeable increase in the charge carrier mobility.[28] It has also been shown that siloles exhibit σ*-π* conjugation due to interaction of the σ*-orbital of the exocyclic $sp^3$ bonds on Si with the π*-orbital of the ring system, thereby lowing the LUMO level when compared to their cyclopentadiene analogues.[34]

If the Si atom in dithienosilole is replaced with Ge, the resulting dithienogermole shows characteristics that are comparable yet still interesting. Of note is the fact that the C-Si and C-Ge bond lengths are very similar, at 1.88 and 1.96 Å, respectively.[39] This is due to the d-block contraction, and results in dithienogermole-containing polymers showing similar packing behaviour to their Si-containing analogues. However, the d-block contraction also means that the electronegativity of Ge is much closer to that of C than of Si,[40] giving dithienogermoles greater stability to bases and nucleophiles than dithienosiloles, which can both improve the stability of devices and allows dithienogermoles to be polymerised via Suzuki coupling, which has been shown to cause degradation of dithienosilole materials.[41]

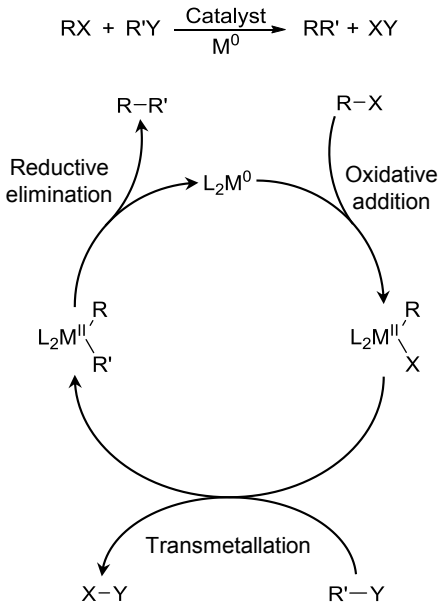
With respect to group 15-containing dithienometalloles, the overwhelming majority of work has focussed on those utilising P as a bridging atom. Although the specific advantages of dithienophospholes are discussed in detail in the introduction to **Chapter 2**, some brief information is also provided here. While group 14 metalloles are $sp^3$-hybridised and thus provide two sites for side chain attachment, metalloles containing group 15 heteroatoms are $sp^2$-hybridised, with an exocyclic side chain usually being connected to the ring structure through an $sp^2$ orbital and a lone pair of electrons occupying a p-orbital. When the heteroatom used is nitrogen, the lone pair is fully involved in the conjugated ring system (analogous to

pyrrole), resulting in highly planar structures. On the other hand, the bonding orbitals of phosphorus show increased s-character, leading to a pyramidal shape around the phosphorus atom.[42,43] As a result, both the R-group and the phosphorus lone pair are outside of the plane of the ring system, leading to reduced aromaticity as well as interesting morphological properties that can lead to traits such as enhanced emission.[44,45] In addition, the oxidation state of phosphorus can be varied between the +3 and +5 states, with trivalent phosphorus readily reacting with oxidising agents or transition metals to form a wide variety of derivatives.[46] In fact, the vast majority of work on the use of phospholes for organic electronics applications has used pentavalent P due to the tendency of the +3 form to oxidise in air. One of the areas investigated in this thesis is whether the d-block contraction has a similar impact on group 15 heterocycles, known as pnictogens, as it does in group 14 – i.e., whether arsoles show improved stability over phospholes in the +3 oxidation state. Further discussion of this phenomenon can be found in **Chapter 2**.

### *1.4 – Polymerisation reactions*

The most important step in the synthesis of a conjugated polymer is the formation of the carbon-carbon bonds between monomeric units. Although in early research into conjugated polymers this was most often performed using either electrochemical or oxidative polymerisation reactions,[47–49] as monomers have become increasingly complex it has become more common to use transition metal catalysed cross-coupling polymerisations, which have a number of advantages over the alternatives, including their relatively high yields, low miscoupling rates, and tolerance for a wide variety of functional groups.[18,50] Despite differences in the precise chemistry of the reactions, they all share a relatively similar catalytic cycle (**Figure 1.10**), and indeed they are related enough that Richard Heck, Ei-ichi Negishi, and Akira Suzuki shared the 2010 Nobel Prize in Chemistry for the discovery of their respective C-C bond formation reactions.[18,51] The vast majority of transition metal catalysed couplings form carbon-carbon bonds between an electrophile with a relatively reactive C-X bond and an organometallic

nucleophile. This takes place via oxidative addition across the C-X bond, followed by transmetallation with the organometallic compound, with a final reductive elimination step forming the carbon-carbon bond and reforming the catalyst.[18] Common examples used for conjugated polymers include the Sonogashira, Kumada, Suzuki, and Stille reactions, with direct heteroarylation also growing in popularity in recent years.[52] Those of relevance to this thesis are the Stille and direct heteroarylation polymerisations, and to a lesser extent the Buchwald-Hartwig reaction, although this was only used for the preparation of monomers, and is not discussed here.




| Coupling Reaction | M | X | Y |
|---|---|---|---|
| **Stille** | **Pd** | **Cl, Br, I** | **$Sn(alkyl)_3$** |
| **Suzuki** | **Pd** | **Cl, Br, I** | **$B(OR)_2$** |
| **Negishi** | **Pd** | **Cl, Br, I** | **Zinc halide** |

**Figure 1.10: Reaction scheme and catalytic cycle of a typical transition metal catalysed cross-coupling reaction (left). General reaction conditions of three common examples are shown on the right**

In Stille coupling, the electrophilic monomer is functionalised with a halogen, typically either bromine or iodine due to their higher reactivity, while the nucleophile is an organostannane and the catalyst is a palladium compound. Whilst the Stille reaction is highly versatile and a large number of pre-functionalised monomers are commercially available, its major drawback is the toxicity of both the organostannyl monomers and the tin-containing by-products, both of which can cause severe harm to human health as well as posing an environmental hazard.[51,53]

On the other hand, direct heteroarylation is a greener, more atom-efficient method of polymerisation in which one monomer has a suitably labile C-H bond and the other is again functionalised with a halogen. A palladium-based catalytic cycle is involved in the reaction, which is also performed under basic conditions in order to cope with the stoichiometric amounts of acid produced by the coupling.[54] Although direct heteroarylation removes the need to use organotin reagents, which makes synthesis of monomers easier as well as the polymerisation itself more environmentally friendly, it also has problems: only certain C-H bonds are suitable for the reaction as many are not reactive enough, there can be a lack of selectivity if other C-H bonds of a similar reactivity are present in either monomer, and the basic conditions can cause problems with monomer/product stability, limiting the applicability of the reaction.[51] The mechanism of direct arylation is still under investigation, although it is currently believed to involve a catalytic cycle of oxidative addition of the aryl halide to the catalyst and cleavage of the C-H bond of the other monomer, followed by formation of the C-C bond by reductive elimination.[52,55] This is largely analogous to the cycle of other coupling reactions (**Figure 1.10**), with the C-H bond cleavage taking the place of transmetallation step.

### *1.5 – Organic field effect transistors*

Field effect transistors (FETs) are used to amplify signals, and can be used as electrical switches or oscillators.[56] Whilst the vast majority of such transistors are currently manufactured using inorganic materials such as silicon due to their high mobilities and on/off ratios, those based on organic materials have also been investigated both due to their potential for application in low-cost, mass produced products such as radio frequency identification (RFID) tags and more specialised applications such as flexible displays, as well as their fundamental differences from FETs based on inorganic materials such as amorphous silicon.[57]

### *1.5.1 – Basics and device architectures*

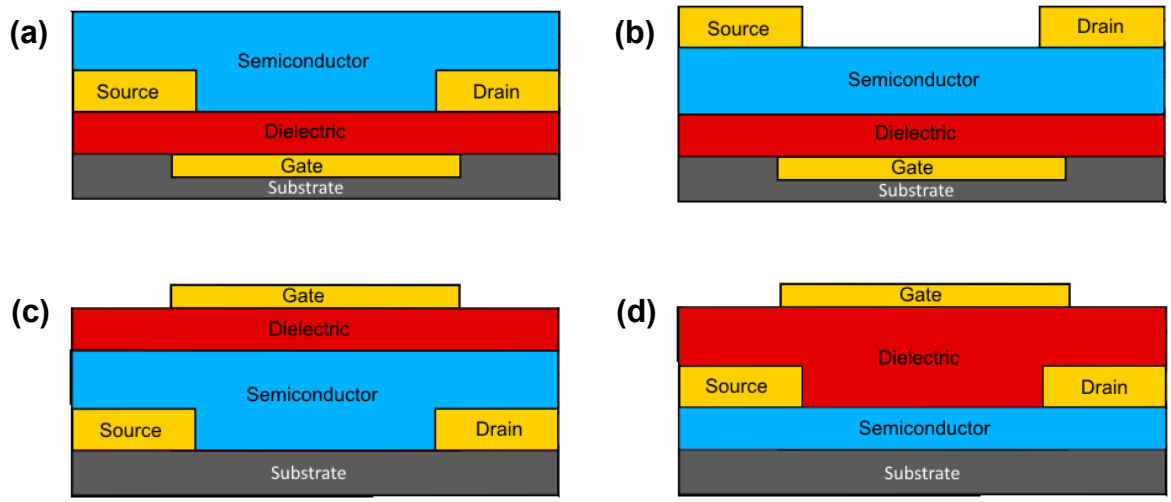



**Figure 1.11: Schematic representations of four different OFET device architectures: (a) bottom-gate, bottom-contact; (b) bottom-gate, top-contact; (c) top-gate, bottom-contact; and (d) top-gate, top-contact**

The three main components of an OFET are the semiconducting layer (a conjugated polymer in this work), an insulating dielectric layer, and three electrodes. However, these key constituents can be arranged in several different ways, providing some key attributes are present. There must be a semiconducting channel between the source and drain electrodes, which must not be in direct contact with each other and should be separated from the gate electrode by a dielectric layer. This leads to four common OFET device architectures, schematics of which can be seen in **Figure 1.11**. The primary difference between them is the location of the electrodes, which impacts not only device behaviour and performance but also the difficulty and scalability of the fabrication techniques due to the different techniques and interlayers required.[57,58]

### *1.5.2 – Operating principles and device characteristics*

The operating principles of OFETs are the same regardless of device architecture. When the device is "on", current flows across the semiconducting channel between the source and drain electrodes, with the potential difference between the drain and the gate electrode being used to modulate the size of the source-drain current. As such, changing the gate voltage ($V_G$) allows the effective size of the semiconducting channel between the source and drain electrodes to be

modified, thereby altering the amount of current flowing through the semiconducting layer. When there is no potential difference between the electrodes, the transistor is said to be unperturbed or "off", and no current flows (**Figure 1.12a**).

When the gate voltage is non-zero but there is still no drain voltage, there will be no current flowing but a charge carrier layer will accumulate at the semiconductor-dielectric interface, forming a channel of mobile charge carriers between the source and drain electrodes (**Figure 1.12b**). In an ideal transistor, this would occur as soon as $V_G \neq 0$, however in reality trap sites must be filled before charge carriers can be mobile. Thus, the gate voltage applied must be higher than the so-called threshold voltage ($V_T$) before a current can flow.

When the gate voltage is greater than the threshold voltage, the charge carriers will begin to flow as the potential difference between the source and drain electrodes is increased, resulting in a drain current being detected. This will increase with increasing drain voltage in what is known as the linear regime (**Figure 1.12c**), which governs device output characteristics until the drain voltage reaches close to the size of the gate voltage. Once this is reached, there will be a pinch-off point and the output characteristics will enter the saturation regime, where drain current no longer changes significantly with increasing drain voltage (**Figure 1.12d**). Higher gate voltages increase the amount of current that can flow before the pinch-off point is reached.

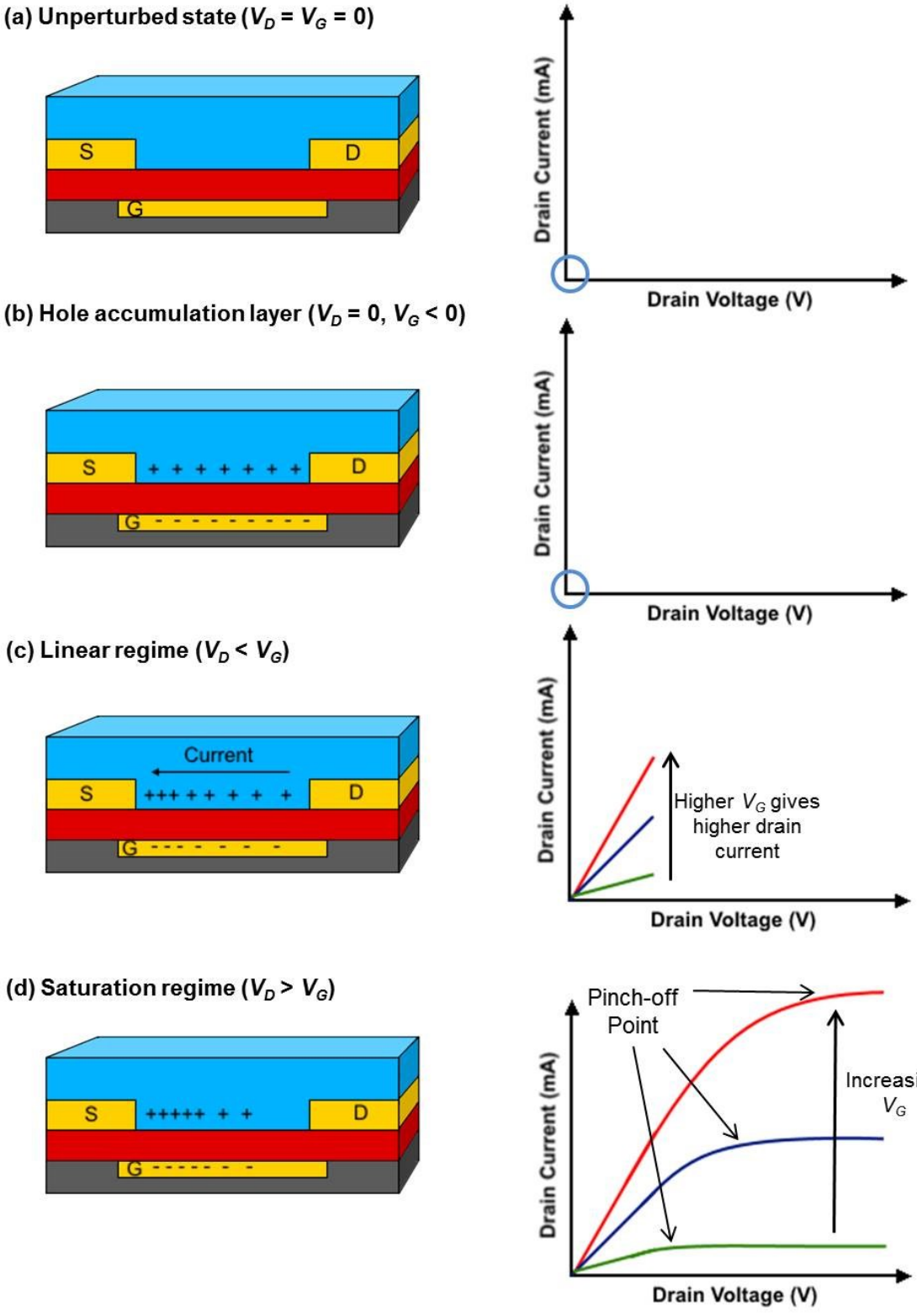



**Figure 1.12: Schematic representations (left) and output characteristics (right) of an ideal p-type OFET device (a) in the unperturbed state, (b) when forming a hole accumulation layer, (c) in the linear regime, and (d) in the saturation regime**

Key device characteristics are the aforementioned threshold voltage ($V_T$), the on/off ratio ($I_{on}/I_{off}$), and the mobility (μ). As already mentioned, the first is a measure of how large the potential required to fill trap sites is. Such traps can be caused by either chemical or morphological impurities in the semiconductor, and are also common at the active interface.[57,59] $V_T$ can be extracted from a plot of the transfer characteristics of a device in the saturation regime, specifically from the position where a tangent of the square root of the drain current would cross the x-axis, as shown in **Figure 1.13**.[57]

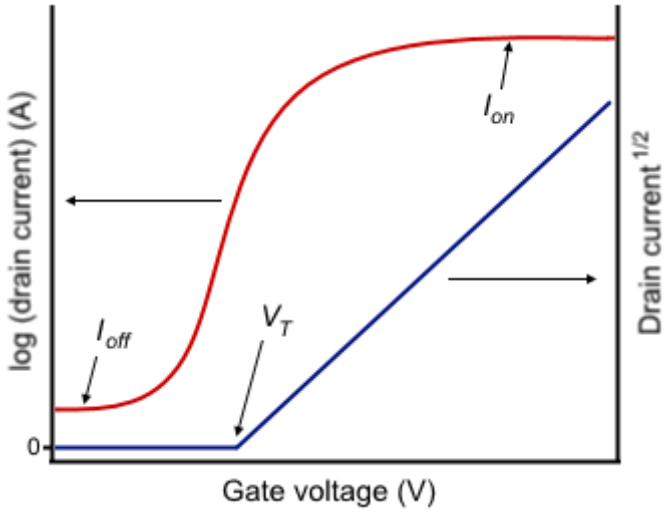



**Figure 1.13: Transfer characteristics for the saturation regime, with the threshold voltage ($V_T$) and on/off currents ($I_{on}$ and $I_{off}$) marked**

The on/off ratio can also be estimated from the transfer characteristics, and is a measure of the difference between the drain currents of a transistor when it is on and when it is off, with larger values being preferable as they indicate better switching behaviour. $I_{on}$ is mostly dependent on the mobility of the semiconductor and the capacitance of the dielectric layer, providing that contact resistance at the source and drain electrodes can be neglected. In an ideal transistor, $I_{off}$ would be zero, however in real devices there is a degree of current leakage (i.e., $I_{off} \neq 0$) due to factors such as interfacial energy differences and semiconductor doping.[57] $I_{off}$ can be minimised by reducing the thickness of the active layer.[60]

The final and arguably most important device characteristic is the mobility, which is a measure of charge transport efficiency measured in charge velocity per unit field.[60] In the linear regime, where $I_D$ is directly proportional to either $V_G$ or $V_D$ at constant drain voltage or constant gate voltage, respectively, mobility can be calculated using the following equation:

$$\mu_{lin} = \frac{\partial I_D}{\partial V_G}\frac{1}{V_D}\frac{L}{WC_0} \qquad \textbf{Equation 1.1}$$

where $\mu_{lin}$ is the linear mobility, $L$ is the channel width (the size of the source and drain contacts), $W$ is the channel length (the distance between the source and drain electrodes), and $C_0$ is the capacitance of the dielectric layer.[58]

However, after the pinch-off point **Equation 1.1** is no longer valid as the current has reached a saturation point and no longer increases substantially with increasing drain voltage. Instead, the square root of the drain current is directly proportional to the gate voltage, as shown in the transfer characteristics (**Figure 1.13**). The gate voltage dependent saturation mobility can be calculated using:[57]

$$\mu_{sat}(V_G) = \frac{\partial I_D}{\partial V_G}\frac{1}{(V_G - V_T)}\frac{L}{WC_0} \qquad \textbf{Equation 1.2}$$

The saturated mobility often gives a more accurate indication of the mobility of a material due to the reduction in contact resistance at high drain voltages. However, it can overestimate the mobility under non-ideal conditions,[61] and so the validity of the saturated mobility should be checked by examining the transfer characteristics of the device. If the saturated mobility is reasonable, the plot of $I_D^{1/2}$ versus $V_G$ should be linear above the threshold voltage (as in **Figure 1.13**), otherwise the linear mobility should be used.[58,62]

### *1.6 – Organic photovoltaics*

Photovoltaic devices operate by converting photons from sunlight into electrical power, with the field having seen a huge expansion in both research and commercialisation over recent

years due to growing concern regarding climate change and energy supply.[63,64] Whilst high-end solar cells are typically made from crystalline silicon or other inorganic materials due to the high efficiencies of these devices, the financial and energetic costs associated with them mean that there is still potential for development of cheaper photovoltaic technologies for new applications.[65] One such alternative is the organic photovoltaic cell, or OPV. As well as being cheaper to produce, OPVs can be manufactured on plastic substrates, giving the potential for the development of lightweight, flexible devices that can be produced on large scales using continuous production techniques such as roll-to-roll gravure printing, spray coating, or inkjet printing.[64,66]

### *1.6.1 – Operating principles*

At a very basic level, OPVs function through the same methods as other solar cell technologies, absorbing photons from sunlight and converting them into electricity. However, there are fundamental differences between how OPVs and traditional inorganic solar cells function. Whilst inorganic materials absorb a photon and immediately produce free charge carriers in the form of an electron-hole pair, in organic materials photoexcitation results in the formation of a coulombically bound electron-hole pair, referred to as an exciton. This is due to the much lower dielectric constants of organic materials, as well as their localised energy states (as opposed to the band structure of those in inorganic semiconductors),[67] and as a result, excitons formed in OPVs require an interface with a material with a different electron affinity or ionisation potential in order to dissociate into free charge carriers.[68] The most common method of achieving this is to use both electron donating and electron accepting materials in the active layer of a device. Although a wide variety of materials have been used for both, those of relevance to this thesis are conjugated polymers and fullerene derivatives for the electron donor and acceptor, respectively.

In most OPV devices with fullerene, the electron donor generally absorbs photons and transports holes to the anode, while the acceptor is used to ensure the excitons dissociate into

free charge carriers and carries electrons to the cathode. Conjugated polymers have a number of characteristics that make them extremely useful as electron donors, including their tuneable band gaps, which can enable them to absorb a broad range of wavelengths of light, and their high absorption coefficients, which means that only thin layers of polymer are required to obtain good absorption yields.[13] On the other hand, fullerene derivatives such as [6,6]-phenyl-$C_{61}$-butyric acid methyl ester ($PC_{61}BM$, **Figure 1.14**) show electron mobilities and LUMO levels that make them suitable electron accepting materials, and also possess solubilising groups that make them soluble in organic solvents and better at blending with conjugated polymers.[18]

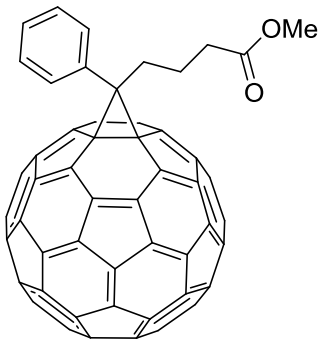



**Figure 1.14: Structure of a common electron accepting unit, $PC_{61}BM$**

During OPV operation, photons are absorbed by the conjugated polymer, resulting in photoexcitation and the formation of an exciton (**Figure 1.15a**). Excitons have limited lifetimes before they decay to the ground state, which means they must diffuse to a donor-acceptor interface within this timeframe in order to dissociate into free charge carriers (**Figure 1.15b**), with the resulting diffusion length generally accepted to be around 10 nm.[69] Upon reaching a donor-acceptor interface, exciton dissociation occurs and free charge carriers are formed (**Figure 1.15c**). After this, the electrons and holes travel through the acceptor/donor materials to the electrodes, resulting in current flowing (**Figure 1.15d**). The precise mechanism of charge transport in OPV devices is the subject of much debate,[63] as well as being beyond the scope of this thesis, and as such it is not discussed here.

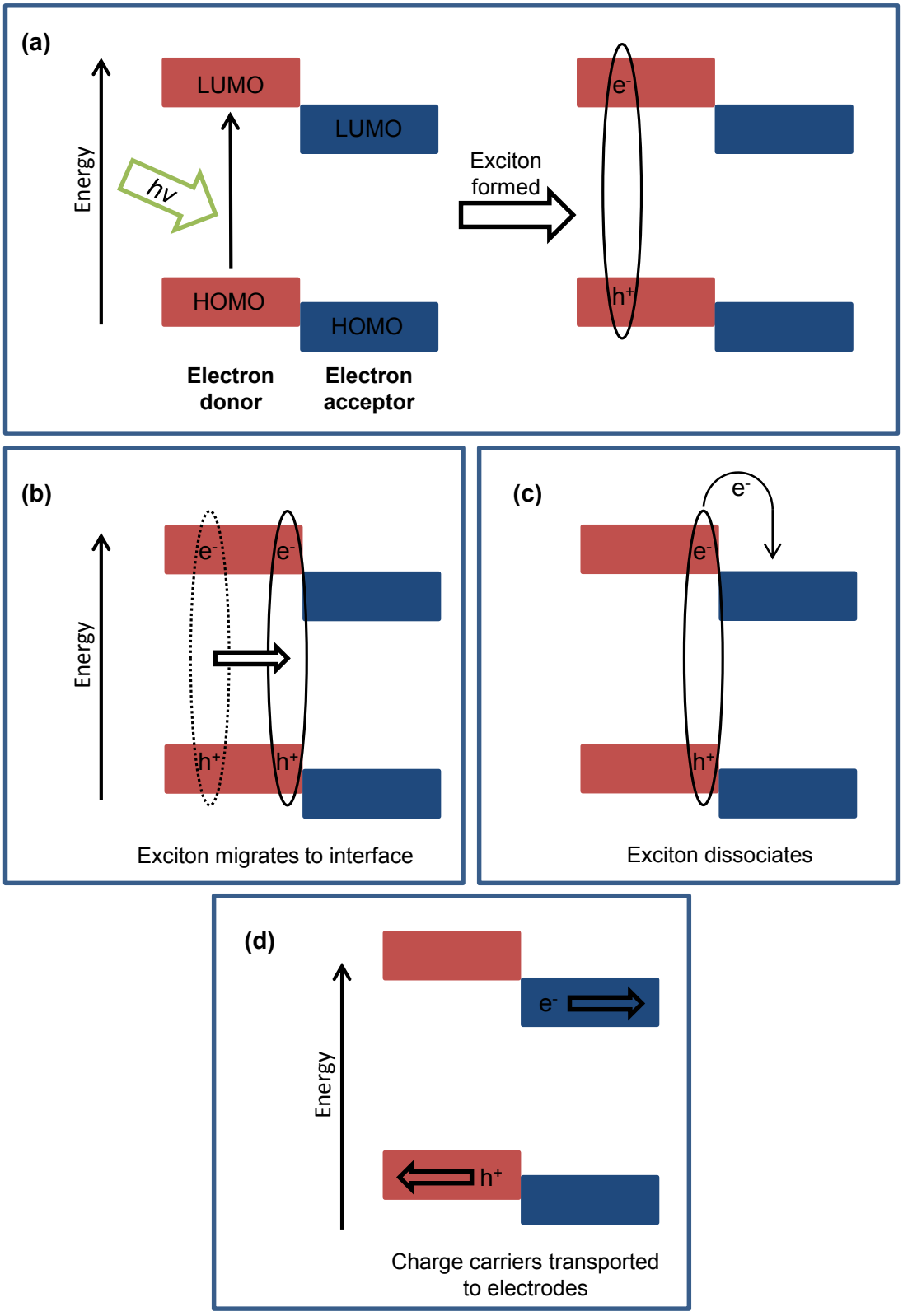



**Figure 1.15: Schematic representations of: (a) photoexcitation of electron donor and exciton formation, (b) exciton migration to the donor-acceptor interface, (c) exciton dissociation to yield free charge carriers, and (d) charge carrier transport to electrodes**

### *1.6.2 – Bulk heterojunction solar cells*

As mentioned above, once a coulombically bound exciton is formed it can travel for approximately 10 nm before decaying back to the ground state. As a result, all excitons should be formed within 10 nm of a donor-acceptor interface in order to maximise the power output of an OPV device, otherwise a large number of excitons will simply decay, thereby wasting the energy of the photon that formed it. This was a significant problem in bilayer donor-acceptor OPV devices, which were initially developed by Tang and coworkers and involve stacking donating and accepting materials to provide a charge-separation interface.[70] Unfortunately all excitons formed outside of the narrow strip around the interface are wasted in such a configuration, resulting in low power conversion efficiencies.[18]




**Figure 1.16: Schematic representations of (a) bilayer heterojunction, and (b) bulk heterojunction active layers for OPV devices**

A common and effective method of remedying this problem is to use a bicontinuous interpenetrating blend of donor and acceptor domains to form a bulk heterojunction (BHJ), as shown in **Figure 1.16**. Rather than first coating one material and then the other, the donor and acceptor are mixed in a solvent and cast as a single active layer with a mixed morphology, dramatically increasing the interfacial area while also reducing the domain sizes, meaning excitons have less far to travel in order to reach an interface. Early research showed that this could lead to ten-fold increases in the efficiencies of solar cells compared to bilayer devices,[71] and further research over the last two decades has resulted in power conversion efficiencies of over 10% for BHJ OPVs.[72,73]

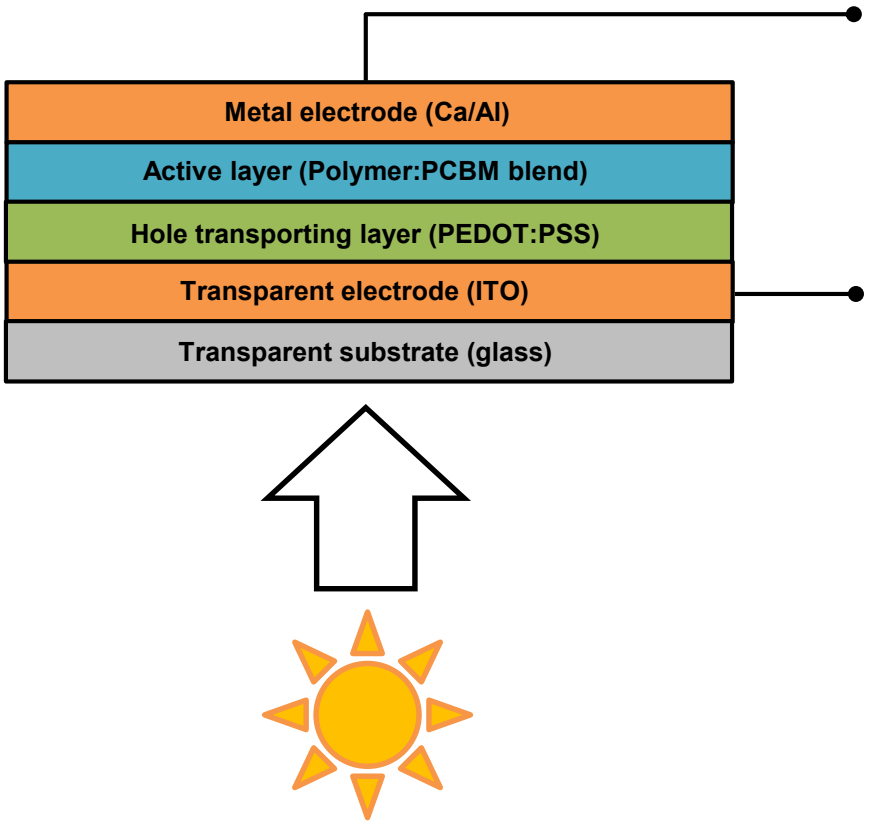



**Figure 1.17: Typical device architecture of a BHJ OPV device, with typical examples of the different layers**

The vast majority of devices discussed in this thesis use a conventional device architecture similar to that shown in **Figure 1.17**. Such devices are typically built on a transparent glass substrate in order to allow light to reach the active layer. The glass is coated with a transparent electrode such as indium tin oxide (ITO), which acts as the anode of the device. This is then coated with a conducting polymer, poly(3,4-ethylenedioxy)thiophene/poly(styrene sulfonate) (PEDOT:PSS), which acts as a hole transporting layer and improves the match between the work function of the ITO anode and the HOMO level of the donor.[65] After this, the BHJ active layer is coated onto the PEDOT:PSS, followed by evaporation of a low work function metallic cathode on the top of the device. Although all that is fundamentally required is for the active layer to be sandwiched between two electrodes with different work functions, additional interlayers such as the hole-transporting PEDOT:PSS layer are often also included to improve device performance by tuning work functions and the interfaces between the different layers.[66] Whilst

there is a vast array of literature regarding optimisation of device architecture, this is beyond the scope of this thesis and is not discussed here.

### *1.6.3 – Device characteristics*

The typical measure of the performance of a photovoltaic device is the power conversion efficiency (PCE). As shown in **Equation 1.3**, the PCE of a device is the product of three key device characteristics: the open circuit voltage ($V_{oc}$), the short circuit current ($J_{sc}$) and the fill factor (FF). In real world applications, it is also affected by the amount and intensity of the light it is exposed to, or the incident photon flux ($P_{in}$); however, in laboratory environments this is standardised by the use of the AM1.5 solar spectrum for device testing, which consists of 100 mW cm$^{-2}$ white light matching the intensity distribution of the sun on the earth's surface at a tilt of 37°.[63] This allows comparison of results from different devices and research groups.

$$PCE = \frac{V_{oc} \cdot J_{sc} \cdot FF}{P_{in}}$$ **Equation 1.3**

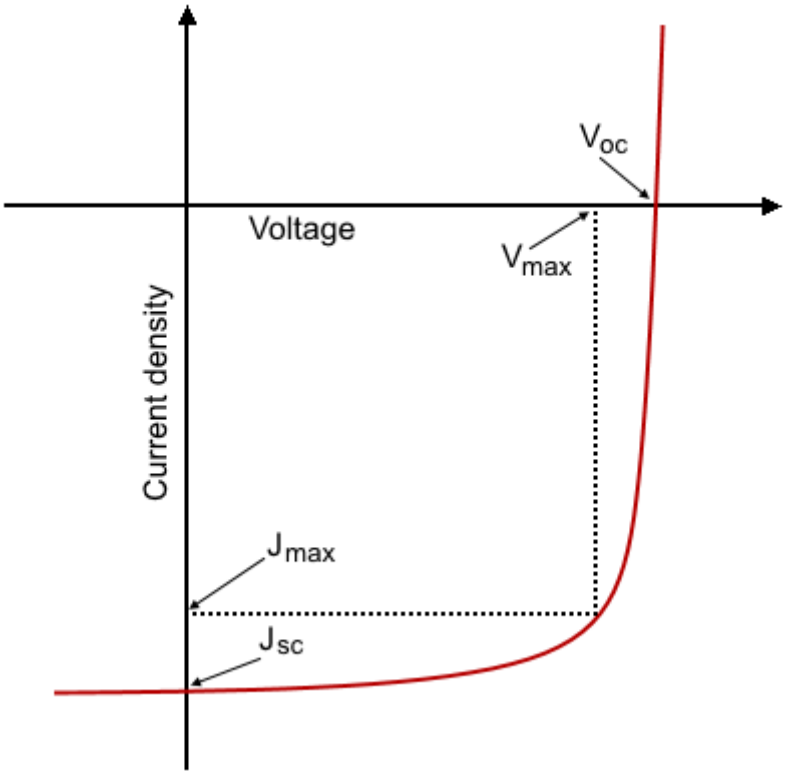



**Figure 1.18: Current-voltage (J-V) curve of an OPV device under illumination, with the positions of important device characteristics marked**

The $V_{oc}$ of a device is a measure of the maximum voltage that can be obtained under open circuit conditions – i.e., when the current is zero. This allows it to be extracted from the J-V curve of a device by finding the point where the curve crosses the x-axis, as shown in **Figure 1.18**. The $V_{oc}$ is largely dictated by the energy gap between the HOMO of the conjugated polymer and the LUMO of the acceptor, and so it is affected by any changes that impact these values. Factors that can increase the $V_{oc}$ are those that make the polymer harder to oxidise (i.e., move the HOMO further from vacuum level) as discussed earlier.[74] However, it is important to consider how the changes being made when tuning the $V_{oc}$ will affect the other device characteristics so that improvements to $V_{oc}$ are not made at the expense of $J_{sc}$ or FF, as this would adversely affect PCE.

On the other hand, the $J_{sc}$ measures the current obtained at a voltage of zero when an OPV device is illuminated – i.e., the current under short-circuit conditions. This means that it can be extracted from the J-V curve of a device in a similar manner to the Voc, as shown in **Figure 1.18**. The primary factor influencing the $J_{sc}$ is the number of photons absorbed by the active layer, which is mostly determined by the band gap of the conjugated polymer and the thickness of the active layer. Smaller band gaps improve the spectral utilisation of a polymer and thus increase the number of photons harvested by the material, whilst thicker active layers can improve the likelihood of a photon being absorbed, thereby having a similar effect. However, active layers that are too thick can be detrimental for charge transport, whilst band gap tuning must take into account the fact that both $V_{oc}$ and device stability both favour low lying HOMO levels in the polymer, so band gap tuning must avoid compromising these if it is to have an overall positive effect on the PCE.[73] There must also be an energetic offset maintained between the polymer LUMO and that of the fullerene, such that it is favourable to split the exciton.

This need to balance $J_{sc}$ and $V_{oc}$ means that the third component of **Equation 1.3**, the fill factor, is of great importance for the PCE. The fill factor is a ratio of the maximum power generated by a device to the maximum theoretical power that it could generate under ideal

conditions. The former is determined from $J_{max}$ and $V_{max}$, while the latter is the product of the $J_{sc}$ and the $V_{oc}$, as shown in **Equation 1.4**.[69]

$$FF = \frac{J_{max} \cdot V_{max}}{J_{sc} \cdot V_{oc}} \qquad \textbf{Equation 1.4}$$

In an ideal photovoltaic device the fill factor would be 1, however this is not seen in practice, with the highest fill factors observed to date being in the region of 0.7–0.8.[75] Although a great deal of research has been conducted into improving the FF of OPVs,[69,75] it has been found that this characteristic is largely determined by factors such as device architecture and morphology, which are not the focus of this thesis. Indeed, FF is often improved during optimisation of OPV devices, and as such it is not of as much interest as $J_{sc}$ and $V_{oc}$ when comparing the performances of different materials, despite its obvious importance when attempting to develop high PCE OPV devices.

### *1.7 – Scope of the thesis*

This thesis focuses on the synthesis and characterisation of peripherally alkylated dithienometalloles and polymers of these materials, as well as their application to OFETs, OPVs, and sensors. As mentioned in **Section 1.3.3**, dithienometalloles have a wide range of attributes that make them useful for organic electronics applications. These moieties commonly have alkyl chains on their central heteroatom that act to confer solubility and processability to the final polymers. However, shifting these alkyl chains to the peripheral 3 and 5 positions allows the use of non-alkylated heteroatoms while maintaining the advantages, enabling use of different heteroatoms such as phosphorus and arsenic or the synthesis of functional molecules capable of responding to chemical stimuli. Although more detailed introductions are provided at the start of each chapter, a brief overview of the work is presented below.

**Chapter 2** of the thesis discusses the synthesis of the first dithieno[3,2-b;2',3'-d]arsole derivative and its copolymerisation with a variety of comonomers to produce polymers for use in OFET devices. In addition, one of the arsole-containing polymers is compared to its

phosphorus-containing analogue in order to investigate the impact of changing the heteroatom in the dithienometallole on polymer behaviour. Finally, some preliminary results on the modification of the arsenic lone pair are presented, along with the synthesis, characterisation, and crystal structure of a dithiazoloarsole analogue.

**Chapter 3** examines the use of polymers containing peripherally alkylated dithienoarsole for OPV applications, specifically comparing the performance of copolymers with benzo[1,2-*b*:4,5-*b*']dithiophene to those containing two-dimensional analogues of this group. In addition, work on donor-acceptor copolymers of benzo[1,2-*b*:4,5-*b*']dithiophene and a 4,7-bis(thiophen-2-yl)-5,6-dicyano-2H-benzo[*d*][1,2,3]triazole moiety is presented.

**Chapter 4** provides details of the synthesis of a dithieno[3,2-b;2',3'-d]pyrrole molecule and its polymerisation with thieno[3,2-*b*]thiophene to yield a polymer for OFET applications. The optoelectronic properties and OFET performance of this polymer was compared with those of analogous materials containing silicon, germanium, and carbonyl bridging groups instead of nitrogen to examine the effect of heteroatoms on polymer behaviour.

**Chapter 5** moves on from device applications of dithienometalloles to examine the use of another peripherally alkylated dithieno[3,2-b;2',3'-d]pyrrole moiety as a sensor for basic solutions. In this system, the use of peripheral alkyl chains allows the use of a secondary amine to bridge the thiophene rings without compromising the solubility of the material. Two types of sensor are discussed, the first being a small molecule colorimetric sensor and the second a polymeric system that could be of use for doping applications.

### *1.8 – References*


1 U. W. Gedde, *Polymer Physics*, Springer Netherlands, Dordrecht, 1999.

2 C. K. Chiang, C. R. Fincher, Y. W. Park, A. J. Heeger, H. Shirakawa, E. J. Louis, S. C. Gau and A. G. MacDiarmid, *Phys. Rev. Lett.*, 1977, **39**, 1098–1101.

3 H. Shirakawa, E. J. Louis, A. G. MacDiarmid, C. K. Chiang and A. J. Heeger, *J. Chem. Soc. Chem. Commun.*, 1977, 578–580.

4 R. Farchioni and G. Grosso, *Organic Electronic Materials*, Springer Berlin Heidelberg, Berlin, Heidelberg, 2001, vol. 41.

5 J.-H. Jou, S. Kumar, A. Agrawal, T.-H. Li and S. Sahoo, *J. Mater. Chem. C*, 2015, **3**, 2974–3002.

6 H. Sirringhaus, *Adv. Mater.*, 2014, **26**, 1319–1335.

7 X. Guo, M. Baumgarten and K. Müllen, *Prog. Polym. Sci.*, 2013, **38**, 1832–1908.

8 S. Löffler, B. Libberton and A. Richter-Dahlfors, *Electronics*, 2015, **4**, 879–908.

9 A. J. Heeger, *J. Phys. Chem. B*, 2001, **105**, 8475–8491.

10 R. E. Peierls, *Quantum Theory of Solids*, Clarendon, Oxford, 1955.

11 Z. Fei, P. Pattanasattayavong, Y. Han, B. C. Schroeder, F. Yan, R. J. Kline, T. D. Anthopoulos and M. Heeney, *J. Am. Chem. Soc.*, 2014, **136**, 15154–15157.

12 R. K. Pai, A. T. N. and H. B., *RSC Adv.*, 2016, **6**, 23760–23774.

13 L. Dou, Y. Liu, Z. Hong, G. Li and Y. Yang, *Chem. Rev.*, 2015, **115**, 12633–12665.

14 T. Izumi, S. Kobashi, K. Takimiya, Y. Aso and T. Otsubo, *J. Am. Chem. Soc.*, 2003, **125**, 5286–5287.

15 C. Müller, *Chem. Mater.*, 2015, **27**, 2740–2754.

16 U. Salzner, J. B. Lagowski, P. G. Pickup and R. A. Poirier, *Synth. Met.*, 1998, **96**, 177–189.

17 J. L. Brédas, *J. Chem. Phys.*, 1985, **82**, 3808.

18 Y.-J. Cheng, S.-H. Yang and C.-S. Hsu, *Chem. Rev.*, 2009, **109**, 5868–5923.

19 F. Wudl, M. Kobayashi and A. J. Heeger, *J. Org. Chem.*, 1984, **49**, 3382–3384.

20 R. S. Kularatne, H. D. Magurudeniya, P. Sista, M. C. Biewer and M. C. Stefan, *J. Polym. Sci. Part A Polym. Chem.*, 2013, **51**, 743–768.

21 G. L. Gibson, T. M. McCormick and D. S. Seferos, *J. Am. Chem. Soc.*, 2012, **134**, 539–547.

22 C. J. Brabec, M. Heeney, I. McCulloch and J. Nelson, *Chem. Soc. Rev.*, 2011, **40**, 1185–1199.

23 L. Lu, T. Zheng, Q. Wu, A. M. Schneider, D. Zhao and L. Yu, *Chem. Rev.*, 2015, **115**, 12666–12731.

24 S. C. Rasmussen, *ChemTexts*, 2016, **2**, 16.

25 G. Zotti, G. Schiavon, A. Berlin, G. Fontana and G. Pagani, *Macromolecules*, 1994, **27**, 1938–1942.

26 C. Soci, I. W. Hwang, D. Moses, Z. Zhu, D. Waller, R. Gaudiana, C. J. Brabec and A. J. Heeger, *Adv. Funct. Mater.*, 2007, **17**, 632–636.

27 Z. Zhu, D. Waller, R. Gaudiana, M. Morana, D. Mühlbacher, M. Scharber and C. Brabec,

*Macromolecules*, 2007, **40**, 1981–1986.

28 M. Morana, H. Azimi, G. Dennler, H. J. Egelhaaf, M. Scharber, K. Forberich, J. Hauch, R. Gaudiana, D. Waller, Z. Zhu, K. Hingerl, S. S. Van Bavel, J. Loos and C. J. Brabec, *Adv. Funct. Mater.*, 2010, **20**, 1180–1188.

29 M. E. Cinar and T. Ozturk, *Chem. Rev.*, 2015, **115**, 3036–3140.

30 S. C. Rasmussen and S. J. Evenson, *Prog. Polym. Sci.*, 2013, **38**, 1773–1804.

31 A. M. Priegert, B. W. Rawe, S. C. Serin and D. P. Gates, *Chem. Soc. Rev.*, 2016, **45**, 922–953.

32 G. L. Gibson and D. S. Seferos, *Macromol. Chem. Phys.*, 2014, **215**, 811–823.

33 S. Parke, M. Boone and E. Rivard, *Chem. Commun.*, 2016, **52**, 9485–9505.

34 J. Chen and Y. Cao, *Macromol. Rapid Commun.*, 2007, **28**, 1714–1742.

35 H. Zhong, Z. Li, F. Deledalle, E. C. Fregoso, M. Shahid, Z. Fei, C. B. Nielsen, N. Yaacobi-Gross, S. Rossbauer, T. D. Anthopoulos, J. R. Durrant and M. Heeney, *J. Am. Chem. Soc.*, 2013, **135**, 2040–2043.

36 M. A. Shameem and A. Orthaber, *Chem. - A Eur. J.*, 2016, **22**, 10718–10735.

37 Z. Fei, R. S. Ashraf, Y. Han, S. Wang, C. P. Yau, P. S. Tuladhar, T. D. Anthopoulos, M. L. Chabinyc and M. Heeney, *J. Mater. Chem. A*, 2015, **3**, 1986–1994.

38 E. I. Carrera and D. S. Seferos, *Macromolecules*, 2015, **48**, 297–308.

39 S. Yamaguchi, Y. Itami and K. Tamao, *Organometallics*, 1998, **17**, 4910–4916.

40 A. C. Spivey, C.-C. Tseng, J. P. Hannah, C. J. G. Gripton, P. de Fraine, N. J. Parr and J. J. Scicinski, *Chem. Commun.*, 2007, 2926.

41 Z. Fei, J. S. Kim, J. Smith, E. B. Domingo, T. D. Anthopoulos, N. Stingelin, S. E. Watkins, J.-S. Kim and M. Heeney, *J. Mater. Chem.*, 2011, **21**, 16257.

42 J. Crassous and R. Réau, *Dalt. Trans.*, 2008, 6865.

43 D. Delaere, M. T. Nguyen and L. G. Vanquickenborne, *J. Organomet. Chem.*, 2002, **643–644**, 194–201.

44 T. Baumgartner and R. Réau, *Chem. Rev.*, 2006, **106**, 4681–4727.

45 M. G. Hobbs and T. Baumgartner, *Eur. J. Inorg. Chem.*, 2007, 3611–3628.

46 Y. Dienes, S. Durben, T. Kárpáti, T. Neumann, U. Englert, L. Nyulászi and T. Baumgartner, *Chem. - A Eur. J.*, 2007, **13**, 7487–7500.

47 A. Berlin, G. Pagani, G. Zotti and G. Schiavon, *Die Makromol. Chemie*, 1992, **193**, 399–409.

48 Y. Wei, C. C. Chan, J. Tian, G. W. Jang and K. F. Hsueh, *Chem. Mater.*, 1991, **3**, 888–897.

49 N. Gospodinova and L. Terlemezyan, *Prog. Polym. Sci.*, 1998, **23**, 1443–1484.

50 S. Xu, E. H. Kim, A. Wei and E. Negishi, *Sci. Technol. Adv. Mater.*, 2014, **15**, 44201.

51 A. Marrocchi, A. Facchetti, D. Lanari, C. Petrucci and L. Vaccaro, *Energy Environ. Sci.*, 2016, **9**, 763–786.

52 T. Bura, J. T. Blaskovits and M. Leclerc, *J. Am. Chem. Soc.*, 2016, **138**, 10056–10071.

53 R. D. Kimbrough, *Environ. Health Perspect.*, 1976, **14**, 51–56.

54 P.-O. Morin, T. Bura and M. Leclerc, *Mater. Horiz.*, 2016, **3**, 11–20.

55 L. G. Mercier and M. Leclerc, *Acc. Chem. Res.*, 2013, **46**, 1597–1605.

56 W. Wu, Y. Liu and D. Zhu, *Chem. Soc. Rev.*, 2010, **39**, 1489–1502.

57 J. Zaumseil and H. Sirringhaus, *Chem. Rev.*, 2007, **107**, 1296–1323.

58 F. So, Ed., *Organic Electronics: Materials, Processing, Devices and Applications*, CRC Press, Boca Raton, USA, 2010.

59 H. Sirringhaus, *Adv. Mater.*, 2005, **17**, 2411–2425.

60 B. Kumar, B. K. Kaushik and Y. S. Negi, *Polym. Rev.*, 2014, **54**, 33–111.

61 E. G. Bittle, J. I. Basham, T. N. Jackson, O. D. Jurchescu and D. J. Gundlach, *Nat. Commun.*, 2016, **7**, 10908.

62 G. Horowitz, P. Lang, M. Mottaghi and H. Aubin, *Adv. Funct. Mater.*, 2004, **14**, 1069–1074.

63 G. Hadziioannou and G. G. Malliaras, Eds., *Semiconducting Polymers: Chemistry, Physics and Engineering*, Wiley-VCH Verlag GmbH & Co. KGaA, Weinheim, FRG, 2nd edn., 2007.

64 W. Cao and J. Xue, *Energy Environ. Sci.*, 2014, **7**, 2123–2144.

65 R. Po, M. Maggini and N. Camaioni, *J. Phys. Chem. C*, 2010, **114**, 695–706.

66 M. C. Scharber and N. S. Sariciftci, *Prog. Polym. Sci.*, 2013, **38**, 1929–1940.

67 S. D. Dimitrov and J. R. Durrant, *Chem. Mater.*, 2014, **26**, 616–630.

68 B. C. Thompson and J. M. J. Fréchet, *Angew. Chemie Int. Ed.*, 2008, **47**, 58–77.

69 M.-H. Jao, H.-C. Liao and W.-F. Su, *J. Mater. Chem. A*, 2016, **4**, 5784–5801.

70 C. W. Tang, *Appl. Phys. Lett.*, 1986, **48**, 183–185.

71 G. Yu, J. Gao, J. C. Hummelen, F. Wudl and A. J. Heeger, *Science (80-. ).*, 1995, **270**, 1789–1791.

72 U. Mehmood, A. Al-Ahmed and I. A. Hussein, *Renew. Sustain. Energy Rev.*, 2016, **57**, 550–561.

73 G. Luo, X. Ren, S. Zhang, H. Wu, W. C. H. Choy, Z. He and Y. Cao, *Small*, 2016, **12**, 1547–1571.

74 N. K. Elumalai and A. Uddin, *Energy Environ. Sci.*, 2016, **9**, 391–410.

75 D. Bartesaghi, I. D. C. Pérez, J. Kniepert, S. Roland, M. Turbiez, D. Neher and L. J. A. Koster, *Nat. Commun.*, 2015, **6**, 7083.

# *Chapter 2*

# *Arsoles in Organic Field Effect Transistors*

Some of the results in this chapter have been published in the following paper: **J. P. Green**, Y. Han, R. Kilmurray, M. A. McLachlan, T. D. Anthopoulos, M. Heeney, *Angew. Chem. Int. Ed.* **2016**, *55*, 7148 (DOI: 10.1002/ange.201602491)

### *2.1 – Introduction*

Researchers in the field of plastic electronics are showing increasing interest in the incorporation of heavier atoms into conjugated materials as replacements for more common elements such as carbon, nitrogen, and sulfur. Examples of this trend can be seen in the use of silicon and germanium from group 14, selenium and tellurium from group 16, and phosphorus from group 15.[1–6] Materials containing these heavy atoms have been observed to show noticeable changes in band gap, energy level, and solid-state packing compared to their lighter analogues,[7] as well as improved intersystem crossing efficiencies that can lead to rapid conversion of singlets to triplets,[8] and in some instances solid-state phosphorescence.[9]

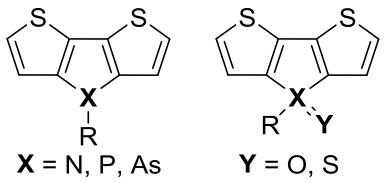



**Figure 2.1: Structures of pnictogen-containing dithienometalloles**

One of the most common classes of group 15 element-containing materials used in conjugated polymers is based around pyrrole and its phosphorus-containing analogue, phosphole, where the aforementioned elements act as bridges between two thiophene rings in a dithienometallole-type system (**Figure 2.1**), with the resulting dithieno[3,2-*b*:2',3'-*d*]pyrrole and dithieno[3,2-*b*:2',3'-*d*]phosphole compounds seeing use in all major areas of plastic electronics.[10–12] Dithienophosphole (DTPh) has attracted particular interest due to the σ-π hyperconjugation observed in the phosphole ring, whereby the σ*-orbital of the exocyclic P-C bond can interact with the π-orbitals of the main ring system.[13] Furthermore, the energy levels of DTPh can be modified by reaction at the phosphorus lone pair using either oxidizing agents or Lewis acids.[14] In fact, the instability of phospholes in the +3 oxidation state can lead to uncontrolled oxidation under ambient conditions, and so the majority of phosphole-containing materials are deliberately oxidized to prevent uncontrolled aging.[15] Unfortunately, this results in the properties of unoxidized phospholes rarely being reported on.

The arsenic-containing analogue of dithienopyrrole and DTPh is dithienoarsole (DTAs). Arsoles have been studied less than their nitrogen- and phosphorus-containing counterparts, likely due to the toxicity of many arsenic precursors, but they have been found to possess many similar characteristics to phospholes, including low aromaticity and tuneable energy levels through lone pair modification.[16–18] Additionally, the arsenic atom is more stable to oxidation to the +5 state than phosphorus due to the poor shielding afforded by the filled 3d orbitals in arsenic, which results in the element possessing relatively tightly bound s-electrons compared to phosphorus.[19–22] As such, arsole-containing polymers are expected to be more resistant to ambient oxidation than their phosphole analogues, allowing the properties of heterocycles containing the pnictogen in the +3 oxidation state to be studied. Despite these interesting potential properties, to the best of my knowledge there have been no reports of arsoles being used in organic electronics applications before this work.

This chapter will discuss the synthesis of a novel dithieno[3,2-*b*:2',3'-*d*]arsole monomer, its oxidative stability, and the polymerization of this material with three different comonomers via Pd-catalysed Stille polymerization. Although polymerization of analogous DTPh materials has been reported in the literature, it has always been performed with the phosphorus in the +5 oxidation state (typically DTPh-oxides), whereas this work investigates the arsole in the +3 oxidation state. The properties of the resulting polymers will be investigated, and their performance in organic field effect transistors (OFETs) will be tested. Additionally, preliminary results relating to the modification of the DTAs lone pair and the synthesis and crystal structure of a dithiazoloarsole analogue are presented.

## *2.2 – Synthesis of dithienoarsole monomers*

### *2.2.1 – Preparation of dithienoarsole*

The synthesis of peripherally alkylated dithienoarsole from a readily available starting material, 3-bromothiophene, is shown in **Figure 2.2**. The initial step involved Kumada cross-

coupling of dodecylmagnesium bromide and **2.1** using a nickel catalyst to yield 3-dodecylthiophene in 82% yield, as previously reported in the literature.[23] The resulting alkythiophene **2.2** was coupled in a head-to-head fashion by lithiation at the less-hindered 5 position with a bulky TMEDA/*n*BuLi complex, followed by addition of $CuCl_2$ to give **2.3** in a 60% yield.[24] Bromination of all four aromatic positions was carried out using elemental bromine and acetic acid, providing an 87% yield of **2.4**.[25] Although it was possible to synthesise **2.6** directly from the tetrabrominated product by dilithiation followed by quenching with methanol or water, it was found that a higher yield was obtained by instead quenching the dianion with TMSCl to give **2.5**, and then removing the silyl groups with TBAF, yielding **2.6** in 95% over two steps as opposed to ~75% over a single step.

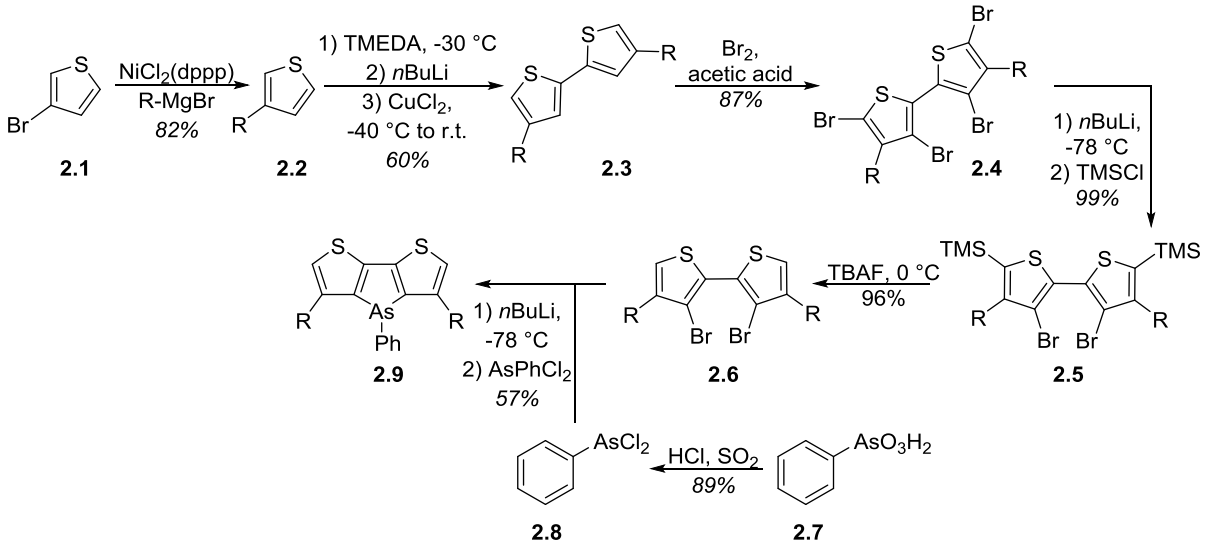



**Figure 2.2: Synthesis of 3,5-didodecyl-4-phenyldithieno[3,2-*b*:2',3'-*d*]arsole (2.9), where R represents dodecyl side chains**

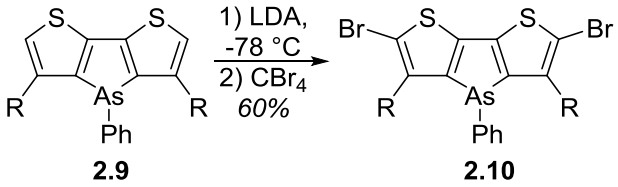
Having **2.6** in hand, it was then necessary to close the arsole ring to produce the target molecule, dithienoarsole **2.9**. Many arsenic-containing compounds are highly toxic, and safety precautions should be used at all times when working with arsoles and their precursors. To perform the ring closure, dichlorophenylarsine (**2.8**) was first synthesised in one step from the commercially available arsenic compound phenylarsonic acid (**2.7**).[26] The resulting arsine is known to be a strong vesicant and lachrymator, but when properly handled it could be used to quench the dilithium salt of **2.6**, which was produced by reaction with *n*BuLi at -78 °C. This ring

closure resulted in a 57% yield of **2.9**, which was a stable, off-white, low melting-point solid that did not show signs of oxidation when stored in air. The presence of the phenyl ring on the arsenic (instead of the solubilizing alkyl chains often seen on the heteroatoms of dithienometalloles) could have resulted in polymers with low solubilities, and so the peripheral alkyl chains at the 3 and 5 positions were a deliberate choice to ensure good polymer solubility and thus good processability.

Synthesis of a dithienoarsole directly from **2.5** was also tested, and was found to yield the disilylated analogue of **2.9**. However, the purification of this product was complicated by proto-desilylation at the 2 and 6 positions during column chromatography. In combination with the high yields of **2.6** previously mentioned, this meant the synthetic route shown in **Figure 2.2**, whereby the silyl groups were removed with TBAF to yield **2.6** before arsole ring closure, was preferable to both the alternatives.

In order to allow polymerisation via Stille coupling, the dithienoarsole first had to be suitably functionalised. As Stille polymerisation takes place between stannylated and halogenated monomers, both bromination and stannylation of the material were investigated to enable maximum synthetic flexibility.

### *2.2.2 – Bromination of dithienoarsole*




**2.9** **2.10**

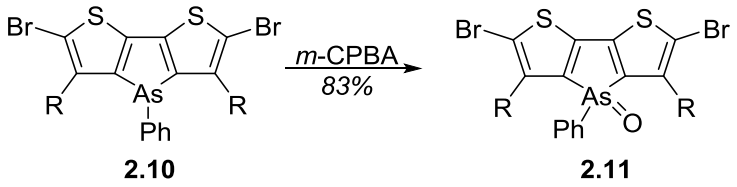
**Figure 2.3: Synthesis of 2,6-dibromo-3,5-didodecyl-4-phenyldithieno[3,2-*b*:2',3'-*d*]arsole (2.10), where R represents dodecyl side chains**

Initial attempts to brominate **2.9** focused on electrophilic bromination using NBS. However, although some product was detected by $^{1}$H NMR and mass spectrometry, it was found that the oxidizing nature of NBS also caused formation of significant amounts of the arsole-oxide, which lowered the yield of this route. This prompted the exploration of non-oxidising bromination

conditions, whereupon it was found that **2.9** could be effectively dilithiated using LDA and the resulting dianion quenched with carbon tetrabromide to give a 60% yield of **2.10,** with minimal formation of the undesired oxide.

#### *2.2.2.1 – Oxidation of dibromo-dithienoarsole*

In order to test the viability of the use of unoxidised arsoles as materials for conjugated polymers, the oxidative stability of **2.10** in ambient air was studied over the course of several weeks. Unfortunately, there have been few reports of arsoles and arsole oxides in the literature,[17] and unlike phosphorus, arsenic cannot be readily investigated by NMR. Although $^{75}$As is an NMR-active species, the large quadrupolar moment of the nucleus and its low resonance frequency mean it is very difficult to detect, and the vast majority of the limited literature regarding $^{75}$As NMR has focused on characterisation of small, relatively symmetric arsenic salts.[27,28]




**2.10** **2.11**

**Figure 2.4: Conversion of 2,6-dibromo-3,5-didodecyl-4-phenyldithieno[3,2-*b*:2',3'-*d*]arsole to its oxide (2.11), where R represents dodecyl chains**

To work around these issues, the arsole oxide equivalent of **2.10**, 2,6-dibromo-3,5-didodecyl-4-phenyldithieno[3,2-*b*:2',3'-*d*]arsole-4-oxide (**2.11**), was deliberately synthesised to allow direct comparison of the pristine arsole and the oxidised product. Initially, this oxidation was attempted using hydrogen peroxide, which is known to give almost quantitative yields when used to oxidise dithienophospholes.[12] Despite this, hydrogen peroxide was found to be ineffective for the oxidation of **2.10**, with a yield of around 40% and the majority of the arsole remaining unoxidised, indicating that a stronger oxidising agent was needed. Use of *m*-CPBA resulted in a significant improvement in the yield of **2.11** to 83%, although a small amount of unreacted starting material was still recovered even when excess oxidant was applied.

Fortunately, as can be seen in **Figure 2.5**, significant differences were observed between the $^{1}$H NMR spectra of **2.10** and **2.11**, making this reaction relatively easy to monitor as well as providing a simple method of checking the monomer for oxidation.

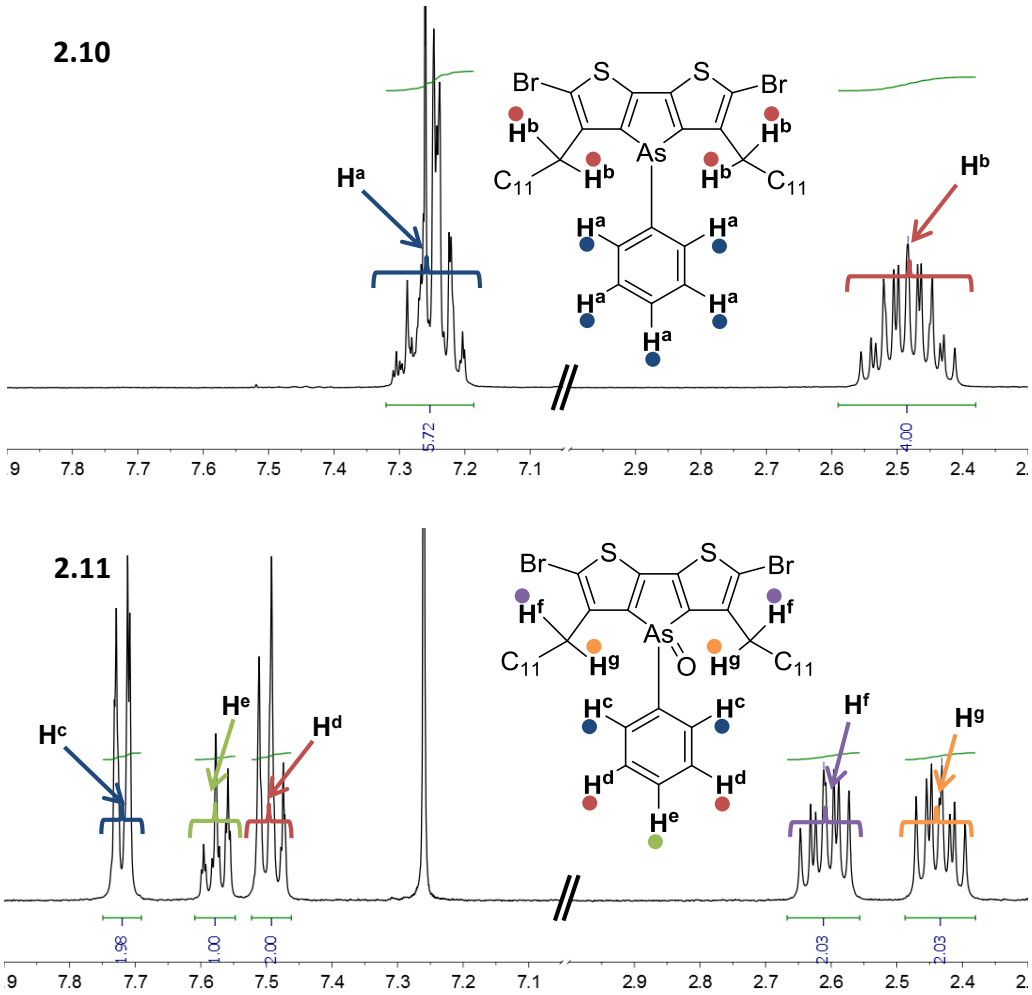



**Figure 2.5: $^{1}$H NMR spectra of 2.10 (top) and 2.11 (bottom) in the regions 7.05–7.90 ppm (left) and 2.30–3.00 ppm (right)**

After oxidation, the phenylic protons split from their original overlapping multiplet at around 7.25 ppm ($H^{a}$), shifting downfield into distinct locations depending on their ring positions. The two *ortho*-protons ($H^{c}$) were most affected by the oxidation, moving to 7.72 ppm, with the single *para*-proton ($H^{e}$) located at 7.58 ppm, and the two *meta*-protons ($H^{d}$) at 7.49 ppm. Similarly, the first two protons on each dodecyl chain also showed a change on oxidation, going from a single complex multiplet centred around 2.48 ppm ($H^{b}$) to two multiplets at 2.61 ppm ($H^{f}$) and 2.43 ppm ($H^{g}$). All of these changes were due to the addition of

an oxygen atom in the place of the lone pair, which withdrew some electron density from the dithienoarsole unit, causing deshielding of the phenylic and alkyl protons. As well as this, the presence of the oxygen atom further restricts the rotation of the alkyl chains at the 3 and 5 positions, increasing the degeneracy of the α-protons on these chains.

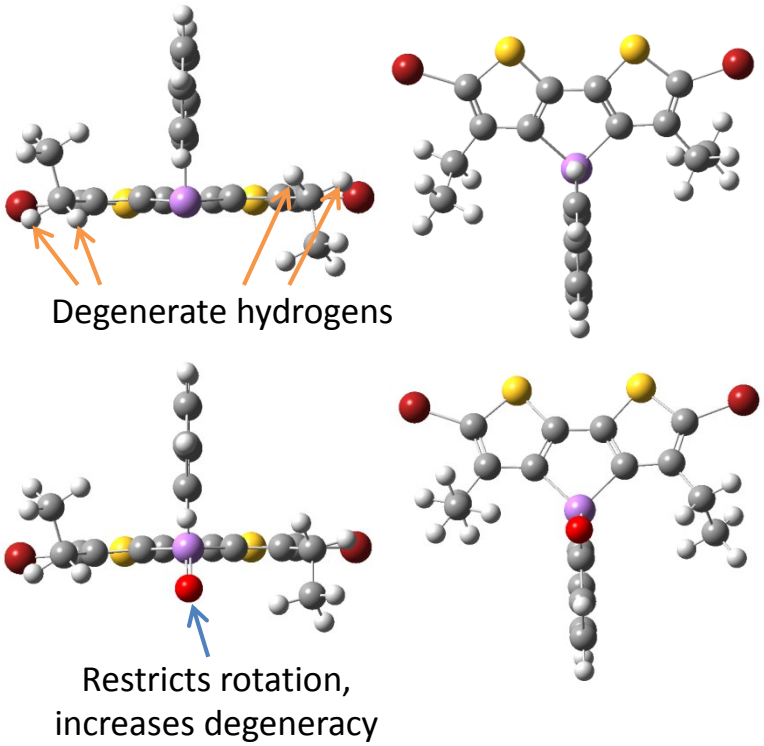



**Figure 2.6: Optimised structures of 2.10 (top) and 2.11 (bottom) as calculated using Gaussian 09 at the B3LYP level of theory with the 6-311G(d,p) basis set**

The differences between the $^{1}$H NMR spectra of **2.10** and **2.11** are complimented by changes in the UV-vis spectrum on oxidation. As shown in **Figure 2.7**, the conversion of the arsole from the +3 to +5 oxidation state was accompanied by a 25 nm red shift in $\lambda_{max}$, likely due to the increased electron-accepting ability of the arsenic atom, analogous to the changes seen when dithienophospholes are oxidised.[29]

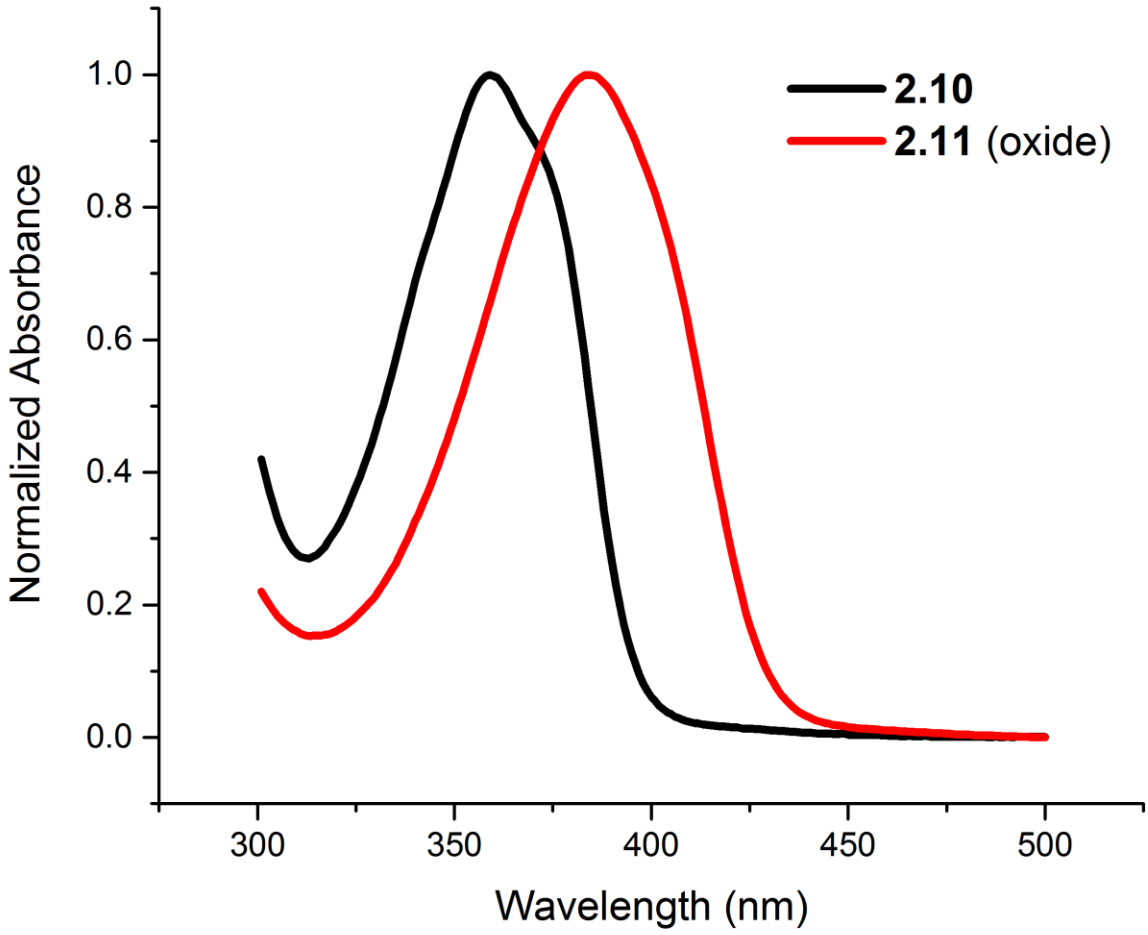



**Figure 2.7: UV-vis spectra of 2.10 and 2.11 in chloroform solutions**

A sample of **2.10** stored for 6 months under ambient conditions displayed no signs of oxidation to **2.11** by $^{1}$H NMR or UV-vis spectroscopy. The resistance of the dithienoarsole unit to oxidation is in agreement with the poor shielding ability of the arsenic 3d orbitals, and contrasts with the susceptibility of the dithienophosphole unit to oxidation. Recent work by Naka et al. has also found that 2,5-diarylarsoles are more air-stable than their phosphole analogues, in agreement with these findings.[17]

### *2.2.3 – Stannylation of dithienoarsole*

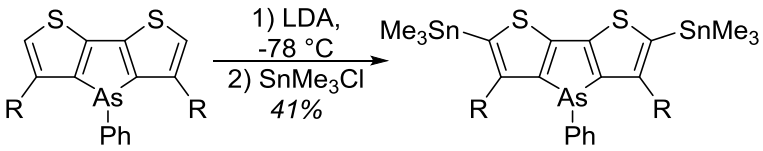



**Figure 2.8: Stannylation of 3,5-didodecyl-4-phenyldithieno[3,2-*b*:2',3'-*d*]arsole, where R represents dodecyl side chains**

As an alternative to the dibromo monomer, the dithienoarsole unit was also stannylated, using similar conditions to those used for the bromination. First, the arsole was dilithiated using LDA, and then the dianion was quenched using trimethylstannyl chloride to give the product. Due to the sensitivity of the stannyl group to the normal phase silica used in column chromatography, compound **2.12** was purified by recycling GPC (hexane, 40 °C) using cross-linked polystyrene columns in order to remove any mono- or non-stannylated material, the presence of which would have decreased the efficiency of the Stille polymerisation. This resulted in a 41% yield of **2.12**, with no signs of oxide formation being visible in the $^{1}$H NMR spectrum.

### *2.3 – Polymerization with vinylene*

Stille polymerisation of 2,6-dibromo-3,5-didodecyl-4-phenyldithieno[3,2-*b*:2',3'-*d*]arsole (**2.10**) was carried out with *trans*-1,2-bis(tributylstannyl)ethene in a microwave reactor, with $Pd(PPh_3)_4$ used as the catalyst. Vinylene was chosen as the comonomer for this reaction because of its proven ability to reduce steric interactions between 3,5-alkylated bridged bithiophenes, which enables planarization of the polymer backbone and hence enhancement of conjugation length.[30]

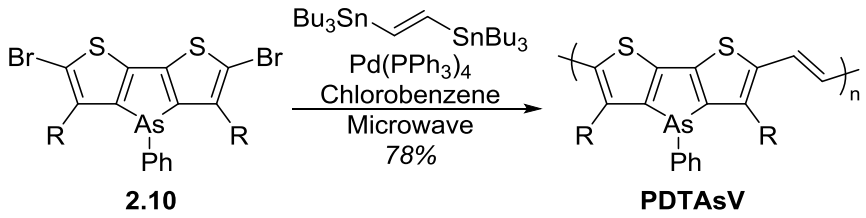



**Figure 2.9: Polymerisation of 2,6-dibromo-3,5-didodecyl-4-phenyldithieno[3,2-*b*:2',3'-*d*]arsole with *trans*-1,2-bis(tributylstannyl)ethane, where R represents dodecyl side chains**

Although the arsenic atom was a potential binding site for the palladium catalyst, there were no indications that this had any detrimental impact on the polymerisation (see **Section 2.4.2**), as expected due to the weaker donor nature of the triphenylarsine ligand in comparison with its triphenylphosphine analogue.[31] After synthesis in the microwave reactor, the polymer was precipitated in methanol and purified by Soxhlet extraction with methanol and acetone in order to remove residual catalyst and low molecular weight oligomers, and then with hexane to provide the crude polymer. This was then washed with the strongly complexing ligand diethylammonium diethyldithiocarbamate in order to remove any remaining traces of catalyst.[32] After a final precipitation into methanol, **PDTAsV** was obtained as a dark blue solid in a yield of 78%. The $M_n$ as determined by GPC in chlorobenzene (80 °C) against polystyrene standards was 12.3 kg/mol, with $M_w$ = 23.6 kg/mol and Đ = 1.92. **PDTAsV** was soluble in a wide range of organic solvents, including hot hexane and a variety of chlorinated solvents such as chloroform and chlorobenzene.

The structure of **PDTAsV** was confirmed by elemental analysis, which was in excellent agreement with the theoretical values, as well as by $^1$H NMR. Despite significant broadening of the signals, the phenylic protons were still clustered around 7.25 ppm indicating that the arsenic was still in the +3 oxidation state, with the vinyl protons being visible at around 6.9 ppm. Together with the matching elemental analysis, this provided a good indication that the material was stable to the polymerisation and purification conditions.

### *2.3.1 – Optical properties*

The absorption spectra of **PDTAsV** in chlorobenzene solution and as a thin film were studied by UV-vis absorption spectroscopy, as shown in **Figure 2.10a**. In chlorobenzene solution, $\lambda_{max}$ of **PDTAsV** was 616 nm, with a strong shoulder at 652 nm. After spin coating from chlorobenzene solution, $\lambda_{max}$ red-shifted to 638 nm with the shoulder appearing at 682 nm, indicating an increase in molecular ordering on transition from the solution to the solid state. The presence of red-shifted shoulders in UV-vis spectra of conjugated polymers is often related to the existence of a more planar state, with the intensity of such shoulders often increasing when films are annealed and decreasing when solutions are heated. In the case of the shoulder observed in **PDTAsV**, however, annealing for 0.5 h at 200 °C under argon only provided a small decrease in the intensity of the shoulder (**Figure 2.10a**), while heating a solution of the polymer resulted in minimal changes to the absorption profile beyond a small decrease and blue shift in absorption due to expansion of the solvent and increased molecular motion, respectively (**Figure 2.10b**).

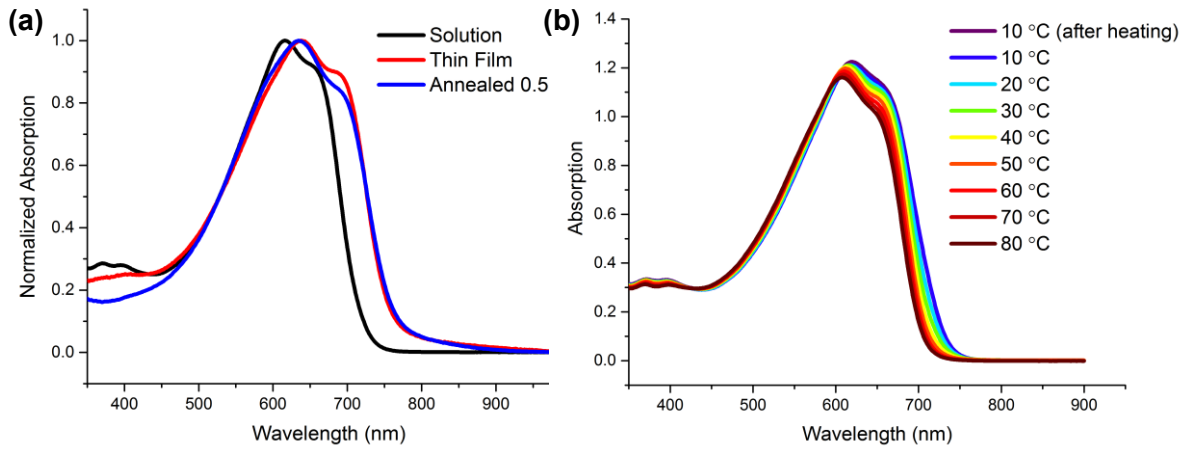



**Figure 2.10: (a) UV-vis absorption spectra of PDTAsV in chlorobenzene solution, as a thin film, and as a thin film after annealing for 0.5 h at 200 °C under argon; (b) solution of PDTAsV in chlorobenzene being heated to 80 °C**

### *2.3.2 – Physical properties*

Wide-angle X-ray diffraction (XRD) was used to provide further insight into the solid state packing behaviour of **PDTAsV**. The polymer was drop cast onto a silicon wafer and probed before and after annealing for 0.5 h at 200 °C, as shown in **Figure 2.11**. The as-cast sample

exhibited a broad, low-intensity peak at 2θ = 4.21°, corresponding to a *d*-spacing of 21.0 Å. Upon annealing, this peak became sharper and more intense, shifting to 2θ = 3.91° and a *d*-spacing of 22.6 Å, which is similar to the value observed for other bridged bithiophene vinylene co-polymers with dodecyl sidechains.[30]

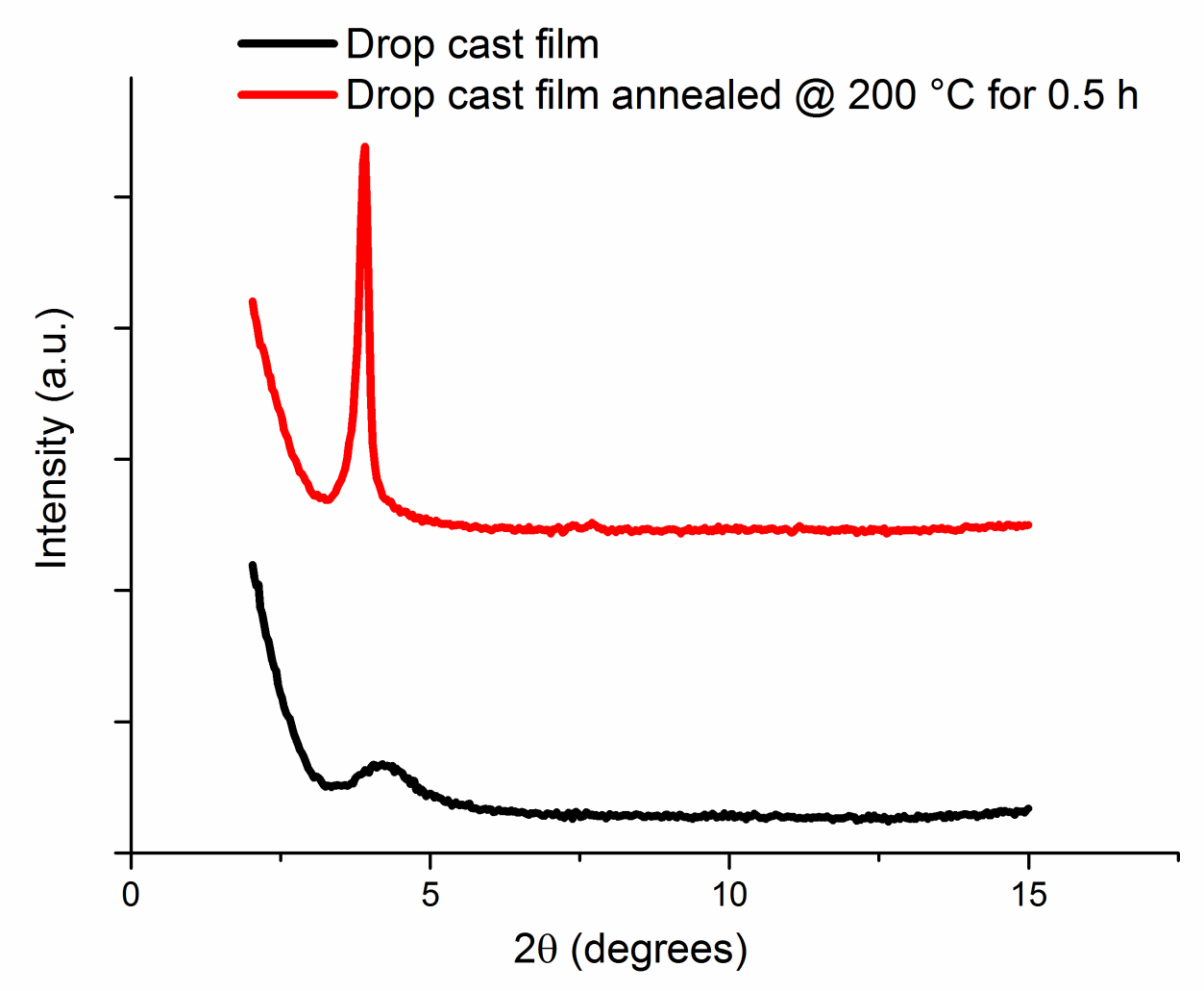



**Figure 2.11: XRD spectra of PDTAsV films drop-cast onto silicon wafers before (black) and after (red) annealing at 200 °C under argon for 0.5 h**

To provide a more detailed and quantifiable analysis of the XRD data, the Scherrer equation (**Equation 2.1**) was used, which gave an indication of the size of the crystallites in the films before and after annealing. In this equation, $L$ represents the crystallite size, $K$ is the Scherrer constant (taken to be 0.9), $\lambda$ is the wavelength of the X-ray source, $\beta$ is the full-width half-maximum of the peak, and $\theta$ is the diffraction angle of the peak.[33]

$$L = \frac{K\lambda}{\beta \times \cos\theta}$$ **Equation 2.1**

In the as-cast film $L$ was found to be 8.9 nm, with this value increasing substantially to 41.7 nm in the annealed film, giving a strong indication of an increase in molecular ordering after annealing. Despite this, there were no visible thermal transitions when the polymer was studied using differential scanning calorimetry (DSC) between 0–300 °C at a rate of 10 °C $min^{-1}$, with the most likely explanations for this being either the limited sensitivity of the DSC setup or that the melting point was above 300 °C.

Thus far, both the UV and XRD data have given some indication that **PDTAsV** was able to crystallise and/or planarise in the solid state. In order to examine the potential monomer and polymer geometries, density functional theory (DFT) calculations were used to predict their conformations at the B3LYP level of theory with the 6311G(d,p) basis set. In order to simplify the calculation, the dodecyl chains were shortened to ethyl and methyl groups for the monomer and polymer systems, respectively.

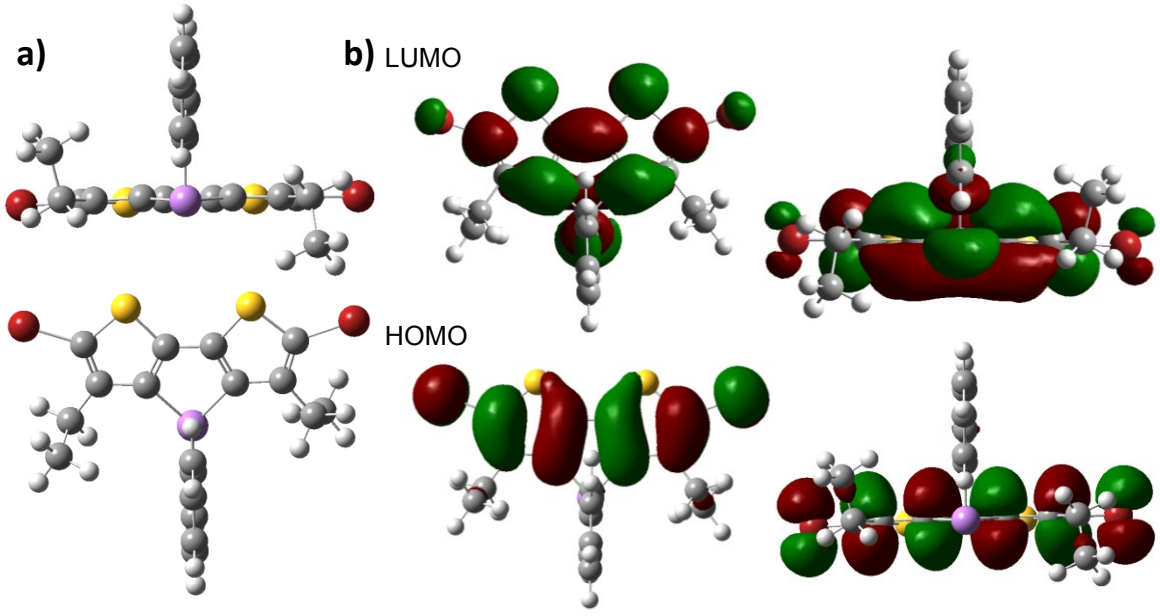



**Figure 2.12: (a) Predicted geometry, and (b) frontier molecular orbitals of 2.10 as calculated using Gaussian at the B3LYP level of theory with the 6-311G(d,p) basis set. LUMOs are shown on the top, HOMOs underneath**

Considering the DTAs monomer initially, the calculations predict the bridged bithiophenes to be perfectly co-planar. As shown in **Figure 2.12**, the phenyl group attached to the bridging arsenic is twisted orthogonally to the fused ring structure, and is almost perpendicular to the molecular plane. In the polymeric system, minimum energy level models of the trimer predicted highly planar backbones, with twists of less than 1° between the dithienoarsole group and the adjacent double bond. This high degree of planarity is due to the vinylene group acting as a spacer between the head-to-head coupled dodecyl sidechains, preventing undesirable torsional twisting between the dithienoarsole units. Additionally, the side-on view shows the exocyclic phenyl groups protruding perpendicularly from the arsole ring, and it is worth noting that although the trimer conformation depicted in **Figure 2.13** has the phenyl rings alternating above and below the plane of the backbone, there was no energy difference between this trimer and those with alternative arrangements (for example, with all the phenyl rings pointing upwards). As such, it is likely that the polymer itself contains a random arrangement of these phenyl groups, with some pointing above the plane of the backbone and others below it. Work by Pelzer et al. has investigated the inversion barriers of unsaturated group 15 heterocycles, and predicted that arsole would have a high cost of inversion at the pyramidal arsenic atom (127.8 kJ $mol^{-1}$ compared to 0 kJ $mol^{-1}$ for pyrrole and 76.2 kJ $mol^{-1}$ for phosphole), with inversion at the dithienoarsole arsenic atom likely being even more energetically unfavourable than this due to the lower HOMO-LUMO gap.[34]

### *2.3.3 – Electronic properties*

DFT calculations of the frontier molecular orbitals of the dithienoarsole monomer were performed using Gaussian 09 at the B3LYP level of theory and using the 6-311G(d,p) basis set, and the results are shown in **Figure 2.12b.** The HOMO was predicted to have a nodal plane through the arsenic atom, while the LUMO possesses some contribution from the σ*-orbital of the As-Ph bond. However, the HOMO does show some communication between the dithienoarsole unit and the excocylic phenyl group, with a small amount of electron density being observed on the latter. The frontier molecular orbitals of the polymer, shown in **Figure**

**2.13**, have similar properties to those of the monomer. Both the HOMO and LUMO are extended over the entire chain, indicating good conjugation through the backbone. The As-Ph σ*-orbital can be seen to contribute to the LUMO again, although only at the central arsole unit, with the two flanking dithienoarsole units not seeing any involvement of this orbital. It can be expected that over a longer chain similar to that seen in the actual polymer, DTAs units towards the centre of the chain would be in similar environments to the central group of this trimer, with those nearer the ends of the chain being more like the flanking groups (i.e., having little contribution from the As-Ph σ*-orbital).

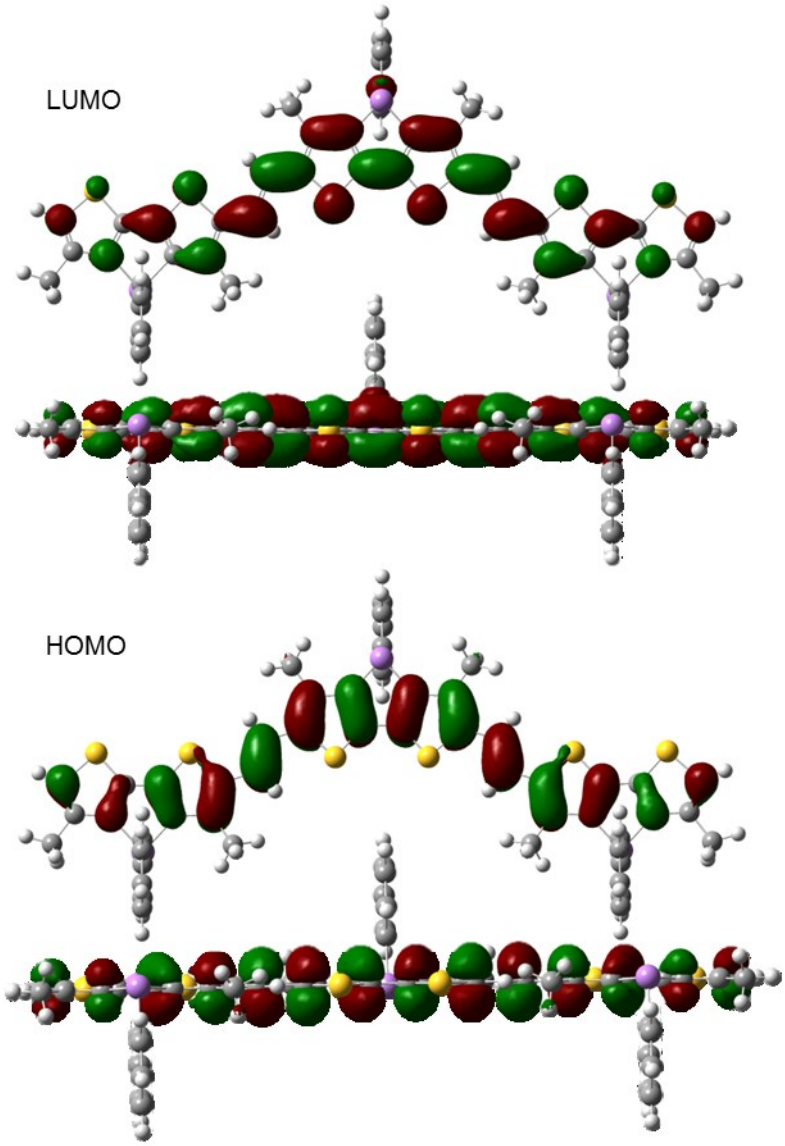



**Figure 2.13: Frontier molecular orbitals of PDTAsV, as calculated using Gaussian 09 at the B3LYP level of theory with the 6-311G(d,p) basis set. LUMOs are shown on the top, HOMOs underneath**

The DFT calculations also provided predictions of the HOMO and LUMO energy levels for the polymer, which were −4.62 eV and −2.64 eV, respectively, giving an expected band gap of 1.98 eV. These values were compared with those obtained using cyclic voltammetry (CV), which was performed on thin films of **PDTAsV** on fluorine-doped indium tin oxide-coated glass (FTO) in a 0.1 M $[Bu_4N][PF_6]$ acetonitrile solution, and the results of which are displayed in **Figure 2.14**.

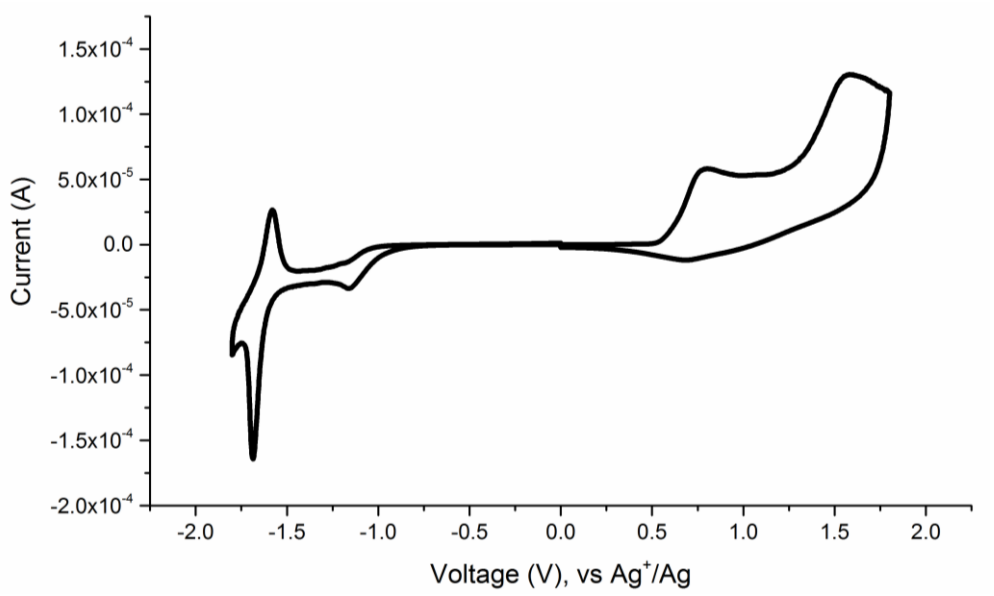



**Figure 2.14: Cyclic voltammogram of PDTAsV as a thin film on FTO in a 0.1 M $[Bu_4N][PF_6]$ acetonitrile solution at a scan rate of 50 mV $s^{-1}$**

The voltammogram shows irreversible oxidation of the polymer corresponding to a HOMO of −5.00 eV (referenced against ferrocene/ferrocenium), with the irreversibility being caused by dissolution of the polymer from the FTO slide into the acetonitrile solution. On the other hand, the reduction peak is highly reversible, with an onset equivalent to a LUMO of −2.78 eV. The smaller peak before the major reduction peak is an artifact caused by the use of FTO (see the voltammogram of blank FTO, **Appendix B**). The measured HOMO and LUMO levels gave an electrochemical band gap of 2.22 eV, which is larger than the optical band gap obtained from the UV-vis spectrum (1.65 eV), while the value predicted by DFT was between these two extremes.

### *2.3.4 – OFET performance*

The performance of **PDTAsV** in top gate, bottom contact field effect transistors was tested. Devices were fabricated on glass substrates using Au (60 nm) source/drain electrodes that were treated with a pentafluorobenzene thiol (PFBT) self-assembled monolayer (SAM) to increase their work function. The polymeric active layer was spin-coated from chlorobenzene, and annealed at 200 °C for 0.5 h before the dielectric (Cytop™) was coated on top. The channel length was 40 μm, and the channel width was 1000 μm.

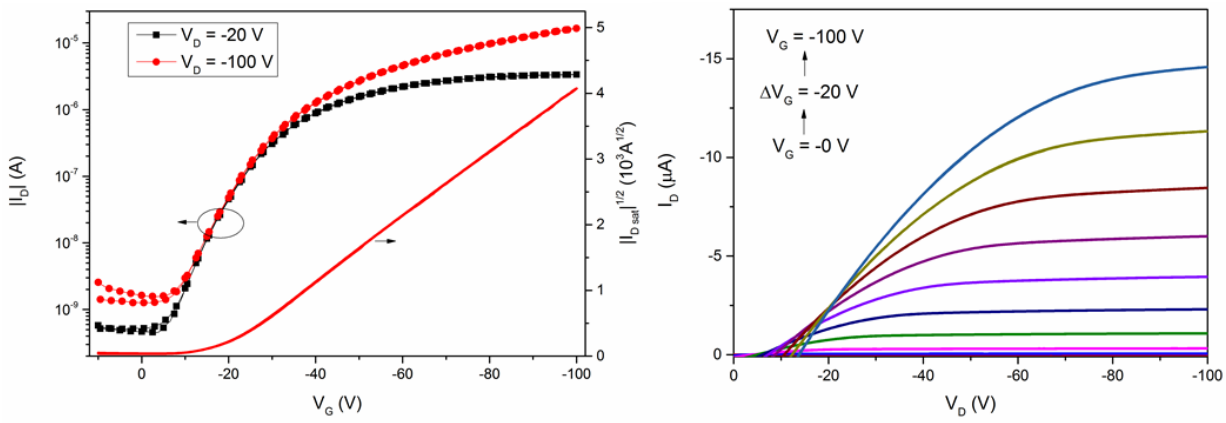



**Figure 2.15: Transfer (left) and output (right) characteristics of top gate, bottom contact OFET devices using PDTAsV as the active layer**

The OFETs exhibited classic p-type semiconducting behaviour with minimal hysteresis between the forward and reverse sweeps, as can be seen in **Figure 2.15**. The threshold voltage of the device was calculated to be −17.6 V, and the on/off ratio was in the $10^4$–$10^5$ region. Examination of the device mobilities (see **Figure 2.16**) showed that saturated mobility was both quite high and relatively independent of the gate voltage, with the average saturated mobility being 0.079 $cm^2\ V^{-1}\ s^{-1}$ and the maximum saturated mobility only slightly higher, at 0.083 $cm^2\ V^{-1}\ s^{-1}$.

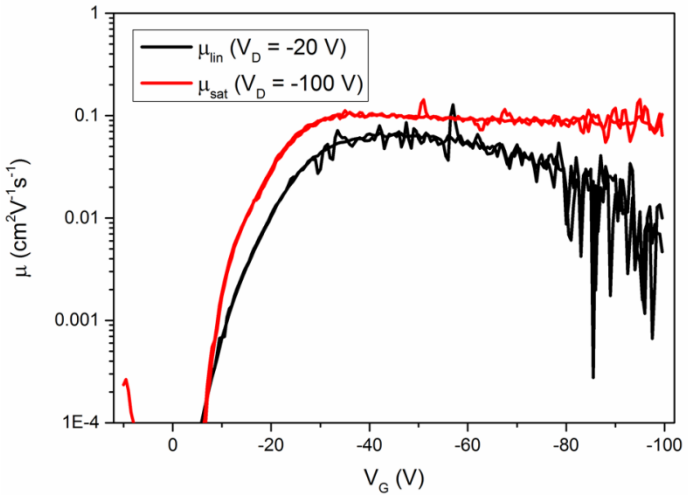
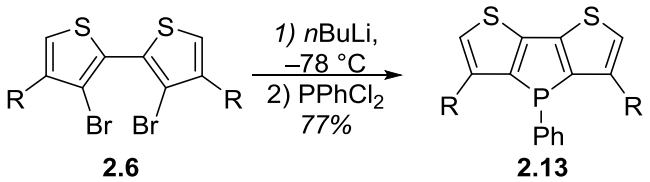



**Figure 2.16: Linear and saturated mobilities of top gate, bottom contact OFET devices using PDTAsV as the active layer**

## *2.4 – Polymerization with bithiophene*

### *2.4.1 – Synthesis of dithienophosphole analogue*

One of the aims of this research was to compare the properties of the dithienoarsole unit with the dithienophosphole (DTPh) analogue. To allow this comparison, 3,5-didodecyl-4-phenyldithieno[3,2-*b*:2',3'-*d*]phosphole (**2.13**) was synthesised via the same route used for the arsole, ending with the ring closure with dichlorophenylphosphine as shown in **Figure 2.17**.




**2.6** **2.13**

**Figure 2.17: Synthesis of 3,5-didodecyl-4-phenyldithieno[3,2-*b*:2',3'-*d*]phosphole (2.13), where R represents dodecyl side chains**

### *2.4.2 – Coordination with transition metal catalysts*

A major consideration when using dithienophosphole and dithienoarsole in polymerisations is ensuring that the pnictogen atom does not coordinate to the transition metal catalyst,[29,35] which can cause catalyst poisoning and lower reaction yield. In phosphole research, this is commonly prevented by oxidising the phosphorus to the +5 oxidation state, thereby ensuring that the lone pair is unavailable for coordination to the catalyst.[14,36] However, this removes the possibility of post-polymerisation functionalization at the pnictogen atom, as well as limiting the variety of compounds studied to those in the +5 state.

In order to determine whether there would be any interaction between the palladium catalyst used for the polymerisation and the dithienopnictogen units, a sample of **2.13** was dissolved in deuterated chloroform and exposed to one equivalent of the catalyst. DTPh was used as the model compound in this study for two reasons, the first being the ease of monitoring changes in phosphorus environment using $^{31}$P NMR, while the second was that phosphorus compounds are stronger ligands than their arsenic equivalents.[31] This meant that if no changes were seen for the phosphole, it would be unlikely that any would occur for the arsole.

**Figure 2.18** shows the $^{31}P$ NMR results of this experiment when tris(dibenzylideneacetone)dipalladium(0) ([$Pd_2dba_3$]) was used as the model catalyst.

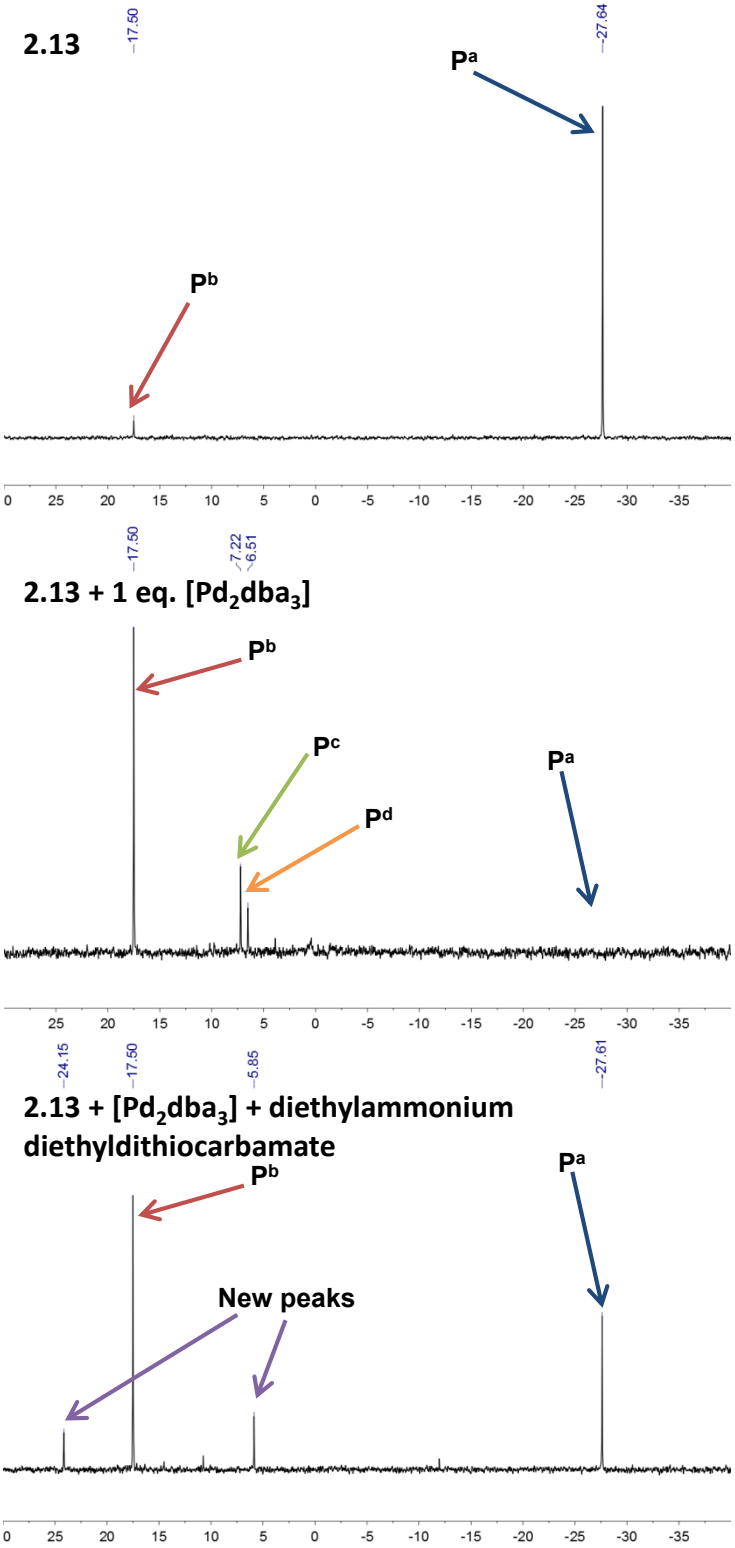



**Figure 2.18: $^{31}P$ NMR spectra of 2.13 before (top) and after (middle) addition of one equivalent of [$Pd_2dba_3$], and after addition of a Pd-complexing salt (bottom) between 30 and −40 ppm**

The $^{31}P$ NMR spectrum of the unreacted phosphole shows two distinct peaks, one at −27.6 ppm corresponding to **2.13** ($P^a$), and a much smaller peak at 17.5 ppm caused by the oxide of this compound ($P^b$). On addition of one equivalent of $Pd_2dba_3$, which contains no phosphorus atoms, $P^a$ disappeared entirely while $P^b$ showed a significant increase in intensity. Interestingly, two additional peaks appeared at 7.2 ppm ($P^c$) and 6.5 ppm ($P^d$) in a 2:1 ratio, potentially indicating the formation of a phosphole-palladium complex similar to one synthesized by Nyulászi et al.[29] Their work discussed the *cis*- and *trans*-isomers of the compound shown in **Figure 2.19a**, with the isomers being produced in a 1:3 ratio by addition of [Pd(1,5-cyclooctadiene)$Cl_2$] to 2,6-bis(trimethylsilyl)4-phenyldithieno[3,2-*b*:2',3'-*d*]phosphole. By analogy with similar compounds,[37] it was suggested that the *trans*-isomer had produced a more shielded $^{31}P$ peak, with the *cis*-isomer being responsible for the other peak. Using similar assumptions, it is proposed that addition of [$Pd_2dba_3$] to **2.13** caused the formation of a palladium complex, [Pd(dba)DTPh]$_2$, which has two possible isomers, as shown in **Figure 2.19b**. Further evidence of complexation can be seen when the strongly coordinating ligand diethylammonium diethyldithiocarbamate was added, which caused the loss of peaks $P^c$ and $P^d$ as well as the return of the $P^a$ peak in the $^{31}P$ NMR spectrum (**Figure 2.18**), although the intensity of $P^a$ was lower than was initially detected due to the substantial amount of phosphole oxide formed, possibly due to incomplete degassing.

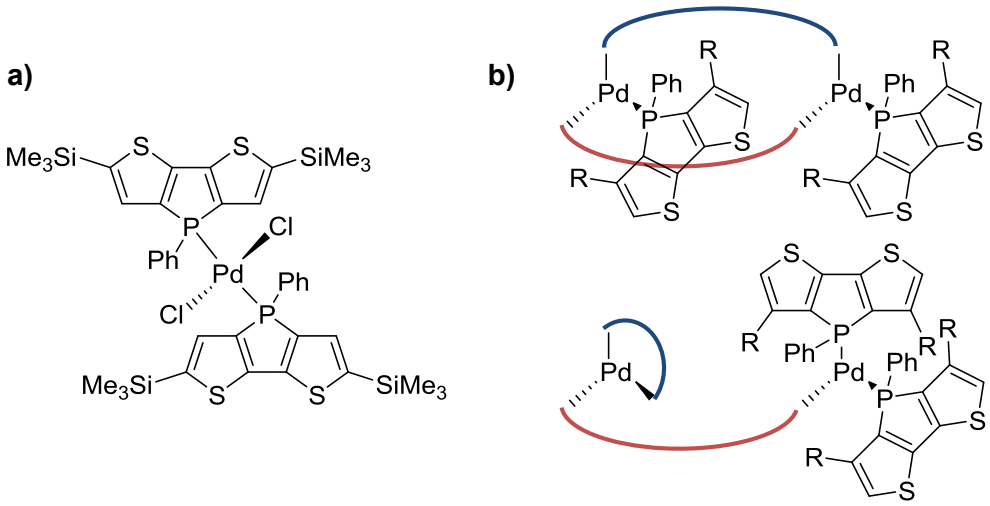



**Figure 2.19: (a) Structure of the dithienophosphole-palladium complex synthesized by Nyulászi et al.; (b) potential isomers of [Pd(dba)DTPh]$_2$, where the arcs represent dibenzylideneacetone ligands and R represents dodecyl groups**

These findings indicated that [$Pd_2dba_3$] was an unsuitable catalyst for polymerization of phospholes and arsoles. Although the polymerization would be performed in the presence of only catalytic amounts of [$Pd_2dba_3$], the complexation of the dithienometallole would alter the stoichiometry of the reaction and potentially the activity of the catalyst, both of which would likely have detrimental effects on the polymerization reaction. As such, we investigated the use of tetrakis(triphenylphosphine)palladium(0) ([$Pd(PPh_3)_4$]) as an alternative catalyst, reasoning that the presence of the triphenylphosphine ligands would be less likely to be replaced with the DTPh group due to their decreased lability.

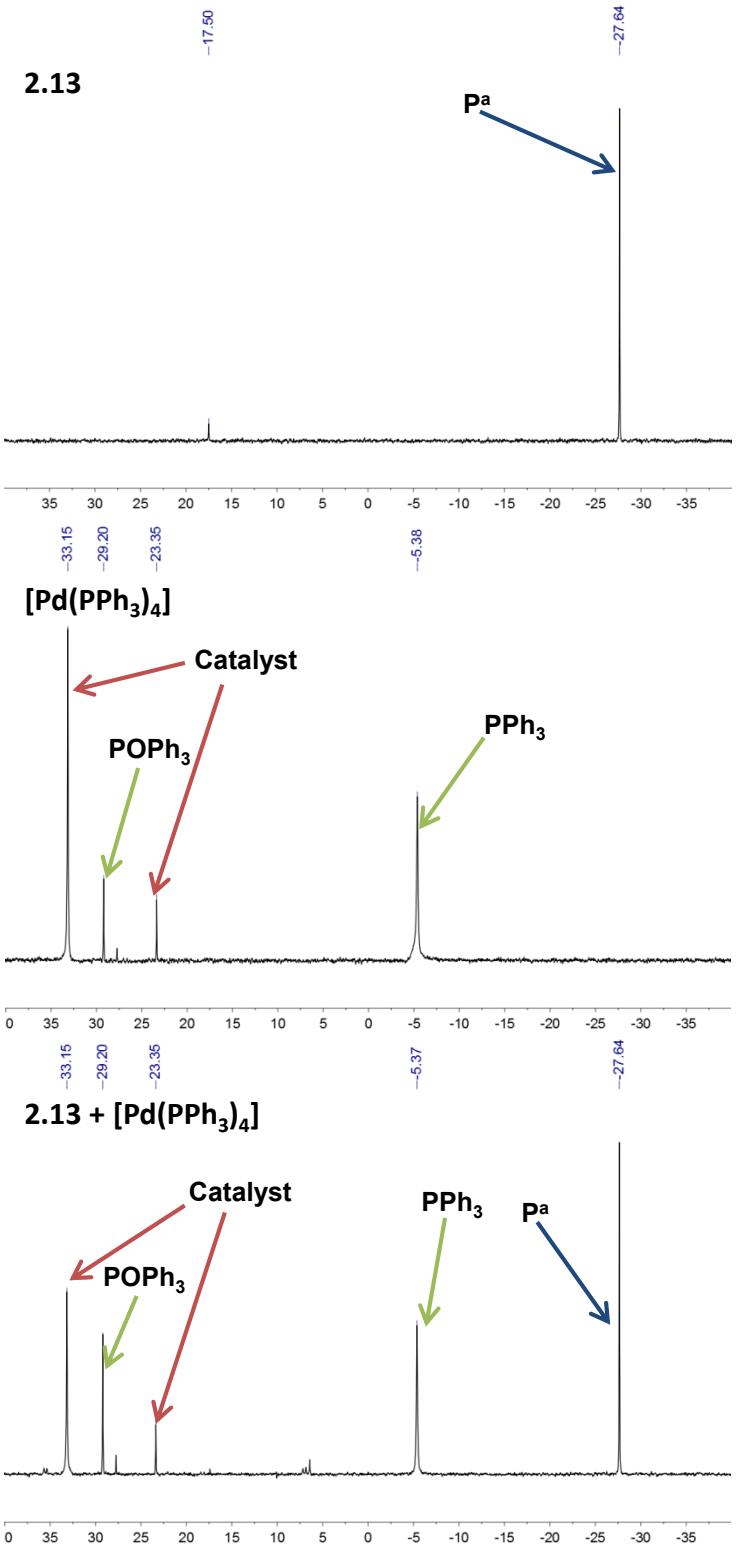



**Figure 2.20: $^{31}$P NMR spectra of 2.13 before (top) and after (bottom) addition of one equivalent of [Pd(PPh$_3$)$_4$], with the middle image showing the spectrum of Pd(PPh$_3$)$_4$**

In contrast to the results seen for [Pd$_2$dba$_3$], the $^{31}$P NMR spectrum of **2.13** showed no changes on exposure to one equivalent of [Pd(PPh$_3$)$_4$]. The catalyst itself showed four peaks in its $^{31}$P NMR spectrum, two relating to free PPh$_3$ and its oxide at –5.4 ppm and 29.2 ppm,

respectively,[38–40] a large peak at 33.2 ppm potentially caused by bis(triphenylphosphine)palladium(0) or another triphenylphosphine-palladium complex,[41,42] and a characteristic [$Pd(PPh_3)_4$] peak at 23.6 ppm.[38] None of these peaks changed position by a significant amount in the presence of one equivalent of **2.13**, suggesting minimal interaction between the DTPh and the palladium, making [$Pd(PPh_3)_4$] an ideal catalyst for the polymerization of the DTPh/DTAs moieties.

### *2.4.3 – Polymerization reactions*

2,6-Bis(trimethylstannyl)-3,5-didodecyl-4-phenyldithieno[3,2-*b*:2',3'-*d*]arsole (**2.12**) and 2,6-bis(trimethylstannyl)-3,5-didodecyl-4-phenyldithieno[3,2-*b*:2',3'-*d*]phosphole (**2.14**) were independently polymerized with 5,5'-dibromo-2,2'-bithiophene via Stille coupling in a microwave reactor, using [$Pd(PPh_3)_4$] as the catalyst. This was to allow direct comparison of the properties of a dithienoarsole in a polymeric system containing a well-understood comonomer with its dithienophosphole analogue.

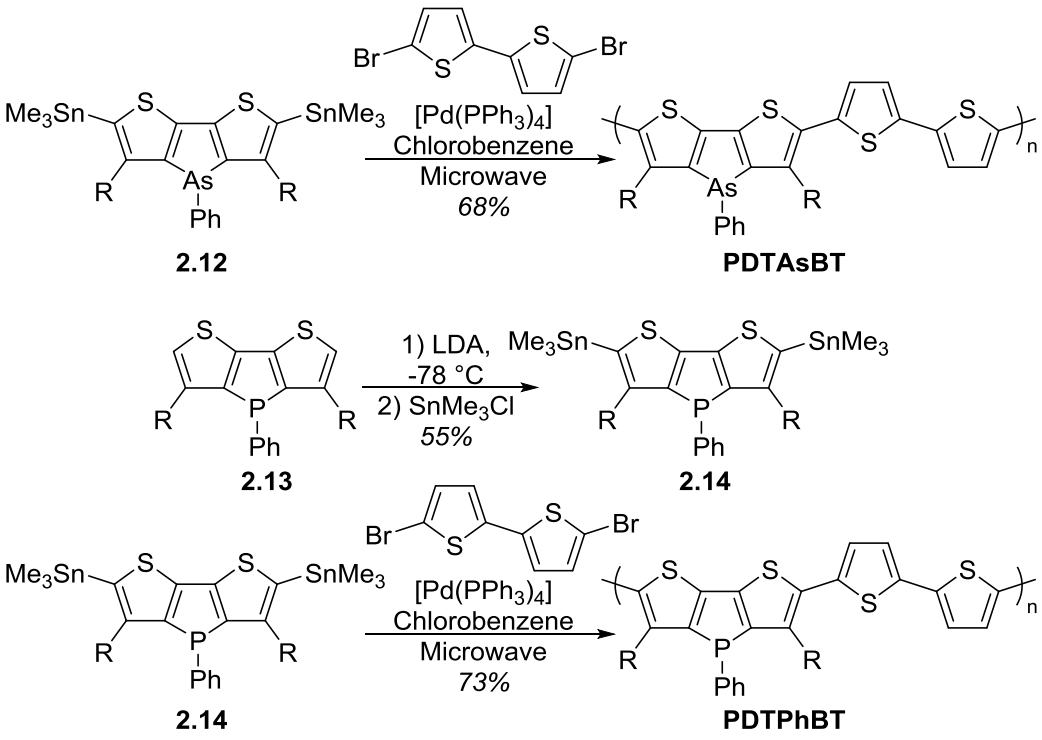



**Figure 2.21: Synthesis of 2,6-bis(trimethylstannyl)-3,5-didodecyl-4-phenyldithieno[3,2-*b*:2',3'-*d*]phosphole (2.14), and polymerization of 2.12 and 2.14 with 5,5'-dibromo-2,2'-bithiophene, where R represents dodecyl chains**

The syntheses of **PDTAsBT** and **PDTPhBT** were carried out in a similar manner to that previously described for **PDTAsV**. After polymerization in the microwave reactor, both materials were precipitated in methanol and purified by Soxhlet extraction with methanol and acetone in order to remove residual catalyst and low molecular weight oligomers, and then with hexane and chloroform to provide the crude polymers. The hexane and chloroform fractions were then combined and washed with the strongly complexing ligand diethylammonium diethyldithiocarbamate in order to remove any remaining traces of catalyst.[32] After a final precipitation into methanol, **PDTAsBT** and **PDTPhBT** were obtained as dark red solids in yields of 68% and 73%, respectively. The molecular weight data as determined by GPC in chlorobenzene (80 °C) against polystyrene standards are shown in **Table 2.1**, and both polymers were soluble in a variety of chlorinated solvents including chloroform and chlorobenzene, as well as displaying some solubility in hot hexane.

**Table 2.1: Molecular weight information for PDTAsBT and PDTPhBT**

| Polymer | $M_n$ (kg/mol) | $M_w$ (kg/mol) | Đ |
|---|---|---|---|
| **PDTAsBT** | 7.1 | 15.4 | 2.17 |
| **PDTPhBT** | 8.3 | 17.9 | 2.16 |

The structures of the polymers were confirmed by $^{1}$H NMR spectroscopy and elemental analysis, both of which were in accordance with predicted values. In the case of **PDTPhBT**, $^{31}$P NMR spectroscopy was also used, and two peaks were observed at −24.5 and −26.1 ppm, both of which are firmly within the expected range of P in the +3 oxidation state.

### *2.4.4 – Optical properties*

The absorption spectra of the polymers in chlorobenzene solution and as thin films were studied using UV-vis spectroscopy, the results of which are shown in **Figure 2.22**. The similarity

of the spectra is noteworthy, with **PDTAsBT** and **PDTPhBT** displaying $\lambda_{max}$ values of 497 nm and 493 nm respectively in chlorobenzene solution, and both having red-shifted $\lambda_{max}$ values of 545 nm as thin films. The only significant difference seen between the phosphole and arsole polymers is a small shoulder visible in the solution spectrum of **PDTAsBT**, likely caused by slight aggregation of the polymer.

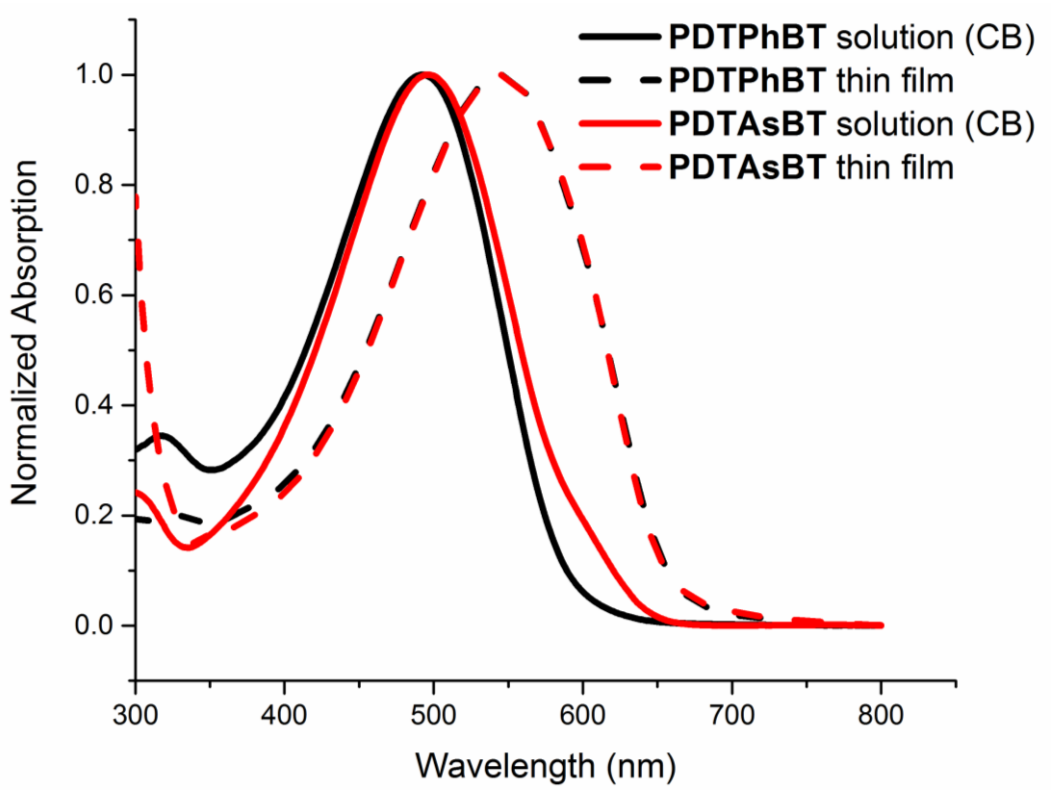



**Figure 2.22: UV-vis absorption spectra of PDTAsBT and PDTPhBT in chlorobenzene solutions and as thin films**

### *2.4.5 – Physical properties*

DFT calculations were carried out to allow comparison of the molecular geometries of **PDTAsBT** and **PDTPhBT** using Gaussian 09 at the B3LYP level of theory and with the 6-311G(d,p) basis set. As shown in **Figure 2.23**, both polymers are predicted to exhibit twisting between the dithienopnictogen groups and the flanking thiophene rings, with the dihedral angle between the two groups being ca. 40° in both materials. This contrasts starkly with the planarity predicted in the structure of **PDTAsV** structure (**Figure 2.13**), with the twist in the bithiophene copolymers being attributed to steric clashes between the dithienopnictogens and the

thiophene rings. These clashes are likely enhanced by the presence of the alkyl chains at the 3/5 positions of the bridged systems, and results in reduced conjugation along the polymer backbone as well as a potential disruption of the π-π stacking between chains. Interestingly, the dithienopnictogen-thiophene bonds adopt a *cis* configuration in the lowest energy conformations of these systems, with both sulfur atoms on the same side of the C-C bonds. This is in contrast to what is usually predicted for thiophene-thiophene polymers, where the inter-ring bonds typically adopt a *trans* configuration such that the sulfurs are on opposite sides of the C-C bonds. However, it was found that for these systems the *trans* configurations were predicted to be ~0.37 kJ/mol higher in energy than the *cis* configurations. These effects all combine to explain the significantly blue shifted $\lambda_{max}$ observed for these polymers when compared to the planar vinylene copolymer (545 nm *vs* 638 nm for **PDTAsV**). However, there were also some similarities between the molecular geometries of the bithiophene copolymers and **PDTAsV**, such as the orthogonality of the phenyl rings to the conjugated backbone, although the excocyclic C–P–phenyl angle is slightly larger than the C–As–Ph angle, at 104° instead of 100°.

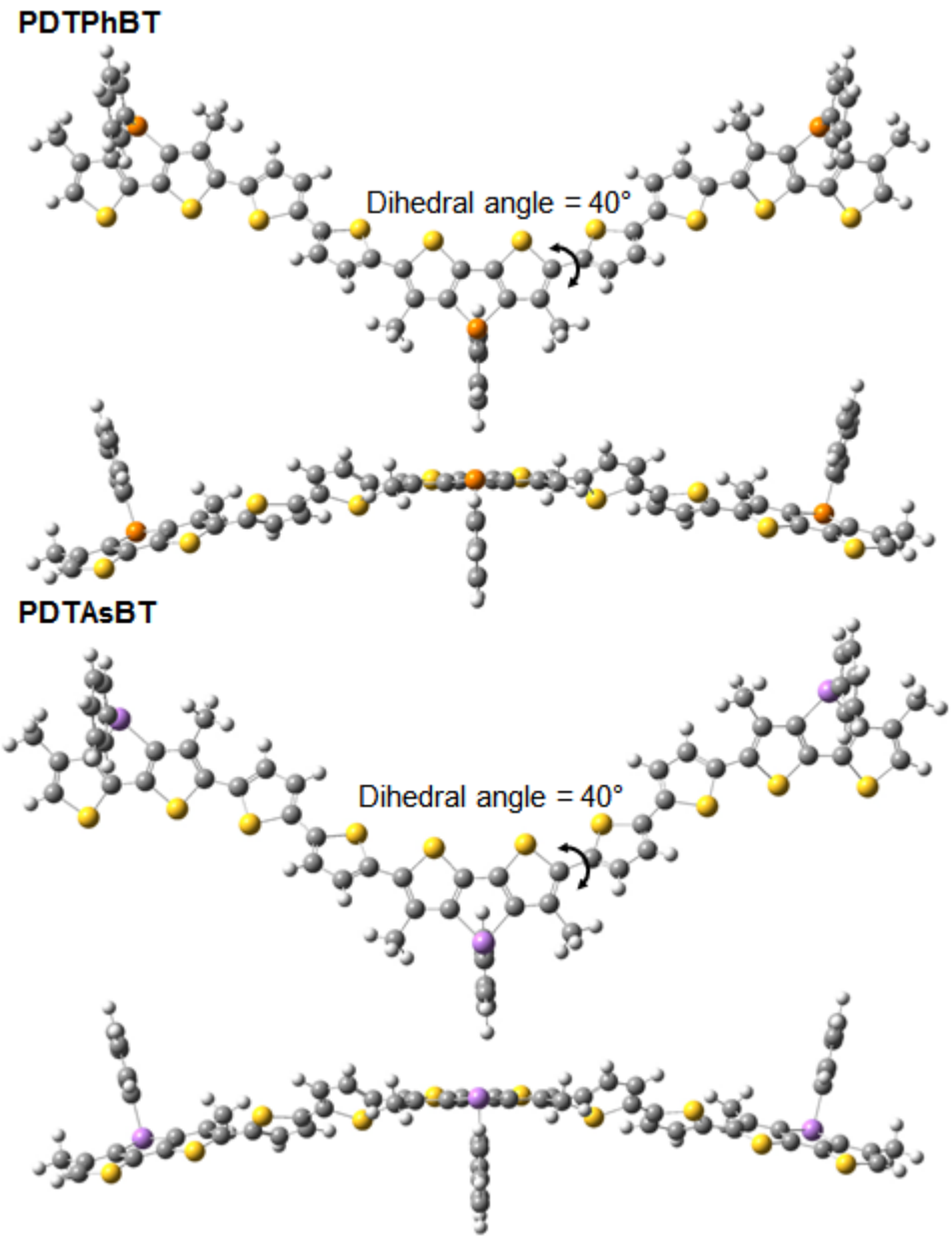



**Figure 2.23: Molecular geometries of PDTPhBT (top) and PDTAsBT (bottom), as calculated using Gaussian at the B3LYP level of theory with the 6-311G(d,p) basis set**

Examining the differential scanning calorimetry (DSC) curves of the two polymers as measured between 0–300 °C at a rate of 10 °C $min^{-1}$, it can be seen that **PDTAsBT** showed no peaks other than machine artefacts. On the other hand, **PDTPhBT** shows a single peak in both the melting (205–220 °C) and cooling cycles (182–177 °C), although it is noticeably sharper in the cooling cycle. This relatively rapid crystallisation has the characteristics of a glass transition, indicating that this is the glass transition temperature ($T_g$) for this material. The differences between the DSC behaviours of **PDTPhBT** and **PDTAsBT** were likely caused by the replacement

of phosphorus with arsenic, which could have increased the temperatures of the transitions in **PDTAsBT** due to the increase in the molecular weight of the dithienometallole unit.

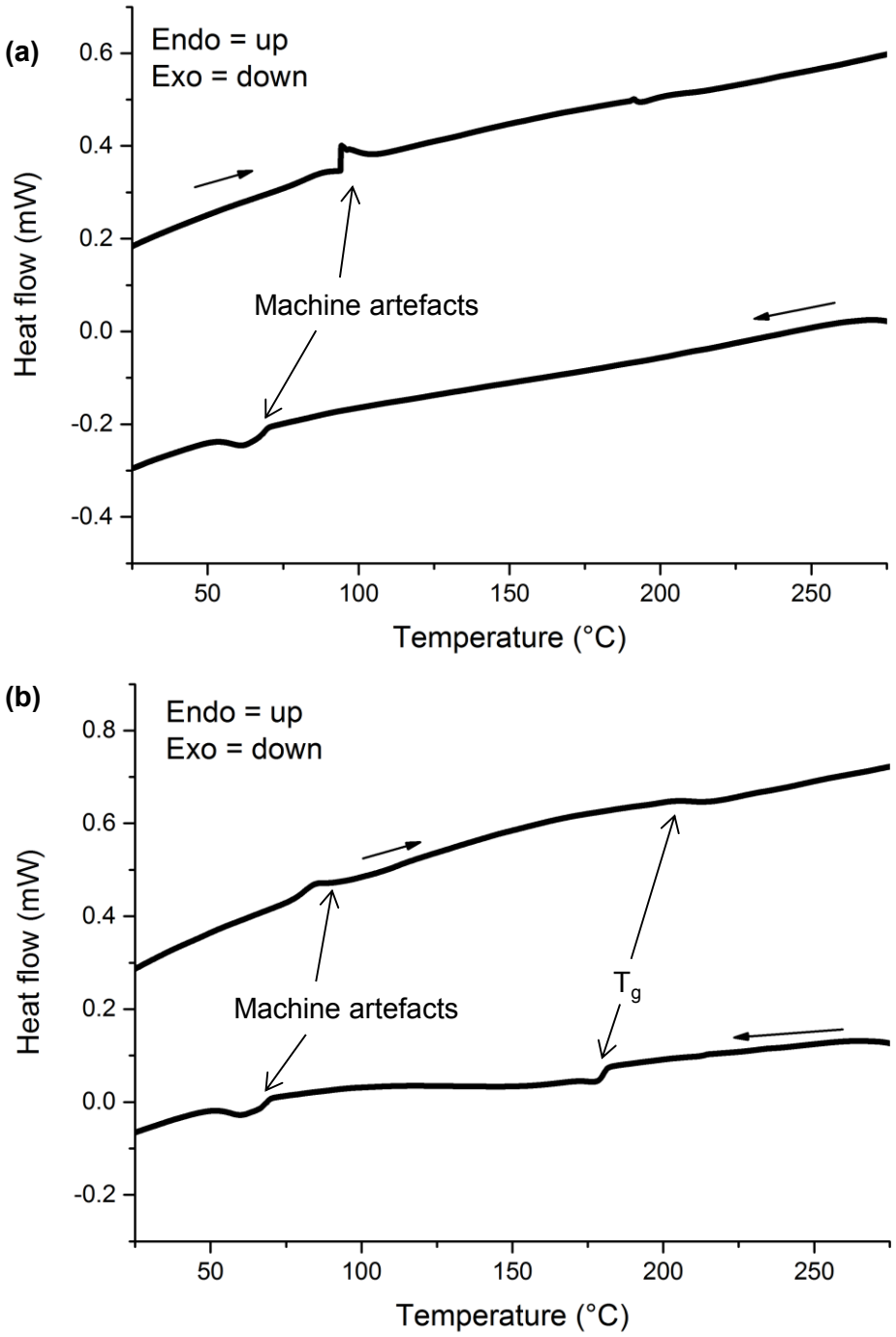



**Figure 2.24: DSC traces of (a) PDTAsBT and (b) PDTPhBT, both from their second heating/cooling cycles**

### *2.4.6 – Electronic properties*

The frontier molecular orbitals of **PDTPhBT** and **PDTAsBT** were predicted using Gaussian 09 at the B3LYP level of theory using the 6-311G(d,p) basis set, and the results are shown in **Figure 2.25**. As was seen for **PDTAsV**, the predicted HOMOs show nodes through the group 15 heteroatoms, and the twists observed in the molecular geometries of **PDTPhBT** and **PDTAsBT** result in the electron densities of the HOMOs and LUMOs of both polymers being more centrally concentrated than was observed for **PDTAsV** due to disruption of the π-π conjugation. As previously mentioned, this helps to account for the almost 100 nm blue shift in the $\lambda_{max}$ of these polymers when compared to the vinylene copolymer. The central bridged dithienopnictogen units of both polymers show contributions from the heteroatom-phenyl σ*-orbital, as was observed for **PDTAsV**.

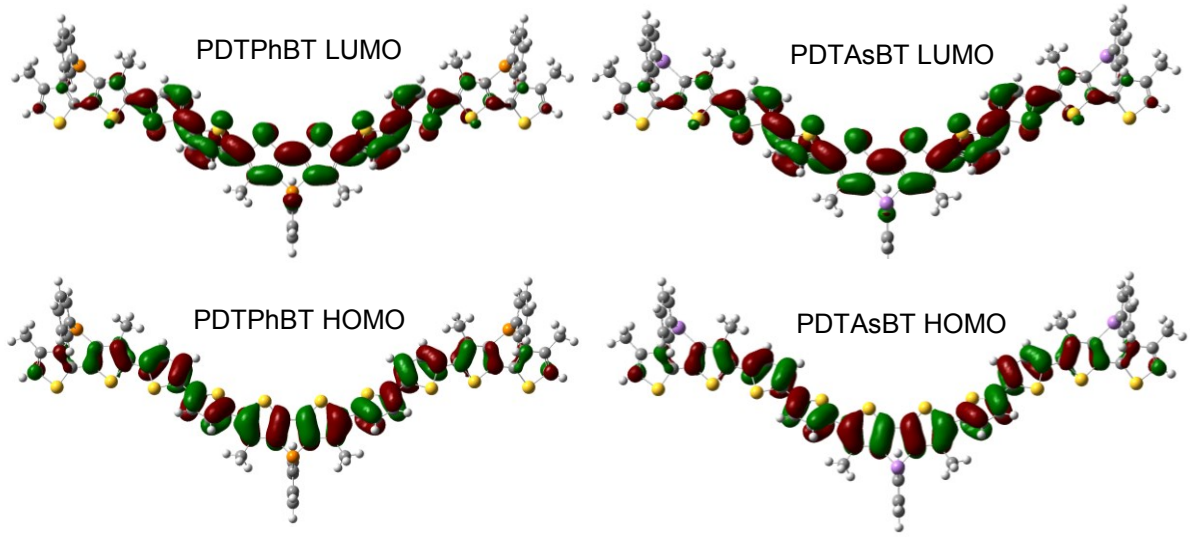



**Figure 2.25: Frontier molecular orbitals of PDTPhBT (left) and PDTAsBT (right), as calculated using Gaussian 09 at the B3LYP level of theory with the 6-311G(d,p) basis set. LUMOs are shown on the top, HOMOs underneath**

The HOMO and LUMO energy levels of both polymers were also predicted using DFT calculations, and showed a high degree of similarity. The predicted HOMO values were −4.97 and −4.99 eV, whilst the LUMO values were −2.60 and −2.58 eV for the arsole and phosphole polymer, respectively. This gave expected band gaps of 2.37 eV for **PDTAsBT** and 2.41 eV for **PDTPhBT**.

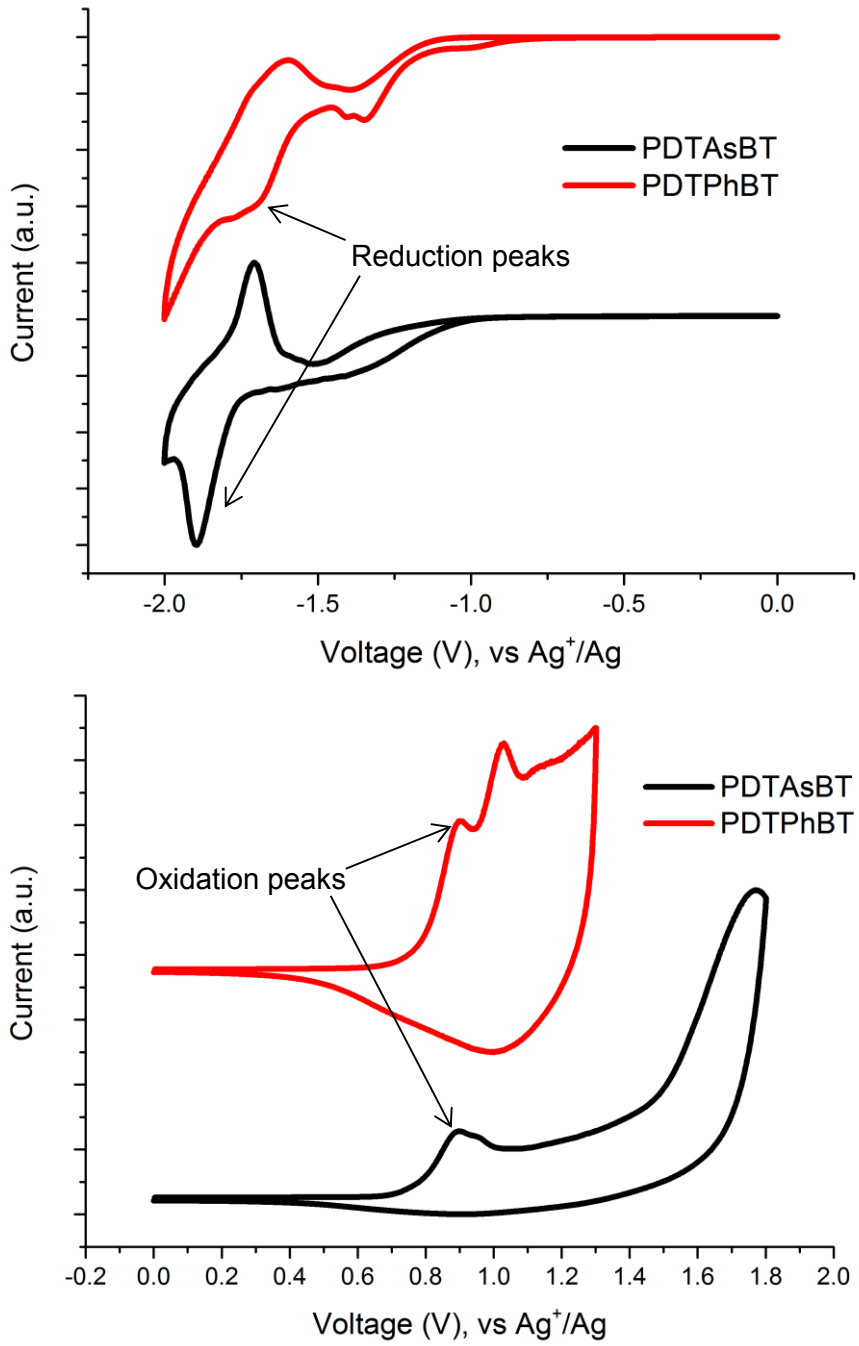



**Figure 2.26: Cyclic voltammograms of PDTAsBT and PDTPhBT as a thin film on FTO in a 0.1 M $[Bu_4N][PF_6]$ acetonitrile solution at a scan rate of 50 mV $s^{-1}$, with reduction cycles on top and oxidation on the bottom. The oxidation and reduction values were taken from the onsets of the indicated peaks**

The voltammograms of the polymers show oxidation peaks with highly similar values that yield HOMO levels of −5.18 and −5.19 eV for the arsole- and phosphole-containing polymers, respectively when referenced against ferrocene/ferrocenium. However, the oxidation peak of **PDTPhBT** appears to show a greater degree of reversibility than that of **PDTAsBT**, likely due to

the lower maximum voltage used for the former measurement. In contrast to the high degree of similarity seen in the oxidation peaks, the reduction peaks of the two polymers are quite dissimilar, appearing at −2.63 and −2.83 eV for the arsole- and phosphole-containing polymers, respectively. Furthermore, it can be seen that the reduction peak of the arsole polymer shows greater reversibility than that of the phosphole polymer, although the reasons for this are unclear. A potential cause of both of these issues could be unintended oxidation of the phosphole group, which has been shown to affect the LUMO much more than the HOMO and would lower the former in the manner observed here.[43] The measured HOMOs and LUMO gave electrochemical band gaps of 2.36 and 2.55 eV for **PDTPhBT** and **PDTAsBT**, respectively. These values are larger than the optical band gaps, although it should be noted that both polymers had the same optical band gap (1.89 eV). The electrochemical band gap of the phosphole polymer is very similar to that predicted by DFT (2.41 eV), while that of the arsole analogue was somewhat larger than its theoretical band gap (2.37 eV).

### *2.4.7 – OFET performance*

The OFET performances of **PDTAsBT** and **PDTPhBT** in top gate, bottom contact devices were compared. Fabrication conditions for **PDTAsBT** were the same as those described in **Section 2.3.4**, while for **PDTPhBT**, slightly smaller source/drain electrodes were used (40 nm instead of 60 nm), and annealing was carried out at 160 °C instead of 200 °C. The channel lengths and widths of both devices were 40 and 1000 μm, respectively.

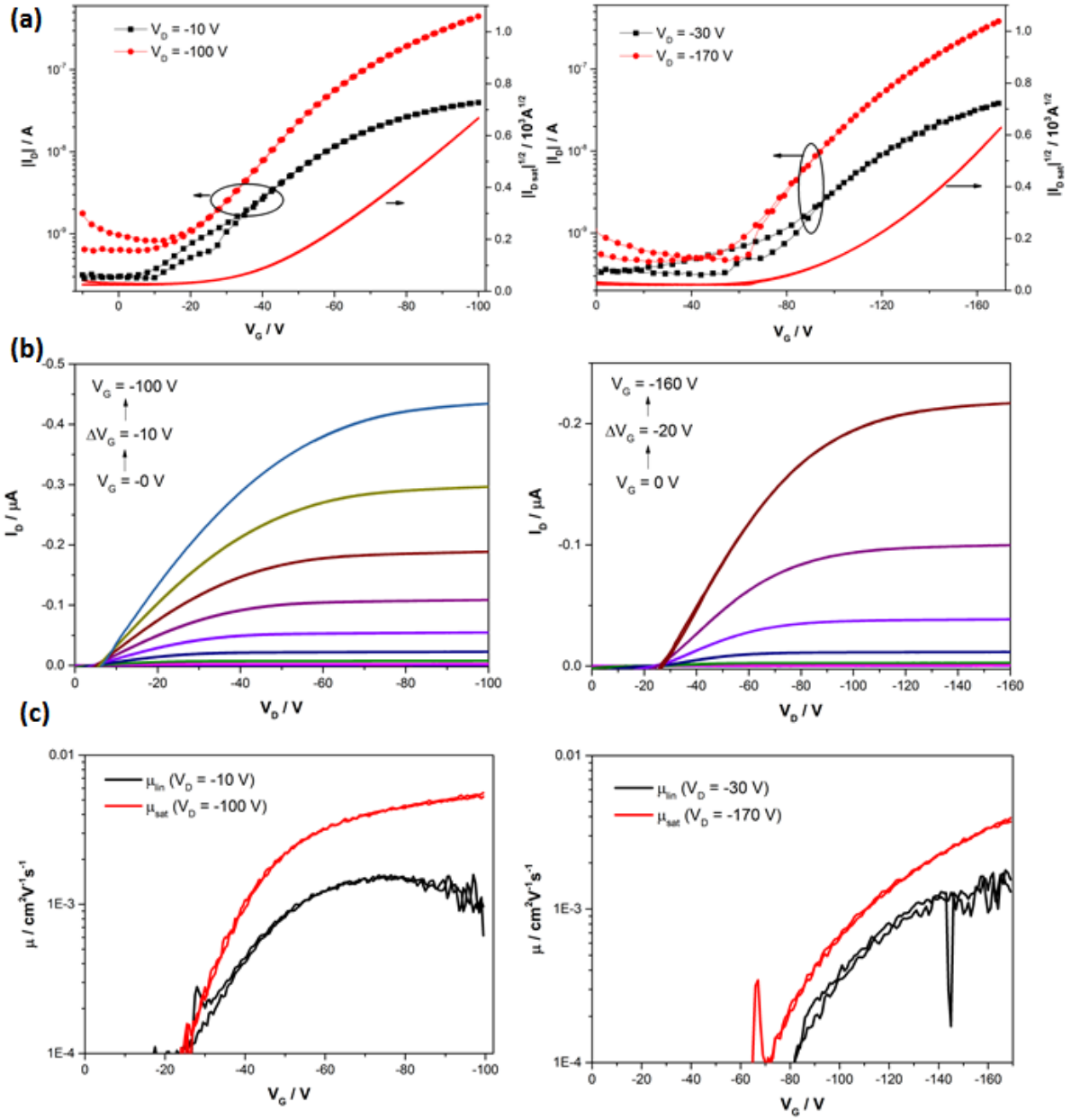



**Figure 2.27: (a) Transfer characteristics, (b) output characteristics, and (c) linear and saturated mobilities of top gate, bottom contact OFET devices using PDTAsBT (left) or PDTPhBT (right) as the active layer**

Both polymers showed p-type semiconducting behaviour with only small degrees of hysteresis between the forward and reverse sweeps, as can be seen in **Figure 2.27a**. As would be expected, neither polymer performed as well as **PDTAsV**, likely due to the much more twisted natures of their backbones and their somewhat lower molecular weights. The mobilities of the two polymers were fairly similar, with the average saturated hole mobilities being $5.0 \times 10^{-3}$ and $3.2 \times 10^{-3}$ $cm^2\ V^{-1}\ s^{-1}$ for **PDTAsBT** and **PDTPhBT**, respectively, and both

polymers showed on/off ratios of ~$10^2$. However, it is also obvious that there are differences between the devices, the major one being the threshold voltage, which was −40.7 V for **PDTAsBT** and −107.1 V for the phosphole equivalent. Although it is difficult to be sure of the precise reason for this, the high degree of similarities between the energy levels of the two polymers and their relatively similar molecular weights makes it possible that the higher reactivity of the phosphorus lone pair causes it to act as a trap site, meaning the voltage must be higher before current starts to flow. Alternatively, some unintentional oxidation of the phosphole polymer may have also occurred, which could also be acting as a trap. This is an interesting prospect that could reveal important differences in the device performances of phosphole- and arsole-containing polymers. Future research in this area should examine the performances of the oxides of these two materials as well as their pristine forms to see if the higher reactivity of the phosphorus lone pair is indeed the source of the increased threshold voltage. If this was the case, it would be expected that functionalization at the lone pair would decrease the threshold voltage of the phosphole polymer more than that of the arsole analogue.

### *2.5 – Polymerization with benzodithiophene*

A commonly used comonomer in plastic electronics is the benzo[1,2-*b*:4,5-*b*']dithiophene (BDT) group, which displays a number of advantages that make it an advantageous addition to conjugated polymeric systems.[44] These are particularly apparent in OFET devices, where the symmetric, planar structure of the BDT group helps to improve π-π stacking between polymer chains,[45,46] while the ability to place solubilising groups on the free positions of the benzyl ring enables solubility to be conferred to the resulting polymers without adverse impacts on backbone planarity.[47] The combination of these advantages allowed BDT-based OFET materials to reach mobilities of 0.25 $cm^2\ V^{-1}\ s^{-1}$ as early as 2007.[48] With these benefits in mind, 2,6-bis(trimethylstannyl)-3,5-didodecyl-4-phenyldithieno[3,2-*b*:2',3'-*d*]arsole (**2.12**) was polymerised with 2,6-dibromo-4,8-dioctodecylbenzo[1,2-*b*:4,5-*b'*]dithiophene via Stille coupling in a microwave reactor, using $[Pd(PPh_3)_4]$ as the catalyst.

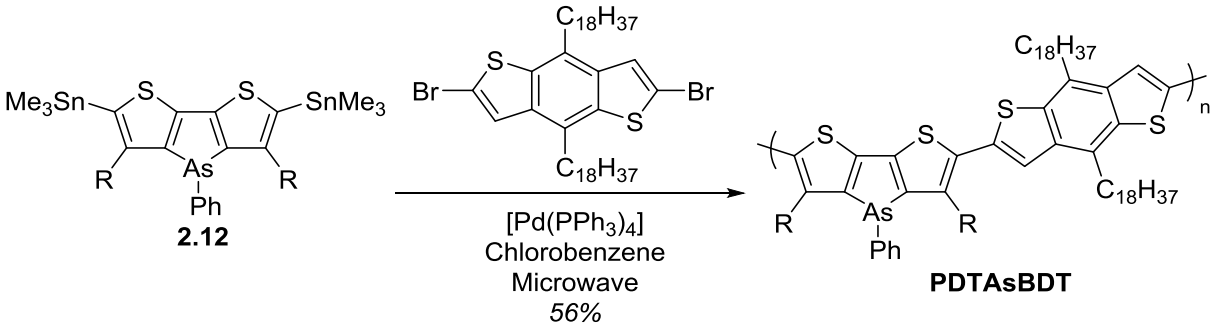



**Figure 2.28: Polymerisation of 2,6-bis(trimethylstannyl)-3,5-didodecyl-4-phenyldithieno[3,2-*b*:2',3'-*d*]arsole with 2,6-dibromo-4,8-dioctodecylbenzo[1,2-*b*:4,5-*b'*]dithiophene, where R represents dodecyl side chains**

The polymer was synthesised and purified in the same manner as described in **Section 2.4.3**, yielding **PDTAsBDT** as a dark red solid in a yield of 56%. The molecular weight as determined by GPC in chlorobenzene (80 °C) against polystyrene standards was 7.0 kg/mol, with $M_w$ = 9.8 kg/mol and Đ = 1.40. The polymer was soluble in a variety of chlorinated solvents including chloroform and chlorobenzene, as well as displaying some solubility in hot hexane. The structure of the polymer was confirmed by $^1$H NMR and elemental analysis.

### *2.5.1 – Optical properties*

The optical properties of **PDTAsBDT** were studied using UV-vis spectroscopy of the polymer in chlorobenzene solution and as a thin film on a glass slide. In solution, the polymer displayed a $\lambda_{max}$ of 474 nm with no noticeable shoulders, while the thin film absorption peak red-shifted to 518 nm with a shoulder at approximately 570 nm, as shown in **Figure 2.29**. The appearance of this shoulder in the solid state indicates an increase in the planarity of the polymer backbone, likely due to reduced twisting between the monomer units and hence improved π-π stacking between polymer chains.

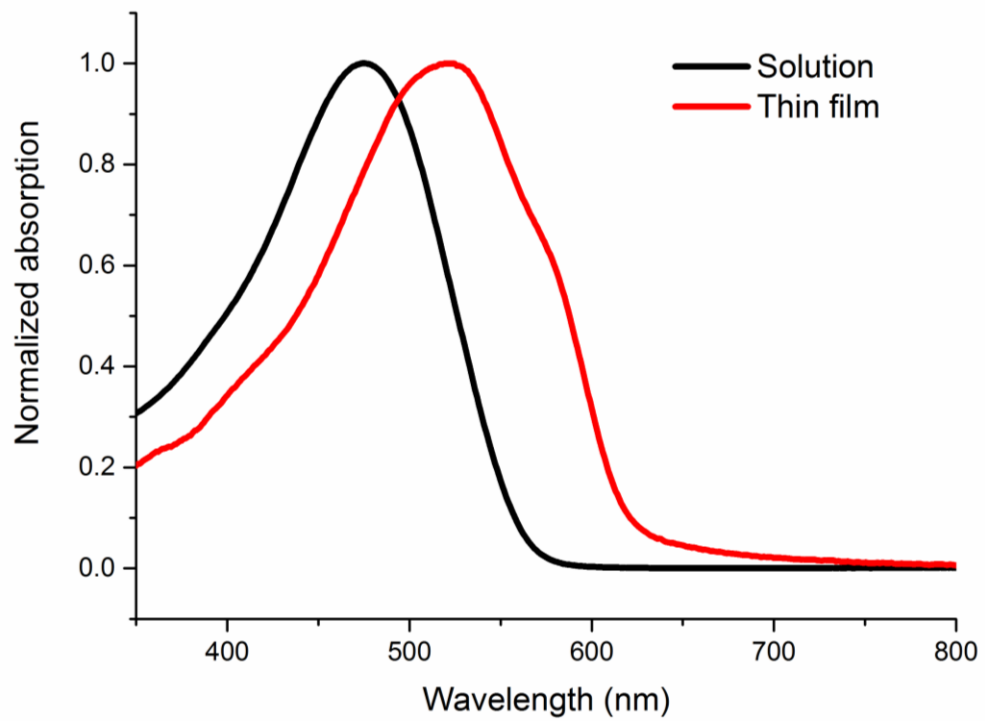



**Figure 2.29: UV-vis absorption spectra of PDTAsBDT in chlorobenzene solution and as a thin film**

### *2.5.2 – Physical properties*

DFT was used to calculate the molecular geometry of **PDTAsBDT** using Gaussian 09 at the B3LYP level of theory and with the 6-311G(d,p) basis set. **Figure 2.30a** shows the results of this calculation, with the predicted structure appearing similar to the bithiophene materials studied in **Section 2.4**. As might be expected, the twists between the dithienoarsole groups and the benzodithiophene comonomers are of a similar magnitude to those seen with bithiophene (39° vs. 40°, respectively), and the lowest energy configuration of **PDTAsBDT** shows the DTAs units as all being in the same plane, with the BDT moieties twisted out of this in a *cis* configuration. As before, it is likely that the source of this twist is the alkyl chains at the 3/5 positions of the dithienoarsole ring, although the fused BDT units should decrease backbone flexibility compared to the bithiophene, which may explain the presence of the shoulder in the thin film UV spectrum as this would aid π-π stacking. No significant peaks were observed in the DSC of **PDTAsBDT** when measured between 0–300 °C at 10 °C $min^{-1}$, indicating either that the polymer was amorphous or that any thermal transitions occurred outside of this temperature range.

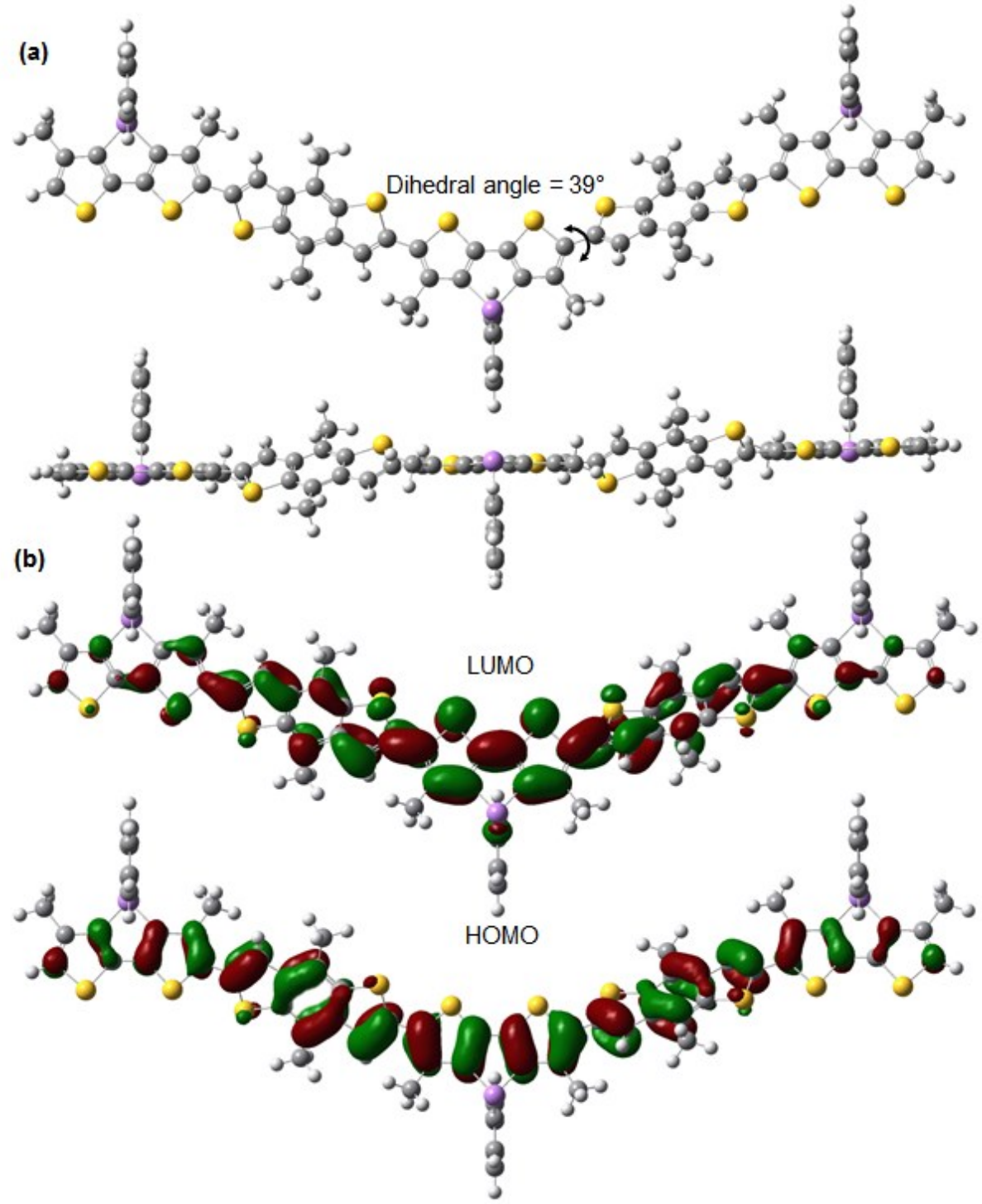



**Figure 2.30: (a) Molecular geometry and (b) frontier molecular orbitals of PDTAsBDT as calculated using Gaussian 09 at the B3LYP level of theory with the 6-311G(d,p) basis set. LUMO is shown on the top, HOMO underneath**

### *2.5.3 – Electronic properties*

As can be seen in **Figure 2.30b**, the frontier molecular orbitals of **PDTAsBDT** were predicted using Gaussian 09 at the B3LYP level of theory using the 6-311G(d,p) basis set. As

with the previous DTAs-containing polymers, the HOMO shows nodes through all the arsenic atoms, and the extent of the electron delocalization can be seen to be similar to that in **PDTAsBT** – i.e., it is slightly centralized, as opposed to the full delocalization predicted for **PDTAsV**. Again, this accounts for the significant blue shift in $\lambda_{max}$ when compared to this latter polymer. The LUMO also shows similarities with **PDTAsBT**, with a similar delocalization pattern and involvement of the arsenic-phenyl $\sigma^*$-orbital on only the central DTAs unit.

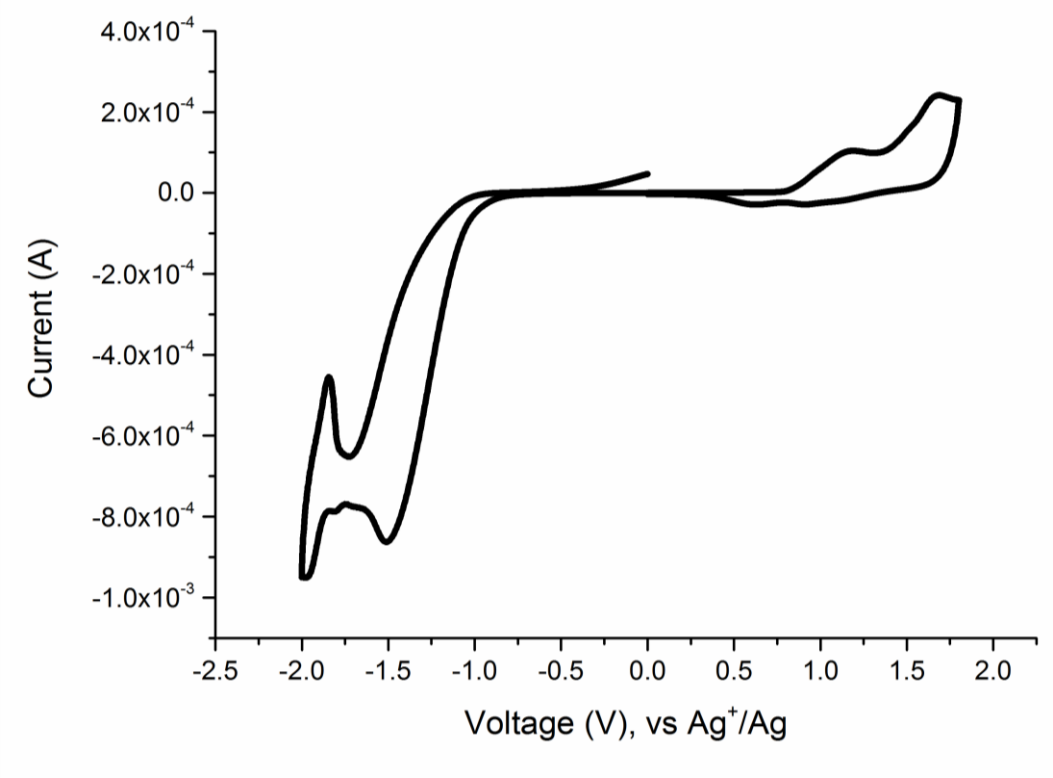



**Figure 2.31: Cyclic voltammogram of PDTAsBDT as a thin film on FTO in a 0.1 M $[Bu_4N][PF_6]$ acetonitrile solution at a scan rate of 50 mV $s^{-1}$**

Predictions of the HOMO and LUMO energy levels gave values of −5.01 and −2.58 eV, respectively, resulting in a predicted band gap of 2.43 eV. When measured using CV as a thin film on FTO in 0.1 M $[Bu_4N][PF_6]$ acetonitrile solution, the HOMO was −5.23 eV, as estimated from the oxidation potential of 0.83 V, while the LUMO was −2.52 eV, giving an electrochemical band gap of 2.71 eV. On the other hand, the optical band gap, calculated from the onset of absorption in the **PDTAsBDT** thin film UV-vis spectrum, was 2.00 eV. Once again, this shows the

trend of the electrochemical band gap being the largest, the theoretical band gap predicting an intermediate value, with the optical band gap being the smallest.

### *2.5.4 – OFET performance*

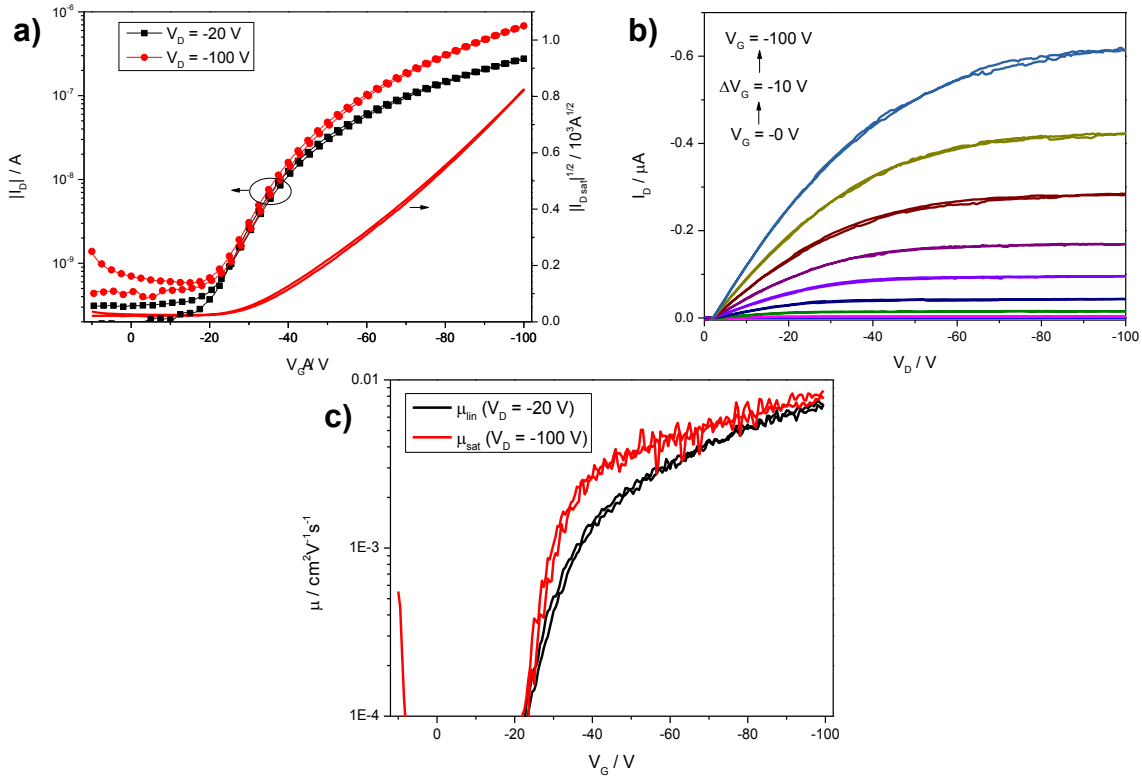



**Figure 2.32: (a) Transfer characteristics, (b) output characteristics, and (c) linear and saturated mobilities of top gate, bottom contact OFET devices using PDTAsBDT as the active layer**

The OFET performance of **PDTAsBDT** was tested in top gate, bottom contact devices, which were fabricated in the same manner as previously described in **Section 2.3.4**, and the results are shown in **Figure 2.32**. As with the previous polymers, the dithienoarsole-benzodithiophene copolymer displayed typical p-type semiconducting behaviour with very little hysteresis observed between the forward and reverse sweeps. The threshold voltage was calculated to be -44.1 V, and the on/off ratio and mobility of the device were approximately an order of magnitude below those observed for **PDTAsV**, at $10^3$–$10^4$ and 0.0084 $cm^2\ V^{-1}\ s^{-1}$ for $I_{on}/I_{off}$ and the maximum saturated mobility, respectively. Unlike for **PDTAsV**, the mobility of **PDTAsBDT** showed a mild dependence on gate voltage, with the average saturated mobility being 0.0066 $cm^2\ V^{-1}\ s^{-1}$, a much larger difference than was observed for the vinylene polymer.

### *2.6 – Dithienoarsole lone pair modification*

One of the most oft-cited advantages of dithienophosphole units is the tunability of their optoelectronic properties through modification of the phosphorus lone pair.[14,15,49] Although the primary goal of this project was to examine the properties of the dithienoarsole analogue in its +3 oxidation state, some time was also spent investigating the modification of the arsenic lone pair to determine the impact this would have on the materials.

The first method of lone pair modification that was investigated was oxidation. Although hydrogen peroxide is reported to give quantitative yields when used to oxidise dithienophosphole,[12] it was found to be ineffective for the oxidation of the dithienoarsole compound **2.10**. For this reason, the stronger oxidising agent *m*-CPBA was used to form the dithienoarsole oxide, and the characterisation and properties of the product **2.11** were discussed previously in **Section 2.2.2.1**. One of the key results of the oxidation was a 25 nm red shift in $\lambda_{max}$ (see **Figure 2.7**), confirming that changes in the arsenic oxidation state affect the optical properties of the material and potentially allowing the use of dithienoarsole compounds for the detection of strong oxidising agents. The advantage of using DTAs-based systems for this over DTPh analogues would be the increased air stability of the arsole group, which would prevent uncontrolled oxidation in the presence of air as well as making sensors more selective towards stronger oxidising agents.

Another common modification of phosphole lone pairs is oxidation with elemental sulfur.[50] It has been observed that these sulfide compounds share absorption and luminescence peaks with their oxide analogues due to their high degrees of similarity, however they exhibit weaker fluorescence intensities, potentially due to heavy atom effects from the sulfur.[51] In order to investigate whether similar fluorescence quenching could be observed in dithienoarsole-sulfides, we attempted to synthesize compound **2.15** from **2.10** under a variety of conditions, monitoring the reactions using UV-vis spectrometry due to the expectation of a 25 nm red shift in the absorption maximum. However, even after heating THF solutions of **2.10** and excess $S_8$

for 72 h, no reaction was observed, likely because elemental sulfur was not a sufficiently strong oxidising agent for **DTAs**. Although disappointing, this was expected due to the low yield of the reaction between **2.10** and $H_2O_2$, which indicates that stronger oxidizing agents are required to modify the arsenic lone pair than the phosphorus.

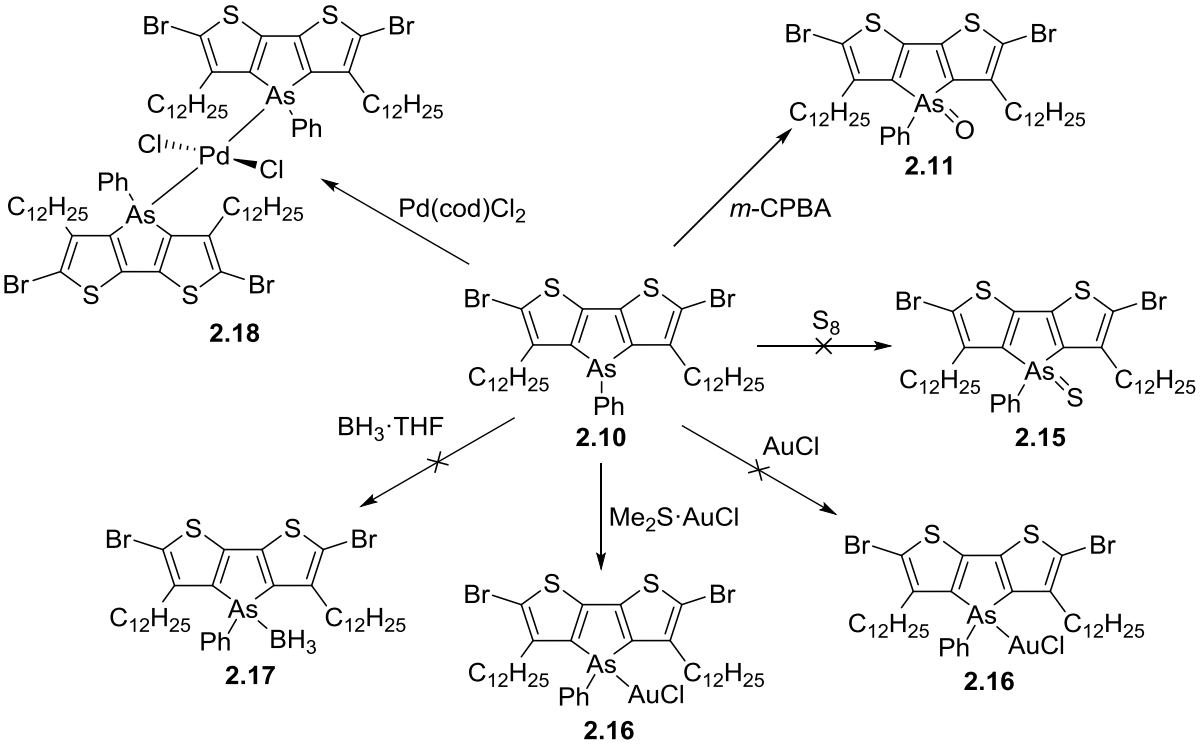



**Figure 2.33: Attempted and successful lone pair functionalizations of DBDTAs**

Other modifications commonly employed to tune dithienophosphole energy levels were also attempted on the **DTAs** monomer, including exposing the material to gold(I) chloride and $BH_3$·THF, neither of which were successful. These investigations into the lone pair modification of dithienoarsole indicate that the group is substantially more stable than its phosphole analogue, requiring stronger oxidising agents to affect changes to the lone pair. Despite this, some promising preliminary results were obtained by using chloro(dimethyl sulphide) gold(I) and dichloro(1,5-cyclooctadiene)palladium(II), which are believed to have yielded compounds **2.16** and **2.18**, respectively, the first as pale but bright yellow crystals and the second as fragile bright orange needles. Although full characterisation of these compounds is not yet complete, in the interest of completeness their structures and $^1$H NMR spectra are shown in **Figure 2.34**.

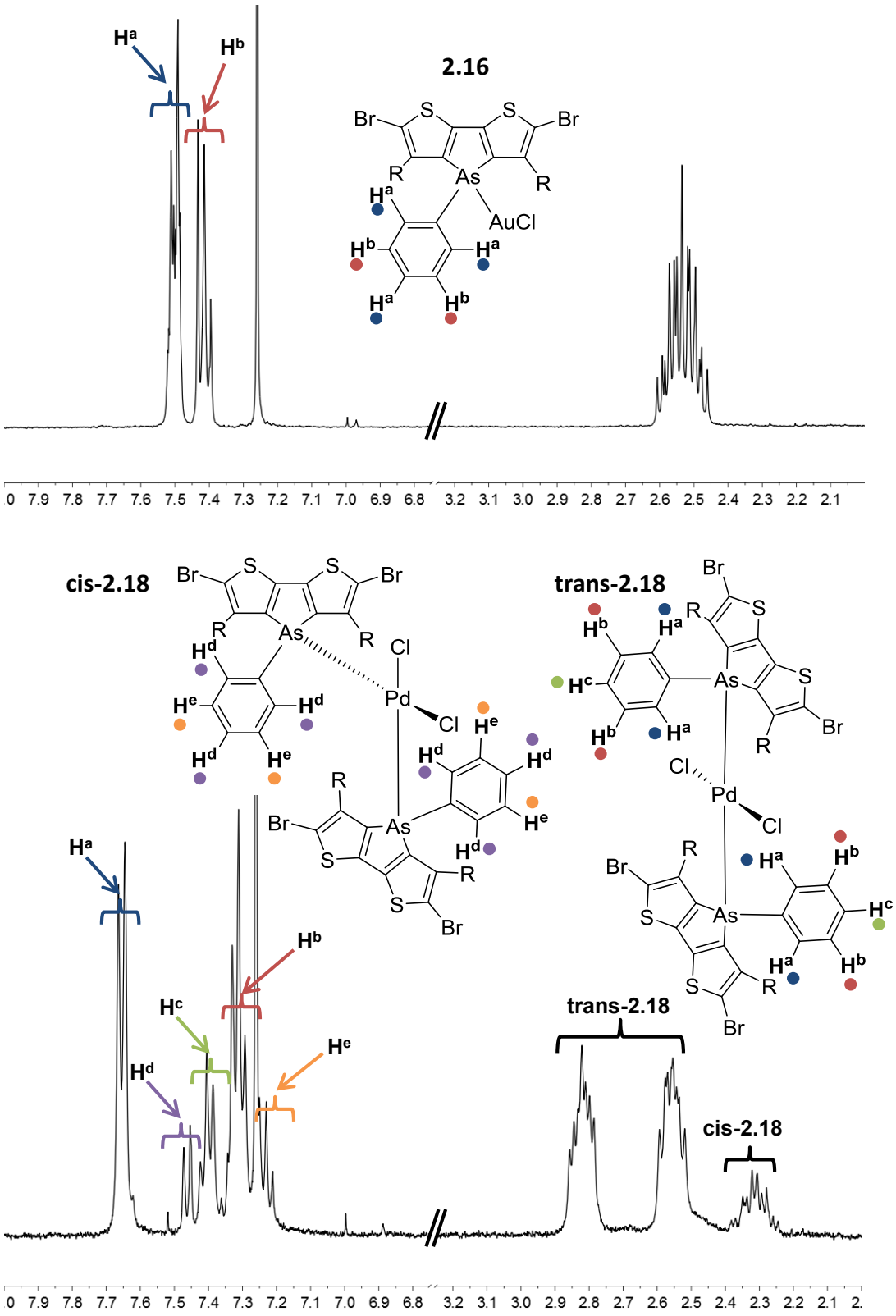



**Figure 2.34: $^1$H NMR spectra of 2.16 (top) and *cis*-2.18 and *trans*-2.18 (bottom) in the regions 6.75–8.00 ppm (left) and 2.00–3.25 ppm (right)**

The NMR spectrum of **2.16** shows a combination of the traits of **2.10** and **2.11**, with the aromatic protons being split apart, albeit only into two groups of peaks rather than the three

observed for **2.11**, while the peaks relating to the protons on the peripheral alkyl chains remain as a single highly complex multiplet. This agrees both with the findings of groups that have investigated gold complexes of dithienophosphole,[35] as well as with the expectation that the arsenic-gold bond would be longer than the arsenic-oxygen bond, allowing rotation of the alkyl chains while still reducing the degeneracy of the phenylic protons.

Due to the presence of both *cis*- and *trans*-isomers of **2.18**, the NMR spectrum of this material is more difficult to interpret. However, it generally seems to agree with results previously obtained by Baumgartner et al. for the phosphole analogue,[29] with aromatic protons at 7.66 and 7.31 ppm likely being caused by the phenyls in the *trans*-isomer, and those at 7.40 and 7.46 ppm to the *cis*-isomer. This gives a *trans*:*cis* ratio of approximately 5:1 as measured from the $^{1}$H NMR, although the inability to use $^{31}$P NMR makes this analysis substantially more difficult than it is for dithienophospholes.

It is hoped that further work will allow us to study both these materials in more detail, and the promising crystals observed so far make us optimistic that X-ray crystallography will be able to confirm the structures, and the interesting photoluminescence properties of the phosphole analogues mean this should be an interesting avenue for future research.

### *2.7 – Ongoing dithiazoloarsole work*

An alternative method of tuning arsole energy levels is altering the structures of the flanking rings. For example, replacing carbon atoms with the more electronegative nitrogen can result in more stable (i.e., lower lying) HOMO and LUMO levels, increasing the air stability of nitrogen-containing heterocycles relative to their carbonaceous analogues.[52–54] Additionally, introduction of thiazole groups in the place of thiophene rings has occasionally been shown to alter the charge transport properties of materials from p-type to n-type.[55–57] The interesting properties attributed to the thiazole group led us to investigate the impact of replacing the dithiophene ring system with a dithiazole group, again bridged by an arsenic atom.

### *2.7.1 – Synthesis of dithiazoloarsole*

Synthesis of dithiazolo[5,4-*b*:4',5'-*d*]arsole (**2.21**) was carried out from 4,4'-dibromo-2,2'-bis(triisopropylsilyl)-5,5'-bithiazole (**2.19**), which was provided by Samuel Cryer, as shown in **Figure 2.35**. The dibromobithiazole was dilithiated using *n*-BuLi at −78 °C, followed by quenching with dichlorophenylarsine (synthesized as described in **Section 2.2.1**) to produce the protected dithiazolo[5,4-*b*:4',5'-*d*]arsole **2.20** as a low melting point yellow solid in a 76% yield. Removal of the diisopropylsilyl groups was affected using TBAF at 0 °C, and the product was recrystallized from acetone to yield the product **2.21** as brown crystals in 47% yield.

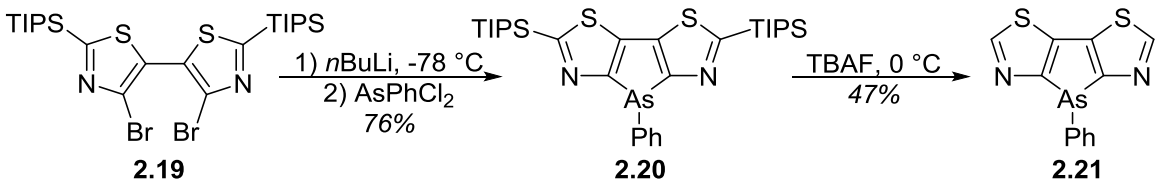



**Figure 2.35: Synthesis of dithiazolo[5,4-*b*:4',5'-*d*]arsole (2.21)**

The structure of **2.21** was confirmed using a combination of $^{1}H$ and $^{13}C$ NMR, mass spectrometry, and X-ray crystallography.

### *2.7.2 – Crystal structure*

Recrystallization of **2.21** from hot acetone provided a single crystal sample that was suitable for structural determination using X-ray crystallography, which both provided confirmation of the structure and allowed a comparison of the crystal structure of the dithiazoloarsole compound with that of the dithiazolophosphole analogue, which has previously been reported by Baumgartner et al.[58] The crystal structure of **2.21** is shown in **Figure 2.36**, and some important bond lengths and angles for **2.21** and its phosphole analogue are listed in **Table 2.2**, while full crystallographic information for **2.21** can be found in **Appendix C**.

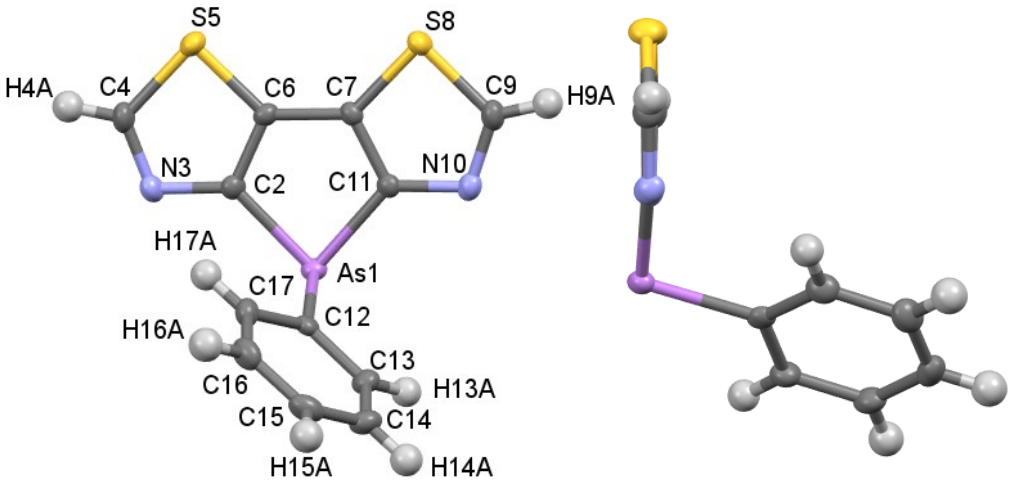



**Figure 2.36: Crystal structure of the dithiazoloarsole compound 2.21, face on (left) and edge on (right), with ellipsoids set to 50% probability. The atom labels used in the image on the left are also used in Table 2.2**

As expected, the dithiazoloarsole shows a great degree of similarity with its phosphole analogue, exhibiting a highly planar ring system with the exocyclic phenyl group protruding almost perpendicularly from the central metallole ring. However, differences do exist between the crystal structures that provide important information regarding the nature of **2.21** and how it compares to its phosphole equivalent.

**Table 2.2: Selected bond lengths (Å) and bond angles (°) for dithiazolophosphole and dithiazoloarsole (2.21). Atomic labels are as shown in Figure 2.36, with X indicating P/As. [a] Information for dithiazolophosphole is from the Baumgartner et al. paper entitled *Dithiazolo[5,4-b:4′,5′-d]phosphole: A Highly Luminescent Electron-Accepting Building Block.*[58]**

| Bond/Angle | Dithiazolophosphole[a] | Dithiazoloarsole (2.21) |
|---|---|---|
| **X1-C2** | 1.815(3) | 1.955(2) |
| **X1-C11** | 1.815(3) | 1.960(2) |
| **X1-C12** | 1.817(6) | 1.954(2) |
| **C2=C6** | 1.371(4) | 1.368(3) |
| **C7=C11** | 1.371(4) | 1.370(3) |
| **C6-C7** | 1.442(4) | 1.443(3) |
| **N3=C4** | 1.297(4) | 1.300(3) |
| **N10=C9** | 1.302(4) | 1.306(3) |
| **C2-N3** | 1.366(4) | 1.369(3) |
| **C11-N10** | 1.370(4) | 1.370(3) |
| **θ(C2-X1-C12)** | 102.7(2) | 99.91(9) |
| **θ(C11-X1-C12)** | 103.4 (2) | 97.89(9) |
| **θ(C2-X1-C11)** | 87.21(13) | 83.85(9) |
| **$\theta_{sum}$(C-X-C)** | 293.3 | 281.7 |

These differences relate to the aromaticity of the pnictogen-containing ring systems. In a perfectly aromatic ring, all the carbon-carbon (or carbon-heteroatom) bonds should be the same length due to resonance between different canonical structures (i.e., electron delocalisation). For example, the C12-C13 and C13-C14 bonds in the phenyl ring of **2.21** are 1.386 and 1.383 Å, respectively, indicating a high degree of aromaticity. However, when aromaticity is less complete, it is common to see alternating longer and shorter bonds that render the molecular structure closer to the double and single bonds that are used to represent aromatic rings in individual resonance structures. This means that bond lengths can be used as a rough measure of the aromaticity of a given ring system by calculating the harmonic oscillator measure of aromaticity (HOMA).[59] The HOMA of a material is a number between 0 and 1 that gives an indication of the degree of aromaticity, with the 1 and 0 values fixed at the aromaticities of benzene and its individual resonance structures (with alternating short-long bonds), respectively. It is generally understood that compounds with HOMA values > 0.5 show aromaticity, values between 0.5 and 0.0 indicate non-aromaticity, and that compounds with negative values show anti-aromatic behaviour.[60]

The most accurate calculation for the HOMAs of aromatic heterocycles currently available was formulated by Martins et al. in 2011, and is referred to as the harmonic oscillator model of heterocyclic electron delocalization, or HOMHED.[61] Through **Equation 2.2**, the HOMHED compares bond lengths as measured by X-ray crystallography ($R_i$) with "optimal" bond lengths ($R_{opt}$), which are calculated by inputting reference single ($R_s$) and double ($R_d$) bonds into **Equation 2.3**, where ω is taken to be 2. The normalization constants, α, are used to account for the differences between the bond types, and n is the total number of C-C and C-heteroatom bonds being studied.

$$HOMHED = 1 - \frac{1}{n}\left\{\alpha_{CC}\sum\left[\left(R_{CC(opt)} - R_i\right)\right]^2 + \alpha_{CN}\sum\left[\left(R_{CN(opt)} - R_i\right)\right]^2 + \alpha_{CS}\sum\left[\left(R_{CS(opt)} - R_i\right)\right]^2 + \alpha_{CX}\sum\left[\left(R_{CX(opt)} - R_i\right)\right]^2\right\} \quad \textbf{Equation 2.2}$$

$$R_{opt} = \frac{(R_S + \omega R_d)}{1 + \omega}$$ **Equation 2.3**

$$\alpha = 2\left[\left(R_{opt} - R_s\right)^2 + \left(R_{opt} - R_d\right)^2\right]^{-1}$$ **Equation 2.4**

**Table 2.3: Calculation parameters and HOMHED values for dithiazolophosphole and dithiazoloarsole. $R_{opt}$ and α were calculated using Equations 2.3 and 2.4, respectively, while HOMHED values were calculated using Equation 2.2. Bond lengths were obtained as follows: [a] taken from the Martins et al. HOMHED paper,[61] [b] taken from *Tables of Bond Lengths* by Watson et al., [c] averages of several C=X bonds in crystal structures available from the Cambridge Structural Database (listed in Appendix C).**

| | C-C | C-N | C-S | C-P | C-As |
|---|---|---|---|---|---|
| $R_s$ (Å) | 1.530[a] | 1.474[a] | 1.819[a] | 1.855[b] | 1.963[b] |
| $R_d$ (Å) | 1.316[a] | 1.271[a] | 1.599[a] | 1.698[c] | 1.847[c] |
| $R_{opt}$ (Å) | 1.387 | 1.339 | 1.672 | 1.750 | 1.886 |
| α | 78.6 | 87.4 | 74.4 | 146.1 | 267.5 |

| | |
|---|---|
| $HOMHED_{phos}$ | 0.8015 |
| $HOMHED_{ars}$ | 0.6863 |

**Table 2.3** shows the values of $R_s$, $R_d$, $R_{opt}$, and α for the five bond types seen in the dithiazolometallole structures, as well as the final HOMHED values of dithiazolophosphole and dithiazoloarsole, which are 0.8015 and 0.6863, respectively. It is immediately apparent on examination of these numbers that both compounds are aromatic, with HOMHED values of greater than 0.5, although the phosphorus-containing material is more aromatic than the arsole analogue as its HOMHED value is closer to 1. This finding is in line with the predicted trends of the aromaticities of pnictogen-containing heterocycles, which are expected to decrease as heavier group 15 elements are used in the rings.[16,34]

Another feature of the dithiazoloarsole crystal structure that shows a significant difference from that of the phosphole analogue is in the molecular packing. Baumgartner and coworkers observed π-π stacking between both the tricyclic rings (with the phenyl groups pointing away from the stacked ring systems) and between the orthogonal phenyl rings, with the stacking distances of these two interactions being 3.57 and 3.96 Å, respectively. On the other hand, the dithiazoloarsole molecules organised themselves into slip-stacked dimeric arrangements

primarily governed by interactions between the faces of the orthogonal phenyl groups and the edges of the tricyclic ring system, as shown in **Figure 2.37**. These interactions have two key distances associated with them – the inter-tricyclic π-π stacking distance, which was 3.56 Å, and the face-edge distance between the phenyl ring and the adjacent thiazole ring, which measured 3.24 Å.

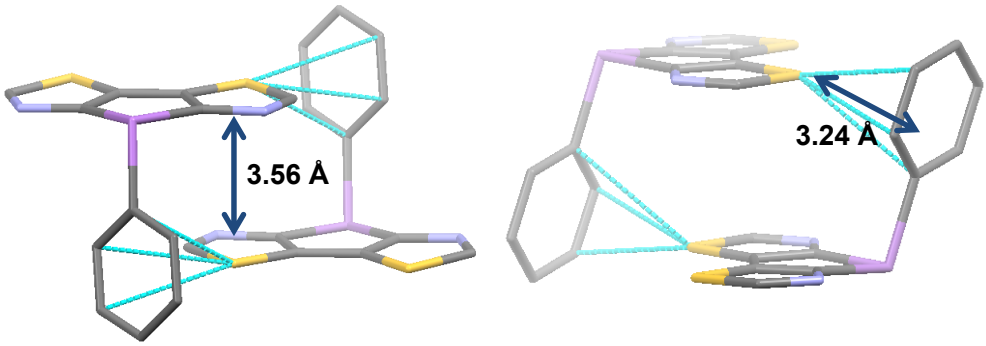



**Figure 2.37: Dimeric arrangement of dithiazoloarsole molecules from two different angles. Light blue lines indicate short contacts between the phenyl rings and the tricyclic systems, while the arrows and associated labels show intermolecular distances between the faces of the two tricyclic rings (left) and the phenyl rings and the edge of the tricyclic rings (right)**

The broader packing arrangement of the material involved arrangements of these dimers in an orthorhombic unit cell with the space group P*bca*, such that molecules in the same row were rotated through ~180° about the longer axis of the tricyclic system, enabling the slip-stacked dimers to tessellate. **Figure 2.38** shows examples of this tessellation from two different angles.

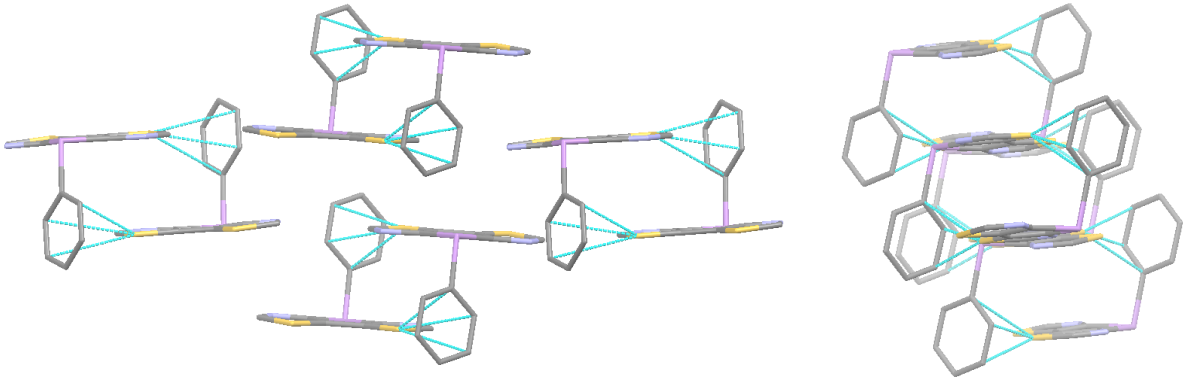


**Figure 2.38: Tessellation of four dimeric dithiazoloarsole structures along the short (left) and long (right) tricyclic axes. Light blue lines represent short contacts between dimers**

### *2.8 – Conclusions*

This chapter has detailed the first reported synthesis of a dithienoarsole heterocycle and shown that unlike the analogous dithienophosphole, it was stable to oxidation in the presence of ambient air. The dithienoarsole was incorporated into a number of soluble conjugated polymer backbones, utilizing vinylene (**PDTAsV**), bithiophene (**PDTAsBT**), and benzodithiophene (**PDTAsBDT**) comonomers, and the optoelectronic properties of these polymers were studied. **PDTAsV** was found to be capable of aggregating and crystallizing in the solid state, and demonstrated promising charge-carrier mobilities in OFET devices. The performance of **PDTAsBT** was compared with its phosphole analogue, and it was found that the arsenic-containing polymer showed improved OFET performance whilst maintaining many of the other properties of the phosphorus-containing polymer. The OFET performance of **PDTAsBDT** was also measured and was found to be relatively similar to that of **PDTAsBT**, which was promising but still somewhat lower than that of **PDTAsV**.

In addition to the polymers and their OFET data, this chapter has also presented some preliminary results regarding the lone pair modification of the dithienoarsole unit. It was found that the improved oxidative stability of the unit over its phosphorus analogue necessitated the use of stronger oxidizing agents to modify the lone pair. Despite this, several different variations of the unit were synthesised, including the dithienoarsole-oxide, the gold(I) chloride complex, and a dimeric dithienoarsole-palladium complex. However, work on these materials is ongoing and the metal-ligand complexes have yet to be fully characterised.

The final section of this chapter described some additional preliminary work on the effect of modifying the structures of the heterocycles that are bridged by the arsenic atom. By replacing the thiophene rings with thiazoles, it was possible to obtain a crystalline material that was studied by X-ray crystallography. Examining the crystal structure indicated that dithiazoloarsole was an aromatic system that displayed less aromaticity than its phosphole equivalent, previously reported by another group. This was in line with a number of predictions

from the literature, and future work in this area will examine the impact of this reduced aromaticity on the properties of the material, as well as attempting to include it in a polymeric system.

Overall, the results presented in this chapter show that dithienoarsole is an interesting building block for both organic electronics and in its own right. In particular, the opportunity to tune the oxidation state of the bridging arsenic atom may offer interesting opportunities for the utilization of these materials in sensing applications.

### *2.9 – Experimental*

Reagents were purchased from Sigma Aldrich and VWR and used with no additional purification, and all reactions were performed using oven-dried glassware under argon using standard Schlenk techniques. Thin layer chromatography (TLC) was performed on silica plates (Merck Kieselgel 60 $F_{254}$ aluminum sheets) and visualized using UV light (254 and 365 nm). Column chromatography was performed on silica gel (Merck Kieselgel 60 230–400 mesh). $^{1}H$, $^{13}C$ NMR, and $^{31}P$ NMR spectra were recorded using Bruker AV-400 spectrometers ($^{1}H$ = 400 MHz, $^{13}C$ = 101 MHz, $^{31}P$ = 162 MHz) at 298 K. Microwave experiments were carried out in a Biotage Initiator (v. 2.3). UV-visible spectroscopy was carried out using a UV-1800 Shimadzu UV-vis spectrometer for both solution and thin-film samples. Thin films of the polymers were prepared by spin coating 5 mg $ml^{-1}$ solutions of polymer in chlorobenzene at 1000 rpm for 60 s. Molecular weights ($M_n$, $M_w$, Đ) were measured using an Agilent Technologies 1200 series GPC at 80 °C, using chlorobenzene as an eluent with two PL mixed B columns in series. The column was calibrated using narrow polydispersity polystyrene standards. X-ray diffraction (XRD) measurements were carried out with a PANalytical X′Pert-pro MRD diffractometer equipped with a nickel-filtered Cu Kα source (1.54 Å) and X′Celerator detector, using current I = 40 mA and accelerating voltage V = 40 kV. Samples were prepared by drop casting onto silicon substrates (100) and annealing was carried out for 30 min at 200 °C under argon, and samples were rotated at 60 rpm during measurements. Cyclic voltammetry (CV) was performed in a

standard three-electrode setup with polymer film on FTO as the working electrode, a Pt mesh as the counter electrode and a Ag wire as the reference electrode. The working electrodes were prepared by spin coating a 10 mg $ml^{-1}$ solution of polymer in chlorobenzene onto FTO-coated glass (supplied by Sigma Aldrich, ~7 Ω/sq) at 1000 rpm for 60 s. Voltammograms were measured using a 0.1 M tetrabutylammonium hexafluorophosphate ($(TBA)PF_6$) solution in acetonitrile as an electrolyte, at a scanning rate of 0.05 V $s^{-1}$. Redox potentials were calibrated against a standard ferrocene/ferrocenium (FOC) system, assuming the energy level of FOC to be 4.8 eV below vacuum. Geometries and frontier molecular orbitals were calculated using density functional theory at the B3LYP level of theory with the 6311G(d,p) basis set, using GaussView 5.0.

### *2.9.1 – Synthesis of 3-dodecylthiophene (2.2)*

Dodecylmagnesium bromide (0.5 M in methyl-THF, 300 ml, 150 mmol) was added dropwise to a stirring solution of 3-bromothiophene (24.46 g, 150 mmol) and dichloro(1,3-bis(diphenylphosphino)propane)nickel (0.812 g, 1.5 mmol) in anhydrous THF (100 ml) over the course of an hour using a dropping funnel. Once addition was complete, the reaction was refluxed overnight, after which it was cooled to room temperature and then quenched by pouring onto crushed ice and 2 M HCl. The product was extracted from this mixture using diethyl ether (3 ×100 ml), and the organic layers were combined and dried over $Mg_2SO_4$. The solvent was removed from the combined organic layers in vacuo, and the resulting material was distilled under reduced pressure to yield 3-dodecylthiophene (**2.2**, b.p. ~106 °C at 0.7 mbar) as a colourless oil (30.96 g, 123 mmol, 82%). $^1$H NMR (400 MHz, $CDCl_3$) δ 7.25 (dd, *J* = 4.9, 3.0 Hz, 1H), 6.96 – 6.92 (m, 2H), 2.64 (t, *J* = 7.6 Hz, 2H), 1.72 – 1.58 (m, 2H), 1.41 – 1.20 (m, 18H), 0.90 (t, *J* = 6.8 Hz, 3H). MS (GCMS) *m/z* = 252.1.

### *2.9.2 – Synthesis of 4,4'-bis(dodecyl)-2,2'-bithiophene (2.3)*

Preparation of **2.3** was performed based on a procedure previously reported by Fei et al.[25] A degassed solution of dry tetramethylethylenediamine (TMEDA) (5.35 ml, 36.5 mmol) in

anhydrous THF (8 ml) was cooled to −30 °C, after which *n*-butyllithium (2.5 M in hexane, 15.7 ml, 39.2 mmol) was added dropwise over 15 min, ensuring the temperature remained at −30 °C. Separately, a solution of 3-dodecylthiophene (**2.2**) (9 g, 35.6 mmol) in dry THF (55 ml) was prepared at room temperature. The cold TMEDA/n-butyllithium solution was added to the solution of **2.2** via cannula over the course of 15 minutes. The combined solution was refluxed for 1 h, and then cooled to −40 °C, after which anhydrous copper (II) chloride (5.27 g, 39.2 mmol) was added and the rapidly stirring mixture was allowed to warm to room temperature overnight. On completion, the reaction was quenched with hydrochloric acid (37%, 12 ml) and water (35 ml). The crude product was extracted with diethyl ether (3 × 30 ml) and the combined organic layers were washed with aqueous sodium sulfite solution (5%, 50 ml) followed by deionised water (2 × 20 ml). After drying the organic phase over sodium sulphate, the solvent was removed *in vacuo*. The product was filtered through a silica pad (eluent: hexane at 50 °C). The solvent was again removed, and the final product was obtained by recrystallization (acetone), yielding 4,4'-bis(dodecyl)-2,2'-bithiophene (**2.3**) as a yellow solid (5.31 g, 10.6 mmol, 59.6%, m.p. 48–49 °C). $^{1}$H NMR (400 MHz, $CDCl_3$) δ 6.98 (s, 2H), 6.77 (s, 2H), 2.56 (t, *J* = 7.9 Hz, 4H), 1.69 – 1.56 (m, 4H), 1.28 (m, 36H), 0.88 (t, *J* = 6.8 Hz, 6H). $^{13}$C NMR (101 MHz, $CDCl_3$) δ 144.13, 137.50, 124.94, 118.83, 32.08, 30.68, 30.55, 29.82 (3C), 29.75, 29.62, 29.52, 29.47, 22.85, 14.29. HRMS (EI$^+$) calculated for $C_{32}H_{54}S_2$ [M$^+$], 502.3667; found, 502.3674.

### *2.9.3 – Synthesis of 3,3',5,5'-tetrabromo-4,4'-bis(dodecyl)-2,2'-bithiophene (2.4)*

Again using the procedure of Fei et al. as a guide,[25] to a solution of 4,4'-bis(dodecyl)-2,2'-bithiophene (**2.3**) (5.22 g, 10.37 mmol) in chloroform (40 ml) and acetic acid (10 ml) stirring in the absence of light was added bromine (2.3 ml, 44.9 mmol). The reaction was stirred in the dark for 2 h at room temperature, then heated to 70 °C overnight. After completion (as monitored by TLC), the reaction was quenched with 5% aqueous sodium sulphite solution (20 ml), extracted with dichloromethane (3 × 20 ml), and the combined organic layers were washed with deionised water (3 × 10 ml). The crude product was dried over magnesium sulfate, filtered, and concentrated in vacuo. The final product was obtained by recrystallization

(acetone), yielding 3,3',5,5'-tetrabromo-4,4'-bis(dodecyl)-2,2'-bithiophene (**2.4**) as a yellow solid (7.36 g, 9.00 mmol, 86.8%, m.p. 66–67 °C). $^{1}$H NMR (400 MHz, $CDCl_3$) δ 2.66 (t, *J* = 7.8 Hz, 4H), 1.62 – 1.50 (m, 4H), 1.46 – 1.21 (m, 36H), 0.88 (t, *J* = 6.8 Hz, 6H). $^{13}$C NMR (101 MHz, $CDCl_3$) δ 141.65, 128.70, 114.76, 111.20, 32.09, 30.49, 29.84, 29.80 (2C), 29.71, 29.52 (3C), 28.71, 22.86, 14.29. MS (MALDI-TOF) *m/z* = 818.6.

### *2.9.4 – Synthesis of 3,3'-dibromo-5,5'-bis(trimethylsilyl)-4,4'-bis(dodecyl)-2,2'-bithiophene (2.5)*

Once more adapting the procedure of Fei and coworkers,[25] a solution of (**2.4**) (7.28 g, 8.90 mmol) in anhydrous THF (120 ml) was cooled to −78 °C, then *n*BuLi (2.5 M in hexane, 7.7 ml, 19.25 mmol) was added dropwise over 10 min. The reaction was stirred and monitored via TLC. After all starting material had been lithiated, trimethylsilyl chloride (1 M in THF, 22 ml, 22 mmol) was added in one portion. The reaction was allowed to warm to room temperature overnight, then the solvent was removed in vacuo, after which the salts were removed using a silica plug (eluent: hexane). The product was purified by column chromatography over silica (eluent: hexane) to yield 3,3'-dibromo-5,5'-bis(trimethylsilyl)-4,4'-bis(dodecyl)-2,2'-bithiophene (**2.5**) as a yellow oil (7.12 g, 8.84 mmol, 99%). $^{1}$H NMR (400 MHz, $CDCl_3$) δ 2.74 – 2.65 (m, 4H), 1.63 – 1.53 (m, 4H), 1.48 – 1.24 (m, 36H), 0.89 (t, *J* = 6.8 Hz, 6H), 0.37 (s, 18H). $^{13}$C NMR (101 MHz, $CDCl_3$) δ 148.62, 135.45, 134.10, 116.72, 32.09, 32.00, 30.92, 30.16, 29.86, 29.81 (3C), 29.77, 29.53 (2C), 22.86, 14.30, 0.29 (3C). MS (MALDI-TOF) *m/z* = 804.7.

### *2.9.5 – Synthesis of 3,3'-dibromo-4,4'-didodecyl-2,2'-bithiophene (2.6)*

To a solution of 3,3'-dibromo-5,5'-bis(trimethylsilyl)-4,4'-bis(dodecyl)-2,2'-bithiophene (**2.5**) (11.11 g, 13.8 mmol) in anhydrous THF (120 ml) at 0 °C was added a solution of TBAF (1 M in THF, 32 ml, 2.3 eq) in three portions, and the resulting solution was stirred for 5 min. Hexane (250 ml) was added, followed by a further 10 min of stirring. The resulting precipitate was removed by filtration through a short silica plug, and the solvent removed under reduced pressure to afford 3,3'-dibromo-4,4'-didodecyl-[2,2'-bithiophene] (**2.6**) as a yellow solid (8.76 g,

13.3 mmol, 96%, m.p. 59–60 °C). $^{1}$H NMR (400 MHz, $CDCl_3$) δ 7.10 (s, 2H), 2.69 – 2.52 (m, 4H), 1.66 (m, 4H), 1.45 – 1.22 (m, 36H), 0.88 (t, *J* = 6.8 Hz, 6H). $^{13}$C NMR (101 MHz, $CDCl_3$) δ 142.44, 121.87 (2C), 115.62, 32.08, 30.95, 29.84, 29.81 (2C), 29.75, 29.59, 29.51 (2C), 29.18, 22.85, 14.28. HRMS (EI$^+$) calculated for $C_{32}H_{51}S_2Br_2$ [M$^+$−H], 657.1799; found, 657.1808.

### *2.9.6 – Synthesis of dichlorophenylarsine (2.8)*

***Caution:*** *$PhAsCl_2$ is highly toxic and a vesicant, and as such should be handled with extreme care. Proper safety equipment should be used at all times, and reactions should be carried out in a well-ventilated fumehood. Treat any spillages and all glassware with dilute bleach to prevent accidental contamination and injury.*

Preparation of dichlorophenylarsine (**2.8**) was carried out following the procedure used by Klufers and coworkers,[26] wherein phenylarsonic acid (**2.7,** 4.99 g, 24.7 mmol) was placed in a flask and HCl (37%, 50 ml) was added, followed by stirring until **2.7** was completely dissolved. Trace $I_2$ was added, and the reaction was heated to 55 °C while $SO_2$ was bubbled through it for 6 h. The reaction was then left undisturbed overnight to allow phase separation to occur, after which the dense bottom layer (containing product) was removed, and the top layer extracted with $CHCl_3$. The combined organic fractions and initial bottom layer were concentrated in vacuo, after which the product was purified by vacuum distillation (~71 °C at 0.5 mbar) to yield dichlorophenylarsine (**2.8**) as a red liquid (4.94 g, 22.2 mmol, 89%). $^{1}$H NMR (400 MHz, $CDCl_3$) δ 7.91 – 7.85 (m, 2H), 7.57 – 7.51 (m, 3H). $^{13}$C NMR (101 MHz, $CDCl_3$) δ 145.43, 132.28, 130.01 (2C), 129.34 (2C). HRMS (EI$^+$) calculated for $C_6H_5Cl_2As$ [M$^+$], 221.8984; found, 221.8980.

### *2.9.7 – Synthesis of 3,5-didodecyl-4-phenyldithieno[3,2-b:2',3'-d]arsole (2.9)*

To a degassed solution of 3,3'-dibromo-4,4'-didodecyl-[2,2'-bithiophene] (**2.6,** 2.00 g, 3.0 mmol) in anhydrous THF (120 ml) at −78 °C was added *n*-BuLi (2.5 M in hexane, 3.64 ml, 9.1 mmol, 3 eq) dropwise over 10 min. After stirring for 1 h at −78 °C, dichlorophenylarsine (**2.8**, 0.41 ml, 3.0 mmol, 1 eq) was added slowly, and the reaction was allowed to warm to room temperature overnight. The reaction was quenched with methanol (10 ml), stirred for 30 min,

and the solvent was removed under reduced pressure. The resulting low melting point solid was dissolved in hexane, filtered through silica (eluent: hexane) to remove salts and then purified by column chromatography over silica (eluent: hexane), to afford 3,5-didodecyl-4-phenyldithieno[3,2-*b*:2',3'-*d*]arsole (**2.9**) as a low melting point, off-white waxy solid (1.09 g, 1.7 mmol, 57%). $^{1}$H NMR (400 MHz, $CDCl_3$) δ 7.30 – 7.26 (m, 2H), 7.25 – 7.17 (m, 3H), 6.80 (s, 2H), 2.55 – 2.49 (m, 4H), 1.51 – 1.41 (m, 4H), 1.35 – 1.07 (m, 40H), 0.88 (t, *J* = 6.8 Hz, 6H). $^{13}$C NMR (101 MHz, $CDCl_3$) δ 149.12 (2C), 143.93 (2C), 143.09, 136.99, 133.09 (2C), 129.07 (2C), 128.83 (2C), 120.14 (2C), 32.09 (2C), 30.86 (2C), 29.86 - 29.81 (overlapping signals, 8C), 29.66 (2C), 29.52 (2C), 29.47 (2C), 29.35 (2C), 22.85 (2C), 14.28 (2C). HRMS (EI$^+$) calculated for $C_{38}H_{57}S_2As$ [M$^+$], 652.3118; found, 652.3118.

### *2.9.8 – Synthesis of 2,6-dibromo-3,5-didodecyl-4-phenyldithieno[3,2-b:2',3'-d]arsole (2.10)*

Fresh LDA was prepared by treating a solution of diisopropylamine (0.29 ml, 2.1 mmol, 3.1 eq) in anhydrous THF (10 ml) at −78 °C with *n*BuLi (2.5 M in hexane, 0.80 ml, 2.0 mmol, 3 eq), followed by stirring for 10 min. This was then added dropwise over 10 min to a degassed solution of 3,5-didodecyl-4-phenyldithieno[3,2-*b*:2',3'-*d*]arsole (**2.9**, 0.43 g, 0.66 mmol) in anhydrous THF (25 ml) at −78 °C. The resulting mixture was allowed to warm to −30 °C over 30 min, and then cooled back to −78 °C. A freshly prepared solution of $CBr_4$ (1 M in THF, 2.65 ml, 2.65 mmol), 3.0 mmol) was cooled to −78 °C and added dropwise via syringe. The mixture was allowed to warm to room temperature overnight, and was then concentrated under reduced pressure. The solid was dissolved in $CH_2Cl_2$ and filtered through basic alumina (eluent: $CH_2Cl_2$). The solvent was removed under reduced pressure and the residue recrystallized (ethanol) to give the product, 2,6-dibromo-3,5-didodecyl-4-phenyldithieno[3,2-*b*:2',3'-*d*]arsole (**2.10**), as a pale yellow solid (0.32 g, 0.39 mmol, 60%, m.p. 65–66 °C). $^{1}$H NMR (400 MHz, $CDCl_3$) δ 7.33 – 7.18 (m, 5H), 2.57 – 2.40 (m, 4H), 1.45 – 0.99 (m, 40H), 0.93 – 0.84 (m, 6H). $^{13}$C NMR (101 MHz, $CDCl_3$) δ 147.91 (2C), 142.70 (2C), 141.40, 136.03, 133.07 (2C), 129.63 (2C), 129.08 (2C), 108.57 (2C), 32.09 (2C), 29.99 (2C), 29.80 (6C), 29.58 (2C), 29.52 (2C), 29.40 (2C), 29.32

(2C), 29.14 (2C), 22.86 (2C), 14.28 (2C). MS (MALDI) m/z = 810.2 ([$M^+$], based on an equal abundance of $^{79}Br$ and $^{81}Br$). Anal. Calcd. for $C_{38}H_{55}AsBr_2S_2$: C, 56.30; H, 6.84. Found: C, 56.28; H, 6.80.

### *2.9.9 – Synthesis of 2,6-dibromo-3,5-didodecyl-4-phenyldithieno[3,2-b:2',3'-d]arsole-4-oxide (2.11)*

To a solution of 2,6-dibromo-3,5-didodecyl-4-phenyldithieno[3,2-*b*:2',3'-*d*]arsole (**2.10**, 50 mg, 0.06 mmol) in dichloromethane (2 ml) was added *m*-CPBA (17 mg, 0.10 mmol, 1.67 eq) in one portion. The reaction was stirred for 5 minutes, after which the solvent was removed in vacuo and the residue purified by column chromatography on neutral alumina (eluent: 20% $CHCl_3$ in hexane). This yielded 2,6-dibromo-3,5-didodecyl-4-phenyldithieno[3,2-*b*:2',3'-*d*]arsole-4-oxide (**2.11**) as a yellow solid (41 mg, 0.05 mmol, 83%). $^1H$ NMR (400 MHz, $CDCl_3$) δ 7.74 – 7.71 (m, 2H), 7.61 – 7.55 (m, 1H), 7.52 – 7.46 (m, 2H), 2.61 (ddd, *J* = 14.1, 9.3, 6.2 Hz, 2H), 2.43 (ddd, *J* = 14.0, 9.4, 6.4 Hz, 2H), 1.39 – 1.01 (m, 40H), 0.88 (t, *J* = 6.8 Hz, 6H). $^{13}C$ NMR (101 MHz, $CDCl_3$) δ 142.98 (2C), 142.83 (2C), 135.46, 132.97 (2C), 131.62, 130.17 (2C), 129.89 (2C), 111.56 (2C), 32.08 (2C), 29.77 (6C), 29.64 (2C), 29.55 (2C), 29.51 (2C), 29.30 (2C), 29.27 (2C), 29.22 (2C), 22.85 (2C), 14.28 (2C). HRMS (ES) calculated for $C_{38}H_{56}S_2AsBr_2O$ ([$M^+$+H], based on 100% abundance of $^{79}Br$), 825.1355; found, 825.1393.

### *2.9.10 – Synthesis of 2,6-bis(trimethylstannyl)-3,5-didodecyl-4-phenyldithieno[3,2-b:2',3'-d]arsole (2.12)*

Fresh LDA was prepared by treating a solution of diisopropylamine (0.37 ml, 2.69 mmol, 3.1 eq) in anhydrous THF (15 ml) at −78 °C with *n*BuLi (2.5 M in hexane, 1.04 ml, 2.60 mmol, 3.0 eq), followed by stirring for 10 min. This was then added dropwise over 10 min to a degassed solution of 3,5-didodecyl-4-phenyldithieno[3,2-*b*:2',3'-*d*]arsole (**2.9**, 0.57 g, 0.87 mmol) in anhydrous THF (25 ml) at −78 °C. The resulting mixture was allowed to warm to 0 °C over 30 min, and then cooled back to −78 °C. After this, $SnMe_3Cl$ (1 M in THF, 2.60 ml, 2.60 mmol, 3.0 eq) was added dropwise via syringe over 10 min. The mixture was allowed to

warm to room temperature overnight, then was washed with water (2 × 10 ml), once with acetonitrile (10 ml), and then extracted with hexane (2 × 15 ml). The product was concentrated under reduced pressure and purified by recycling preparative GPC (40 °C, hexane) to yield 2,6-bis(trimethylstannyl)-3,5-didodecyl-4-phenyldithieno[3,2-*b*:2',3'-*d*]arsole (**2.12**) as an off-white oil (0.34 g, 0.35 mmol, 41%). $^1$H NMR (400 MHz, $CDCl_3$) δ 7.32 – 7.27 (m, 2H), 7.25 – 7.16 (m, 3H), 2.58 – 2.48 (m, 2H), 2.47 – 2.38 (m, 2H), 1.46 – 1.00 (m, 40H), 0.91 – 0.86 (m, 6H), 0.36 (s, 18H).

### *2.9.11 – Stille polymerization of 2,6-dibromo-3,5-didodecyl-4-phenyldithieno[3,2-b:2',3'-d]arsole with trans-1,2-bis(tributylstannyl)ethene (PDTAsV)*

An oven-dried high-pressure microwave tube was charged with 2,6-dibromo-3,5-didodecyl-4-phenyldithieno[3,2-*b*:2',3'-*d*]arsole (**2.10**, 82.2 mg, 0.101 mmol), *trans*-1,2-bis(tributylstannyl)ethene (61.4 mg, 0.101 mmol), and $Pd(PPh_3)_4$ (2.3 mg, 0.002 mmol). The tube was sealed with a septum and flushed with Ar, after which degassed chlorobenzene was added (0.5 ml). The mixture was thoroughly degassed with Ar, after which the inlet was removed. The vial was then placed in a microwave reactor and heated as follows: 4 min at 100 °C, 120 °C, and 140 °C, 20 min at 160 °C, and 120 min at 180 °C. After cooling to room temperature, the resulting polymer was precipitated into methanol and filtered into a Soxhlet thimble. The polymer was extracted (Soxhlet) with methanol, acetone, and hexane in that order. The hexane fraction was concentrated under reduced pressure and the resulting polymer was dissolved in chloroform, warmed to 50 °C and stirred in the presence of diethylammonium diethyldithiocarbamate (10 mg) for 1 h. The solution was concentrated in vacuo, dissolved in a minimal amount of hot chlorobenzene and the polymer collected by re-precipitation into methanol followed by vacuum filtration. After drying under vacuum, polymer **PDTAsV** was collected (54 mg, 79%). GPC (chlorobenzene): $M_n$ 12,300 g/mol, $M_w$ 23,700 g/mol, Đ 1.92. $^1$H NMR (500 MHz, 323 K, $CDCl_3$) δ 7.31 (broad, 2H), 7.21 (broad, 3H), 6.92 (broad, 2H), 2.56 (broad, 4H), 1.26 (broad, 40H), 0.87 (broad, 6H). Anal. Calcd. For $C_{40}H_{57}AsS_2$: C, 70.97; H, 8.49. Found: C, 70.91; H, 8.42.

### *2.9.12 – Synthesis of 3,5-didodecyl-4-phenyldithieno[3,2-b:2',3'-d]phosphole (2.13)*

To a degassed solution of 3,3'-dibromo-4,4'-didodecyl-[2,2'-bithiophene] **2.6** (0.51 g, 0.77 mmol) in anhydrous THF (40 ml) at −78 °C was added *n*-BuLi (2.5 M in hexane, 0.95 ml, 2.31 mmol, 3 eq) dropwise over 10 min. After stirring for 1 h at −78 °C, dichlorophenylphosphine (0.19 ml, 1.39 mmol, 1.8 eq) was added slowly, and the reaction was allowed to warm to room temperature overnight. The reaction was quenched with methanol (10 ml), stirred for 30 min, then the product was extracted with dichloromethane (2 × 20 ml). The solvent was removed under reduced pressure, and the resulting low melting point solid was dissolved in hexane, filtered through silica (eluent: hexane) to remove salts and then purified by column chromatography over silica (eluent: hexane), to afford 3,5-didodecyl-4-phenyldithieno[3,2-*b*:2',3'-*d*]phosphole (**2.13**) as a low melting point, off-yellow waxy solid (0.36 g, 0.59 mmol, 77%). $^{1}$H NMR (400 MHz, $CDCl_3$) δ 7.10 (s, 2H), 2.67 – 2.56 (m, 4H), 1.73 – 1.60 (m, 4H), 1.48 – 1.19 (m, 36H), 0.88 (t, *J* = 6.7 Hz, 6H). $^{31}$P NMR (162 MHz, $CDCl_3$) δ −27.7. $^{13}$C NMR (101 MHz, $CDCl_3$) δ 147.37 (d, *J*(C,P) = 8.0 Hz), 142.95 (d, *J*(C,P) = 16.5 Hz), 141.95 (d, *J*(C,P) = 3.0 Hz), 133.74 (d, *J*(C,P) = 21.7 Hz, 2C), 132.27 (d, *J*(C,P) = 14.1 Hz, 2C), 129.84, 128.71 (d, *J*(C,P) = 8.4 Hz), 120.51 (d, *J*(C,P) = 5.4 Hz, 2C), 32.09 (2C), 30.28 (2C), 29.81 (2C), 29.67 (2C), 29.57 – 29.33 (overlapping peaks, 12C), 22.86 (2C), 14.29 (2C). HRMS (EI$^+$) calculated for $C_{38}H_{57}S_2P$ [M$^+$], 608.3639; found, 608.3630.

### *2.9.13 – Synthesis of 2,6-bis(trimethylstannyl)-3,5-didodecyl-4-phenyldithieno[3,2-b:2',3'-d]phosphole (2.14)*

Fresh LDA was prepared by treating a solution of diisopropylamine (0.06 ml, 0.42 mmol, 2.1 eq) in anhydrous THF (2 ml) at −78 °C with *n*-BuLi (2.5 M in hexane, 0.18 ml, 0.46 mmol, 2.3 eq), followed by stirring for 10 min. This was then added dropwise over 10 min to a degassed solution of 3,5-didodecyl-4-phenyldithieno[3,2-*b*:2',3'-*d*]phosphole (**2.13**, 0.12 g, 0.20 mmol) in anhydrous THF (10 ml) at −78 °C. After 10 min, $SnMe_3Cl$ (1 M in THF, 0.46 ml, 0.46 mmol, 2.3 eq) was added dropwise via syringe over 10 min. The mixture was allowed to warm to room temperature over 20 min, then was washed with water (2 × 5 ml), once with

acetonitrile (5 ml), and then extracted with hexane (2 × 10 ml). The product was then concentrated under reduced pressure and purified by recycling preparative GPC (40 °C, hexane) to yield 2,6-bis(trimethylstannyl)-3,5-didodecyl-4-phenyldithieno[3,2-*b*:2',3'-*d*]phosphole (**2.14**) as an off-white oil (0.09 g, 0.11 mmol, 55%). $^{1}$H NMR (400 MHz, $CDCl_3$) δ 7.37 – 7.27 (m, 3H), 7.26 – 7.20 (m, 2H), 2.54 – 2.35 (m, 4H), 1.52 – 1.00 (m, 40H), 0.94 – 0.85 (m, 6H), 0.37 (s, 18H). $^{31}$P NMR (162 MHz, $CDCl_3$) δ −30.4.

### *2.9.14 – Stille polymerization of 2,6-bis(trimethylstannyl)-3,5-didodecyl-4-phenyldithieno[3,2-b:2',3'-d]arsole with 5,5'-dibromo-2,2'-bithiophene (PDTAsBT)*

An oven-dried high-pressure microwave tube was charged with 2,6-bis(trimethylstannyl)-3,5-didodecyl-4-phenyldithieno[3,2-*b*:2',3'-*d*]arsole (**2.12**, 47.9 mg, 0.050 mmol), 5,5'-dibromo-2,2'-bithiophene (15.9 mg, 0.050 mmol), and $Pd(PPh_3)_4$ (1.2 mg, 0.001 mmol). The tube was sealed with a septum and flushed with Ar, after which degassed chlorobenzene was added (0.5 ml). The mixture was thoroughly degassed with Ar, after which the inlet was removed. The vial was then placed in a microwave reactor and heated as follows: 2 min at 100 °C, 120 °C, 140 °C, and 160 °C, 10 min at 180 °C, and 40 min at 200 °C. After cooling to room temperature, the resulting polymer was precipitated into methanol and filtered into a Soxhlet thimble. The polymer was extracted (Soxhlet) with methanol, acetone, hexane, and chloroform in that order. The combined hexane and chloroform fractions were concentrated under reduced pressure and the resulting polymer was dissolved in chlorobenzene, warmed to 50 °C and stirred in the presence of diethylammonium diethyldithiocarbamate (10 mg) for 1 h. The solution was concentrated in vacuo, dissolved in a minimal amount of hot chlorobenzene and the polymer collected by re-precipitation into methanol followed by vacuum filtration. After drying under vacuum, polymer **PDTAsBT** was collected (58 mg, 68%). GPC (chlorobenzene): $M_n$ 7,100 g/mol, $M_w$ 15,400 g/mol, Đ 2.17. $^{1}$H NMR (400 MHz, 323 K, $CDCl_3$) δ 7.39 – 7.27 (broad m, 5H), 7.25 – 7.00 (broad m, 4H), 2.85 – 2.56 (broad m, 4H), 1.43 – 0.97 (broad m, 40H), 0.89 (broad t, $J$ = 6.6 Hz, 6H). Anal. Calcd. for $C_{49}H_{59}AsS_4$: C, 67.78; H, 7.30. Found: C, 67.48; H, 7.17.

### *2.9.15 – Stille polymerization of 2,6-bis(trimethylstannyl)-3,5-didodecyl-4-phenyldithieno[3,2-b:2',3'-d]phosphole with 5,5'-dibromo-2,2'-bithiophene (PDTPhBT)*

An oven-dried high-pressure microwave tube was charged with 2,6-bis(trimethylstannyl)-3,5-didodecyl-4-phenyldithieno[3,2-*b*:2',3'-*d*]phosphole (**2.14**, 99.0 mg, 0.106 mmol), 5,5'-dibromo-2,2'-bithiophene (34.3 mg, 0.106 mmol), and $Pd(PPh_3)_4$ (2.3 mg, 0.002 mmol). The tube was sealed with a septum and flushed with Ar, after which degassed chlorobenzene was added (0.5 ml). The mixture was thoroughly degassed with Ar, after which the inlet was removed. The vial was then placed in a microwave reactor and heated as follows: 2 min at 100 °C, 120 °C, 140 °C, and 160 °C, 10 min at 180 °C, and 40 min at 200 °C. After cooling to room temperature, the resulting polymer was precipitated into methanol and filtered into a Soxhlet thimble. The polymer was extracted (Soxhlet) with methanol, acetone, hexane, and chloroform in that order. The combined hexane and chloroform fractions were concentrated under reduced pressure and the resulting polymer was dissolved in chlorobenzene, warmed to 50 °C and stirred in the presence of diethylammonium diethyldithiocarbamate (10 mg) for 1 h. The solution was concentrated in vacuo, dissolved in a minimal amount of hot chlorobenzene and the polymer collected by re-precipitation into methanol followed by vacuum filtration. After drying under vacuum, polymer **PDTPhBT** was collected (59 mg, 73%). GPC (chlorobenzene): $M_n$ 8,300 g/mol, $M_w$ 17,900 g/mol, Đ 2.16. $^1$H NMR (400 MHz, $CDCl_3$) δ 7.52 – 7.25 (broad m, 5H), 7.17 – 6.95 (broad m, 4H), 2.56 (broad m, 4H), 1.36 – 1.00 (broad m, 40H), 0.87 (broad t, $J$ = 5.1 Hz, 6H). $^{31}$P NMR (162 MHz, $CDCl_3$) δ −24.5, −26.1. Anal. Calcd. for $C_{49}H_{59}PS_4$: C, 71.64; H, 7.71. Found: C, 71.48; H, 7.83.

### *2.9.16 – Stille polymerization of 2,6-bis(trimethylstannyl)-3,5-didodecyl-4-phenyldithieno[3,2-b:2',3'-d]arsole with 2,6-dibromo-4,8-dioctodecylbenzo[1,2-b:4,5-b']dithiophene (PDTAsBDT)*

An oven-dried high-pressure microwave tube was charged with 2,6-bis(trimethylstannyl)-3,5-didodecyl-4-phenyldithieno[3,2-*b*:2',3'-*d*]arsole (**2.12**, 344.9 mg, 0.352 mmol), 2,6-dibromo-

4,8-dioctodecylbenzo[1,2-*b*:4,5-*b'*]dithiophene (300.7 mg, 0.352 mmol), and $Pd(PPh_3)_4$ (8.2 mg, 0.007 mmol). The tube was sealed with a septum and flushed with Ar, after which degassed chlorobenzene was added (3 ml). The mixture was thoroughly degassed with Ar, after which the inlet was removed. The vial was then placed in a microwave reactor and heated as follows: 2 min at 100 °C, 120 °C, 140 °C, and 160 °C, 10 min at 180 °C, and 40 min at 200 °C. After cooling to room temperature, the resulting polymer was precipitated into methanol and filtered into a Soxhlet thimble. The polymer was extracted (Soxhlet) with methanol, acetone, hexane, and chloroform in that order. The combined hexane and chloroform fractions were concentrated under reduced pressure and the resulting polymer was dissolved in chlorobenzene, warmed to 50 °C and stirred in the presence of diethylammonium diethyldithiocarbamate (10 mg) for 1 h. The solution was concentrated in vacuo, dissolved in a minimal amount of hot chlorobenzene and the polymer collected by re-precipitation into methanol followed by vacuum filtration. After drying under vacuum, polymer **PDTAsBDT** was collected (263 mg, 56%). GPC (chlorobenzene): $M_n$ 7,000 g/mol, $M_w$ 9,800 g/mol, Đ 1.40. $^1$H NMR (400 MHz, 323 K, $CDCl_3$) δ 7.49 – 7.21 (broad m, 7H), 3.24 – 3.07 (broad m, 4H), 2.98 – 2.49 (broad m, 4H), 1.93 – 1.76 (broad m, 4H), 1.62 – 1.06 (broad m, 100H), 0.94 – 0.84 (broad m, 12H). Anal. Calcd. for $C_{84}H_{131}AsS_4$: C, 75.06; H, 9.82. Found: C, 71.34; H, 10.13.

### *2.9.17 – Synthesis of 2,6-dibromo-3,5-didodecyl-4-phenyldithieno[3,2-b:2',3'-d]arsole-4-gold(I) chloride (2.16)*

Chlorodimethylsulfide gold(I) (5 mg, 0.017 mmol) was added to a solution of 2,6-dibromo-3,5-didodecyl-4-phenyldithieno[3,2-*b*:2',3'-*d*]arsole (**2.10**, 9 mg, 0.011 mmol) in degassed DCM (0.5 ml) and stirred at room temperature overnight. The solvent was then removed under vacuum and the residue purified by column chromatography on neutral alumina (eluent: 20% $CHCl_3$ in hexane) to yield 2,6-dibromo-3,5-didodecyl-4-phenyldithieno[3,2-*b*:2',3'-*d*]arsole-4-gold(I) chloride as a pale, bright yellow solid (**2.16**, 6 mg, 0.006 mmol, 54%). $^1$H NMR (400 MHz, $CDCl_3$) δ 7.53 – 7.47 (m, 3H), 7.44 – 7.38 (m, 2H), 2.62 – 2.45 (m, 4H), 1.41 – 0.94 (m, 40H), 0.88 (t, $J$ = 6.8 Hz, 6H). MS (MALDI-TOF) = 1007.8 ($M^+$–Cl).

### *2.9.18 – Synthesis of bis-(2,6-dibromo-3,5-didodecyl-4-phenyldithieno[3,2-b:2',3'-d]arsole)-4-palladium(II) dichloride (2.18)*

Dichloro(1,5-cyclooctadiene)palladium(II) (2 mg, 0.007 mmol) was added to a solution of 2,6-dibromo-3,5-didodecyl-4-phenyldithieno[3,2-*b*:2',3'-*d*]arsole (**2.10**, 11 mg, 0.014 mmol) in degassed DCM (0.5 ml) and stirred at room temperature overnight. The solvent was then removed under vacuum and the residue purified by recrystallization from a mixture of DCM/MeOH to yield a 5:1 mixture of *trans*- and *cis*-bis-(2,6-dibromo-3,5-didodecyl-4-phenyldithieno[3,2-b:2',3'-d]arsole)-4-palladium(II) dichloride as a bright orange solid (**2.18**, 5 mg, 0.003 mmol, 43%). $^{1}$H NMR (400 MHz, $CDCl_3$) δ 7.65 (d, *J* = 7.8 Hz, 2H), [7.49 – 7.44 (m, 0.17 eq, *cis*-isomer)] 7.40 (t, *J* = 7.4 Hz, 1H), 7.31 (t, *J* = 7.6 Hz, 2H), [7.25 – 7.20 (m, 0.37 eq, *cis*-isomer)], 2.87 – 2.76 (m, 2H), 2.60 – 2.49 (m, 2H), [2.39 – 2.23 (m, 0.39 eq, *cis*-isomer)], 1.43 – 0.95 (m, 40H), 0.88 (t, *J* = 6.8 Hz, 6H).

### *2.9.19 – Synthesis of 2,6-bis(triisopropylsilyl)-4-phenyl-dithiazolo[5,4-b:4',5'-d]arsole (2.20)*

To a degassed solution of 2,2'-bis(triisopropylsilyl)-4,4'-dibromo-5,5'-dithiazole (**2.19**, supplied by Samuel Cryer) (3.00 g, 4.70 mmol) in anhydrous THF (150 ml) at −78 °C was added *n*BuLi (2.5 M in hexane, 4 ml, 9.87 mmol, 2.1 eq) dropwise over 10 min. The solution was stirred at this temperature for 30 min, then warmed to 0 °C over 10 min, and finally cooled back down to −78 °C. Dichlorophenylarsine (**2.8**, 0.63 ml, 4.70 mmol, 1 eq) was added slowly, and the reaction was allowed to warm to room temperature over the course of 1 h. After a further 1 h of stirring at room temperature, the reaction was quenched with methanol (10 ml), stirred for 30 min, and the solvent was removed under reduced pressure. The resulting brown oil was dissolved in hexane and filtered through basic alumina (eluent: hexane) to remove salts, after which the solvent was removed in vacuo to afford 2,6-bis(triisopropylsilyl)-4-phenyl-dithiazolo[5,4-b:4',5'-d]arsole (**2.20**) as a low melting point pale brown solid (2.24 g, 3.55 mmol, 76%). $^{1}$H NMR (400 MHz, $CDCl_3$) δ 7.54 – 7.50 (m, 2H), 7.21 – 7.17 (m, 3H), 1.49 (p, *J* = 7.5 Hz, 6H), 1.16 (t, *J* = 7.6 Hz, 36H). $^{13}$C NMR (101 MHz, $CDCl_3$) δ 172.03 (2C), 168.67, 137.97 (2C),

137.16 (2C), 132.24 (2C), 128.64 (2C), 128.24, 18.66 (36 C), 11.89 (6C). HRMS ($EI^+$) calculated for $C_{30}H_{48}N_2Si_2S_2As$ [$M^+$+H], 631.2013; found, 631.2020.

### *2.9.20 – Synthesis of 4-phenyl-dithiazolo[5,4-b:4',5'-d]arsole (2.21)*

To a solution of 2,6-bis(triisopropylsilyl)-4-phenyl-dithiazolo[5,4-b:4',5'-d]arsole (**2.20**) (2.01 g, 3.18 mmol) in anhydrous THF (60 ml) at 0 °C was added a solution of TBAF (1 M in THF, 9.5 ml, 3 eq) in three portions, and the resulting solution was stirred for 5 min. After allowing the reaction to warm to room temperature over the course of 1 h, the reaction was quenched with water (10 ml) then extracted with diethyl ether (3 × 20 ml). The combined organic layers were washed with water (2 ×10 ml) and brine (10 ml), then dried over sodium sulfite. The solvent was removed under reduced pressure and the product was recrystallized (acetone) to afford 4-phenyl-dithiazolo[5,4-b:4',5'-d]arsole (**2.21**) as brown, needle-like crystals (0.48 g, 1.50 mmol, 47%, m.p. 150–151 °C). $^1$H NMR (400 MHz, $CDCl_3$) δ 8.88 (s, 2H), 7.41 – 7.36 (m, 2H), 7.26 – 7.21 (m, 3H). $^{13}$C NMR (101 MHz, $CDCl_3$) δ 166.71 (2C), 153.58, 135.86 (2C), 134.33 (2C), 132.48 (2C), 129.18, 129.15 (2C). HRMS ($EI^+$) calculated for $C_{12}H_8N_2S_2As$ [$M^+$+H], 318.9345; found, 318.9348.

## *2.10 – References*


1. A. M. Priegert, B. W. Rawe, S. C. Serin, and D. P. Gates, *Chem. Soc. Rev.*, 2016, **45**, 922–953.
2. M. Jeffries-El, B. M. Kobilka, and B. J. Hale, *Macromolecules*, 2014, **47**, 7253–7271.
3. J. Crassous and R. Réau, *Dalton Trans.*, 2008, 6865.
4. E. I. Carrera and D. S. Seferos, *Macromolecules*, 2015, **48**, 297–308.
5. M. A. Shameem and A. Orthaber, *Chem. - A Eur. J.*, 2016, **22**, 10718–10735.
6. S. Parke, M. Boone, and E. Rivard, *Chem. Commun.*, 2016, **52**, 9485–9505.
7. X. He and T. Baumgartner, *RSC Adv.*, 2013, **3**, 11334–11350.
8. R. D. Pensack, Y. Song, T. M. McCormick, A. A. Jahnke, J. Hollinger, D. S. Seferos, and G. D. Scholes, *J. Phys. Chem. B*, 2014, **118**, 2589–2597.
9. G. He, B. D. Wiltshire, P. Choi, A. Savin, S. Sun, A. Mohammadpour, M. J. Ferguson, R. McDonald, S. Farsinezhad, A. Brown, K. Shankar, and E. Rivard, *Chem. Commun.*, 2015, **51**,

5444–5447.

10. T. Baumgartner and R. Réau, *Chem. Rev.*, 2006, **106**, 4681–4727.

11. S. C. Rasmussen and S. J. Evenson, *Prog. Polym. Sci.*, 2013, **38**, 1773–1804.

12. T. Baumgartner, T. Neumann, and B. Wirges, *Angew. Chemie Int. Ed.*, 2004, **43**, 6197–6201.

13. Y. Ren and T. Baumgartner, *Dalton Trans.*, 2012, **41**, 7792–7800.

14. Y. Dienes, S. Durben, T. Kárpáti, T. Neumann, U. Englert, L. Nyulászi, and T. Baumgartner, *Chem. - A Eur. J.*, 2007, **13**, 7487–7500.

15. C. Romero-Nieto and T. Baumgartner, *Synlett*, 2013, **24**, 920–937.

16. M. P. Johansson and J. Juselius, *Lett. Org. Chem.*, 2005, **2**, 469–474.

17. M. Ishidoshiro, Y. Matsumura, H. Imoto, Y. Irie, T. Kato, S. Watase, K. Matsukawa, S. Inagi, I. Tomita, and K. Naka, *Org. Lett.*, 2015, **17**, 4854–4857.

18. G. Märkl and H. Hauptmann, *Angew. Chemie Int. Ed.*, 1972, **11**, 441–441.

19. A. M. Gregson, S. M. Wales, S. J. Bailey, and P. A. Keller, *J. Organomet. Chem.*, 2015, **785**, 77–83.

20. A. M. Gregson, S. M. Wales, S. J. Bailey, A. C. Willis, and P. A. Keller, *J. Org. Chem.*, 2015, **80**, 9774–9780.

21. C. J. O'Brien, Z. S. Nixon, A. J. Holohan, S. R. Kunkel, J. L. Tellez, B. J. Doonan, E. E. Coyle, F. Lavigne, L. J. Kang, and K. C. Przeworski, *Chem. - A Eur. J.*, 2013, **19**, 15281–15289.

22. P. Cao, C. Y. Li, Y. B. Kang, Z. Xie, X. L. Sun, and Y. Tang, *J. Org. Chem.*, 2007, **72**, 6628–6630.

23. X. Cheng, X. Dong, R. Huang, X. Zeng, G. Ungar, M. Prehm, and C. Tschierske, *Chem. Mater.*, 2008, **20**, 4729–4738.

24. H. Usta, A. Facchetti, and T. J. Marks, *J. Am. Chem. Soc.*, 2008, **130**, 8580–8581.

25. Z. Fei, Y. Kim, J. Smith, E. B. Domingo, N. Stingelin, M. A. McLachlan, K. Song, T. D. Anthopoulos, and M. Heeney, *Macromolecules*, 2012, **45**, 735–742.

26. R. Betz, M. M. Reichvilser, E. Schumi, C. Miller, and P. Klüfers, *Zeitschrift für Anorg. und Allg. Chemie*, 2009, **635**, 1204–1208.

27. C. Raeck and S. Berger, *European J. Org. Chem.*, 2006, **2006**, 4934–4937.

28. A. Faucher, V. V. Terskikh, and R. E. Wasylishen, *Solid State Nucl. Magn. Reson.*, 2014, **61–62**, 54–61.

29. T. Baumgartner, W. Bergmans, T. Kárpáti, T. Neumann, M. Nieger, and L. Nyulászi, *Chem. - A Eur. J.*, 2005, **11**, 4687–4699.

30. Z. Fei, X. Gao, J. Smith, P. Pattanasattayavong, E. Buchaca Domingo, N. Stingelin, S. E. Watkins, T. D. Anthopoulos, R. J. Kline, and M. Heeney, *Chem. Mater.*, 2013, **25**, 59–68.

31. V. Farina and B. Krishnan, *J. Am. Chem. Soc.*, 1991, **113**, 9585–9595.

32. D. G. (Dan) Patel, K. R. Graham, and J. R. Reynolds, *J. Mater. Chem.*, 2012, **22**, 3004–3014.

33. H.-L. Cheng, J.-W. Lin, F.-C. Wu, W.-R. She, W.-Y. Chou, W.-J. Shih, and H.-S. Sheu, *Soft Matter*, 2011, **7**, 351–354.

34. S. Pelzer, K. Wichmann, R. Wesendrup, and P. Schwerdtfeger, *J. Phys. Chem. A*, 2002, **106**, 6387–6394.

35. Y. Dienes, M. Eggenstein, T. Neumann, U. Englert, and T. Baumgartner, *Dalton Trans.*, 2006, 1424–1433.

36. Y. Ren, Y. Dienes, S. Hettel, M. Parvez, B. Hoge, and T. Baumgartner, *Organometallics*, 2009, **28**, 734–740.

37. M. Ogasawara, K. Yoshida, and T. Hayashi, *Organometallics*, 2001, **20**, 1014–1019.

38. C. N. Farthing and P. Koc, 1998, **7863**, 6661–6672.

39. G. S. Ananthnag, J. T. Mague, and M. S. Balakrishna, *Dalton Trans.*, 2015, **44**, 3785–3793.

40. M. R. Mason and J. G. Verkade, *Organometallics*, 1992, **11**, 2212–2220.

41. H. Urata, H. Suzuki, Y. Moro-oka, and T. Ikawa, *J. Organomet. Chem.*, 1989, **364**, 235–244.

42. D. S. McGuinness, N. Saendig, B. F. Yates, and K. J. Cavell, *J. Am. Chem. Soc.*, 2001, **123**, 4029–4040.

43. Y. Matano and H. Imahori, *Org. Biomol. Chem.*, 2009, **7**, 1258.

44. X. Guo, M. Baumgarten, and K. Müllen, *Prog. Polym. Sci.*, 2013, **38**, 1832–1908.

45. L. Huo and J. Hou, *Polym. Chem.*, 2011, **2**, 2453–2461.

46. T. E. Kang, T. Kim, C. Wang, S. Yoo, and B. J. Kim, *Chem. Mater.*, 2015, **27**, 2653–2658.

47. P. Sista, M. C. Biewer, and M. C. Stefan, *Macromol. Rapid Commun.*, 2012, **33**, 9–20.

48. H. Pan, Y. Li, Y. Wu, P. Liu, B. S. Ong, S. Zhu, and G. Xu, *J. Am. Chem. Soc.*, 2007, **129**, 4112–4113.

49. M. Stolar and T. Baumgartner, *Chem. Asian J.*, 2014, **9**, 1212–25.

50. H.-C. Su, O. Fadhel, C.-J. Yang, T.-Y. Cho, C. Fave, M. Hissler, C.-C. Wu, and R. Reau, *J. Am. Chem. Soc.*, 2006, **128**, 983–995.

51. Z. Wang, A. Y. Y. Woo, and T. Baumgartner, *Aust. J. Chem*, 2013, **66**, 1171–1178.

52. M. Al-Hashimi, J. G. Labram, S. Watkins, M. Motevalli, T. D. Anthopoulos, and M. Heeney, *Org. Lett.*, 2010, **12**, 5478–5481.

53. U. H. F. Bunz, *Chem. - A Eur. J.*, 2009, **15**, 6780–6789.

54. A. Zhang, C. Xiao, D. Meng, Q. Wang, X. Zhang, W. Hu, X. Zhan, Z. Wang, R. A. J. Janssen, and

W. Li, *J. Mater. Chem. C*, 2015, **3**, 8255–8261.

55. Y. Zhao, Y. Guo, and Y. Liu, *Adv. Mater.*, 2013, **25**, 5372–5391.

56. Y. Lin, H. Fan, Y. Li, and X. Zhan, *Adv. Mater.*, 2012, **24**, 3087–3106.

57. Y. Yamashita, *Chem. Lett.*, 2009, **38**, 870–875.

58. X. He, A. Y. Y. Woo, J. Borau-Garcia, and T. Baumgartner, *Chem. - A Eur. J.*, 2013, **19**, 7620–7630.

59. E. D. Raczyńska, M. Hallman, K. Kolczyńska, and T. M. Stępniewski, *Symmetry*, 2010, **2**, 1485–1509.

60. A. Mrozek, J. Karolak-Wojciechowska, P. Amiel, and J. Barbe, *J. Mol. Struct.*, 2000, **524**, 151–157.

61. C. P. Frizzo and M. A. P. Martins, *Struct. Chem.*, 2012, **23**, 375–380.

# *Chapter 3*

# *Conjugated Polymers for Use in Organic Solar Cells*

### *3.1 – Introduction*

This chapter discusses the application of several different classes of polymers to organic photovoltaic (OPV) applications, all of which contain variations of the BDT unit discussed in **Chapter 2**. As mentioned there, BDT has several advantageous characteristics as a comonomer for use in conjugated polymers,[1,2] and although the requirements of OPVs are somewhat different from those of OFETs, with more focus on factors such as the importance of ensuring good charge separation, there is a degree of overlap between the two. As discussed in **Chapter 2**, the rigid, planar structure of BDT allows packing motifs that benefit charge carrier mobility, while the energy levels of the material can be easily tuned by alteration of the side chains on the benzyl ring.[3] BDT has been used in a huge number of polymers, and PCEs of OPV devices using BDT-containing polymers have increased from 1.6% when it was first used in 2008 to over 11% in 2016.[4,5] For these reasons it was decided that BDT would be a good initial comonomer to allow investigation of the potential of two different units for OPV applications.

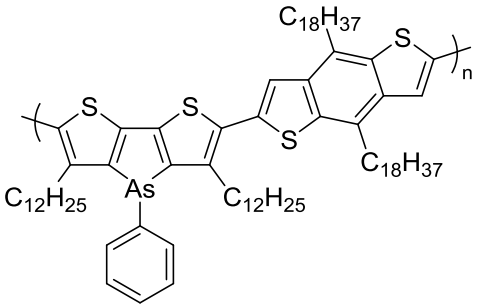
The first half of this chapter discusses the application of the dithieno[3,2-*b*:2',3'-*d*]arsole moieties synthesised in **Chapter 2** (**2.9** and its derivatives) to OPV applications. The first polymer tested was **PDTAsBDT** (previously tested in OFET devices), followed by two analogous polymers that contained two-dimensional BDT groups that have been shown to provide improved OPV device efficiency.[3,6] The impact of various processing conditions on device performance and characteristics is also discussed.

The second half of the chapter explores the use of a donor-acceptor style polymer consisting of a BDT electron donor group and a dicyanobenzotriazole-containing electron acceptor for OPV applications. Donor-acceptor polymers are often used in OPV devices as they show greatly improved performances over all-donor polymers due to their easily tuned band gaps.[7–10] Again, the impact of processing conditions and device architecture on the device performances of the polymers is discussed.

### *3.2 – Photovoltaic performance of PDTAsBDT*

The first polymer explored for OPV applications was **PDTAsBDT**, which showed promising performance in OFET devices (**Section 2.5.4**). This copolymer of dithienoarsole and BDT was synthesised by Stille polymerisation of **2.12** and 2,6-dibromo-4,8-dioctodecylbenzo[1,2-*b*:4,5-*b'*]dithiophene using a microwave reactor – the details of this reaction can be found in **Section 2.5**. A detailed description of the optical, physical, and electronic properties of **PDTAsBDT** can also be found in **Section 2.5**; however, a brief summary of some key attributes can be found in **Table 3.1**.

**Table 3.1: Properties of PDTAsBDT**

| | |
|---|---|
| **Structure** |  |
| $M_n$, $M_w$, Đ | 7.0 kg/mol, 9.8 kg/mol, 1.40 |
| $\lambda_{max}$, $\lambda_{should}$ (thin film) | 518, 570 nm |
| Optical band gap | 2.00 eV |
| Predicted HOMO, LUMO, band gap | −5.01, −2.56, 2.44 eV |
| HOMO, LUMO, band gap from CV | −5.23, −2.52, 2.71 eV |
| Average saturated mobility | 0.0066 $cm^2 V^{-1} s^{-1}$ |

In addition to the measurements of the HOMO and LUMO of **PDTAsBDT** using CV, the work function of the polymer, which is analogous to the HOMO, was determined using photoelectron spectroscopy in air (PESA). For a film spun from a 20 mg $ml^{-1}$ solution of the polymer at

1500 rpm, this method gave an ionisation potential of 5.16±0.05 eV, relatively close to the value of the HOMO as measured using CV (−5.23 eV).

The photovoltaic properties of **PDTAsBDT** were tested by Dr. Hyojung Cha in bulk heterojunction (BHJ) devices with conventional device architectures of the form ITO/PEDOT:PSS/active layer/Ca/Al. The active layer consisted of a 1:3 w/w blend of **PDTAsBDT** and $PC_{71}BM$ spin coated from 40 mg $ml^{-1}$ solutions in dichlorobenzene (DCB) using two different conditions – one device was prepared by spin coating at 3000 rpm, while a second was spun at 1500 rpm and then annealed at 120 °C. The J-V curves of devices with active layers deposited under different conditions are shown in **Figure 3.1**, and the key device parameters are listed in **Table 3.2**.

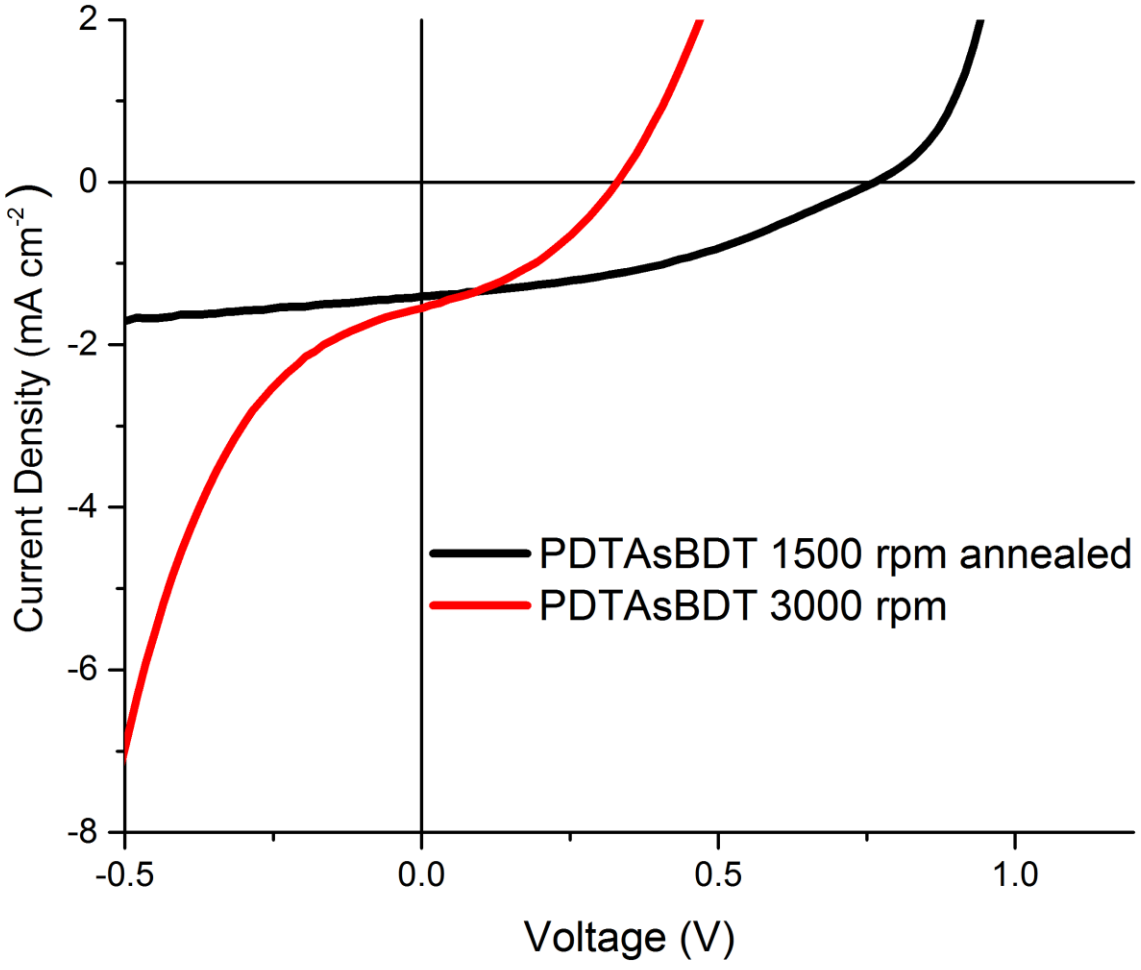



**Figure 3.1: J-V curves of polymer solar cells containing 1:3 w/w PDTAsBDT:$PC_{71}BM$ blends as the active layer**

**Table 3.2: Device characteristics of PDTAsBDT-containing OPVs. Values listed are averages of three and six devices for the annealed and unannealed materials, respectively**

| Annealing Step | None | 120 °C |
|---|---|---|
| Spin speed (rpm) | 3000 | 1500 |
| $J_{sc}$ (mA cm$^{-2}$) | 1.28±0.32 | 1.37±0.06 |
| $V_{oc}$ (V) | 0.27±0.04 | 0.72±0.06 |
| FF | 0.35±0.02 | 0.38±0.02 |
| PCE$^{ave}$ (%) | 0.12±0.05 | 0.38±0.05 |
| PCE$^{max}$ (%) | 0.19 | 0.42 |

Devices fabricated under both conditions showed low performance, with power conversion efficiencies (PCEs) of below 0.5% due to poor device characteristics (in particular $J_{sc}$ and fill factor). However, it is immediately apparent that reducing the spin speed and annealing the active layer provided a significant improvement in device performance, with the average PCE increasing from 0.12% to 0.38%, predominantly due to the increase in the open-circuit voltage ($V_{oc}$) from 0.27 to 0.72 V. Although a number of factors affect the $V_{oc}$, by far the greatest is the difference between the HOMO of the electron donor (the polymer) and the LUMO of the acceptor ($PC_{71}BM$).[11–13] However, other factors also come into play, and as the polymer had the same structure in both cases, the likely reasons for the observed increase in $V_{oc}$ can be narrowed down to those related to morphology. The first possibility is that the reduced spin speed allowed the active layer to adopt a more favourable morphology due to the lower solvent evaporation rate, improving the $V_{oc}$, while the second is that the annealing step provided enough energy for the polymer and PCBM to rearrange and phase segregate, increasing the $V_{oc}$ in a

similar manner. However, neither possibility can be entirely ruled out with the information available; indeed a combination of the two is the most likely cause of the change in $V_{oc}$.

The photocurrents and FFs of both devices were rather poor. The optimisation of both is known to depend strongly on the active layer morphology, since excitons must be able to reach a donor/acceptor interface, and the resulting charges must also be extracted via percolating networks. In addition, active layer thickness plays a role, with thicker layers absorbing more light, usually at the cost of reduced charge extraction due to the low mobility of organic materials. Device configuration is also important, but is the same in both cases here.

### *3.3 – 2D-Benzodithiophene-based polymers*

As can be seen in the above section and in **Section 1.6.3**, there are three different routes to improving the PCE of an OPV: by increasing the $J_{sc}$, the $V_{oc}$, or the fill factor. As the fill factor can most effectively be influenced by changing device configuration and film microstructure, only the $V_{oc}$ and $J_{sc}$ can realistically be altered through changing polymer structure. One of the most effective strategies for improving the performances of BDT-containing polymers is to use a two-dimensional BDT structure, where the side chains contain additional conjugated groups.[3] This allows the conjugation to extend onto the side chains, which can enable the energy levels (and thus absorption spectrum) of a polymer to be tailored as required.[6,14] This relatively easy method of altering the energy levels of polymers was utilized by replacing the C18 alkyl chains of **PDTAsBDT** with alkylthienyl groups in order to enhance the absorption spectrum of the polymer.

### *3.3.1 – Polymerizations with 2D-benzodithiophenes*

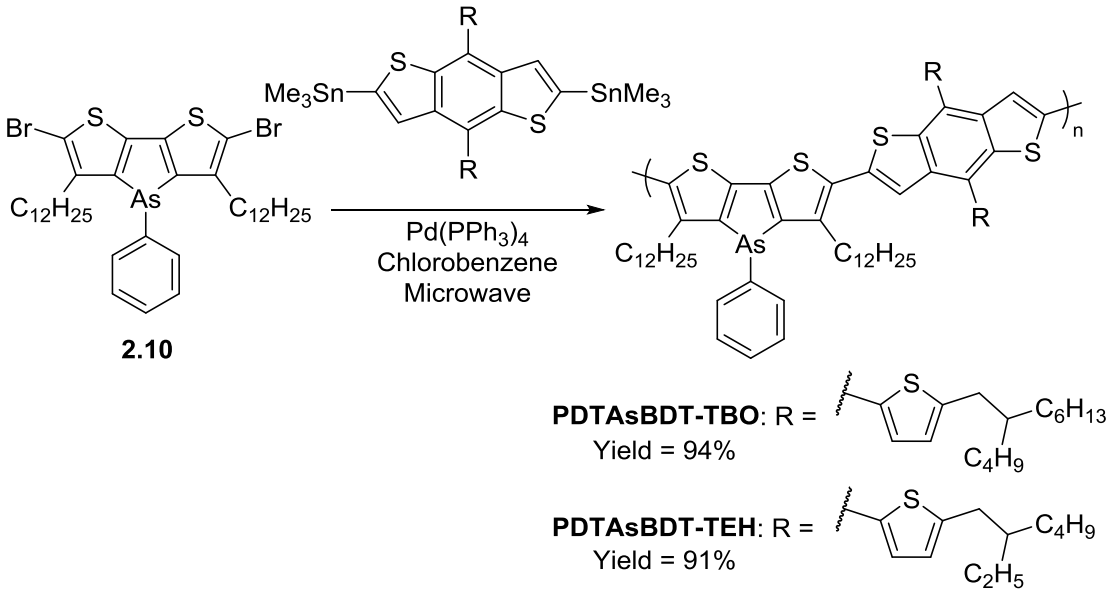



**Figure 3.2: Polymerisation of 2,6-dibromo-3,5-didodecyl-4-phenyldithieno[3,2-*b*:2',3'-*d*]arsole with 2,6-bis-trimethylstannyl-4,8-(5-alkylthiophene)-benzo[1,2-*b*:4,5-*b'*]dithiophenes with butyloctyl- and ethylhexyl-thienyl side chains**

The polymers were synthesized by Stille polymerisation of the dibromo-dithienoarsole derivative (**2.10**) and 2,6-bis-trimethylstannyl-4,8-(5-alkylthiophene)-benzo[1,2-*b*:4,5-*b'*]dithiophenes using a microwave reactor and $Pd(PPh_3)_4$ as the catalyst, as shown in **Figure 3.2**. The first BDT co-monomer used had branched 2-butyloctyl chains on the 5-positions of the thienyl side chains; however, during Soxhlet purification the high solubility of **PDTAsBDT-TBO** caused the entire polymer to be extracted into hexane. Such poor separation of polymer chains with different molecular weights is known to be detrimental to devices, and so shorter 2-ethylhexyl chains were used instead for **PDTAsBDT-TEH** to allow better separation of the molecular weights through Soxhlet extraction. This was only partly successful, since hexane extraction still removed a significant portion of the polymer. Nevertheless, a small percentage of higher weight polymer was isolated as a chloroform-soluble fraction. The yields and molecular weight data of the two dark red polymers as determined by GPC in chlorobenzene (80 °C) against polystyrene standards are shown in **Table 3.3**. It is worth noting that both polymers exhibited significantly higher molecular weights than **PDTAsBDT**, possibly due to either their improved solubilities or the use of brominated DTAs instead of stannylated DTAs.

**Table 3.3: Polymer information for 2D-PDTAsBDT polymers**

| Polymer | Fraction | Yield | $M_n$ (kg/mol) | $M_w$ (kg/mol) | Đ |
|---|---|---|---|---|---|
| **PDTAsBDT-TBO** | **Hexane** | 93.5% | 14.0 | 27.0 | 1.93 |
| **PDTAsBDT-TEH** | **Hexane** | 83.7% | 20.0 | 37.2 | 1.86 |
| | **$CHCl_3$** | 7.3% | 30.0 | 50.4 | 1.68 |

The structures of the polymers were confirmed by $^1$H NMR and elemental analysis, both of which were in good agreement with expectations. Both polymers were soluble in a wide range of organic solvents, as indicated by their solubility in hot hexane during Soxhlet extraction, including chloroform, chlorobenzene, toluene, hot hexane, and hot THF.

### *3.3.2 – Optical properties*

The absorption spectra of the hexane fractions of the two polymers both in chlorobenzene solutions and as thin films spun from chloroform are shown in **Figure 3.3** (the optical properties of the chloroform fraction of **PDTAsBDT-TEH** were not studied due to the low amount of material recovered). It can be seen that the solution spectra were relatively similar, with the slightly higher molecular weight of the ethylhexyl-containing polymer resulting in a minor red shift from 507 nm to 511 nm, and an earlier onset of absorption at ~620 nm instead of ~580 nm. In the thin film spectra, the $\lambda_{max}$ of **PDTAsBDT-TBO** was 539 nm, while that of **PDTAsBDT-TEH** was 536 nm. Both polymers also showed intense shoulders at 577 nm, likely due to aggregation of the backbone in the thin film state.

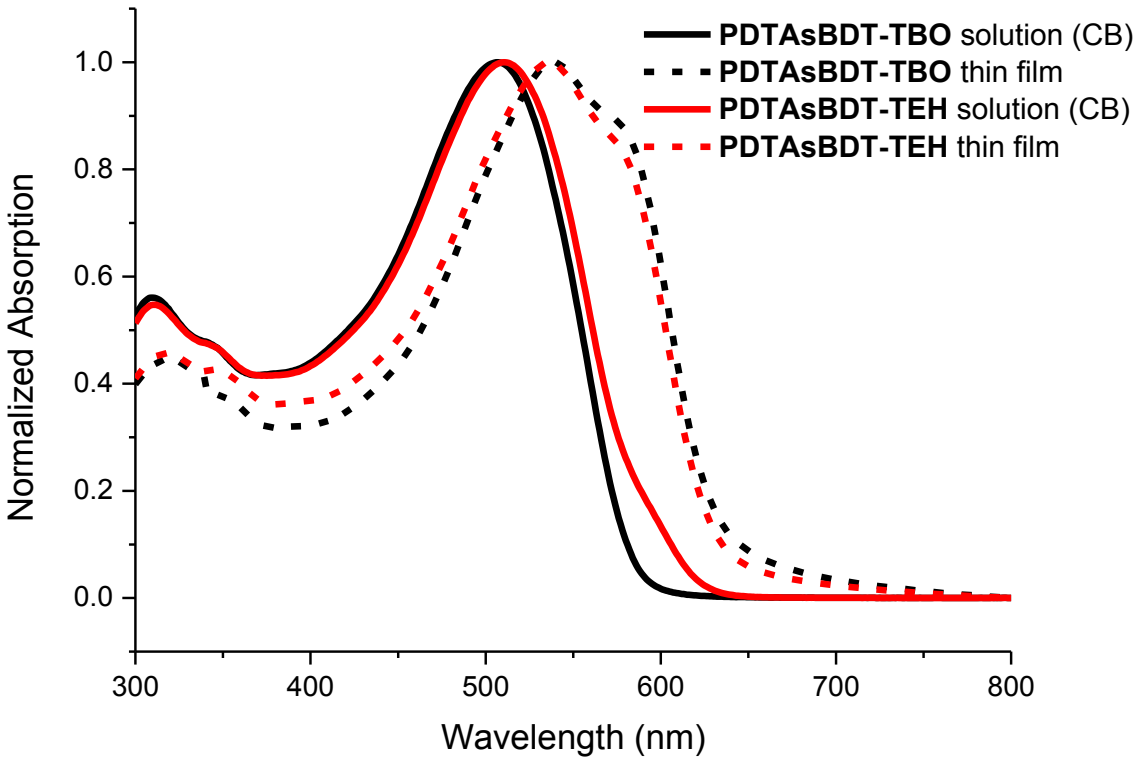



**Figure 3.3: UV-vis absorption spectra of hexane fractions of 2D-PDTAsBDT polymers in chlorobenzene solutions and as thin films**

Compared to the UV spectrum of **PDTAsBDT** (**Figure 2.29**), the 2D-BDT-containing polymers have $\lambda_{max}$ values that are red-shifted by 20–30 nm as well as exhibiting substantially more intense shoulders in the thin film state, indicating that the expected increase in the absorption of the polymers in the visible spectrum did occur. This may also relate to the increased molecular weight of the two polymers. This provides promising evidence that these polymers would perform better in OPV devices than the 1D-BDT equivalent.

### *3.3.3 – Physical and electronic properties*

**Figure 3.4** shows the molecular geometry of the lowest energy conformation of the polymers as well as the frontier molecular orbitals, both predicted by DFT using Gaussian 09 at the B3LYP level of theory and with the 6-311G(d,p) basis set. As all the alkyl chains were shortened to methyl groups to simplify the calculation, both polymers had the same structure for the purposes of the theoretical study.

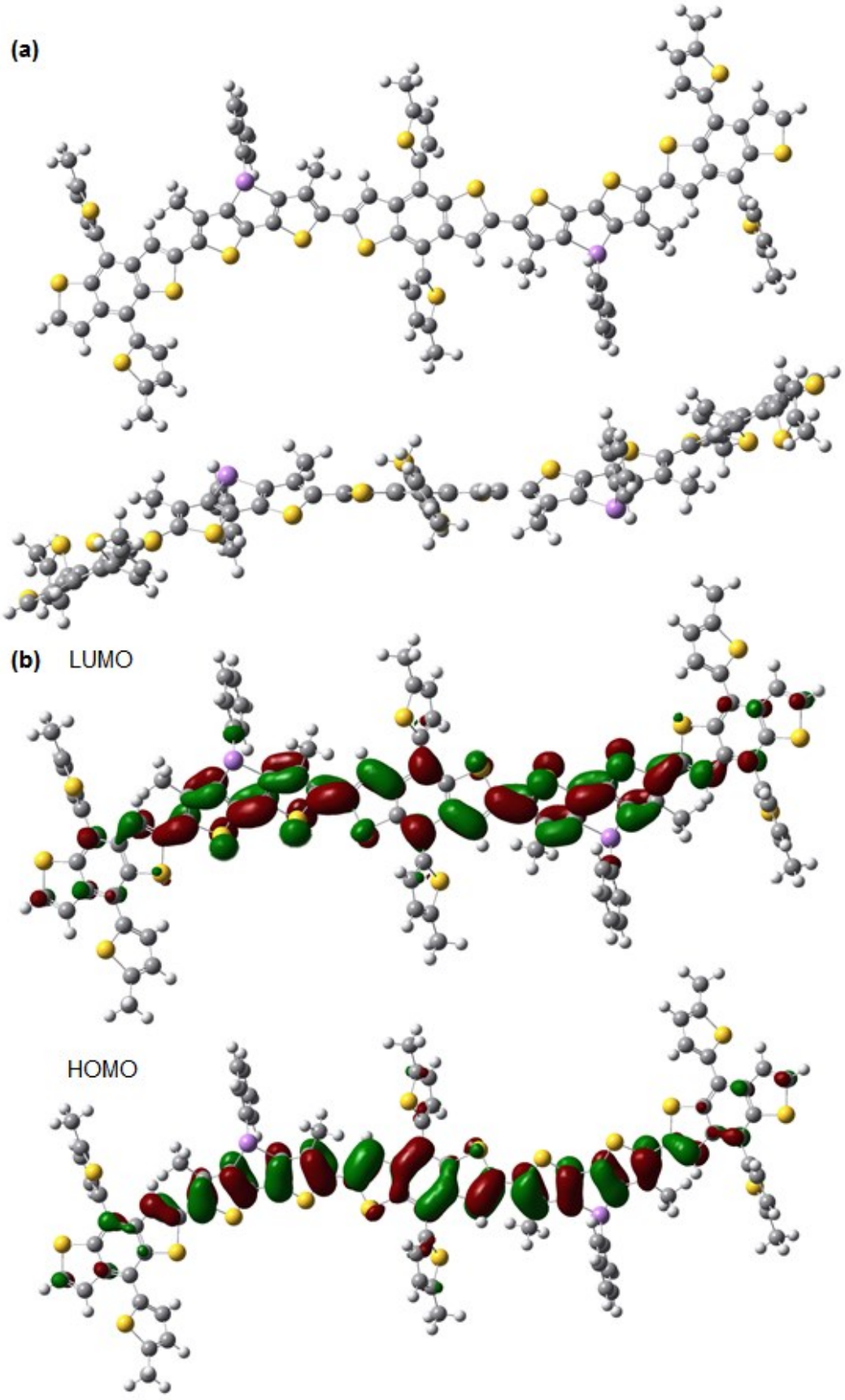



**Figure 3.4: (a) Molecular geometry and (b) frontier molecular orbitals of 2D-PDTAsBDT polymers as calculated using Gaussian 09 at the B3LYP level of theory with the 6-311G(d,p) basis set. LUMO is shown on the top, HOMO underneath**

It can be seen that the backbone of the 2D material is structurally very similar to the 1D-**PDTAsBDT**, with dihedral angles between the dithienoarsole and benzodithiophene rings of approximately 35°, a slight decrease from the 38° twist seen in **PDTAsBDT** (**Section 2.5.2**). Again, this twist between the thienyl-flanked ring systems can be attributed to steric clashes between the peripheral methyls on the DTAs units and the BDTs. The twist between the 2D thiophenes and the benzenes is much more substantial than this, with the dihedral angle between the two rings averaging 60°. As was seen for all the other polymers containing peripherally alkylated dithienometalloles modelled in this thesis, the lowest energy conformation shows the DTAs-BDT units in a *cis* geometry, with the sulfurs of the adjacent thiophenes pointing in the same direction. This is unlike other systems where thiophenes are alkylated at the 3-position (such as P3HT), which usually show a *trans* conformation. The *cis* structure shown was predicted to be 6.62 kJ/mol lower in energy than the equivalent *trans* structure.

Other than the thienyl side chains, the frontier molecular orbitals of the 2D-BDT-containing polymers are very similar to those of **PDTAsBDT**, as would be expected. There is again a series of nodes through the arsenic atoms in the HOMO and a small amount of involvement of the arsenic-phenyl $\sigma^*$-orbitals in the LUMO. Although a small amount of electron density can be seen on the two central pendant thienyls, there is none visible on the outer side chains in either the HOMO or the LUMO, likely due to the aforementioned twist between the rings as well as the fact that the frontier molecular orbitals appear to be slightly more centralised in this polymer than in **PDTAsBDT**. However, it should be taken into consideration that these calculations were performed assuming that materials were single molecules in the gas phase, and it can therefore be expected that the side chains would planarise with respect to the backbone in the solid state, increasing the amount of electron density on them. It is possible that differences between the solution and thin film UV-visible absorption spectra of the polymers are a result of this phenomenon, as the thienyls could be more twisted in solutions, affording single peaks, and then planarise on forming a thin film, resulting in the intense, red-shifted shoulders seen for

both polymers. The predicted HOMO and LUMO values given by the DFT calculations were −4.97 and −2.63 eV, respectively, resulting in an estimated band gap of 2.34 eV. As was hoped, this represents a stabilization of the LUMO compared to that of **PDTAsBDT**, which was −2.56 eV, whilst the HOMO remained relatively unchanged.

The cyclic voltammograms of the two polymers (**Figure 3.5**) show irreversible oxidation peaks that indicate HOMOs of −5.33 and −5.34 eV (referenced against ferrocene/ferrocenium and measured from the onsets of oxidation) for **PDTAsBDT-TBO** and **PDTAsBDT-TEH**, respectively. The reduction onset peaks were also measured from pristine films, and yielded LUMO levels of −3.22 and −3.26 eV for **PDTAsBDT-TBO** and **PDTAsBDT-TEH**, respectively. This gives electrochemical band gaps of 2.11 eV for **PDTAsBDT-TBO** and 2.08 eV for **PDTAsBDT-TEH**, which are within the experimental error of CV (±0.1 eV) of each other, indicating that altering the alkyl chains did not substantially change the electrochemical properties of the polymers, as would be expected. The electrochemical band gap was larger than the optical band gap (~1.97 eV), with the difference being due to the energy required to dissociate the electron-hole pair and allow current to flow in the electrochemical measurement, which is often referred to as the exciton binding energy.

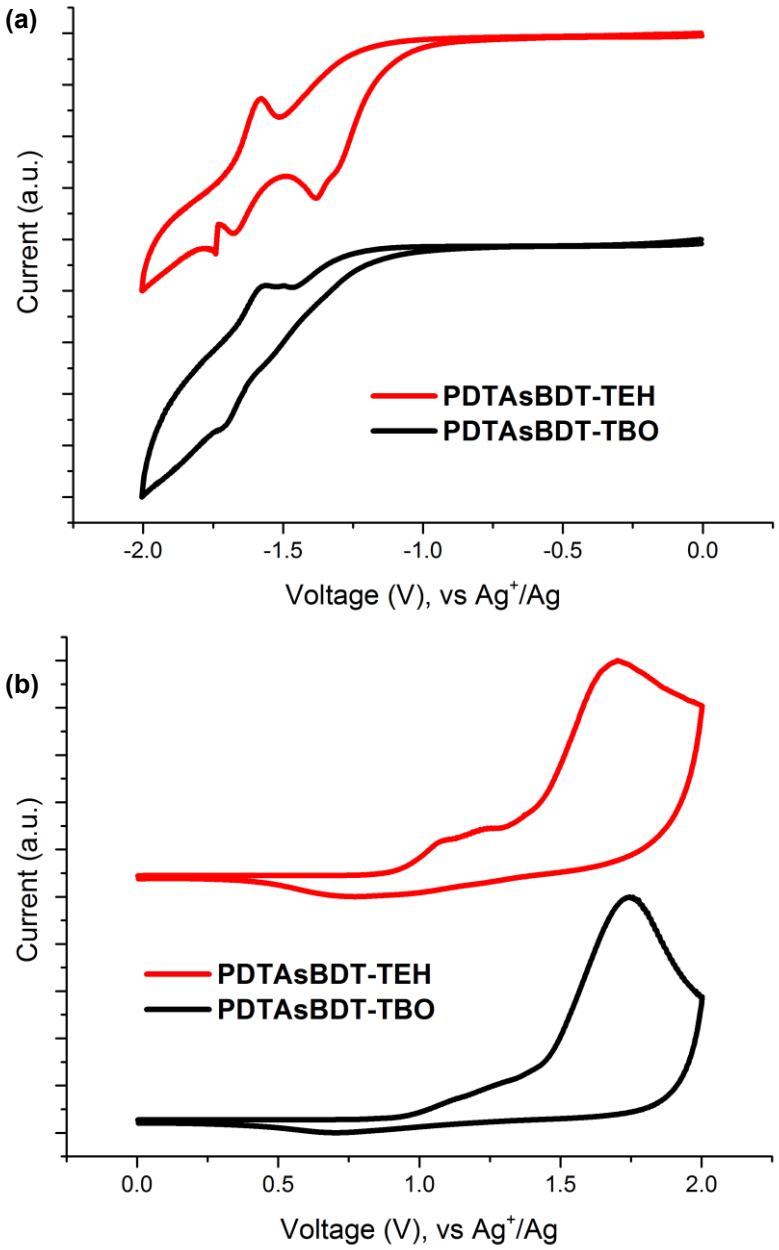



**Figure 3.5: Cyclic voltammograms showing (a) the reduction cycles and (b) the oxidation cycles of the 2D-PDTAsBDT-containing polymers, taken as thin films on FTO in 0.1 M $Bu_4NPF_6$ acetonitrile solutions at a scan rate of 50 mV $s^{-1}$**

As with **PDTAsBDT**, the ionisation potentials of the 2D analogues were measured using PESA. For **PDTAsBDT-TEH**, the film was spun from a 20 mg $ml^{-1}$ solution of the polymer at 1500 rpm, yielding a work function of 5.29±0.05 eV, while the work function of **PDTAsBDT-TBO** was measured from a film spun from a 40 mg $ml^{-1}$ solution at 1000 rpm, likely because the high solubility of the polymer made it difficult to obtain good films. This gave an ionisation potential of 5.22±0.05 eV, meaning that the PESA-measured ionisation potentials of both

polymers were within experimental error of each other, and relatively close to the oxidation potentials as observed using CV.

### *3.4 – OPV performance*

As with **PDTAsBDT**, the OPV properties of the 2D-BDT-containing polymers were tested by Dr. Hyojung Cha in bulk heterojunction devices with conventional architectures (ITO/PEDOT:PSS/active layer/Ca/Al). A number of different conditions for fabrication of the active layers were tested, with the effects of the ratio of polymer to $PC_{71}BM$, solvents, blend concentration, spin speed, annealing steps, and use of additives on device performance all being investigated for both polymers, while the ethylhexyl polymer was also tested in inverted cells (ITO/ZnO/Active layer/$MoO_3$/Ag).

The starting point for testing the OPV properties of the polymers was the conditions previously used by Park and coworkers, who recently reported an analogous polymer consisting of peripherally alkylated dithienophosphole-oxide and a 2D-BDT comonomer with decylthienyl side chains (**PDTP-BDTT**, see **Tables 3.4** and **3.5**).[15]

**Table 3.4: Properties of PDTP-BDTT from work by Park et al.**[15]

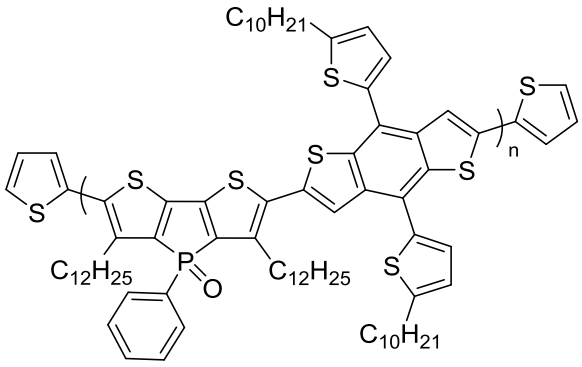
| | |
|---|---|
| **Structure** |  |
| $M_n$, $M_w$, Đ | 22.0 kg/mol, 40.9 kg/mol, 1.86 |
| $\lambda_{max}$ **(thin film)** | 551 nm |
| **HOMO, LUMO, band gap from CV** | −5.58, −3.66, 1.92 eV |

**Table 3.5: Photovoltaic performances of polymers under conditions reported by Park et al. (i.e., optimized for PDTP-BDTT)**

| Polymer | Spin speed (rpm) | $V_{oc}^{max}$ ($V_{oc}^{avg}$) (V) | $J_{sc}^{max}$ ($J_{sc}^{avg}$) (mA cm$^{-2}$) | $FF^{max}$ ($FF^{avg}$) | $PCE^{max}$ ($PCE^{avg}$) (%) |
|---|---|---|---|---|---|
| **PDTP-BDTT**[15,a] | - | 0.87 (-) | 13.2 (-) | 0.531 (-) | 6.10 (5.98) |
| **PDTAsBDT-TBO**[b] | 1500 | 0.82 (0.75±0.05) | 5.8 (4.98±0.73) | 0.411 (0.37±0.03) | 1.97 (1.39±0.36) |
| **PDTAsBDT-TEH**[b] | 1500 | 0.77 (0.78±0.01) | 6.7 (5.87±0.68) | 0.435 (0.44±0.05) | 2.25 (2.02±0.19) |

[a] average data obtained from eight devices; [b] average data obtained from four devices

Park et al. reported that the optimal conditions for the photovoltaic performance of **PDTP-BDTT** were a 40 mg ml$^{-1}$ solution of a 1:4 blend ratio of polymer:$PC_{71}BM$ in DCB with 0.5% (v/v) of 1,8-octanedithiol (ODT) as an additive, with the active layer being annealed at 120 °C

after processing.[15] Spin coating speed was not noted in their work, as they directly measured device thickness instead.

It is immediately apparent on examining the results shown in **Table 3.5** that the conditions used by Park et al. were unsuitable for the arsole-containing polymers. Only the $V_{oc}$ values of our devices even approached those obtained by the other group, likely indicating significant differences in the active layer morphology. Although it is possible that these problems could have been due to the substitution of phosphorus for arsenic or the unoxidised nature of the heteroatom, it is more likely that switching the decyl chain on the thienyl groups to branched alternatives significantly changed the morphology of the polymer:PCBM blend. As such, improvements in device performance were sought through alteration of the fabrication conditions. This optimisation was performed by Dr. Hyojung Cha, and investigated the effects of spin speed, blend concentration and ratio, solvent, additives, and annealing steps on device characteristics and PCE. The conclusion was that the best conditions for OPVs using **PDTAsBDT-TBO** were the use of a 40 mg ml$^{-1}$ solution of a 1:3 blend of polymer:$PC_{71}BM$ in DCB with no additives or annealing steps. On the other hand, the optimal conditions for OPVs containing **PDTAsBDT-TEH** were the use of a 20 mg ml$^{-1}$ solution of a 1:3 blend of polymer:$PC_{71}BM$ in chlorobenzene with no additives and an annealing step at 120 °C after spin coating of the active layer. The J-V curves of the highest performing devices are shown in **Figure 3.6**, while **Table 3.6** shows the conditions used and device characteristics obtained for the two polymers.

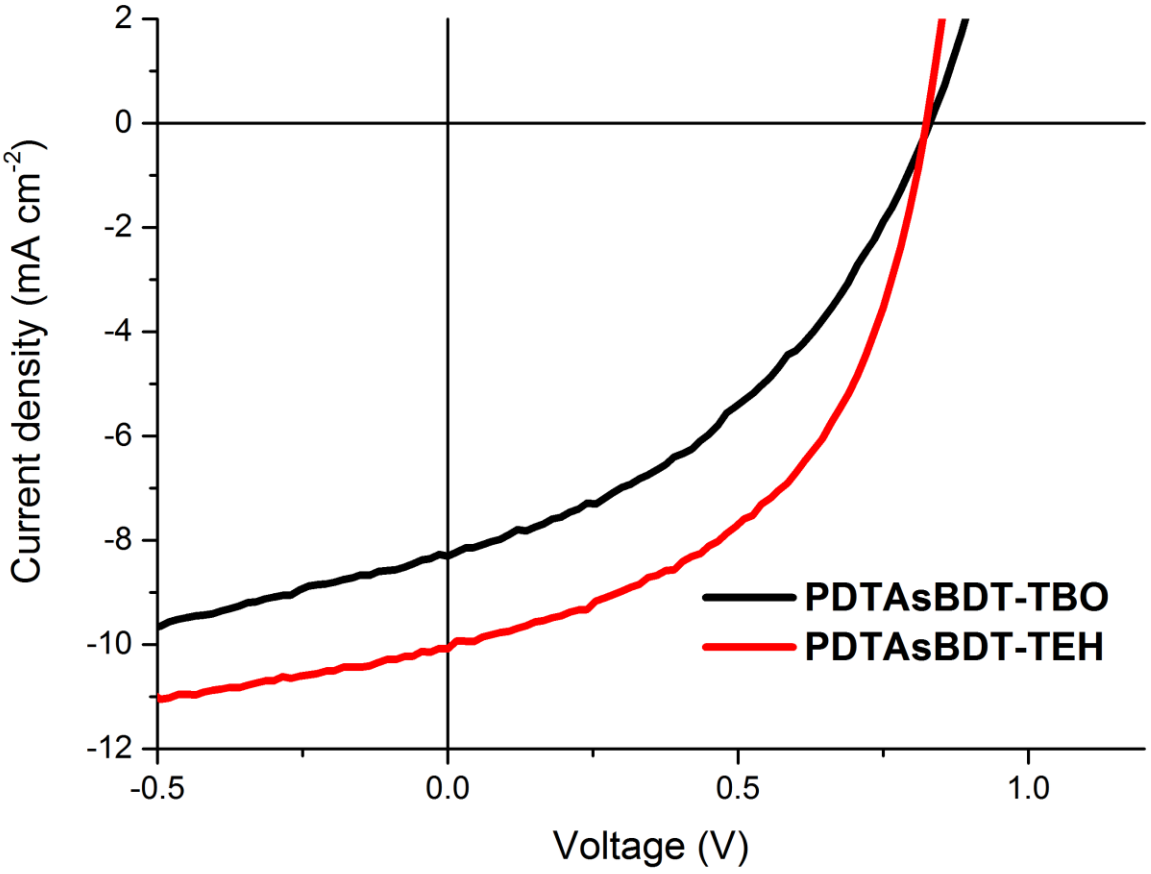



**Figure 3.6: J-V curves of best performing optimised OPV devices containing arsole polymer:$PC_{71}BM$ blends as the active layers. Device fabrication details are shown in Table 3.6**

**Table 3.6: Photovoltaic performances and device characteristics for OPVs fabricated using arsole-containing polymers under optimized conditions. Values listed are averages of nine and six devices for PDTAsBDT-TBO and PDTAsBDT-TEH, respectively**

| **Polymer** | **PDTAsBDT-TBO** | **PDTAsBDT-TEH** |
|---|---|---|
| **Ratio** | **1:3** | |
| **Solvent** | DCB | CB |
| **Concentration (mg ml$^{-1}$)** | 40 | 20 |
| **Annealing (°C)** | - | 120 |
| **Spin Speed (rpm)** | 2000 | 1500 |
| **$J_{sc}$ (mA cm$^{-2}$)** | 7.69±1.27 | 7.16±2.92 |
| **$V_{oc}$ (V)** | 0.74±0.21 | 0.83±0.01 |
| **FF** | 0.37±0.03 | 0.48±0.01 |
| **PCE$^{ave}$ (%)** | 2.09±0.65 | 2.86±1.18 |
| **PCE$^{max}$ (%)** | 2.73 | 4.04 |

Devices fabricated using the polymer with the shorter alkyl side chains (**PDTAsBDT-TEH**) clearly showed much better performance than the butyloctyl-containing alternative. Indeed, even the best performing **PDTAsBDT-TBO** device gave a lower PCE than the average of the **PDTAsBDT-TEH** cells, at 2.73% and 2.86%, respectively. Examination of the device characteristics shows that the average $J_{sc}$ values of the two polymers were relatively similar, at 7.69 and 7.16 mA cm$^{-2}$ for **PDTAsBDT-TBO** and **PDTAsBDT-TEH**, respectively. However, both polymers showed substantial variation in $J_{sc}$ values, with the best performing **PDTAsBDT-TEH** device having a short-circuit current that was almost 3 mA cm$^{-2}$ higher than the average. The

difference in the $J_{sc}$ can be clearly seen when comparing the J-V curves of the two best performing devices (**Figure 3.6**), and was possibly a result of a thicker **PDTAsBDT-TEH**-containing active layer due to the lower spin speed used for this polymer.

The $V_{oc}$ and FF were also both noticeably larger in the **PDTAsBDT-TEH** devices, providing evidence that the device performances were related to the morphologies of the active layers. This could also explain the lower performances of these materials than the phosphole-containing analogue reported by Park et al., which used straight decyl chains on the thienyl moieties rather than branched groups, as the morphology would be expected to change substantially on such a change. Further research regarding the 2D-PDTAsBDT polymers will investigate the morphological differences between the active layers of these devices more thoroughly.

**PDTAsBDT-TEH** was also tested in inverted OPV devices (ITO/ZnO/Active layer/$MoO_3$/Ag) with 1% cyanonaphthalene as an additive to see if changing device architecture had any substantial impact on performance. The device characteristics can be seen in **Table 3.7**, while **Figure 3.7** shows the J-V curves. Despite a number of different fabrication conditions being tested, the inverted devices did not show any significant improvement over conventional cells, with the highest PCE being 4.06%, an increase of only 0.02%.

**Table 3.7: Photovoltaic performances and device characteristics for OPVs fabricated using PDTAsBDT-TEH in inverted devices**

| Conditions | 1:3 blend with $PC_{71}BM$ in CB with 1% cyanonaphthalene | | | |
|---|---|---|---|---|
| Spin speed (rpm) | 1500 | | 2000 | |
| Annealing step | None | 120 °C | None | 120 °C |
| $J_{sc}$ (mA cm$^{-2}$) | 9.25 | 8.69 | 9.81 | 8.68 |
| $V_{oc}$ (V) | 0.88 | 0.87 | 0.92 | 0.89 |
| Fill Factor | 0.47 | 0.49 | 0.45 | 0.47 |
| PCE (%) | 3.81 | 3.71 | 4.06 | 3.65 |

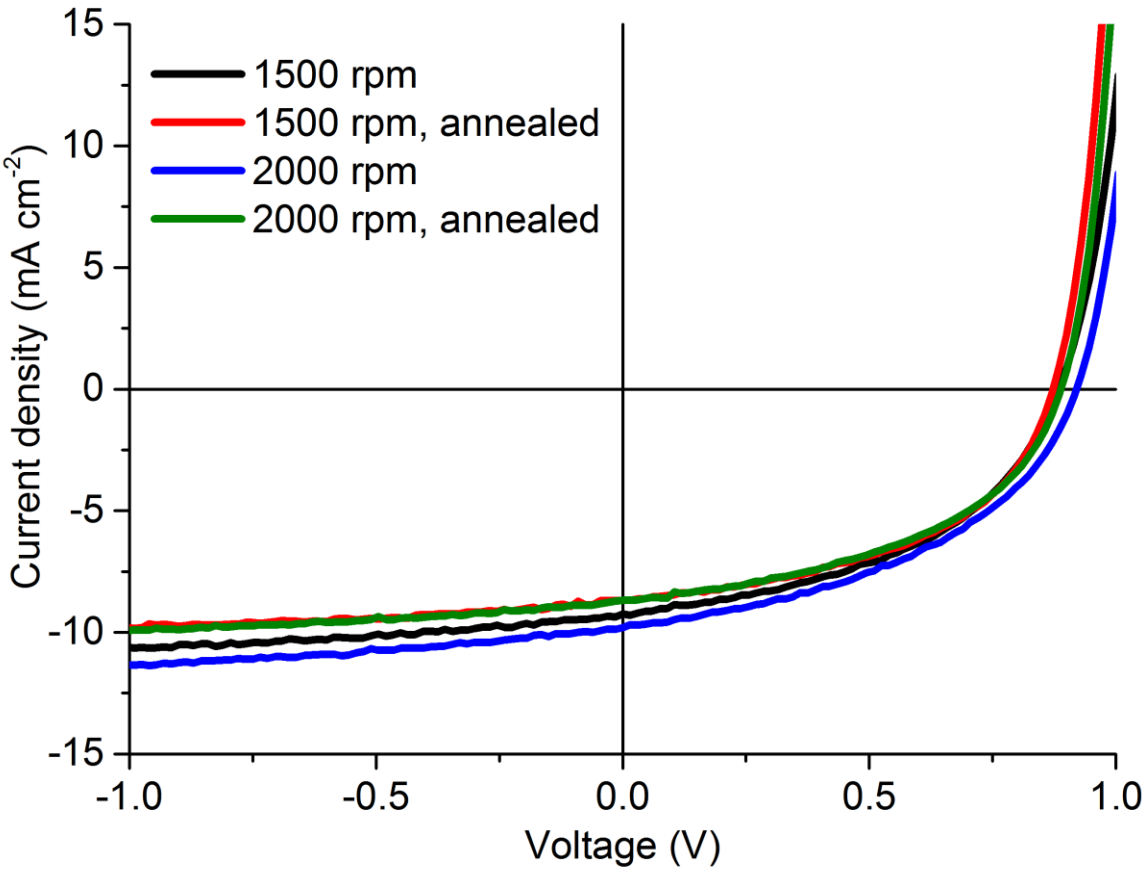



**Figure 3.7: J-V curves of inverted OPV devices prepared using different fabrication conditions using PDTAsBDT-TEH in the active layers**

These results show that As-containing monomers have some potential for use in OPV devices, although further work on lowering their band gaps will be necessary to obtain truly high-performing solar cells. In addition, the results were not as good as those reported for a phosphole-oxide-containing analogue, although the reasons for this reduction in performance are not entirely clear at this point and will need to be investigated further.

### *3.5 – Donor-acceptor polymers for OPV materials*

A common technique for designing highly efficient conjugated polymers for OPV applications involves the synthesis of donor-acceptor (D-A) copolymers, which contain alternating electron-rich and electron-poor units in the polymer backbone.[16] The hybridization of the orbitals of the two units lowers the band gap of the resultant polymer, with the HOMO being largely dependent on the donor and the LUMO on the acceptor, allowing excellent tunability of polymer properties.[17–19] Dithienometalloles including dithienopyrrole,[20,21] dithienosilole,[22] and dithienogermole[23,24] have been successfully used as electron donating moieties in a number of D-A conjugated polymers, whilst the majority of papers reporting dithienophosphole-oxide-containing polymers credit them as electron accepting groups.[15,25] It is currently unclear where dithienoarsoles stand on the donor-acceptor spectrum, however this would likely depend on the specifics of the polymer in question. What is beyond doubt is that successfully utilizing D-A structures will prove to be an invaluable tool for improving the device efficiencies of DTAs-containing polymers.

With this potential future application for arsoles in mind, we decided to conduct a preliminary investigation into the use of D-A copolymers for OPV applications. This involved the synthesis and characterization of the polymers **PDCBTzBDT-TEH** and **PDCBTzBDT-TBO**, the structures of which are shown in **Figure 3.8**. The polymers utilized the 2D-BDT units discussed in the previous section as the electron donating moiety, while 2-(2-butyloctyl)-4,7-di(2-thienyl)-2*H*-benzo[*d*][1,2,3]triazole-5,6-dicarbonitrile (DCBTz) acted as the electron acceptor.

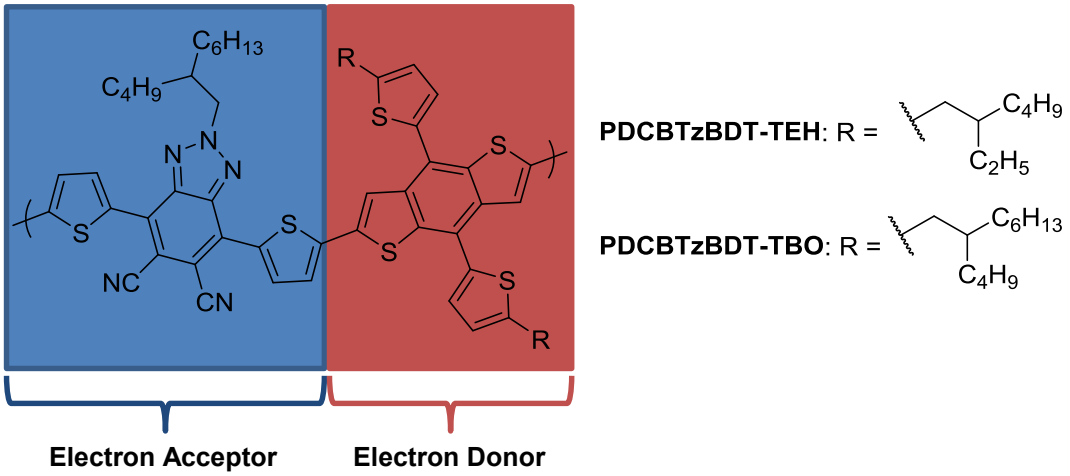



**Figure 3.8: Structures of D-A polymers containing 2D-BDT and DCBTz as the electron donor and electron acceptor, respectively**

Electron deficient benzo[*d*][1,2,3]triazole units were first used as acceptor groups in D-A conjugated polymers by Cao et al. in 2010, who synthesised a number of D-A dithienyl-benzotriazole (DTBTz)-containing copolymers and examined their OPV characteristics.[26] However, the moiety began to attract more attention in 2011 when You and coworkers found that copolymers of difluoro-DTBTz and BDT substantially outperformed P3HT in solar cells, with PCEs of over 7%.[27] Since this paper, work relating to benzotriazole-containing polymers has often focused on fine-tuning the energy levels of the final polymers by modifying the benzo ring either directly, for example by substitution of carbon atoms for nitrogens to yield pyridine or diazine analogues, or by substitution of the benzylic protons with alternative functionalities such as fluoro- or cyano-groups.[28] When combined with changes to the structure of the comonomer, this strategy allows the band gap of the polymer to be tuned to optimal levels for different applications or device configurations.

### *3.6 – Synthesis of dicyanobenzotriazole monomer*

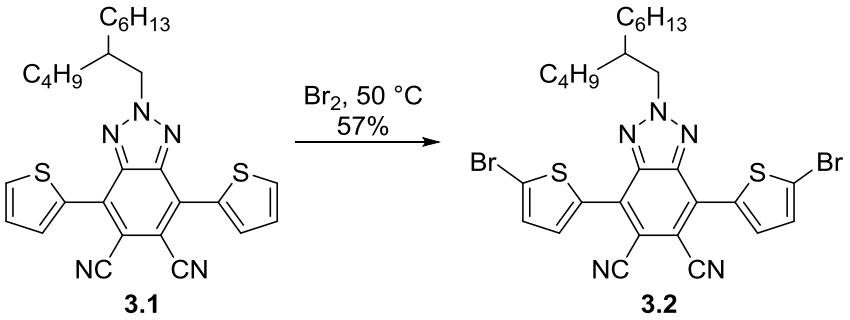



**Figure 3.9: Synthesis of 4,7-bis(5-bromothiophen-2-yl)-2-(2-butyloctyl)-5,6-dicyano-2H-benzo[*d*][1,2,3]triazole (3.2)**

4,7-bis(5-bromothiophen-2-yl)-2-(2-butyloctyl)-5,6-dicyano-2H-benzo[*d*][1,2,3]triazole (**3.2**) was synthesised from 4,7-bis(thiophen-2-yl)-2-(2-butyloctyl)-5,6-dicyano-2H-benzo[*d*][1,2,3]triazole (**3.1**, provided by Abby Casey). The reaction was carried out using excess elemental bromine in chloroform in the absence of light, as it has previously been reported that the dicyanobenzodithiadiazole analogue of **3.1** requires harsher bromination conditions than the difluorobenzothiadiazole, which could be adequately brominated using two equivalents of NBS.[29] This is believed to be due to the strongly electron withdrawing nature of the cyano groups, which results in reduced electron density at the 5 and 5' positions of the molecule. It was found that utilizing bromine and purifying the product by column chromatography in a 1:1 mixture of DCM and hexane yielded monomer **3.2** in a yield of 57%.

### *3.7 – Polymerisation with benzodithiophene derivatives*

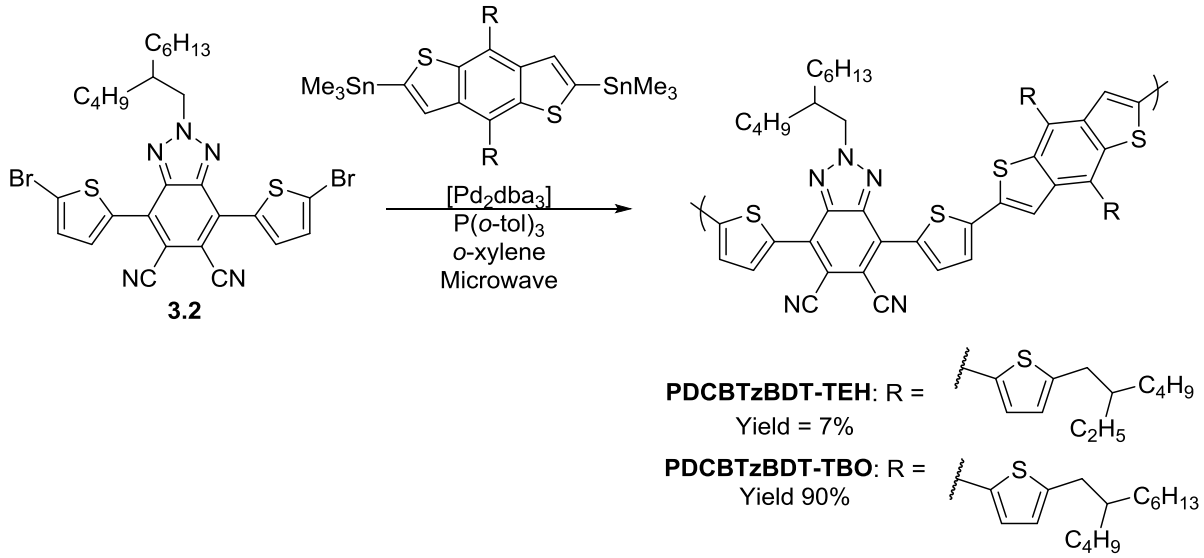



**Figure 3.10: Polymerisation of 4,7-bis(5-bromothiophen-2-yl)-2-(2-butyloctyl)-5,6-dicyano-2H-benzo[*d*][1,2,3]triazole with 2,6-bis-trimethylstannyl-4,8-(5-alkylthiophene)-benzo[1,2-*b*:4,5-*b'*]dithiophenes with butyloctyl- and ethylhexyl-thienyl side chains**

The dibromo monomer **3.2** was polymerised with 2,6-bis-trimethylstannyl-4,8-(5-alkylthiophene)-benzo[1,2-*b*:4,5-*b'*]dithiophenes with ethylhexyl- and butyloctyl-thienyl side chains via Stille polymerisation in a microwave reactor, using a $[Pd_2dba_3]/P(o\text{-tol})_3$ system as the catalyst. The first material synthesised was **PDCBTzBDT-TEH** – however, in an inversion of the situation observed for **PDTAsBDT-TBO** and **PDTAsBDT-TEH**, it was found that none of this shorter-side-chained material was recovered from the hexane fraction during Soxhlet purification, and only a 4% yield was obtained from the chloroform fraction. After further extraction with chlorobenzene, which yielded an additional 3%, the remaining material was dissolved in hot 1,2,4-trichlorobenzene (TCB) and precipitated in methanol; however, this material was highly insoluble, and no molecular weight information was collected for the more soluble fractions due to concerns that they would precipitate in the GPC apparatus.

To rectify these problems, the butyloctyl analogue (**PDCBTzBDT-TBO**) was synthesised to increase the solubility of the resultant polymer, which proved much more successful, with yields of 42% and 48% from the chloroform and chlorobenzene fractions of the Soxhlet extraction, respectively. The masses, yields, and (where appropriate) molecular weight data of the various

fractions of the two dark blue polymers as determined by GPC in chlorobenzene (80 °C) against polystyrene standards are shown in **Table 3.8**.

**Table 3.8: Polymer information for PDCBTzBDT polymers**

| Polymer | Fraction | Mass (mg) | Yield | $M_n$ (kg/mol) | $M_w$ (kg/mol) | Đ |
|---|---|---|---|---|---|---|
| **PDCBTzBDT-TEH** | **$CHCl_3$** | 12 | 4% | - | - | - |
| | **CB** | 10 | 3% | - | - | - |
| **PDCBTzBDT-TBO** | **$CHCl_3$** | 76 | 42% | 26.0 | 87.5 | 3.37 |
| | **CB** | 88 | 48% | 78.2 | 114.3 | 1.46 |

The structures of the polymers were confirmed by $^1$H NMR and elemental analysis, which agreed with expected values. As previously mentioned, the ethylhexyl polymer had very low solubility, requiring trichlorobenzene to fully dissolve all the fractions, while the solubility of the butyloctyl polymer depended on the fraction – the $CHCl_3$ material was soluble in hot chloroform and chlorobenzene, while the CB fraction required hot chlorobenzene or TCB to ensure full dissolution.

### *3.7.1 – Optical properties*

**Figure 3.11a** shows the chloroform fractions of both polymers in trichlorobenzene solutions and as thin films. In solution, both spectra showed the same features, with two peaks at 591 ($\lambda_{max}$) and 633 nm ($\lambda_{sh}$). However, the relative intensity of these depended on the polymer, with the former being stronger in **PDCBTzBDT-TEH** and the latter in **PDCBTzBDT-TBO**. A similar phenomenon can be observed in the thin film spectra, with the peaks occurring at 611 and 641 nm as a result of red shifts of 20 and 8 nm, respectively.

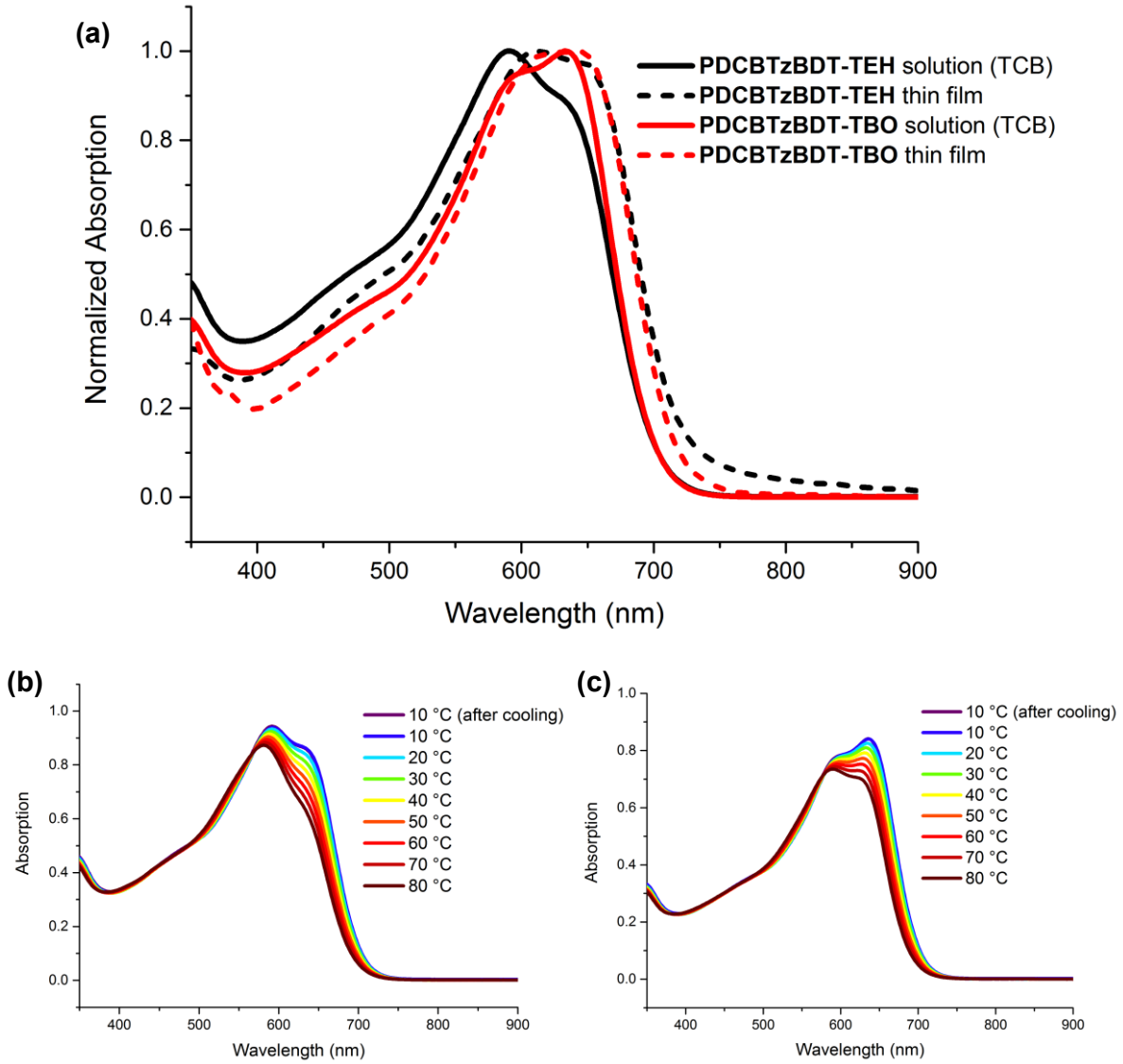



**Figure 3.11: (a) UV-vis absorption spectra of PDCBTzBDT polymers in TCB solutions and as thin films; (b) variable temperature solution spectra of PDCBTzBDT-TEH in TCB; (c) variable temperature solution spectra of PDCBTzBDT-TBO in TCB**

Examining the spectra of the polymers as their solutions were heated from 10–80 °C (**Figure 3.11b and c**), it is clear that the peak at the longer wavelength was caused by aggregation of the polymer chains in the solutions, as its relative intensity decreased as temperature increased for both polymers. For **PDCBTzBDT-TBO** the intensity of the longer wavelength shoulder relative to $\lambda_{max}$ was still high, even at 80 °C, whereas for the ethylhexyl analogue it was noticeably lower. This may be related to differences in the molecular weights of the two polymers, although without the GPC data for **PDCBTzBDT-TEH** it is difficult to confirm this. Nevertheless, it seems likely that the reduced solubility of the polymer with the shorter

side chains led to the chloroform fraction containing lower molecular weight material, resulting in the reduced intensity of $\lambda_{sh}$ as lower $M_n$ chains aggregate less.

### *3.7.2 – Physical and electronic properties*

The molecular geometry of the polymers as well as the frontier molecular orbitals are shown in **Figure 3.12**, both of which were predicted by DFT using Gaussian 09 at the B3LYP level of theory and with the 6-311G(d,p) basis set. As all the alkyl chains were shortened to methyl groups to simplify the calculation, both polymers had the same structure for the purposes of the theoretical study.

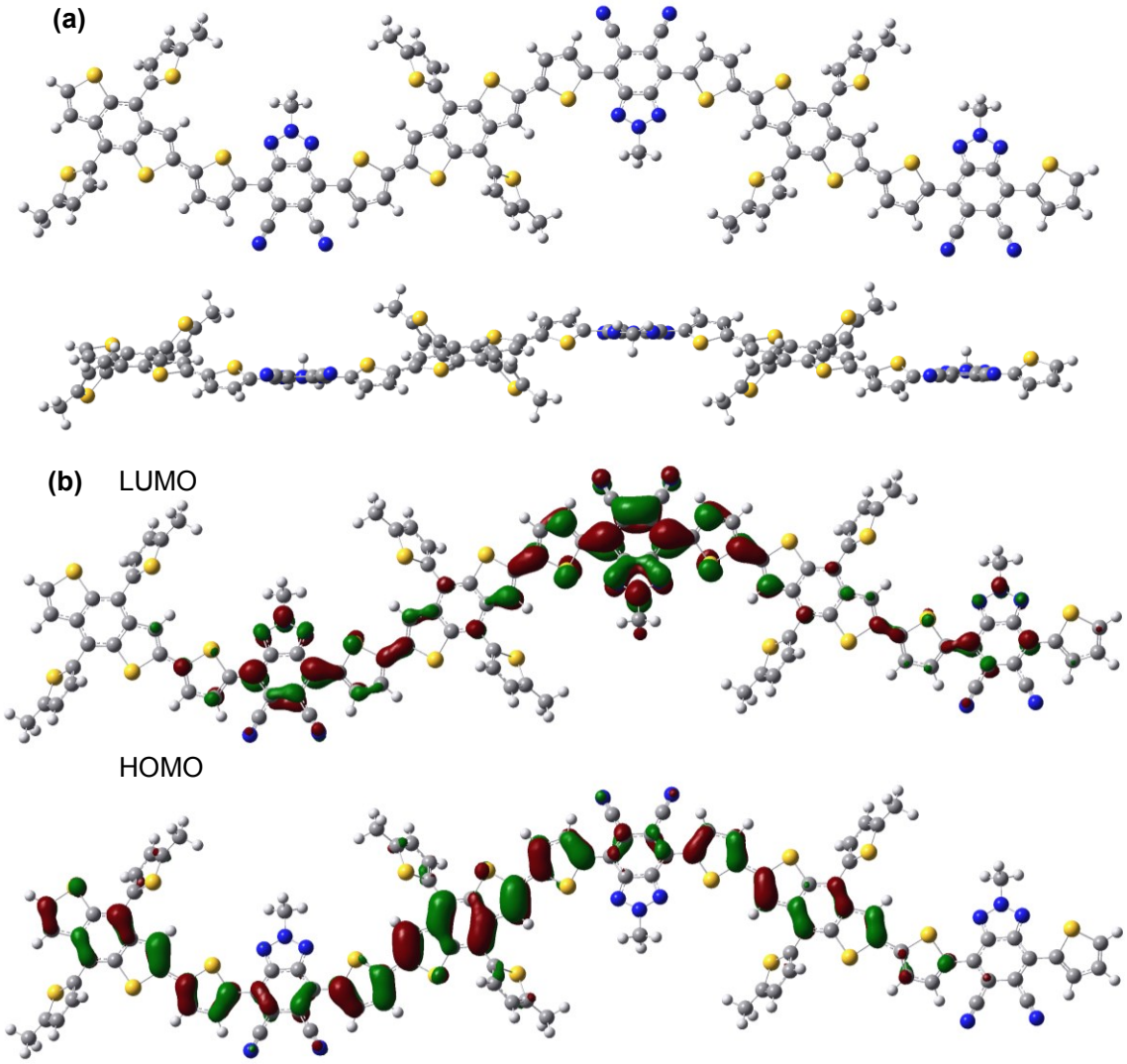



**Figure 3.12: (a) Molecular geometry and (b) frontier molecular orbitals of PDCBTzBDT polymers as calculated using Gaussian 09 at the B3LYP level of theory with the 6-311G(d,p) basis set. LUMO is shown on the top, HOMO underneath**

It can immediately be seen that the polymer adopts a highly planar backbone conformation, albeit with the thiophene spacers twisted slightly out of the plane by ~28°, in the same manner as has previously been observed in the dithiophene-dicyanobenzothiadiazole moiety.[29] Note that the conformation of the T-BTz-T unit was in accordance with previous results regarding dicyanobenzothiazoles flanked with two thienyl groups, in which the minimum energy configuration has the thienyl groups *cis* to the thiadiazole ring (i.e., the sulfur of the thienyl pointing towards the thiadiazole).[29] The planarity of the system would aid the π-π stacking and aggregation of polymer chains that is responsible for the intense $\lambda_{sh}$ peak in the UV spectra of the polymers. In addition, the high degree of planarity allows excellent delocalisation of the HOMO along the backbone, which should be highly beneficial for charge carrier transport in devices. On the other hand, the LUMO is localised primarily on the electron accepting benzotriazole units, as was expected from the donor-acceptor structure of the repeat unit. As was seen with the 2D-PDTAsBDT polymers, the thienyl side chains are twisted out of the plane of the molecule by approximately 60°, limiting their interaction with the frontier molecular orbitals. However, as before it should be remembered that the calculations were performed assuming that the material was a single molecule in the gas phase, and thus the side chains might be expected to planarise with respect to the backbone in the solid state, increasing their degree of conjugation.

The predicted HOMO and LUMO values of the structure were −5.38 and −3.53 eV, respectively, resulting in an expected band gap of 1.85 eV. While both energy levels are below those of the arsole-containing 2D-BDT polymers, the LUMO is more substantially stabilised, primarily due to the donor-acceptor nature of the polymer structure, and this results in a band gap that is much lower than that predicted for the arsole-containing 2D-BDT polymers (2.34 eV). When measured using CV as a thin film on FTO in 0.1 M $[Bu_4N][PF_6]$ acetonitrile solution the HOMO of both polymers was −5.82 eV, as estimated from the oxidation potential of 1.46 V and referenced against ferrocene/ferrocenium. The optical band gaps as measured from the thin film UV spectra were 1.71 and 1.73 eV for the ethylhexyl and butyloctyl polymers,

respectively, giving estimated LUMO levels of −4.11 and −4.09 eV for **PDCBTzBDT-TEH** and **PDCBTzBDT-TBO**, respectively. However, this estimation does not account for the exciton binding energy, and thus the actual LUMO levels as measured by CV would be expected to higher than this, although they proved too difficult to measure. The high degree of similarity between the CVs of the materials imply that any differences in molecular weight and polymer chain arrangement in thin films had a negligible impact on the electrochemical properties of the polymers. However, the optical band gaps are slightly below that predicted by DFT, with the most likely reason for this being extension of the conjugation length either due to the fact that only a trimer was modelled, as well as increased planarization of the molecular structure in the solid state compared to the gas phase used for the theoretical calculation, or the presence of the intense shoulders in the optical spectra due to chain aggregation/stacking.

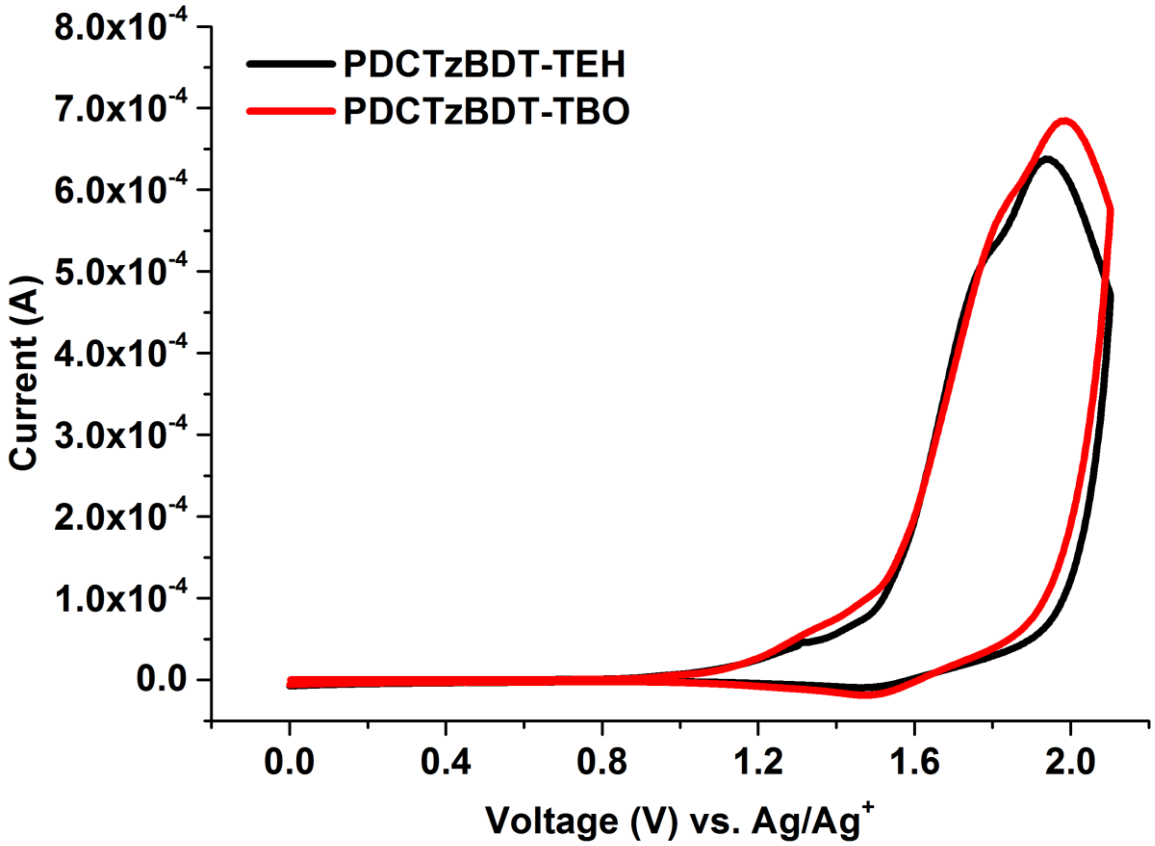



**Figure 3.13: Cyclic voltammograms of PDTCTzBDT-TEH and PDTCTzBDT-TBO as thin films on FTO in 0.1 M [$Bu_4N$][$PF_6$] acetonitrile solutions at a scan rate of 100 mV $s^{-1}$. Measurements performed by Abby Casey and reproduced from her PhD thesis with permission.**[30]

### *3.8 – OPV performance*

The OPV performances of the **PDCBTzBDT** polymers were tested by Dr. Pabitra Tuladhar in bulk heterojunction devices with conventional architectures (ITO/HTL/active layer/Ca/Al) and two different hole transport layers (HTL): PEDOT:PSS and copper(I) thiocyanate (CuSCN). The HTL functions to smooth the surface of the ITO electrode and alter its work function, so altering this allows optimisation of the device architecture to ensure a good energy level match between the HOMO of the polymers and the ITO electrode to achieve the highest possible device efficiency. Previous work has shown that CuSCN provides much better energy level matching with triazole-containing polymers as their low-lying HOMOs match well with the work function of CuSCN (5.5 eV).[28,31]

#### *3.8.1 – Ethylhexyl polymer*

**Table 3.9** shows the OPV characteristics of a reprecipitated sample of the TCB fraction of **PDCBTzBDT-TEH** in solar cells with PEDOT:PSS and CuSCN interlayers, while **Figure 3.14** shows the J-V curves of the highest performing devices. The active layers were spun at 700 rpm from a 20 mg/ml solution of a 1:2 w/w blend of **PDCBTzBDT-TEH** and $PC_{61}BM$ in TCB. The low solubility of the polymer even when heated at 135 °C for 6 h in TCB meant that the yield of working devices was low, so values are averaged over a relatively low numbers of pixels.

**Table 3.9: Photovoltaic performances and device characteristics for OPVs fabricated using different HTLs. Values listed are averages of three and six devices for the PEDOT:PSS and CuSCN devices, respectively**

| Polymer | HTL | $J_{sc}$ (mA cm$^{-2}$) | $V_{oc}$ (V) | FF | PCE (PCE$^{max}$) (%) |
|---|---|---|---|---|---|
| **PDCBTzBDT-TEH** | PEDOT:PSS | 5.73±0.1 | 0.93±0.01 | 0.30±0.03 | 1.58±0.12 (1.68) |
| | CuSCN | 9.94±1.1 | 0.87±0.01 | 0.39±0.06 | 3.43±0.57 (3.84) |

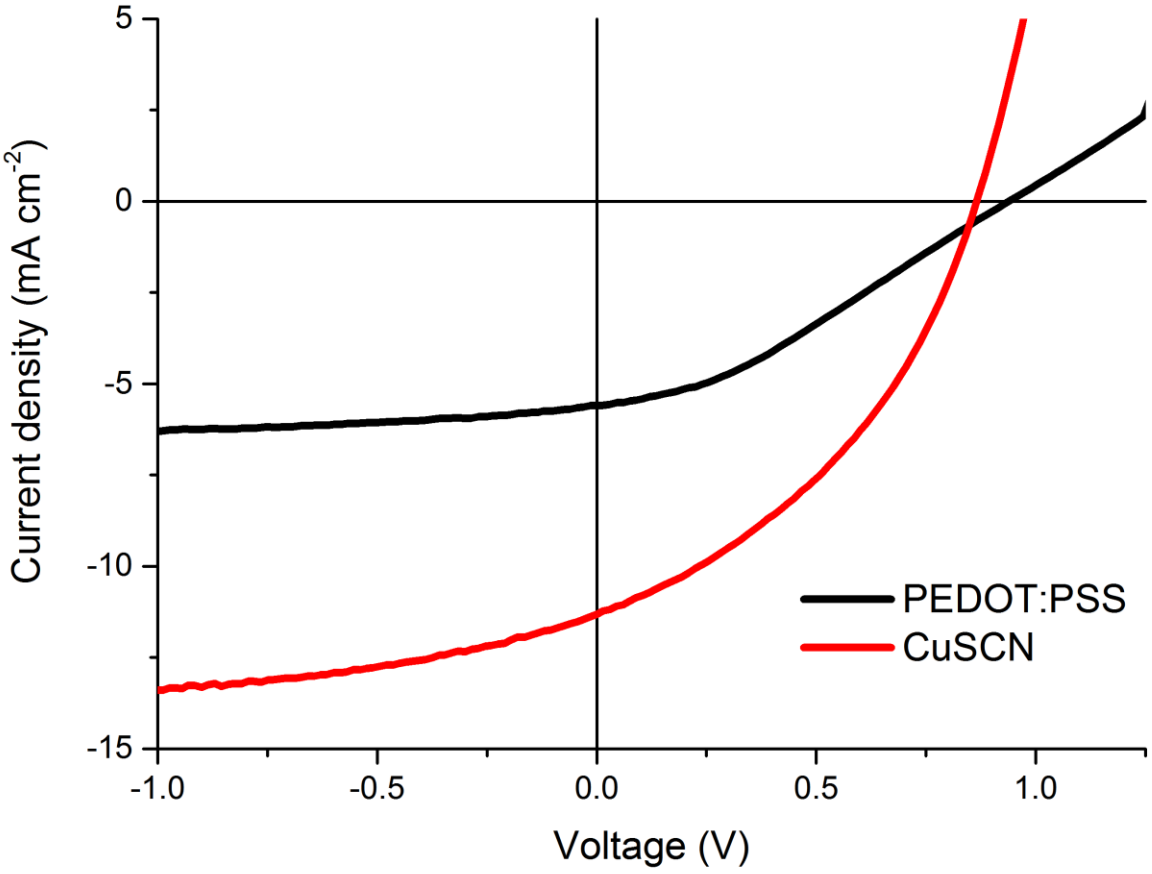



**Figure 3.14: J-V curves of best performing optimised OPV devices containing PDCBTzBDT-TEH:$PC_{61}BM$ blends as the active layers with PEDOT:PSS and CuSCN HTLs**

A number of factors make it immediately clear that the CuSCN material acted as a more effective interlayer for the ethylhexyl polymer than PEDOT:PSS. The first is the PCE, which improved by over 120% when CuSCN was used instead of PEDOT:PSS (3.84% cf. 1.68%). You and coworkers have previously reported that using CuSCN instead of PEDOT:PSS in OPV devices containing 1D-PDCBTzBDT resulted in improve device efficiencies, which they attributed to the work function of CuSCN (5.5 eV cf. 5.0 eV for PEDOT:PSS). This was believed to provide better energy level matching with the HOMO of their polymer (−5.73 eV), thereby improving the $V_{oc}$.[32] However, in the 2D material studied here, the $V_{oc}$s of devices made with CuSCN were similar to those made with PEDOT:PSS, and the primary cause of the increased PCE was the vastly higher $J_{sc}$ in the CuSCN devices, as well as the marginal increase in fill factor, as can be seen in both **Table 3.9** and **Figure 3.14**. The variety of factors that can affect the $J_{sc}$ mean that it is difficult to determine the exact cause of its increase, although it is highly likely that the increased

transparency of the copper-based interlayer material in the visible region played at least some role, as this has been reported to improve absorption in the active layer (and therefore $J_{sc}$) previously.[32,33] The overall performances of OPVs using both PEDOT:PSS and CuSCN were somewhat disappointing, failing to break the 4% mark. The most likely reason for this was deemed to be the low solubility of the material, which made film formation difficult and would be expected to have unfavourable consequences for the active layer morphology.

### *3.8.2 – Butyloctyl polymer*

The OPV characteristics of the $CHCl_3$ and CB fractions of **PDCBTzBDT-TBO** in solar cells with PEDOT:PSS and CuSCN interlayers are shown in **Table 3.10**, while **Figure 3.15** shows the J-V curves of the highest performing devices. The active layers were spun at 700 rpm from 24 mg/ml solutions of a 1:2 w/w blend of the **PDCBTzBDT-TBO** fraction required and $PC_{61}BM$ in TCB.

**Table 3.10: Photovoltaic performances and device characteristics for OPVs using the $CHCl_3$ and CB fractions of PDCBTzBDT-TBO and different HTLs**

| Polymer | Fraction | HTL | $J_{sc}$ (mA cm$^{-2}$) | $V_{oc}$ (V) | FF | PCE (PCE$_{max}$) |
|---|---|---|---|---|---|---|
| **PDCBTzBDT-TBO** | $CHCl_3$ | PEDOT:PSS [a] | 11.25±0.61 | 0.95±0.03 | 0.57±0.03 | 6.12±0.76 (6.93) |
| | | CuSCN [b] | 11.37±1.46 | 0.88±0.01 | 0.50±0.01 | 5.02±0.60 (5.76) |
| | CB | PEDOT:PSS [a] | 12.98±0.71 | 0.96±0.03 | 0.42±0.02 | 5.21±0.32 (5.49) |
| | | CuSCN [b] | 13.21±1.21 | 0.91±0.02 | 0.38±0.02 | 4.48±0.41 (5.00) |

[a] Averages of six devices
[b] Averages of five devices

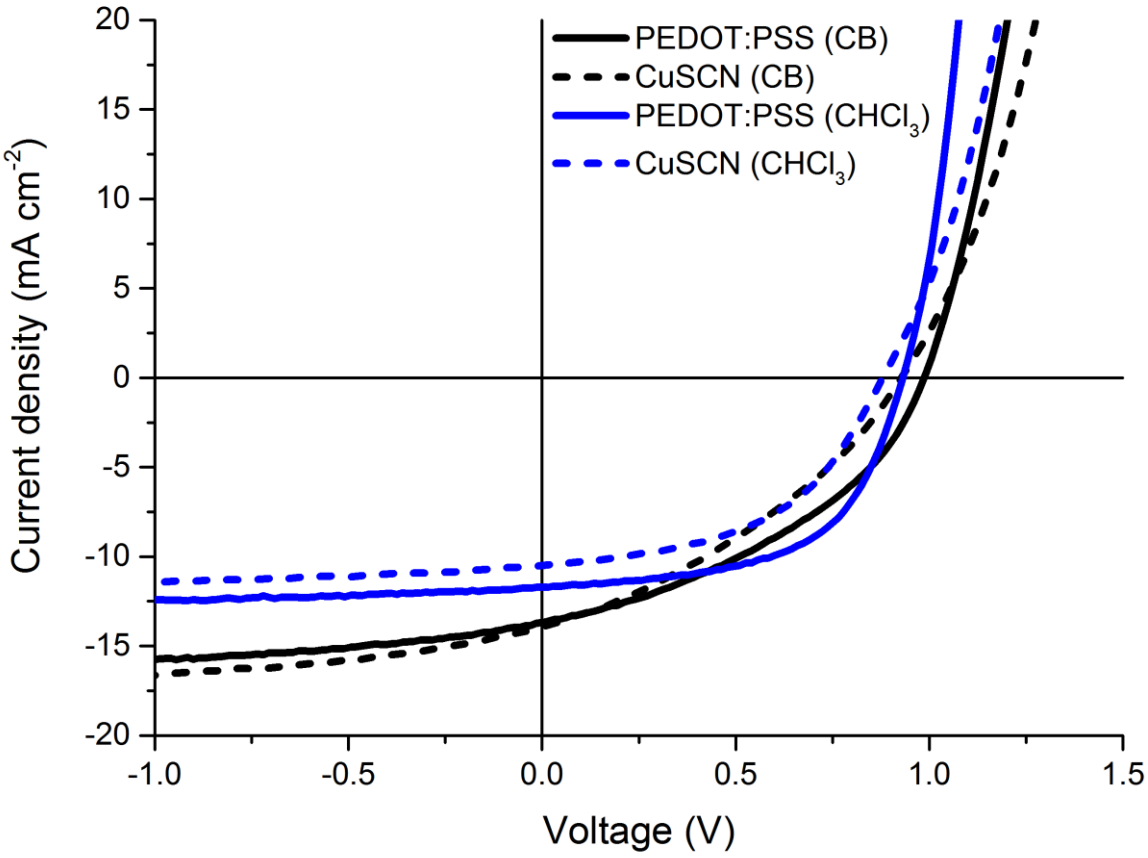



**Figure 3.15: J-V curves of best performing optimised OPV devices utilizing chloroform or chlorobenzene fractions of PDCBTzBDT-TBO in blends with $PC_{61}BM$ as the active layers with PEDOT:PSS and CuSCN HTLs**

All of the devices fabricated using the butyloctyl polymer showed improved PCEs over those that utilised the ethylhexyl analogue, with the maximum value reached being almost 7%. This was most likely because the longer alkyl chains enhanced the solubility of the material, allowing better film formation and thus active layer morphologies that were more suitable for devices. Both the $J_{sc}$ and FF of the **PDCBTzBDT-TBO** devices were higher than those of the **PDCBTzBDT-TEH** cells, again probably due to improvements in active layer morphology.

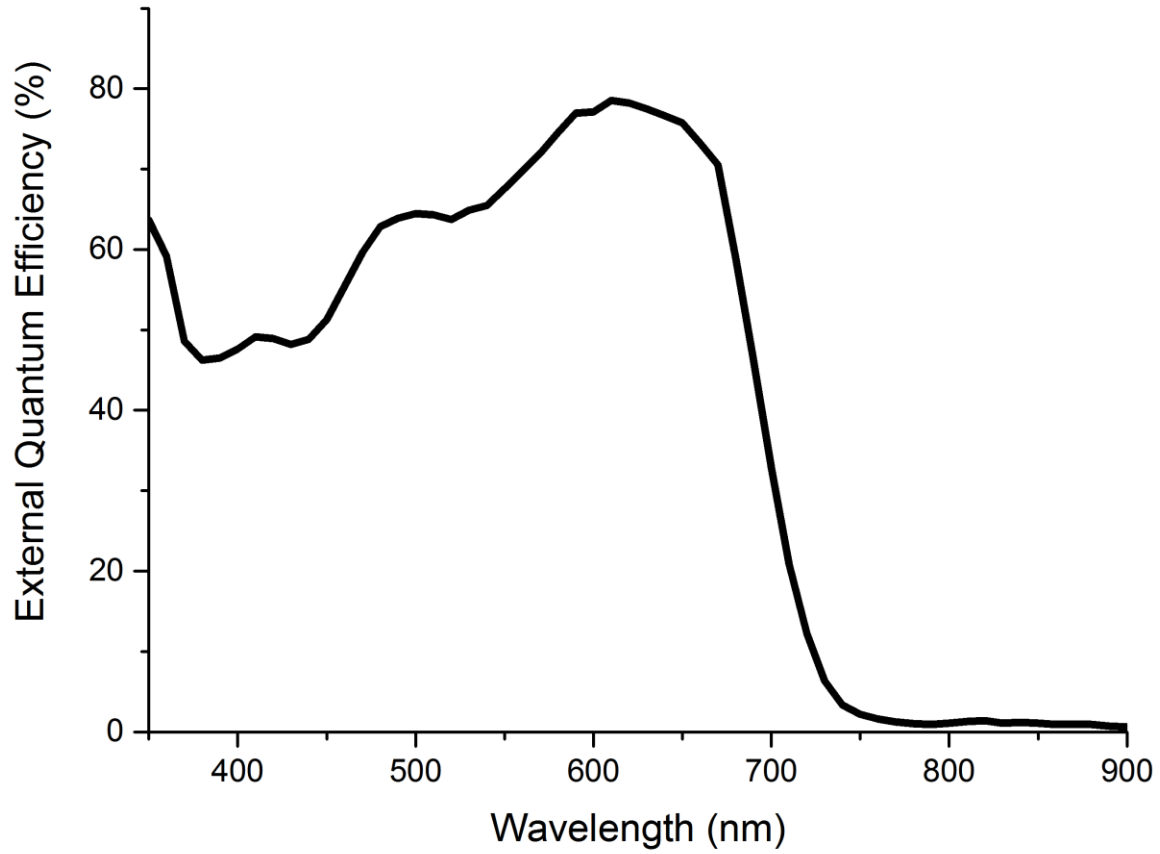



**Figure 3.16: External quantum efficiency of a device fabricated using PDCBTzBDT-TBO (chloroform fraction) with PEDOT:PSS as the hole transporting layer**

Looking at trends within the **PDCBTzBDT-TBO** devices, it can be seen that the highest $J_{sc}$ values obtained were for those that used CuSCN, probably due to the aforementioned improved transparency of the thiocyanate interlayer over PEDOT:PSS and/or slight differences in the interfacial morphologies. However, the higher $V_{oc}$s and FFs of the PEDOT:PSS-containing cells more than made up for this, meaning that the best overall performances were given by devices that used PEDOT:PSS as the HTL. The reason for the improvement in the $V_{oc}$ and FF could be differences in how the interfacial energies of the active layers and the HTLs affected the overall morphologies of the blends – however, more detailed morphological studies would be needed to provide further evidence of this.

It can also be seen that the $CHCl_3$ fraction of **PDCBTzBDT-TBO** outperformed the CB fraction with both interlayers, again despite the higher $J_{sc}$ of the latter. In this case, it is clear that differences in the FF played the largest role, as those of the lower molecular weight fraction

were approximately 0.5, with the higher molecular weight material being around 0.4. This implies that molecular weight (and therefore solubility) played a role in determining the morphology of the active layer, which in turn can affect device performance, as the less soluble CB fraction performed significantly less well than the more soluble $CHCl_3$ material. However, once again a more detailed analysis of precisely what role morphology plays requires a more detailed study using techniques that are capable of examining the active layer directly. **Figure 3.16** shows the external quantum efficiency (EQE) of a device fabricated using the $CHCl_3$ fraction of **PDCBTzBDT-TBO** with PEDOT:PSS as the hole transporting layer. The device showed good photocurrent generation close to $\lambda_{max}$ of the polymer, with lower values obtained at lower wavelengths. This indicates relatively good photocurrent generation by the polymer, in agreement with the observed $J_{sc}$ value.

### *3.9 – Conclusions*

This chapter has examined the OPV performances of three different classes of conjugated polymers: a copolymer of DTAs and BDT moieties, two analogues of this material that utilized 2D-BDT units, and two donor-acceptor copolymers of 2D-BDT and dithiophene-dicyanobenzotriazole. The initial results when using **PDTAsBDT** in the active layer were somewhat disappointing, with a maximum PCE of 0.42% being obtained. Fortunately, replacing the C18 side chains with two-dimensional BDT analogues containing pendant branched-alkylthienyl groups drastically improved the efficiency, with maximum PCEs of 2.73 and 4.04% being achieved for **PDTAsBDT-TBO** and **PDTAsBDT-TEH**, respectively. However, these values were still not quite as high as those achieved by Park and coworkers for their phosphole-oxide containing analogue,[15] although the precise reasons for this difference are currently unclear. Two potential explanations are the oxidation of the pnictogen atom in Park's work, or the fact that they employed straight-chained decylthienyl groups as their 2D pendant systems. Finally, donor-acceptor polymers consisting of 2-(2-butyloctyl)-4,7-di(2-thienyl)-2*H*-benzo[*d*][1,2,3]triazole-5,6-dicarbonitrile as electron accepting groups and the aforementioned

2D-BDT moieties as electron donors were synthesised, and their OPV properties were examined. It was found that the longer butyloctyl side chains were necessary to ensure that the solubility of the resulting polymer was sufficient for fabrication of good OPV devices. Despite previous work showing that use of CuSCN as a hole transport layer with BDT-DTBTz polymers gave increased PCEs, we found that PEDOT:PSS actually gave the highest performing devices with **PDCBTzBDT-TBO**.

### *3.10 – Experimental*

General experimental details can be found in **Section 2.9**, as can the synthesis of compound **2.10**. Ionisation potentials were measured by photoelectron spectroscopy in air (PESA) on a Riken Keiki AC-2 PESA spectrometer at CSIRO by Adam Creamer. Polymer thin films were prepared by spin coating 5 mg $ml^{-1}$ solutions in chlorobenzene onto glass substrates. PESA samples were run with a light intensity of 5 nW and data processed with a power number of 0.5.

To fabricate arsole-containing OPV devices (performed by Dr. Hyojung Cha), prepatterned ITO-coated glass with a sheet resistance of ≈15 Ω $square^{-1}$ (PsioTec Ltd, UK) was used as the substrate. It was cleaned by sequential sonications in detergent, deionised water, acetone, and isopropanol for 5 min each. After exposure to oxygen plasma for 8 min at 100 W, a ZnO electron transport layer (40 nm) was prepared by spin coating a ZnO precursor solution (diethyl zinc) at 4000 rpm. Active layer solutions (controlled ratios and concentrations of D:A; 1:3-1:4 and 30–40 mg $mL^{-1}$) prepared in various solvents (CB, *o*-DCB, or mixed solvent) were deposited by spin-coating onto the ZnO layer. To completely dissolve the polymer, the active layer solutions were stirred on a hot plate at 80 °C overnight. A MoOx (10 nm)/Ag (100 nm) anode layer was then deposited by thermal evaporation under vacuum through a shadow mask to complete the BHJ cell. Current-voltage (J-V) characteristics were measured under AM1.5 solar illumination using a xenon lamp.

To fabricate devices containing **PDCBTzBDT** polymers with PEDOT:PSS as a HTL (performed by Dr. Pabitra Tuladhar), ITO-coated glass substrates were washed by ultrasonication in acetone and isopropyl alcohol, then dried before undergoing oxygen plasma treatment. A thin layer of PEDOT:PSS was spin-coated onto the substrate and dried at 150 °C for 30 min. The active layer, consisting of polymer and $PC_{61}BM$ in a 1:2 ratio, was deposited by spin coating from 20-24 mg $ml^{-1}$ TCB solutions at 700 rpm onto the PEDOT:PSS layer. A Ca (30 nm)/Al (100 nm) cathode layer was then deposited by thermal evaporation under vacuum through a shadow mask to complete the BHJ cell. Current-voltage (J-V) characteristics were measured under AM1.5 solar illumination using a xenon lamp.

For devices with a CuSCN HTL layer (again performed by Dr. Tuladhar), 20 mg/ml of CuSCN was dissolved in diethylsulfide by stirring for 1 h under a nitrogen atmosphere in a glovebox. The saturated CuSCN solution was then filtered through a 0.45 μm PTFE syringe filter and spun-cast onto ITO substrates (cleaned as before) at 2000 rpm for 60 s and then annealed at 100 °C for 30 min to give a thin film with a thickness of 40 nm. Device fabrication then continued as described previously, with spin coating of the active layer followed by evaporation of the cathode layer.

### *3.10.1 – Stille polymerisation of 2,6-dibromo-3,5-didodecyl-4-phenyldithieno[3,2-b:2',3'-d]arsole with 2,6-bis(trimethylstannyl)-4,8-bis[5-(2-butyloctyl)thiophen-2-yl]-benzo[1,2-b:4,5-b']dithiophene (PDTAsBDT-TBO)*

An oven-dried high-pressure microwave tube was charged with 2,6-dibromo-3,5-didodecyl-4-phenyldithieno[3,2-*b*:2',3'-*d*]arsole (**2.10**, 100.0 mg, 0.123 mmol), 2,6-bis(trimethylstannyl)-4,8-bis[5-(2-butyloctyl)thiophen-2-yl]-benzo[1,2-b:4,5-b']dithiophene (125.3 mg, 0.123 mmol), and $Pd(PPh_3)_4$ (3.0 mg, 0.002 mmol). The tube was sealed with a septum and flushed with Ar, after which degassed chlorobenzene was added (2 ml). The mixture was thoroughly degassed with Ar, after which the inlet was removed. The vial was then placed in a microwave reactor and heated as follows: 4 min at 100 °C, 120 °C, and 140 °C, 20 min at 160 °C, and 60 min at 180 °C.

After cooling to room temperature, the resulting polymer was precipitated into methanol and filtered into a Soxhlet thimble. The polymer was extracted (Soxhlet) with methanol, acetone, and hexane in that order. The hexane fraction was concentrated under reduced pressure and the resulting polymer was dissolved in chlorobenzene, warmed to 50 °C and stirred in the presence of diethylammonium diethyldithiocarbamate (10 mg) for 1 h. The solution was concentrated in vacuo, dissolved in a minimal amount of hot chlorobenzene and the polymer collected by re-precipitation into methanol followed by vacuum filtration. After drying under vacuum, the polymer **PDTAsBDT-TBO** was collected (154.5 mg, 94%). GPC (chlorobenzene): $M_n$ 14,000 g/mol, $M_w$ 27,000 g/mol, Đ 1.93. $^1$H NMR (400 MHz, 323 K, $CDCl_3$) δ 7.77 – 7.50 (broad m, 2H), 7.38 – 7.27 (broad m, 5H), 7.26 – 7.19 (broad m, 2H), 6.96 – 6.81 (broad m, 2H), 2.93 – 2.70 (broad m, 8H), 1.82 – 1.65 (broad m, 2H), 1.59 – 1.03 (broad m, 72H), 0.96 – 0.83 (broad m, 18H). Anal. Calcd. for $C_{80}H_{111}AsS_6$: C, 71.70; H, 8.35. Found: C, 70.42; H, 8.52.

### *3.10.2 – Stille polymerisation of 2,6-dibromo-3,5-didodecyl-4-phenyldithieno[3,2-b:2',3'-d]arsole with 2,6-bis(trimethylstannyl)-4,8-bis[5-(2-ethylhexyl)thiophen-2-yl]-benzo[1,2-b:4,5-b']dithiophene (PDTAsBDT-TEH)*

An oven-dried high-pressure microwave tube was charged with 2,6-dibromo-3,5-didodecyl-4-phenyldithieno[3,2-*b*:2',3'-*d*]arsole (**2.10**, 100.1 mg, 0.123 mmol), 2,6-bis(trimethylstannyl)-4,8-bis[5-(2-ethylhexyl)thiophen-2-yl]-benzo[1,2-b:4,5-b']dithiophene (111.1 mg, 0.123 mmol), and $Pd(PPh_3)_4$ (3.0 mg, 0.002 mmol). The tube was sealed with a septum and flushed with Ar, after which degassed chlorobenzene was added (2 ml). The mixture was thoroughly degassed with Ar, after which the inlet was removed. The vial was then placed in a microwave reactor and heated as follows: 4 min at 100 °C, 120 °C, and 140 °C, 20 min at 160 °C, and 60 min at 180 °C. After cooling to room temperature, the resulting polymer was precipitated into methanol and filtered into a Soxhlet thimble. The polymer was extracted (Soxhlet) with methanol, acetone, hexane, and chloroform in that order. The hexane and chloroform fractions were concentrated under reduced pressure and the resulting polymer samples were dissolved in chlorobenzene, warmed to 50 °C and stirred in the presence of diethylammonium diethyldithiocarbamate

(10 mg) for 1 h. The solutions were then concentrated in vacuo, dissolved in minimal amounts of hot chlorobenzene and the polymer samples collected by re-precipitation into methanol followed by vacuum filtration. After drying under vacuum, two fractions of the polymer **PDTAsBDT-TEH** were collected: hexane (126.5 mg, 83.7%), GPC (chlorobenzene): $M_n$ 20,000 g/mol, $M_w$ 37,200 g/mol, Đ 1.86; chloroform (11 mg, 7.3%), GPC (chlorobenzene): $M_n$ 30,000 g/mol, $M_w$ 50,400 g/mol, Đ 1.68. $^1$H NMR (400 MHz, 323 K, $CDCl_3$) δ 7.77 – 7.47 (broad m, 2H), 7.38 – 7.19 (broad m, 7H), 6.95 – 6.83 (broad m, 2H), 2.94 – 2.66 (broad m, 8H), 1.75 – 1.64 (broad m, 2H), 1.56 – 1.05 (broad m, 56H), 1.00 – 0.81 (broad m, 18H). Anal. Calcd. for $C_{72}H_{95}AsS_6$: C, 70.43; H, 7.80. Found: C, 70.46; H, 7.57.

### *3.10.3 – Synthesis of 4,7-bis(5-bromothiophen-2-yl)-2-(2-butyloctyl)-5,6-dicyano-2H-benzo[d][1,2,3]triazole (3.2)*

Bromine (0.300 g, 1.877 mmol) was added to a solution of 4,7-bis(thiophen-2-yl)-2-(2-butyloctyl)-5,6-dicyano-2H-benzo[d][1,2,3]triazole (**3.1**, 0.410 mg, 0.817 mmol) in chloroform (20 ml), and the reaction was stirred in the dark. The reaction was monitored by TLC and $^1$H NMR, and after 24 h an additional equivalent of $Br_2$ (0.131 mg, 0.817 mmol) was added in small portions over 6 h until the reaction reached completion. The reaction was quenched with saturated sodium sulfite and extracted with DCM (3 × 20 ml). The combined organic layers were dried over $Mg_2SO_4$ and concentrated in vacuo. The crude product was purified by column chromatography over silica (eluent: DCM/hexane in a 1:1 ratio) to yield 4,7-bis(5-bromothiophen-2-yl)-2-(2-butyloctyl)-5,6-dicyano-2H-benzo[d][1,2,3]triazole (**3.2**) as a yellow solid (0.310 mg, 0.470 mmol, 57%). $^1$H NMR (400 MHz, $CDCl_3$) δ 8.07 (d, $J$ = 4.1 Hz, 2H), 7.24 (d, $J$ = 4.1 Hz, 2H), 4.79 (d, $J$ = 6.4 Hz, 2H), 2.33 – 2.21 (m, 1H), 1.47 – 1.22 (m, 16H), 0.94 – 0.83 (m, 6H). $^{13}$C NMR (101 MHz, $CDCl_3$) δ 142.51 (2C), 134.83 (2C), 132.15 (2C), 130.98 (2C), 129.91 (2C), 119.78 (2C), 116.76 (2C), 107.56 (2C), 61.07, 39.47, 31.94, 31.53, 31.29, 29.68, 28.58, 26.30, 23.08, 22.79, 14.22 (2C). EI-HRMS (*m/z*): Calculated for $C_{28}H_{28}N_5S_2Br_2$ [$M^+$−H]: 656.0153, found 656.0133

### *3.10.4 – Stille polymerisation of 4,7-bis(5-bromothiophen-2-yl)-2-(2-butyloctyl)-5,6-dicyano-2H-benzo[d][1,2,3]triazole with 2,6-bis(trimethylstannyl)-4,8-bis[5-(2-ethylhexyl)thiophen-2-yl]-benzo[1,2-b:4,5-b']dithiophene (PDCBTzBDT-TEH)*

An oven-dried high-pressure microwave tube was charged with 24,7-bis(5-bromothiophen-2-yl)-2-(2-butyloctyl)-5,6-dicyano-2H-benzo[d][1,2,3]triazole (**3.2**, 200.1 mg, 0.303 mmol), 2,6-bis(trimethylstannyl)-4,8-bis[5-(2-ethylhexyl)thiophen-2-yl]-benzo[1,2-b:4,5-b']dithiophene (274.1 mg, 0.303 mmol), $Pd_2dba_3$ (5.5 mg, 0.005 mmol), and $P(o\text{-tol})_3$ (7.4 mg, 0.024 mmol). The tube was sealed with a septum and flushed with Ar, after which degassed *o*-xylene was added (2 ml). The mixture was thoroughly degassed with Ar, after which the inlet was removed. The vial was then placed in a microwave reactor and heated as follows: 2 min at 100 °C, 120 °C, 140 °C, and 160 °C, 10 min at 180 °C, and 30 min at 200 °C. After cooling to room temperature, the resulting polymer was precipitated into methanol and filtered into a Soxhlet thimble. The polymer was extracted (Soxhlet) with methanol, acetone, hexane, chloroform, and chlorobenzene in that order. The material that remained in the thimble after extraction was dissolved in hot TCB and precipitated in methanol, and **PDCBTzBDT-TEH** was collected as a dark blue solid by vacuum filtration. Chloroform fraction: 12 mg (yield = 4%), chlorobenzene fraction: 10 mg (yield = 3%). Chloroform fraction: $^1$H NMR (400 MHz, TCE-$d_2$, 130 °C) δ 8.45 – 8.23 (m, 2H), 7.95 – 7.61 (m, 2H), 7.60 – 7.28 (m, 4H), 7.15 – 6.95 (m, 2H), 5.00 – 4.80 (br, 2H), 3.21 – 2.93 (m, 4H), 2.51 – 2.32 (br, 1H), 2.01 – 1.73 (br, 3H), 1.74 – 1.27 (m, 31H), 1.26 – 0.89 (m, 18H).

### *3.10.5 – Stille polymerisation of 4,7-bis(5-bromothiophen-2-yl)-2-(2-butyloctyl)-5,6-dicyano-2H-benzo[d][1,2,3]triazole with 2,6-bis(trimethylstannyl)-4,8-bis[5-(2-butyloctyl)thiophen-2-yl]-benzo[1,2-b:4,5-b']dithiophene (PDCBTzBDT-TBO)*

An oven-dried high-pressure microwave tube was charged with 4,7-bis(5-bromothiophen-2-yl)-2-(2-butyloctyl)-5,6-dicyano-2H-benzo[d][1,2,3]triazole (**3.2**, 100.2 mg, 0.152 mmol), 2,6-bis(trimethylstannyl)-4,8-bis[5-(2-butyloctyl)thiophen-2-yl]-benzo[1,2-b:4,5-b']dithiophene (154.1 mg, 0.152 mmol), $Pd_2dba_3$ (2.9 mg, 0.003 mmol), and $P(o\text{-tol})_3$ (3.8 mg, 0.012 mmol). The

tube was sealed with a septum and flushed with Ar, after which degassed *o*-xylene was added (2 ml). The mixture was thoroughly degassed with Ar, after which the inlet was removed. The vial was then placed in a microwave reactor and heated as follows: 2 min at 100 °C, 120 °C, 140 °C, and 160 °C, 10 min at 180 °C, and 30 min at 200 °C. After cooling to room temperature, the resulting polymer was precipitated into methanol and filtered into a Soxhlet thimble. The polymer was extracted (Soxhlet) with methanol, acetone, hexane, chloroform, and chlorobenzene in that order. The chloroform and chlorobenzene **PDCBTzBDT-TBO** fractions were concentrated in vacuo, redissolved in minimal amounts of hot chlorobenzene and reprecipitated into methanol, then collected by vacuum filtration as dark blue solids. Chloroform fraction: 76 mg (yield = 42%), GPC (80 °C, chlorobenzene): $M_n$ 26,000 g/mol, $M_w$ 87,510 g/mol, Đ 3.37. Chlorobenzene fraction: 88 mg (yield = 48%), GPC (80 °C, chlorobenzene): $M_n$ 78,200 g/mol, $M_w$ 114,300 g/mol, Đ 1.46. $^1$H NMR (400 MHz, TCE-$d_2$, 130 °C) δ 8.47 – 8.30 (m, 2H), 7.93 – 7.69 (m, 2H), 7.65 – 7.33 (m, 4H), 7.18 – 7.00 (m, 2H), 4.98 – 4.77 (m, 2H), 3.21 – 2.93 (m, 4H), 2.53 – 2.33 (m, 1H), 2.04 – 1.81 (m, 3H), 1.72 – 1.27 (m, 47H), 1.16 – 0.85 (m, 18H). Anal. Calcd. for $C_{70}H_{85}N_5S_6$: C, 70.72; H, 7.21; N, 5.89. Found: C, 70.62; H, 7.11; N, 5.84.

### *3.11 – References*


1. R. K. Pai, A. T. N., and H. B., *RSC Adv.*, 2016, **6**, 23760–23774.
2. H. Yao, L. Ye, H. Zhang, S. Li, S. Zhang, and J. Hou, *Chem. Rev.*, 2016, **116**, 7397–7457.
3. X. Guo, M. Baumgarten, and K. Müllen, *Prog. Polym. Sci.*, 2013, **38**, 1832–1908.
4. J. Hou, M.-H. Park, S. Zhang, Y. Yao, L.-M. Chen, J.-H. Li, and Y. Yang, *Macromolecules*, 2008, **41**, 6012–6018.
5. W. Zhao, D. Qian, S. Zhang, S. Li, O. Inganäs, F. Gao, and J. Hou, *Adv. Mater.*, 2016, **28**, 4734–4739.
6. L. Huo, J. Hou, S. Zhang, H.-Y. Chen, and Y. Yang, *Angew. Chemie Int. Ed.*, 2010, **49**, 1500–1503.
7. Z. Zhang and J. Wang, *J. Mater. Chem.*, 2012, **22**, 4178.
8. Y. Li and Y. Zou, *Adv. Mater.*, 2008, **20**, 2952–2958.

9. C. J. Brabec, M. Heeney, I. McCulloch, and J. Nelson, *Chem. Soc. Rev.*, 2011, **40**, 1185–1199.

10. R. Po, M. Maggini, and N. Camaioni, *J. Phys. Chem. C*, 2010, **114**, 695–706.

11. F. B. Kooistra, J. Knol, F. Kastenberg, L. M. Popescu, W. J. H. Verhees, J. M. Kroon, and J. C. Hummelen, *Org. Lett.*, 2007, **9**, 551–554.

12. C. J. Brabec, N. S. Sariciftci, and J. C. Hummelen, *Adv. Funct. Mater.*, 2001, **11**, 15–26.

13. N. K. Elumalai and A. Uddin, *Energy Environ. Sci.*, 2016, **9**, 391–410.

14. P. Sista, M. C. Biewer, and M. C. Stefan, *Macromol. Rapid Commun.*, 2012, **33**, 9–20.

15. K. H. Park, Y. J. Kim, G. B. Lee, T. K. An, C. E. Park, S.-K. Kwon, and Y.-H. Kim, *Adv. Funct. Mater.*, 2015, **25**, 3991–3997.

16. H. Zhou, L. Yang, S. C. Price, K. J. Knight, and W. You, *Angew. Chemie Int. Ed.*, 2010, **49**, 7992–7995.

17. Q. T. Zhang and J. M. Tour, *J. Am. Chem. Soc.*, 1997, **119**, 5065–5066.

18. X. Wang, Y. Sun, S. Chen, X. Guo, M. Zhang, X. Li, Y. Li, and H. Wang, *Macromolecules*, 2012, **45**, 1208–1216.

19. Y. Li, *Acc. Chem. Res.*, 2012, **45**, 723–733.

20. X. Zhang, T. T. Steckler, R. R. Dasari, S. Ohira, W. J. Potscavage, S. P. Tiwari, S. Coppée, S. Ellinger, S. Barlow, J.-L. Brédas, B. Kippelen, J. R. Reynolds, and S. R. Marder, *J. Mater. Chem.*, 2010, **20**, 123.

21. E. Zhou, J. Cong, K. Tajima, C. Yang, and K. Hashimoto, *Macromol. Chem. Phys.*, 2011, **212**, 305–310.

22. J. S. Kim, Z. Fei, D. T. James, M. Heeney, and J.-S. Kim, *J. Mater. Chem.*, 2012, **22**, 9975–9982.

23. C. M. Amb, S. Chen, K. R. Graham, J. Subbiah, C. E. Small, F. So, and J. R. Reynolds, *J. Am. Chem. Soc.*, 2011, **133**, 10062–10065.

24. J. Ohshita, M. Miyazaki, M. Nakashima, D. Tanaka, Y. Ooyama, T. Sasaki, Y. Kunugi, and Y. Morihara, *RSC Adv.*, 2015, **5**, 12686–12691.

25. M. G. Hobbs and T. Baumgartner, *Eur. J. Inorg. Chem.*, 2007, 3611–3628.

26. L. Zhang, C. He, J. Chen, P. Yuan, L. Huang, C. Zhang, W. Cai, Z. Liu, and Y. Cao, *Macromolecules*, 2010, **43**, 9771–9778.

27. S. C. Price, A. C. Stuart, L. Yang, H. Zhou, and W. You, *J. Am. Chem. Soc.*, 2011, **133**, 4625–4631.

28. W. Li, L. Yan, H. Zhou, and W. You, *Chem. Mater.*, 2015, **27**, 6470–6476.

29. A. Casey, Y. Han, Z. Fei, A. J. P. White, T. D. Anthopoulos, and M. Heeney, *J. Mater. Chem. C*, 2015, **3**, 265–275.

30. A. Casey, PhD Thesis, Imperial College London, 2016.

31. P. Pattanasattayavong, N. Yaacobi-Gross, K. Zhao, G. O. N. Ndjawa, J. Li, F. Yan, B. C. O'Regan, A. Amassian, and T. D. Anthopoulos, *Adv. Mater.*, 2013, **25**, 1504–1509.

32. N. Yaacobi-Gross, N. D. Treat, P. Pattanasattayavong, H. Faber, A. K. Perumal, N. Stingelin, D. D. C. Bradley, P. N. Stavrinou, M. Heeney, and T. D. Anthopoulos, *Adv. Energy Mater.*, 2015, **5**, 1401529.

33. A. Patra, N. Chaudhary, R. Chaudhary, J. P. Kesari, and S. Chand, *J. Mater. Chem. C*, 2015, **3**, 11886–11892.

# *Chapter 4*

# *Effect of the Dithienometallole Bridging Group on OFET Properties*

### *4.1 – Introduction*

Early work on the use of bridged thiophene units for plastic electronics applications focused on materials that used carbon as the bridging atom to give 4*H*-cyclopenta[2,1-*b*:3,4-*b*']dithiophene (CPDT, see **Figure 1.9**), which was often alkylated at the bridging carbon to improve the solubility of the resulting polymers.[1] Later, the use of other group 14 elements including silicon and germanium was investigated to give analogous materials,[2,3] which demonstrated subtly different optoelectronic properties. Changing the bridging atom to sulfur resulted in dithieno[3,2-*b*:2',3'-*d*]thiophene (DTT), which shows high thermo- and photostability but is limited in its potential for functionalisation, leading to solubility problems unless a suitable co-monomer is employed.[4–6] Interest in dithieno[3,2-*b*:2',3'-*d*]pyrrole (DTP) stemmed from the ability to functionalise DTP at the nitrogen, allowing the incorporation of the positive attributes of both DTT (increased stability) and materials bridged with group 14 elements (alkylation to improve solubility).[7]

The vast majority of research into bridged bithiophenes uses the bridging atom as the sole point of alkylation, which is required to confer the necessary solubility for the materials to be solution-processable.[8] Alkyl chains are particularly important in CPDT-containing systems and their analogues because the increased planarity conferred by bridging ring systems reduces solubility, meaning that bridged monomers require longer or more heavily branched solubilising groups than their unfused analogues. However, this presents two problems – the first is that it can add unnecessary complexity to the synthesis of the monomers,[9] and the second is the significant effect that longer alkyl chains have on the packing motifs of the molecules.[10] Fortunately, these problems can be at least somewhat mitigated by the inclusion of alkyl chains at other positions on the rings, allowing more varied functionality on the bridging heteroatom. This can allow either the use of shorter alkyl chains at the heteroatom, such as employing a dimethylsilyl group as a bridge between thiophene rings,[11] or functionalization of the bridge as seen in cyclopenta[2,1-*b*:3,4-*b*']dithiophen-4-one-containing materials, where the bridging carbon takes the form of a carbonyl group.[12]

In this chapter, the synthesis of peripherally alkylated DTP and its polymerization with thieno[3,2-*b*]thiophene (TT) via three different methods is described. These polymerizations include two different forms of Stille coupling (one with brominated DTP and the other with the stannylated analogue) and direct heteroarylation polymerization. Furthermore, the optoelectronic properties and OFET performance of the resulting alternating DTP-TT polymer are compared with three analogous materials utilizing dibutylsilyl, dibutylgermyl, and carbonyl bridging groups between the thiophene rings instead of the alkylamine group used in dithienopyrrole.

## *4.2 – Synthesis of dithienopyrrole monomers*

### *4.2.1 – Preparation of dithienopyrrole*

Synthesis of 3,5-didodecyl-4N-hexyldithieno[3,2-*b*:2',3'-*d*]pyrrole (**4.1**) was performed as shown in **Figure 4.1**, using 3,3'-dibromo-2,2'-bithiophene (**2.6**) as a starting material that was prepared through the route described in **Chapter 2**. This compound was then ring-closed with hexylamine via the Buchwald-Hartwig reaction using [$Pd_2dba_3$] as a catalyst with 2,2'-bis(diphenylphosphino)-1,1'-binaphthyl (BINAP) as a ligand, combined with sodium tert-butoxide ($Na^tBuO$) as a base in refluxing toluene to give **4.1** as a yellow oil in a 48% yield after purification by column chromatography. Attempts were also made to perform ring closure with 2-ethyl-1-hexylamine to obtain a branched alkyl chain on the nitrogen, however the reaction only yielded 3'-bromo-4,4'-didodecyl-*N*-(2-ethylhexyl)-2,2'-bithiophene-3-amine, likely due to steric clashes between the ethylhexyl group and the peripheral dodecyl chains.

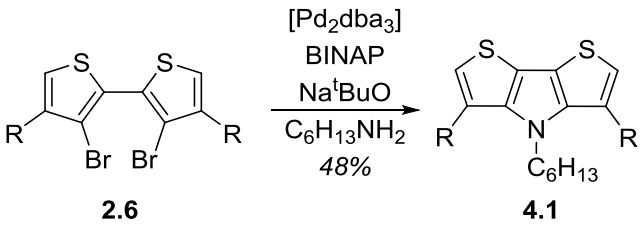
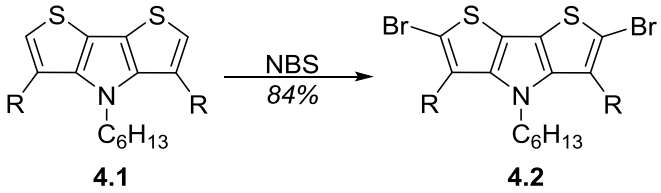



**Figure 4.1: Synthesis of 3,5-didodecyl-4N-hexyldithieno[3,2-*b*:2',3'-*d*]pyrrole, where R represents dodecyl side chains**

To enable polymerization of **4.1** via Stille coupling, both the dibrominated and distannylated monomers were prepared in order to allow polymerization via different conditions, while unfunctionalized **4.1** was also used for polymerization via direct heteroarylation.

### *4.2.2 – Bromination of dithienopyrrole*

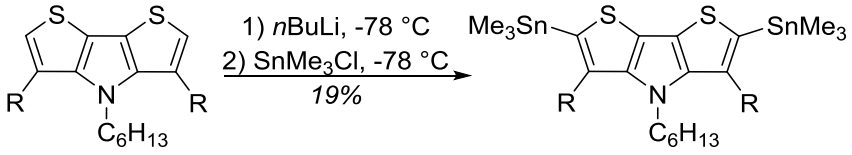



**4.1** **4.2**

**Figure 4.2: Synthesis of 2,6-dibromo-3,5-didodecyl-4N-hexyldithieno[3,2-*b*:2',3'-*d*]pyrrole (4.2), where R represents dodecyl side chains**

The brominated monomer **4.2** was prepared via electrophilic bromination using N-bromosuccinimide (NBS). Stirring the reaction in the absence of light at 0 °C for 2 h followed by purification by flash chromatography yielded the product in an 84% yield. This monomer was then polymerized with distannylated thieno[3,2-*b*]thiophene.

### *4.2.3 – Stannylation of dithienopyrrole*




**4.1** **4.3**

**Figure 4.3: Synthesis of 2,6-distannyl-3,5-didodecyl-4N-hexyldithieno[3,2-*b*:2',3'-*d*]pyrrole (4.2), where R represents dodecyl side chains**

To allow the Stille polymerisation of the dithienopyrrole group with brominated comonomers, **4.1** was functionalized with trimethylstannyl groups. The compound was first dilithiated using a TMEDA/*n*BuLi complex, then quenched with trimethylstannyl chloride to give the product. The instability of the stannyl group meant that the compound could not be purified by column chromatography, while the abundance of alkyl groups present resulted in it taking the form of an oil, rendering recrystallization impossible. The compound was therefore

purified by recycling GPC (hexane, 40 °C) to remove mono- and non-stannylated material, resulting in **4.3** being obtained in a 19% yield.

### *4.2.4 – Polymerizations with thienothiophene*

Synthesis of copolymers of DTP with TT was attempted via three different methods, with varying degrees of success. The primary reason for the choice of TT as the co-monomer for this study was its improved properties over bithiophene, which has previously been used as a comonomer for the examination of dithienogermole and dithienosilole materials.[9] Use of TT in polymers has previously been shown to result in increased polymer planarity, leading to higher charge carrier mobilities due to improved π-π stacking and greater delocalisation along the polymer backbone.[13,14] These properties make TT an excellent unit for use in push-pull type polymers for OFET applications.[15,16]

#### *4.2.4.1 – Polymerization via direct heteroarylation with 2,6-dibromothieno[3,2-b]thiophene*

The first technique used for the attempted polymerization of DTP with TT was direct heteroarylation, which is a coupling reaction capable of forming C-C bonds between aryl halides and activated C-H bonds on aromatic species.[17] This technique has several advantages over the other polymerization methods discussed in this thesis, not least of which are the significant reduction in the toxicity of both the chemistry required to perform this type of reaction and waste produced by it.[18] While Stille polymerizations require the use of dangerous and often unstable organotin reagents and produce stoichiometric amounts of halogenated organotin waste, direct heteroarylation makes use of only unfunctionalized and halogenated monomers, both improving the safety and environmental credentials of the chemistry as it produces acid as the by-product instead.[19] Additionally, it allows for the synthesis of polymers that cannot be accessed through traditional organometallic cross-coupling reactions due to the instability of their organometallic monomers.[20]

Previous work by the Horie and Scherf groups has shown that polymerization of unfunctionalized bridged bithiophenes such as CPDT and dithienosilole is possible by direct heteroarylation,[21,22] and furthermore we had already obtained some promising results from direct arylation of dithienopyrroles, which are discussed in **Chapter 5**. For these reasons, direct heteroarylation was the first polymerization method attempted.

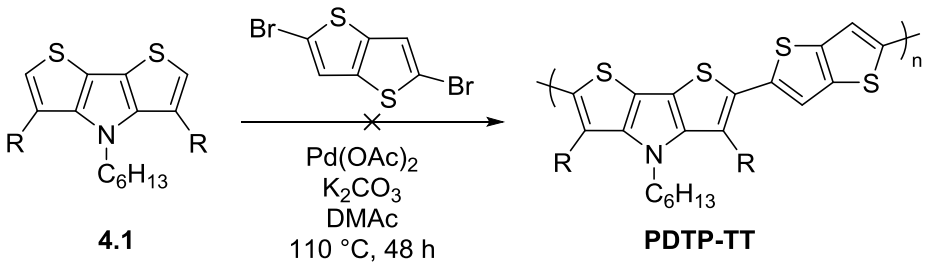



**Figure 4.4 – Direct heteroarylation polymerization of DTP and dibromo-TT to form PDTP-TT, where R represents dodecyl side chains**

Polymerization of 3,5-didodecyl-4N-hexyldithieno[3,2-*b*:2',3'-*d*]pyrrole (**4.1**) with 2,6-dibromo-thieno[3,2-*b*]thiophene was carried out in dimethylacetamide using palladium acetate ($Pd(OAc)_2$) as a catalyst and potassium carbonate as a base, which is necessary to quench the hydrobromic acid produced during the coupling. The reaction was carried out using an oil bath rather than a microwave reactor, and thus required a significantly longer reaction time than analogous microwave-assisted polymerizations. After 48 h at 110 °C the reaction was cooled to room temperature and was poured into cold stirring methanol. However, the attempted Soxhlet extraction of the polymer was unsuccessful, with no polymer being recovered even from the chloroform fraction. After transferring the solid mass to a glass thimble, an additional Soxhlet extraction was attempted using chlorobenzene, although no additional polymer was recovered. While it cannot be proven due to the insolubility of the material, the most likely explanation for this result is that miscoupling occurred at the TT C-H positions during the polymerization, resulting in formation of a highly insoluble cross-linked network. Similar behaviour has been observed in some other direct heteroarylation polymerizations, and can sometimes be minimised by careful control of the reaction conditions.[22,23] However, due to the time- and

material-intensive nature of such reaction optimisation, it was decided to try different polymerisation methods instead.

#### *4.2.4.2 – Polymerization via Stille coupling with 2,6-bis(trimethylstannyl)-thieno[3,2-b]thiophene*

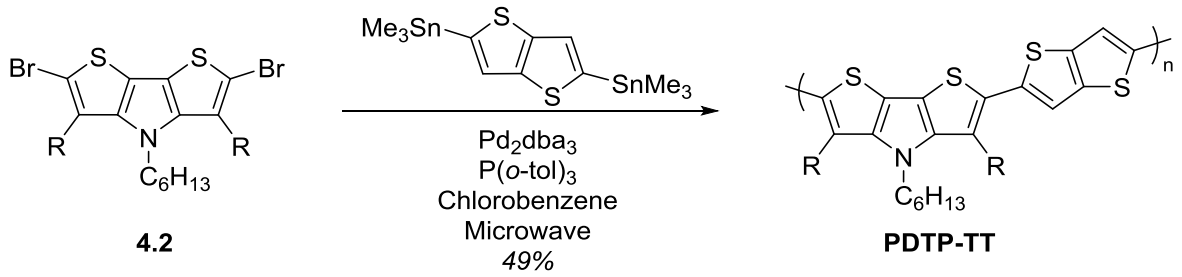



**Figure 4.5 – Stille polymerization of dibromo-DTP with bis(trimethylstannyl)-TT, where R represents dodecyl side chains**

Stille polymerization of 2,6-dibromo-3,5-didodecyl-4N-hexyldithieno[3,2-*b*:2',3'-*d*]pyrrole (**4.2**) with 2,6-bis(trimethylstannyl)-thieno[3,2-*b*]thiophene was performed in a microwave reactor using $Pd_2dba_3$ as the catalyst and tri(*o*-tolyl)phosphine as a ligand. The resulting polymer was precipitated in methanol and purified by Soxhlet extraction with methanol and acetone in order to remove catalyst and low molecular weight oligomers. The polymer was then extracted into hexane and chloroform. Due to the small amount of polymer in the chloroform, the fractions were combined and precipitated into methanol to yield **PDTP-TT** as a dark red solid with a yield of 49%. The $M_n$ as determined by GPC in chlorobenzene (80 °C) against polystyrene standards was 7.6 kg/mol, with an $M_w$ of 13.1 kg/mol and a Đ of 1.80. Such a low $M_n$ value for a polymer containing dithienopyrrole is far from unheard of, with many non-donor-acceptor DTP copolymers synthesised by Stille coupling having sub-10 kg/mol weights.[5,24–26]

#### *4.2.4.3 – Polymerization via Stille coupling with 2,6-dibromothieno[3,2-b]thiophene*

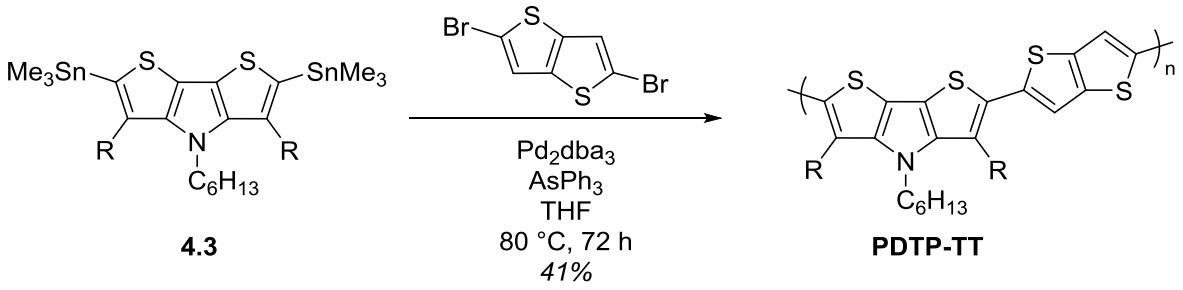



**Figure 4.6 – Stille polymerization of bis(trimethylstannyl)-DTP with dibromo-TT, where R represents dodecyl side chains**

**PDTP-TT** was also synthesised via traditional (i.e., non-microwave-assisted) Stille coupling using the distannyl-DTP unit and the dibrominated TT moiety, with $Pd_2dba_3$ as the catalyst and triphenylarsine ($AsPh_3$) as a ligand. This slightly softer ligand was chosen as it has been found to improve reaction rates in Stille couplings,[27] which we hoped might lead to higher molecular weights in polymerisations. However, after heating at 80 °C for 72 h and purifying the polymer as before, the molecular weight of the **PDTP-TT** synthesised in this way was found to be almost identical to that synthesised in the microwave reactor (**Section 4.2.4.2**), with the $M_n$ as determined by GPC in chlorobenzene (80 °C) against polystyrene standards being 7.6 kg/mol, the $M_w$ = 12.3 kg/mol, and Đ = 1.62.

**PDTP-TT** from both Stille couplings was soluble in a wide range of organic solvents, including hot hexane and a variety of chlorinated solvents such as chloroform and chlorobenzene. The structure of the polymers was confirmed by proton NMR and elemental analysis, both of which agreed with theoretical values. The polymer synthesised using the distannyl-DTP was used for subsequent analysis of optoelectronic and device properties, simply because this polymerisation was performed on a larger scale, which allowed us to ensure that the same batch was used for everything.

### *4.3 – Comparison with other dithienometallole-thienothiophene polymers*

Previous work by the Heeney group has compared peripherally alkylated dithienogermole- and dithienosilole-containing copolymers, finding that the differences caused by changing the

bridging atom in this case were minimal.[9] The primary reason for this was the similarity of the Si and Ge bridging atoms in terms of size and bonding modes. Both are in group 14 of the periodic table and bond in a tetrahedral manner similar to $sp^3$ carbon, with the average C-Si bond length being 1.88 Å, whilst C-Ge is only slightly longer at 1.96 Å.[28] It is expected that changing the bridging group more significantly, for example to nitrogen (group 15) or a carbonyl group ($sp^2$-bonded carbon), will result in a much more significant change in properties. To investigate this hypothesis, this section compares the properties of four different dithienometallole-containing polymers, utilizing nitrogen, germanium, silicon, and carbonyl as bridging groups.

For this study, thieno[3,2-*b*]thiophene (TT) was used as a comonomer for all four dithienometalloles due to the reported improvements in transistor properties it provides over bithiophene. Use of TT has been shown to result in increased planarity, leading to higher charge carrier mobility due to improved π-π stacking, and greater delocalisation along the polymer backbone.[13,14] This makes TT an excellent unit for use in push-pull type polymers for application OFET devices.

Analogues of **PDTP-TT** using silicon, germanium, and carbonyl as bridging groups were prepared by Dr. Zhuping Fei via similar techniques to those described above. The structures of all four polymers are shown in **Figure 4.7**, where it can be seen that the tetrahedral bonding motifs of the silicon and germanium required **PDTSi-TT** and **PDTGe-TT** to have two alkyl chains on their heteroatoms instead of the one present on the pyrrolic nitrogen. Due to the $sp^2$ nature of the C=O bond in **PDTC-TT**, there was no alkyl chain on the bridging atom for this polymer. Molecular weight information for all four polymers can be found in **Table 4.1**. The Si and Ge bridged polymers both have similar molecular weights and dispersities, with the $M_n$ of both being significantly higher than the N-bridged polymer. The high dispersity of the carbonyl polymer most likely relates to the tendency of the polymer to aggregate in solution, even in chlorobenzene at 80 °C.

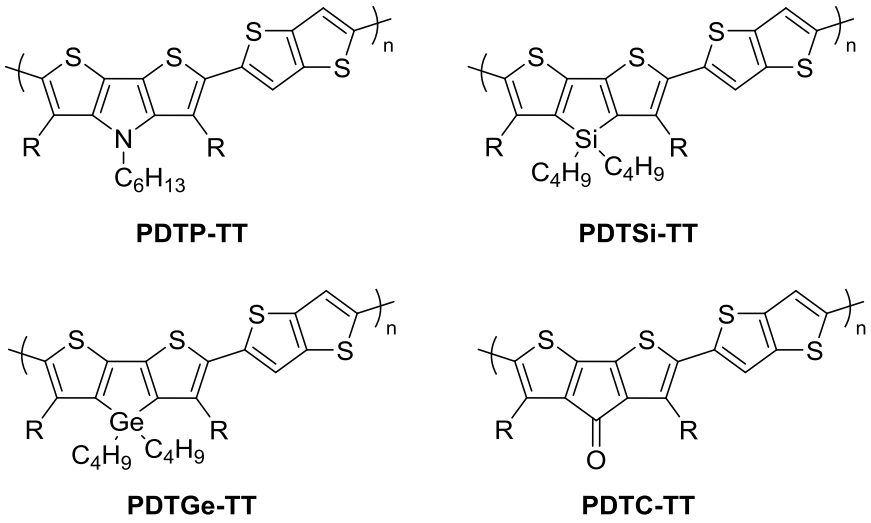



**Figure 4.7: Structures of the dithienometallole-containing polymers, where R represents dodecyl side chains**

**Table 4.1: Molecular weight information for the dithienometallole-containing polymers as measured by GPC in chlorobenzene (80 °C) against polystyrene standards**

| Polymer | $M_n$ (kg/mol) | $M_w$ (kg/mol) | Đ |
|---|---|---|---|
| PDTP-TT | 7.6 | 13.1 | 1.80 |
| PDTSi-TT | 29.9 | 52.7 | 1.76 |
| PDTGe-TT | 23.2 | 42.4 | 1.83 |
| PDTC-TT | 35.2 | 372.6 | 10.58 |

### *4.3.1 – Computational calculations*

In order to establish the effect of changing the bridging heteroatom on polymer geometry, theoretical calculations of the molecular geometries of the four polymers were carried out via DFT using Gaussian 09 at the B3LYP level of theory with the 6-311(d,p) basis set. To simplify the calculations, all alkyl chains were shortened to methyl groups. **Figure 4.8** shows the predicted structures of trimers of all four polymers, from both edge-on and face-on perspectives.

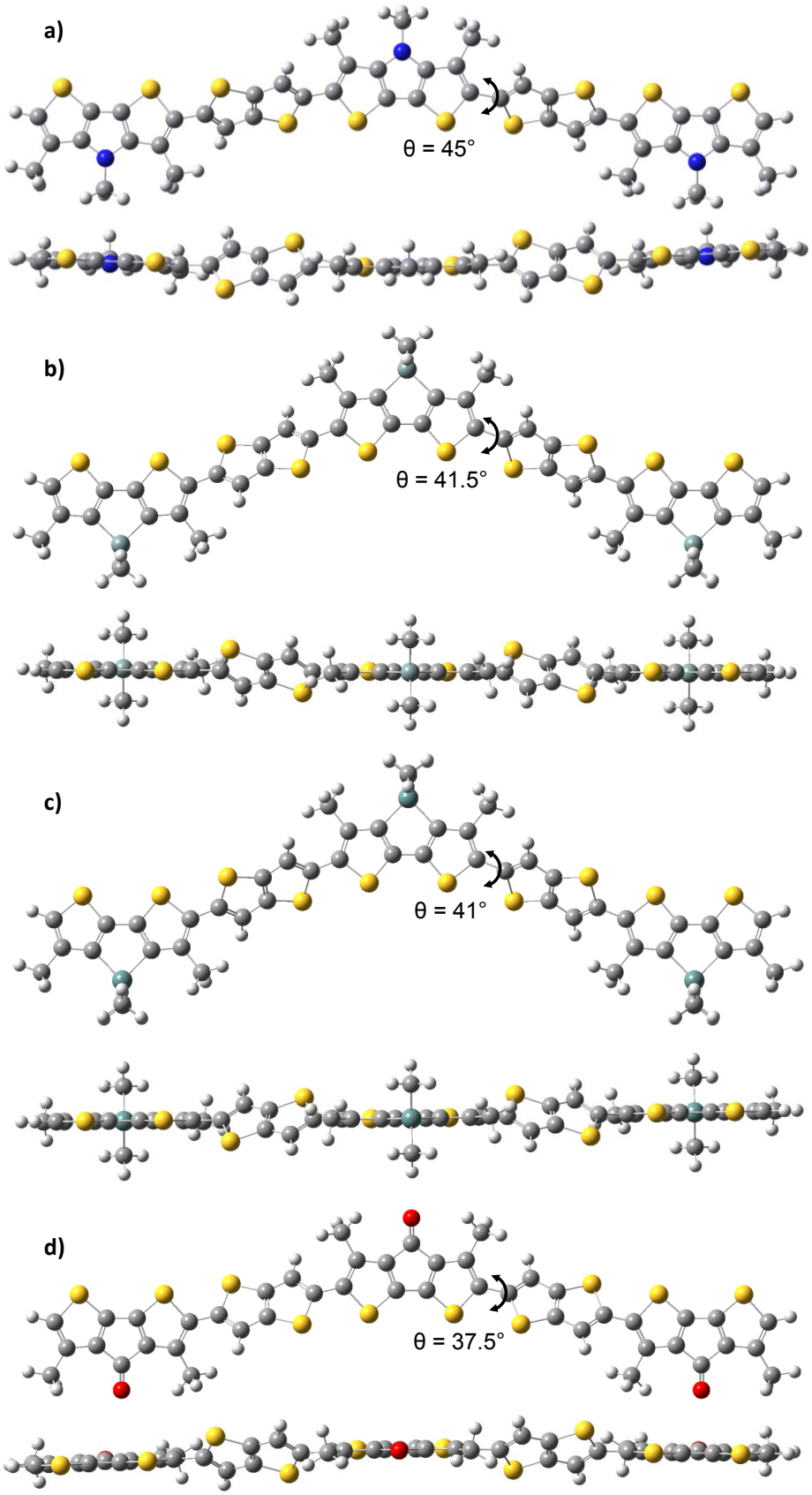



**Figure 4.8: Molecular geometries of: (a) PDTP-TT, (b) PDTSi-TT, (c) PDTGe-TT, and (d) PDTC-TT, as calculated using Gaussian 09 at the B3LYP level of theory with the 6-311G(d,p) basis set**

The four polymers show similar conformations, with planar dithienometallole groups connected by TTs that are twisted slightly out of the plane of the backbone in the *cis* conformation seen for other peripherally alkylated dithienometalloles-containing polymers investigated in this thesis. However, the degree of this twist varies between the polymers, and the difference can be described in terms of the dihedral angle between the dithienometallole and TT, which decreased from 45° for the N-bridged polymer to 41.5° for **PDTSi-TT**, 41° for **PDTGe-TT**, and 37.5° for **PDTC-TT**. The cause of this change is likely the shorter C-N bond length (1.39 Å compared to 1.89, 1.98, and 1.50 Å for C-Si, C-Ge, and C-C, respectively), as well as the fact that the alkyl chains on the nitrogen atoms are in the same plane as the dithienometallole ring system, while the Si/Ge groups are exogenic and the carbonyl has no alkyl chains. The combination of these two factors causes a steric clash, reducing the free space in the vicinity of the peripheral alkyl chain next to the DTP-TT bond and thus forcing the TT further out of the plane in **PDTP-TT**. This increased crowding may also help to explain the lower molecular weights of DTP-containing polymers, as similar effects could hinder the 2- and 6-positions of the monomer and reduce its reactivity by making oxidative addition (or transmetallation, as appropriate) more difficult.

The DSC curves of the four polymers showed no peaks between 0 and 300 °C when measured at 10 °C $min^{-1}$, possibly indicating relatively amorphous backbone structures, which would be expected due to the twisted natures of their backbones, or that the backbone melt was above 300 °C.

The frontier molecular orbital distributions of the polymers were also predicted using DFT under the same conditions as the geometries. **Figure 4.9** shows the predicted LUMO and HOMO distributions of the polymers. The HOMO images of the polymers are very similar, showing extended conjugation throughout the trimers and no involvement of the bridging heteroatoms, with electron density being almost entirely confined to the double bonds of the ring systems.

However, the LUMOs tell a different story, with substantial changes in energy density being predicted between the N-, Si-/Ge-, and carbonyl-bridged polymers.

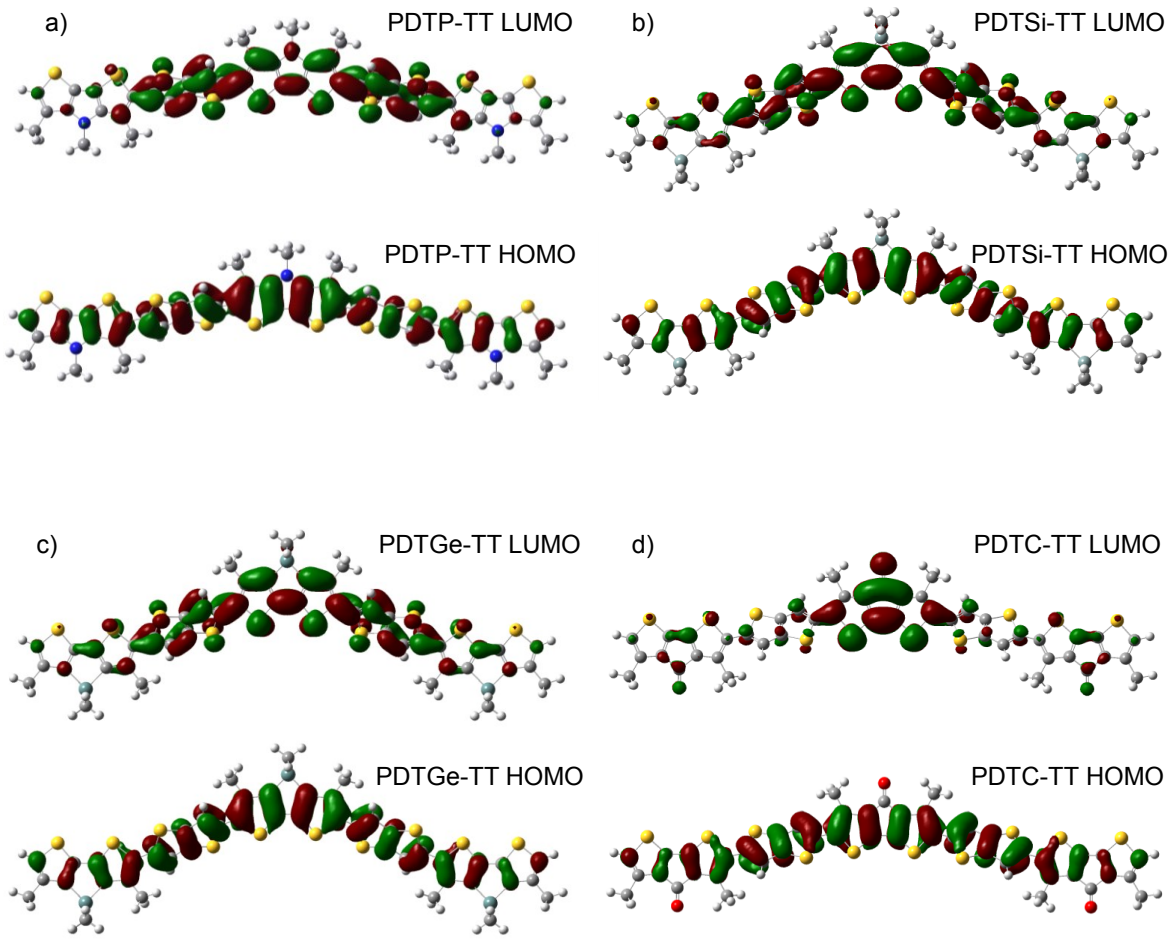



**Figure 4.9: Frontier molecular orbitals of (a) PDTP-TT, (b) PDTSi-TT, (c) PDTGe-TT, and (d) PDTC-TT, as calculated using Gaussian 09 at the B3LYP level of theory with the 6-311G(d,p) basis set. LUMOs are shown on the top, HOMOs underneath**

The LUMOs of **PDTSi-TT** and its germole analogue show a great deal of similarity, with orbital density in both systems being spread predominantly across the central dithienometallole and its two flanking thienothiophene groups. Interestingly, the orbital density diagrams suggest there in no significant interaction of the low lying lying σ* orbitals of the Si/Ge atoms with the π* orbitals of the conjugated carbon framework, at least in the LUMO.

The primary difference between the LUMO of **PDTP-TT** and the other materials is the presence of orbital density on the bridging N, which is not seen in **PDTSi-TT** or **PDTGe-TT**. Note that the N atom acts as a π-donor, with the orbital centred on N being out-of-phase with

the adjacent orbitals and therefore acting to destabilise the LUMO. In contrast, the carbonyl of **PDTC-TT** acts as a π-acceptor, with the C=O π* orbital being in-phase with the adjacent bithiophene LUMO. In both cases the interaction of the heteroatom is likely due to the $sp^2$ hybridization of the bridging atoms. On the other hand, the absence of orbital density on the bridging atoms of **PDTSi-TT** and **PDTGe-TT** is due to the $sp^3$ character of their hybridization, and helps to explain the limited differences between the energy levels of these two systems.[29,30] These finding are in line with those of Marder and coworkers, who investigated the impact of changing the bridging group of dithienometalloles on their electrochemical properties.[31]

**Table 4.2: Energy levels and band gaps of dithienometallole-containing polymers, as calculated using Gaussian 09 at the B3LYP level of theory with the 6-311G(d,p) basis set**

| Polymer | HOMO (eV) | LUMO (eV) | Band gap (eV) |
|---|---|---|---|
| **PDTP-TT** | −4.81 | −2.14 | 2.67 |
| **PDTSi-TT** | −4.96 | −2.49 | 2.47 |
| **PDTGe-TT** | −4.93 | −2.46 | 2.47 |
| **PDTC-TT** | −5.23 | −3.42 | 1.81 |

DFT and TD-DFT calculations also provided predictions of the HOMO and LUMO levels of all four polymers, which can be found in **Table 4.2**, as can the expected band gaps of the materials. The values provide further evidence of the impact of the bridging heteroatom on the properties of the dithienometallole-containing polymers. As noted in the discussion of the frontier molecular orbitals, the absence of appreciable HOMO density on the bridging atom suggests that the major impact of the bridging group on the HOMO energy will be inductive. The inductive effects of the various substituents can be estimated using their Hammett parameters. In this case, the meta parameters were used as the DFT calculations suggest that the major impact is

inductive, and the effect of resonance is reduced in the meta parameters. The $\sigma_{meta}$ values of -$GeMe_3$ ($\sigma_{meta}$ = 0.00), -$SiMe_3$ ($\sigma_{meta}$ = −0.04), -C=OMe ($\sigma_{meta}$ = 0.38), and -NHEt ($\sigma_{meta}$ = −0.24) were taken as close approximations to the bridging groups used.[32] The correlation of the $\sigma_{meta}$ parameter with the HOMOs, LUMOs, and band gaps of the materials are shown in **Figure 4.10**.

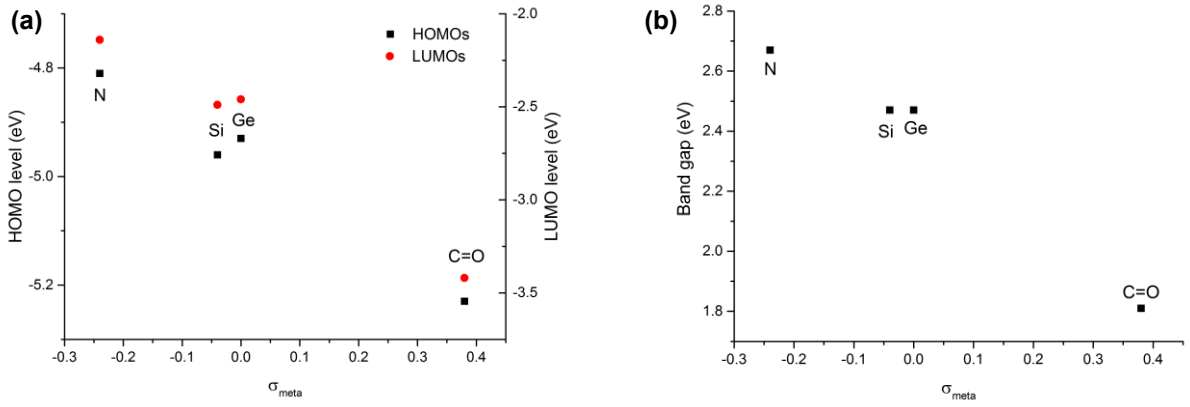



**Figure 4.10: Correlation of Hammett parameters of bridging groups with the (a) HOMO and LUMO levels and (b) band gaps of dithienometallole-containing polymers, as predicted using Gaussian 09 at the B3LYP level of theory with the 6-311G(d,p) basis set**

It can be seen that **PDTP-TT** is predicted to have the highest lying HOMO, in agreement with the electron donation from the N atom. Meanwhile, the Si- and Ge-containing polymers are predicted to have very similar energy levels to each other, in agreement with their similar Hammett values and reflecting the minimal effect that changing the bridging heteroatom from Si to Ge is expected to have on the conformational and electronic structure of the system. Both the HOMOs and the LUMOs of these two polymers are predicted to be below those of **PDTP-TT**, which is an agreement with the inductive effects of Si versus N (for example, $\sigma_{meta}$ = −0.04 versus −0.24). The raising of the LUMO value for the N-bridged polymer versus Si/Ge can be explained by the π-donor effect of the N, as explained earlier.

The energy levels of **PDTC-TT** are predicted to be significantly different from those of the other three polymers, with both a much deeper HOMO level, in agreement with the inductively withdrawing carbonyl group, and a significantly narrower band gap due to the strong π-acceptor nature of the ketone. Both of these changes indicate that altering the bridging

heteroatom from the $sp^3$-type bonding motif seen for **PDTSi-TT** and **PDTGe-TT** to the carbonylic $sp^2$-bonding of **PDTC-TT** results in a significant stabilization of the energy levels of the material. Furthermore, the localization of the LUMO on the central DTC unit (as seen in **Figure 4.9d**) appears to indicate that the **PDTC-TT** material exhibits some donor-acceptor behaviour that is not seen in the other polymers, helping to explain the much narrower band gap of this material.[33]

### *4.3.2 – Optical properties*

The UV-vis absorption spectra for all four polymers in solutions and as thin films can be seen in **Figure 4.11**, while a summary of the results, including $\lambda_{max}$ values for solution and thin films and the optical band gaps of the polymers as calculated from the thin film data, can be found in **Table 4.3**. Solution spectra were obtained from chlorobenzene, and thin films were cast from chlorobenzene onto glass slides at room temperature.

**Table 4.3: Optical properties of dithienometallole-containing polymers**

| Polymer | $\lambda_{max}$ solution (nm) | $\lambda_{max}$ thin film (nm) | Optical band gap (eV) |
|---|---|---|---|
| **PDTP-TT** | 466 | 503 | 2.09 |
| **PDTSi-TT** | 494 | 514 | 1.99 |
| **PDTGe-TT** | 494 | 504 | 1.96 |
| **PDTC-TT** | 439 (strong peak at 644) | 455 (strong peak at 704) | 1.44 |

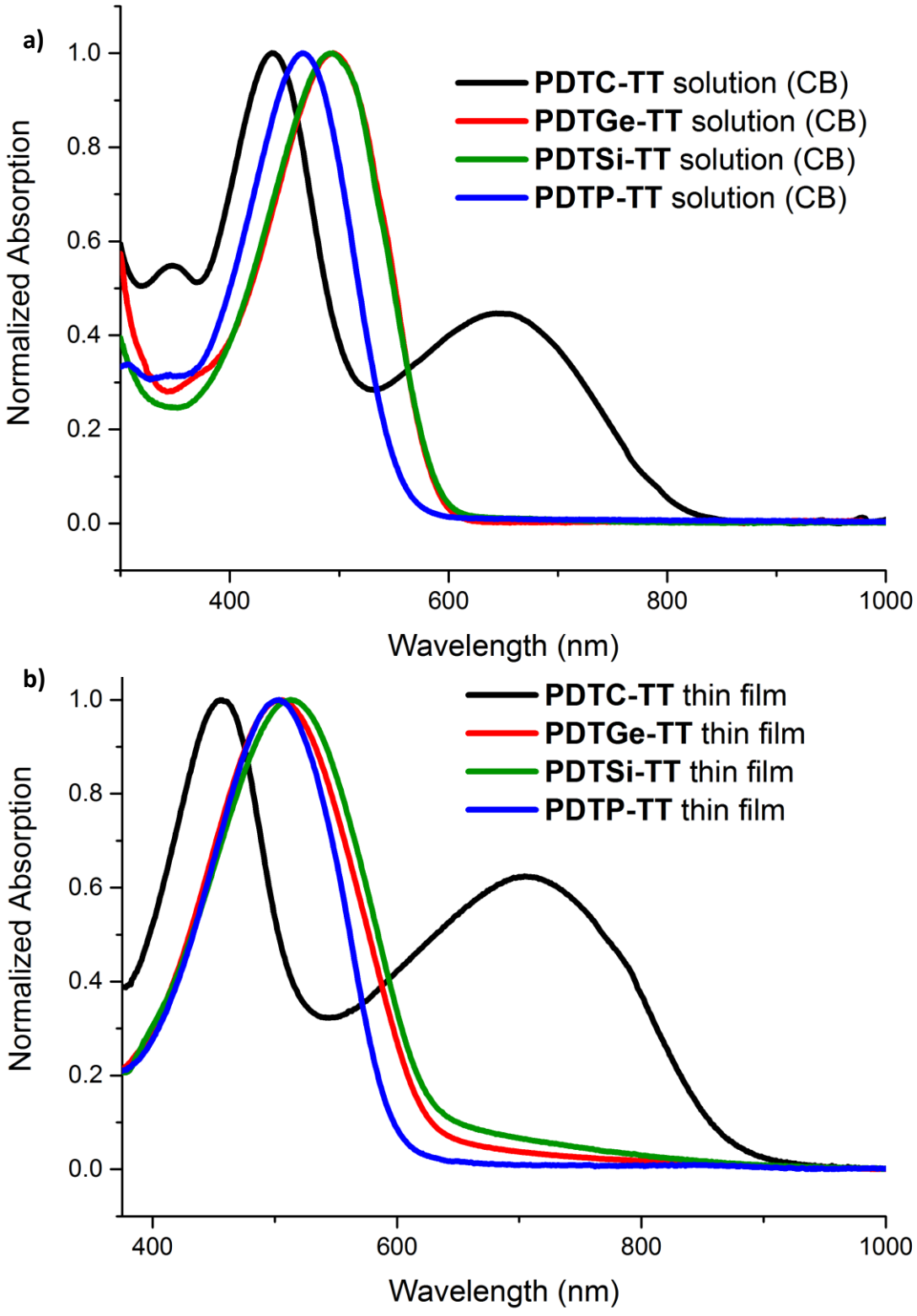



**Figure 4.11: UV-vis absorption spectra of dithienometallole-containing polymers (a) in chlorobenzene solutions, and (b) as thin films on glass slides**

The solution spectra for **PDTSi-TT** and **PDTGe-TT** are almost identical, with a single peak at 494 nm. In **PDTP-TT**, the $\lambda_{max}$ was blue-shifted to 466 nm, indicating a larger band gap, in

accordance with the predictions of the DFT calculations. The strongest **PDTC-TT** peak is blue-shifted even further than **PDTP-TT,** to 439 nm. However, there is a strong secondary peak at 704 nm, which is a typical indication of donor-acceptor behaviour occurring in dithienoketone-containing polymers, further corroborating the low band gap predicted by DFT as well as the highly localised LUMO. [34,35]

Examining the thin film spectra gives a similar picture to that of the solution phase. The $\lambda_{max}$ values of all four polymers red shift between solution and thin film, with **PDTP-TT** showing the largest shift (37 nm), putting the **PDTP-TT** $\lambda_{max}$ peak much closer to those of the **PDTSi-TT** and **PDTGe-TT** in thin films. This could be misinterpreted as an indication that the band gap had not increased as much as expected; however, when measuring the optical band gaps of the polymers from their onsets of absorption the values are much more in line with those predicted by DFT due to the narrower nature of the **PDTP-TT** peak. The thin film spectrum of **PDTC-TT** shows a small red shift in $\lambda_{max}$ of 16 nm, but a much larger shift in the secondary peak (60 nm). This causes an enhancement in the absorption profile of the polymer, such that it covers a broader range of the visible light spectrum. This is likely a consequence of increased π-π stacking of the polymer in the solid state.[34] Also of note is an increase in the relative intensity of the secondary peak when compared to $\lambda_{max}$ from 0.44:1 in solution to 0.62:1 as a thin film. In previously reported dithienoketone-containing polymers, similar increases in the intensity of secondary peaks at longer wavelengths have been attributed to increased interchain stacking in the solid state,[36] which is likely the cause here as well.

### *4.3.3 – Electronic properties*

The oxidative behaviour of all four polymers was studied by performing CV on thin films of the materials on FTO slides in 0.1 M $[Bu_4N][PF_6]$ acetonitrile solutions at a scan rate of 50 mV $s^{-1}$, with the voltammograms being shown in **Figure 4.12** and the measured HOMOs (referenced against ferrocene/ferrocenium, which we take to be 4.8 eV) and LUMOs (estimated by addition of the optical band gap to the HOMO) being listed in **Table 4.4**. In all cases the

oxidation peak was clearly observed, and appeared to be quasi-reversible. It can be seen that the polymers follow the general trends predicted by DFT, with **PDTP-TT** having the highest HOMO, followed by **PDTSi-TT** and **PDTGe-TT** in close succession, with **PDTC-TT** having a deeper HOMO.

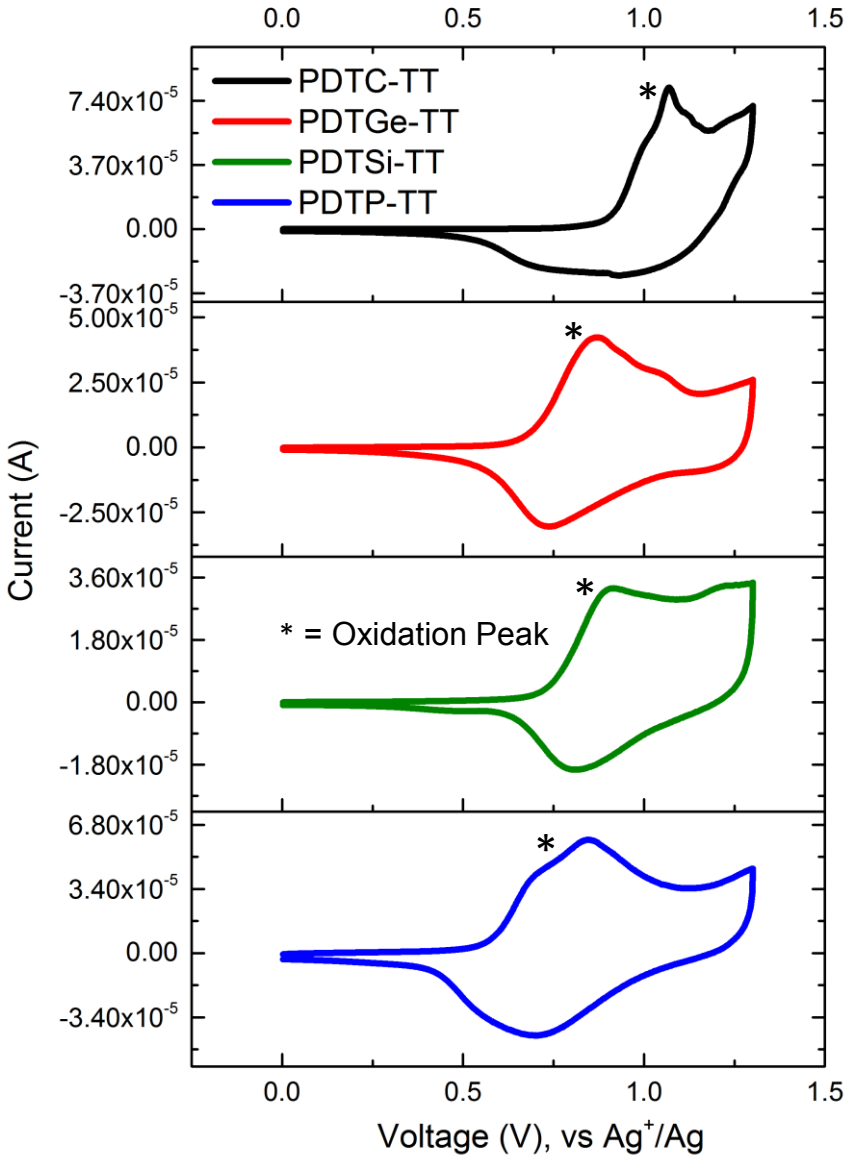



**Figure 4.12: Cyclic voltammograms showing the oxidation peaks of (from top to bottom) PDTC-TT, PDTGe-TT, PDTSi-TT, and PDTP-TT as thin films on FTO in 0.1 M $[Bu_4N][PF_6]$ acetonitrile solutions at a scan rate of 50 mV $s^{-1}$**

**Table 4.4: HOMOs and LUMOs of dithienometallole-containing polymers, with HOMOs measured from the onsets of the oxidation peaks and referenced against ferrocene/ferrocenium, and LUMOs estimated by addition of the optical band gaps**

| Polymer | HOMO (eV) | LUMO (eV) | Optical band gap (eV) |
|---|---|---|---|
| **PDTP-TT** | −4.98 | −2.89 | 2.09 |
| **PDTSi-TT** | −5.14 | −3.15 | 1.99 |
| **PDTGe-TT** | −5.08 | −3.12 | 1.96 |
| **PDTC-TT** | −5.31 | −3.87 | 1.44 |

### *4.3.4 – OFET performance*

The performances of the polymers in top gate, bottom contact field effect transistors were investigated. Devices were fabricated on glass substrates using Au (40 nm) source/drain electrodes that were treated with a pentafluorobenzene thiol (PFBT) self-assembled monolayer (SAM) to increase their work function. The polymeric active layer was spin-coated from chlorobenzene, and annealed at 160 °C for 0.5 h before the dielectric (Cytop™) was coated on top. The channel length was 40 μm, and the channel width was 1000 μm.

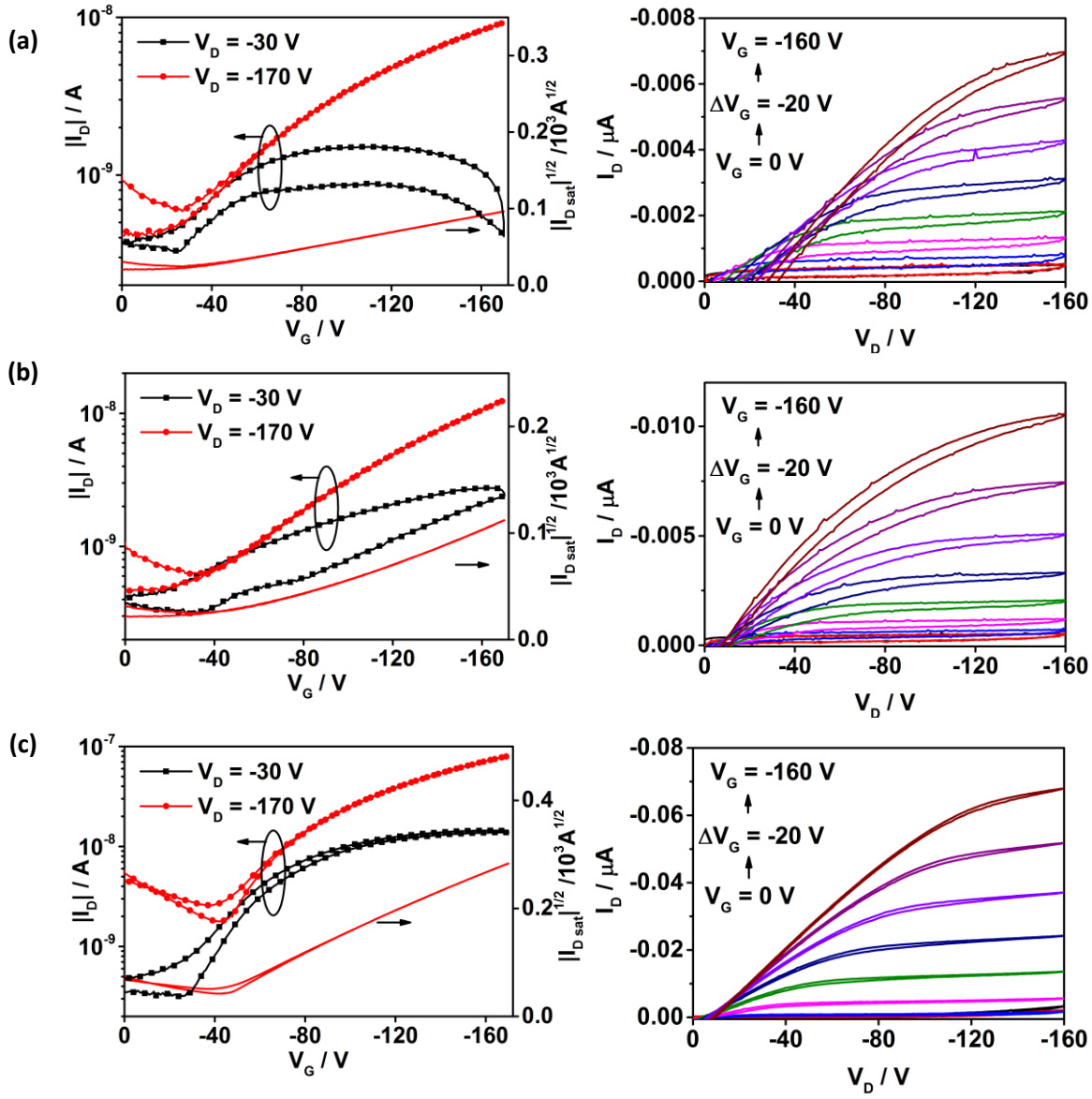



**Figure 4.13: Transfer (left) and output (right) characteristics of top gate, bottom contact OFET devices using (a) PDTSi-TT, (b) PDTGe-TT, and (c) PDTC-TT as the active layer**

**Table 4.5: OFET characteristics for polymers in top gate, bottom contact transistors**

| Polymer | $\mu_{sat\ (average)}$ ($cm^2V^{-1}s^{-1}$) | $\mu_{sat\ (maximum)}$ ($cm^2V^{-1}s^{-1}$) | $\mu_{lin\ (average)}$ ($cm^2V^{-1}s^{-1}$) | $V_{Th}$ (V) | $I_{on}/I_{off}$ |
|---|---|---|---|---|---|
| **PDTP-TT** | - | - | - | - | - |
| **PDTSi-TT** | $1.1\times10^{-5} \pm 1.9\times10^{-6}$ | $1.4\times10^{-5}$ | - | 7.4 ± 2.1 | $10–10^2$ |
| **PDTGe-TT** | $2.0\times10^{-5} \pm 9.3\times10^{-6}$ | $3.2\times10^{-5}$ | - | −51.5 ± 3.8 | $10–10^2$ |
| **PDTC-TT** | $1.6\times10^{-4} \pm 4.5\times10^{-5}$ | $2.0\times10^{-4}$ | $3.1\times10^{-4} \pm 2.1\times10^{-5}$ | −29.3 ± 2.1 | $10–10^2$ |

It is immediately apparent that the OFET performances of the polymers were poor – indeed, **PDTP-TT** did not produce any usable data at all, likely due to its low molecular weight causing dewetting of the material during spin coating. However, **PDTSi-TT**, **PDTGe-TT**, and **PDTC-TT** all showed p-type semiconducting behaviour, although the transistor devices did not exhibit ideal devices characteristics. In particular, it is apparent from the output characteristics that there was some gate leakage for **PDTSi-TT** and **PDTGe-TT**. In the linear regime there is also significant hysteresis observed in the output plots, again possibly relating to gate leakage or the presence of mobile ions in the dielectric layer, although more detailed studies of the OFET properties would be necessary to confirm this.[37]

Both **PDTSi-TT** and **PDTGe-TT** exhibited similar transistor performances, with similar saturated charge carrier mobilities. This is in accordance with previous reports of similar polymers, in which very similar FET data was observed.[9] It is also in agreement with the optoelectronic properties of both polymers. The only significant difference is in the threshold voltages observed in the devices. However, given the relatively poor device performance combined with the gate leakage observed, the reasons for this are unclear. In addition to this problem, the low source-drain currents of the germole- and silole-containing polymers were

below the amount of gate leakage, which meant they were too low to allow determination of their linear mobilities.

In contrast to this, the device performance of **PDTC-TT** was much better, with minimal hysteresis observed between forward and reverse sweeps and a well-defined linear regime. Some contact resistance could be observed in the output plots for these devices, most likely related to the low lying LUMO level of the polymer. The saturated mobility was an order of magnitude higher than those of the other polymers, with an average value of $1.6 \times 10^{-4}$ $cm^2$ $V^{-1}$ $s^{-1}$. Additionally, the source-drain current of this device was high enough to allow calculation of the linear mobility, which was $3.1 \times 10^{-4}$ $cm^2$ $V^{-1}$ $s^{-1}$. These results suggest that the PDTC co-monomer is the most promising of those investigated in terms of transistor properties.

### *4.4 – Conclusions*

In this chapter, a peripherally alkylated dithienopyrrole material was synthesised and polymerised with thienothiophene to yield **PDTP-TT**. The properties of this polymer were then compared with those of three analogous materials that contained different group 14/15 heteroatoms (Si, Ge, and C=O) as bridging groups in their dithienometallole ring systems in order to examine the effect of the heteroatom on the resulting polymers. Despite differences between the molecular weights of the materials, it was found that the optoelectronic properties of the polymers varied significantly according to the bridged group. These results could be rationalised with the help of DFT calculations. OFET devices of the four polymers were also investigated. All polymers exhibited relatively low charge carrier mobilities, but again differences were found depending on the heteroatom. Polymers that were more planar and had higher molecular weights outperformed more twisted, shorter-chained analogues. However, there were additional complications to these patterns that warrant further study, including whether **PDTP-TT** can work in OFETs with different device geometry and electrodes.

### *4.5 – Experimental*

General experimental details can be found in **Section 2.9**, as can the synthesis of compound **2.6**. **PDTSi-TT**, **PDTGe-TT**, and **PDTC-TT** were synthesised by Dr. Zhuping Fei via Stille polymerisation techniques similar to those detailed in previously published papers.[9,12]

#### *4.5.1 – Synthesis of 3,5-didodecyl-4N-hexyldithieno[3,2-*b*:2',3'-*d*]pyrrole (4.1)*

Over 5 min, hexylamine (0.2 ml, 1.53 mmol) was added dropwise to a stirring solution of 3,3'-dibromo-4,4'-didodecyl-2,2'-bithiophene (**2.6**) (0.922 g, 1.395 mmol), [$Pd_2dba_3$] (65 mg, 0.071 mmol), 2,2'-bis(diphenylphosphino)-1,1'-binaphthyl (0.176 g, 0.283 mmol), and sodium *t*-butoxide (0.649 g, 6.75 mmol) in degassed anhydrous toluene (20 ml). The resulting mixture was refluxed at 120 °C for 12 h in the absence of light. After completion, the reaction was quenched with water (5 ml) and the aqueous and organic layers separated. The aqueous layer was extracted with DCM (2 × 10 ml), and the combined organic layers were washed with water (3 × 5 ml). The resulting solution was dried over sodium sulfate and the solvent was removed in vacuo. The crude product was then purified by column chromatography over silica (eluent: DCM/hexane in a 1:6 ratio) to give 4,4'-bis(dodecyl)-N-(hexyl)-dithieno[3,2-*b*:2',3'-*d*]pyrrole (**4.1**) as a dark yellow oil (0.398 g, 0.663 mmol, 48%). $^1$H NMR (400 MHz, $CDCl_3$) δ 6.71 (s, 2H), 4.37 – 4.27 (m, 2H), 2.86 – 2.72 (m, 4H), 1.84 – 1.67 (m, 6H), 1.51 – 1.22 (m, 42H), 0.89 (t, *J* = 6.8 Hz, 9H). $^{13}$C NMR (101 MHz, $CDCl_3$) δ 142.88 (2C), 128.04 (2C), 118.30 (2C), 116.11 (2C), 46.30, 32.95, 32.08 (2C), 31.65, 30.16 (2C), 29.84 – 29.52 (overlapping peaks, 16C), 29.09, 26.53, 22.85 (2C), 22.73, 14.28 (2C), 14.11. HRMS ($ES^+$) calculated for $C_{38}H_{66}NS_2$ [M+H], 600.4637; found, 600.4642.

#### *4.5.2 – Synthesis of 2,6-dibromo-3,5-didodecyl-4N-hexyldithieno[3,2-*b*:2',3'-*d*]pyrrole (4.2)*

To a solution of 3,5-didodecyl-4N-hexyldithieno[3,2-*b*:2',3'-*d*]pyrrole (**4.1**, 117 mg, 0.195 mmol) in chloroform (2 ml) at 0 °C was added NBS (76 mg, 0.429 mmol), and the reaction was stirred for 2 h at 0 °C in the dark. The reaction was monitored by TLC, and on completion

quenched with saturated sodium sulfite (2 ml). The organic and aqueous layers were separated, with the latter being extracted with DCM (2 × 5 ml). The combined organic layers were washed twice with water (5 ml), dried over sodium sulfate and the solvent removed in vacuo. The crude product was purified by flash chromatography over silica (eluent: hexane, 5% triethylamine) to yield 2,6-dibromo-3,5-didodecyl-4N-hexyldithieno[3,2-*b*:2',3'-*d*]pyrrole (**4.2**, 124 mg, 0.164 mmol, 84%) as an unstable oil. The compound degraded rapidly at room temperature and was used as made. $^1$H NMR (400 MHz, $CDCl_3$) δ 4.29 – 4.16 (m, 2H), 2.82 – 2.75 (m, 4H), 1.77 – 1.68 (m, 2H), 1.68 – 1.58 (m, 4H), 1.50 – 1.21 (m, 42H), 0.88 (t, *J* = 6.8 Hz, 9H).

### *4.5.3 – 2,6-Bis(trimethylstannyl)-3,5-didodecyl-4N-hexyldithieno[3,2-b:2',3'-d]pyrrole (4.3)*

To a thoroughly degassed solution of 3,5-didodecyl-4N-hexyldithieno[3,2-*b*:2',3'-*d*]pyrrole (**4.1**, 1.24 g, 2.06 mmol) in anhydrous hexane (120 ml) at 0 °C was added TMEDA (0.93 ml, 6.17 mmol), followed by *n*-BuLi (2.5 M in hexane, 2.47 ml, 6.17 mmol) dropwise over 10 min. The reaction was stirred for 2 h at 0 °C, after which $Me_3SnCl$ (1 M in THF, 6.17 ml, 6.17 mmol) was added in one portion. After warming to room temperature overnight, the solution was washed twice with water (10 ml), once with acetonitrile (10 ml), and then the combined washings were extracted with hexane (2 × 20 ml). The combined organic layers were then concentrated under reduced pressure and purified by recycling preparative GPC (40 °C, hexane) to yield 2,6-bis(trimethylstannyl)-3,5-didodecyl-4N-hexyldithieno[3,2-*b*:2',3'-*d*]pyrrole (**4.3**) as a pale yellow oil (0.355 g, 0.384 mmol, 19%). $^1$H NMR (400 MHz, $CDCl_3$) δ 4.27 – 4.18 (m, 2H), 2.81 – 2.67 (m, 4H), 1.78 – 1.56 (m, 6H), 1.50 – 1.19 (m, 42H), 0.94 – 0.81 (m, 9H), 0.40 (s, 18H).

### *4.5.4 – Polymerizations of 3,5-didodecyl-4N-hexyldithieno[3,2-b:2',3'-d]pyrrole monomers with thieno[3,2-b]thiophene comonomers*

Polymerization of DTP with TT was carried out via three different techniques, as detailed below. Characterization of the polymer is provided after the third technique, and all data

included in this chapter (e.g., electrochemical data, UV spectroscopy) were obtained from the polymer sample yielded by the third polymerization (using stannylated DTP).

***Method A: Direct heteroarylation polymerization of 3,5-didodecyl-4N-hexyldithieno[3,2-b:2',3'-d]pyrrole with 2,5-dibromothieno[3,2-b]thiophene***

An oven-dried high-pressure microwave tube was charged with 3,5-didodecyl-4N-hexyldithieno[3,2-*b*:2',3'-*d*]pyrrole (**4.1**) (108.9 mg, 0.181 mmol), 2,5-dibromothieno[3,2-*b*]thiophene (54.0 mg, 0.181 mmol), $Pd(OAc)_2$ (1.4 mg, 0.007 mmol), and $K_2CO_3$ (34.0 mg, 0.246 mmol). The tube was sealed with a septum and flushed with Ar, after which degassed dimethylacetamide was added (3.5 ml). The mixture was thoroughly degassed with Ar, after which the inlet was removed. The reaction was heated at 110 °C for 48 h in the dark using an oil bath, then after cooling to room temperature the resulting polymer was poured into methanol and filtered into a Soxhlet thimble. Extraction of the polymer was attempted using methanol, acetone, hexane, and chloroform in that order; however, the material was found to be largely insoluble and a soluble fraction could not be obtained in any significant amount or characterized.

***Method B: Stille polymerization of 2,6-dibromo-3,5-didodecyl-4N-hexyldithieno[3,2-b:2',3'-d]pyrrole with 2,5-bis(trimethylstannyl)thieno[3,2-b]thiophene***

An oven-dried high-pressure microwave tube was charged with 2,6-dibromo-3,5-didodecyl-4N-hexyldithieno[3,2-*b*:2',3'-*d*]pyrrole (**4.2**) (113.9 mg, 0.150 mmol), 2,5-bis(trimethylstannyl)thieno[3,2-*b*]thiophene (70.0 mg, 0.150 mmol), $Pd_2dba_3$ (2.8 mg, 0.003 mmol), and tris(o-tolyl)phosphine (3.8 mg, 0.012 mmol). The tube was sealed with a septum and flushed with Ar, after which degassed chlorobenzene was added (3 ml). The mixture was thoroughly degassed with Ar, after which the inlet was removed. The vial was then placed in a microwave reactor and heated as follows: 5 min at 100 °C, 140 °C, and 160 °C, and 30 min at 200 °C. After cooling to room temperature, the resulting polymer was precipitated into methanol and filtered into a Soxhlet thimble. The polymer was extracted (Soxhlet) with methanol, acetone, hexane, and chloroform, in that order. The combined hexane and chloroform

fractions were concentrated under reduced pressure and the resulting polymer was dissolved in chlorobenzene, warmed to 50 °C and stirred in the presence of diethylammonium diethyldithiocarbamate (10 mg) for 1 h. The solution was concentrated in vacuo, dissolved in a minimal amount of chlorobenzene and the polymer collected by re-precipitation into methanol followed by vacuum filtration. After drying under vacuum, the polymer **PDTP-TT** was collected (57 mg, 49%). GPC (chlorobenzene): $M_n$ 7,600 g/mol, $M_w$ 13,100 g/mol, Đ 1.80. $^1$H NMR (500 MHz, TCE-$d_2$, 373 K) δ 7.62 – 7.22 (m, 2H), 4.43 (s, 2H), 3.11 (s, 3H), 2.99 – 2.79 (m, 1H), 1.98 – 1.70 (m, 6H), 1.59 – 1.30 (m, 42H), 1.02 – 0.91 (m, 9H). Anal. Calcd. For $C_{44}H_{65}NS_4$: C, 71.78; H, 8.90; N,1.90. Found C, 71.62; H, 8.96; N, 1.93.

***Method C: Stille polymerization of 2,6-bis(trimethylstannyl)-3,5-didodecyl-4N-hexyldithieno[3,2-b:2',3'-d]pyrrole with2,5-dibromothieno[3,2-b]thiophene***

An oven-dried high-pressure microwave tube was charged with 2,6-bis(trimethylstannyl)-3,5-didodecyl-4N-hexyldithieno[3,2-*b*:2',3'-*d*]pyrrole (**4.3**) (344.7 mg, 0.372 mmol), 2,5-dibromothieno[3,2-*b*]thiophene (111.0 mg, 0.372 mmol), $Pd_2dba_3$ (8.5 mg, 0.009 mmol), and triphenylarsine (22.9 mg, 0.074 mmol). The tube was sealed with a septum and flushed with Ar, after which degassed anhydrous THF was added (5 ml). The mixture was thoroughly degassed with Ar, after which the inlet was removed. The reaction was heated at 80 °C for 72 h in the dark using an oil bath, then after cooling to room temperature the resulting polymer was poured into methanol and filtered into a Soxhlet thimble. The polymer was extracted (Soxhlet) with methanol, acetone, hexane, and chloroform, in that order. The combined hexane and chloroform fractions were concentrated under reduced pressure and the resulting polymer was dissolved in chlorobenzene, warmed to 50 °C and stirred in the presence of diethylammonium diethyldithiocarbamate (10 mg) for 1 h. The solution was concentrated in vacuo, dissolved in a minimal amount of chlorobenzene and the polymer collected by re-precipitation into methanol followed by vacuum filtration. After drying under vacuum, the polymer **PDTP-TT** was collected (112 mg, 41%). GPC (chlorobenzene): $M_n$ 7,600 g/mol, $M_w$ 12,300 g/mol, Đ 1.62. $^1$H NMR (500 MHz, TCE-$d_2$, 373 K) δ 7.62 – 7.22 (m, 2H), 4.43 (s, 2H), 3.11 (s, 3H), 2.99 – 2.79 (m, 1H), 1.98 –

1.70 (m, 6H), 1.59 – 1.30 (m, 42H), 1.02 – 0.91 (m, 9H). Anal. Calcd. For $C_{44}H_{65}NS_4$: C, 71.78; H, 8.90; N, 1.90. Found: C, 71.59; H, 8.99; N, 1.95.

### *4.6 – References*


1. G. Zotti, G. Schiavon, A. Berlin, G. Fontana, and G. Pagani, *Macromolecules*, 1994, **27**, 1938–1942.

2. L. Liao, L. Dai, A. Smith, M. Durstock, J. Lu, J. Ding, and Y. Tao, *Macromolecules*, 2007, **40**, 9406–9412.

3. C. M. Amb, S. Chen, K. R. Graham, J. Subbiah, C. E. Small, F. So, and J. R. Reynolds, *J. Am. Chem. Soc.*, 2011, **133**, 10062–10065.

4. C. Taliani, R. Danieli, R. Zamboni, P. Ostoja, and W. Porzio, *Synth. Met.*, 1987, **18**, 177–182.

5. S. C. Rasmussen and S. J. Evenson, *Prog. Polym. Sci.*, 2013, **38**, 1773–1804.

6. M. E. Cinar and T. Ozturk, *Chem. Rev.*, 2015, **115**, 3036–3140.

7. A. Berlin, G. Pagani, G. Zotti, and G. Schiavon, *Die Makromol. Chemie*, 1992, **193**, 399–409.

8. Y. Zhang, J. Zou, H.-L. Yip, Y. Sun, J. A. Davies, K.-S. Chen, O. Acton, and A. K.-Y. Jen, *J. Mater. Chem.*, 2011, **21**, 3895.

9. Z. Fei, Y. Kim, J. Smith, E. B. Domingo, N. Stingelin, M. A. McLachlan, K. Song, T. D. Anthopoulos, and M. Heeney, *Macromolecules*, 2012, **45**, 735–742.

10. W. Pisula, H. N. Tsao, D. Dudenko, D. M. Cho, S. R. Puniredd, Y. Zhao, A. Mavrinskiy, J. Shu, M. R. Hansen, M. Baumgarten, and K. Müllen, *Polymers*, 2013, **5**, 833–846.

11. J. S. Kim, Z. Fei, D. T. James, M. Heeney, and J.-S. Kim, *J. Mater. Chem.*, 2012, **22**, 9975–9982.

12. Z. Fei, X. Gao, J. Smith, P. Pattanasattayavong, E. Buchaca Domingo, N. Stingelin, S. E. Watkins, T. D. Anthopoulos, R. J. Kline, and M. Heeney, *Chem. Mater.*, 2013, **25**, 59–68.

13. X. Wang, Y. Sun, S. Chen, X. Guo, M. Zhang, X. Li, Y. Li, and H. Wang, *Macromolecules*, 2012, **45**, 1208–1216.

14. D. Gedefaw, M. Tessarolo, W. Zhuang, R. Kroon, E. Wang, M. Bolognesi, M. Seri, M. Muccini, and M. R. Andersson, *Polym. Chem.*, 2014, **5**, 2083–2093.

15. T. Lei, Y. Cao, X. Zhou, Y. Peng, J. Bian, and J. Pei, *Chem. Mater.*, 2012, **24**, 1762–1770.

16. I. Meager, R. S. Ashraf, S. Rossbauer, H. Bronstein, J. E. Donaghey, J. Marshall, B. C. Schroeder, M. Heeney, T. D. Anthopoulos, and I. McCulloch, *Macromolecules*, 2013, **46**, 5961–5967.

17. L. G. Mercier and M. Leclerc, *Acc. Chem. Res.*, 2013, **46**, 1597–1605.

18. L.-C. Campeau and K. Fagnou, *Chem. Commun.*, 2006, 1253.

19. J. Kuwabara, T. Yasuda, S. J. Choi, W. Lu, K. Yamazaki, S. Kagaya, L. Han, and T. Kanbara, *Adv. Funct. Mater.*, 2014, **24**, 3226–3233.

20. D. J. Schipper and K. Fagnou, *Chem. Mater.*, 2011, **23**, 1594–1600.

21. S. Kowalski, S. Allard, and U. Scherf, *ACS Macro Lett.*, 2012, **1**, 465–468.

22. S. W. Chang, H. Waters, J. Kettle, Z. R. Kuo, C. H. Li, C. Y. Yu, and M. Horie, *Macromol. Rapid Commun.*, 2012, **33**, 1927–1932.

23. K. Okamoto, J. Zhang, J. B. Housekeeper, S. R. Marder, and C. K. Luscombe, *Macromolecules*, 2013, **46**, 8059–8078.

24. X. Hu, M. Shi, L. Zuo, Y. Nan, Y. Liu, L. Fu, and H. Chen, *Polymer*, 2011, **52**, 2559–2564.

25. E. Zhou, M. Nakamura, T. Nishizawa, Y. Zhang, Q. Wei, K. Tajima, C. Yang, and K. Hashimoto, *Macromolecules*, 2008, **41**, 8302–8305.

26. S. Zhang, Y. Guo, H. Fan, Y. Liu, H. Chen, G. Yang, X. Zhan, Y. Liu, Y. Li, and Y. Yang, *J. Polym. Sci. Part A Polym. Chem.*, 2009, **47**, 5498–5508.

27. V. Farina and B. Krishnan, *J. Am. Chem. Soc.*, 1991, **113**, 9585–9595.

28. S. Yamaguchi, Y. Itami, and K. Tamao, *Organometallics*, 1998, **17**, 4910–4916.

29. G. L. Gibson and D. S. Seferos, *Macromol. Chem. Phys.*, 2014, **215**, 811–823.

30. M. Moon, B. Walker, J. Lee, S. Y. Park, H. Ahn, T. Kim, T. H. Lee, J. Heo, J. H. Seo, T. J. Shin, J. Y. Kim, and C. Yang, *Adv. Energy Mater.*, 2015, **5**, 1402044.

31. S. Barlow, S. A. Odom, K. Lancaster, Y. A. Getmanenko, R. Mason, V. Coropceanu, J.-L. Brédas, and S. R. Marder, *J. Phys. Chem. B*, 2010, **114**, 14397–14407.

32. C. Hansch, A. Leo, and R. W. Taft, *Chem. Rev.*, 1991, 165–195.

33. X. Guo, M. Baumgarten, and K. Müllen, *Prog. Polym. Sci.*, 2013, **38**, 1832–1908.

34. K.-C. Li, Y.-C. Hsu, J.-T. Lin, C.-C. Yang, K.-H. Wei, and H.-C. Lin, *J. Polym. Sci. Part A Polym. Chem.*, 2009, **47**, 2073–2092.

35. C. Zhang, J. Sun, Q. Qiao, and J. Li, *Polymer*, 2014, **55**, 4677–4683.

36. W.-C. Yen, B. Pal, J.-S. Yang, Y.-C. Hung, S.-T. Lin, C.-Y. Chao, and W.-F. Su, *J. Polym. Sci. Part A Polym. Chem.*, 2009, **47**, 5044–5056.

37. M. Egginger, S. Bauer, R. Schwödiauer, H. Neugebauer, and N. S. Sariciftci, *Monatshefte für Chemie - Chem. Mon.*, 2009, **140**, 735–750.

# *Chapter 5*

# *Dithienopyrrole-Containing Molecules as Sensors*

### *5.1 – Introduction*

The field of chemical sensing currently makes use of a wide variety of technologies, including mass spectrometry,[1] electrical and electrochemical systems,[2–4] NMR spectroscopy,[5] fluorescence-based sensing,[6–8] and colorimetric methods,[9–11] amongst others.[12,13] Each of these techniques has both advantages and disadvantages associated with them – for example, mass spectrometry can allow highly accurate detection of analytes, but it requires bulky and expensive analytical equipment to perform as well as specialized staff capable of analysing the results. Whilst this is acceptable for certain applications, for others they can be unreasonable restrictions for any one of a number of reasons, for example in scenarios where results are required immediately or in real time, such as the detection of explosives in the field,[9] or where sensors need to be understood by laypersons, for example workplace monitoring of toxic gases.[14] In these cases, simple optical colorimetric sensors are often a better option, as they give rapid results, often have lower detection limits than alternatives, and an obvious colour change is much more difficult to misinterpret than most alternatives.[7,15,16]

The majority of fluorescence and colorimetric sensors have the same basic mechanism of action that enables them to function, in which an analyte recognition site is connected to a chromophore (or fluorophore) such that interaction with the substrate causes a change in the absorption and/or fluorescence spectra of the molecule.[17] There are a vast number of variations on this formula that allow different mechanisms of action, including intensity-based detection,[18] use of polarised light,[19] fluorescence lifetime-based sensing,[20] wavelength-shift sensing,[21] and two-band wavelength-ratiometric sensing,[22] amongst others. Each of these has advantages and disadvantages that can make them suitable or unsuitable for a given application.[6,23] Despite this variety, most organic sensors have a common basis, with the extent of the changes in the optical/fluorescence properties being dependent on three factors: the difference between its electronic structure before and after detection of the analyte, the nature of the interaction between the sensor and the substrate, and the electronic properties of the analyte.[24]

Another potential use for conjugated materials that are capable of changing their electronic state in the presence of specific materials is doping. Although there are no actual doping results in this chapter, rendering a detailed discussion of the different types of doping unnecessary, a dithienopyrrole-based polymer capable of being deprotonated by certain materials has been developed. As this material has strong potential for use in doping applications, a brief overview of n-doping in organic semiconductor follows.

The two major categories of doped organic semiconductors are the same as those observed in inorganic semiconductors – n-type and p-type. In n-type doping, the dopant adds electrons to the LUMO of the host material, leading to the production of negative charge carriers, while in p-doping the dopant removes electrons from the HOMO of the host, thereby creating holes. Although the field of organic electronics began with the discovery of the metallic conduction behaviour of polyacetylene doped with iodine,[25] the use of halide gases for doping has been found to result in unstable devices due to the high diffusion rates of the ions, and as such the vast majority of work since then has focussed on the use of undoped organic semiconductors.[26] However, molecular doping minimizes the effect of diffusion by using much larger materials as dopants, and as such has begun attracting attention due to its combination of the advantages of doping with increased device stability.

Doping of organic semiconductors has been shown to be capable of producing conductivity increases of several orders of magnitude, with the increased charge carrier density leading to a reduction in both losses and the fields required to drive currents, allowing operation of devices at lower voltages.[27] Additional benefits of doping include the fact that the conductivity can be tuned by controlling the amount of dopant used, giving a useful method of controlling OSC properties,[28,29] and the simplicity of the method, with dopants often able to be co-deposited with the host material, meaning there is no requirement for extra processing steps.[30,31]

This chapter describes the synthesis and method of action of a colorimetric base sensor based on the deprotonation of a pyrrolic nitrogen in a conjugated small molecule, as well as the

inclusion of this moiety in a conjugated polymer for potential doping applications. One of the advantages of positioning solubilising alkyl chains away from the bridging heteroatoms of conjugated materials is that it allows the inclusion of more interesting functional groups at the bridging site than simple alkyl chains. In **Chapter 4**, this was exploited by using a carbonyl group at the bridging site between two thiophene rings to give a cyclopenta[2,1-*b*:3,4-*b*′]dithiophen-4-one analogue, as previously reported by Fei and coworkers.[32] In this chapter, this same ability of peripheral alkyl chains to enable the use of more unusual groups at bridging sites was used to investigate the use of dithienopyrroles for detection of analytes via deprotonation.

### *5.2 – Attempted synthesis of NH-dithienopyrrole*

The original target molecule for the sensor material was 3,5-didodecyl-4NH-dithieno[3,2-*b*:2',3'-*d*]pyrrole (**5.2**). A number of different routes to this compound were investigated, with varying degrees of success. Initial work focussed on attempting direct synthesis of the end product via conversion of the dibromo-bithiophene (**2.6**) to the mono-azide, to be followed by thermally-induced ring closure. This route is shown in **Figure 5.1**.

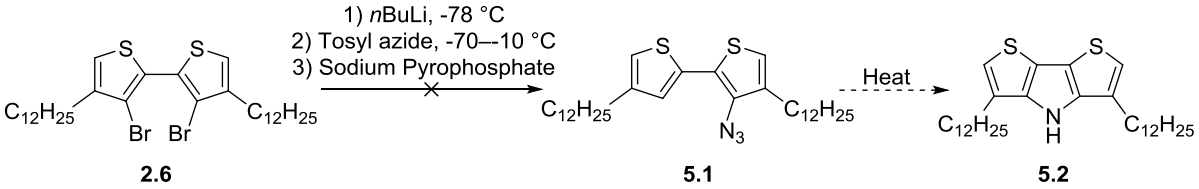



**Figure 5.1: Attempted synthesis of 3,5-didodecyl-4NH-dithieno[3,2-*b*:2',3'-*d*]pyrrole via the azide**

The attempted synthesis of the azide **5.1** was inspired by the work of Spagnolo et al., who prepared the non-alkylated analogue via lithiation of the mono-brominated bithiophene followed by reaction of the lithiated material with tosyl azide.[33] Although this article reported that they managed to obtain the product in a reasonable yield (72%), the synthesis of **5.1** was unsuccessful, likely due to degradation of the azide product during purification. Had the reaction been a success, the intention was to ring close via thermally-induced ring closure and

loss of nitrogen, which has been used by Smith and coworkers to produce carbazole and various analogues, as well as by Zanirato for the synthesis of a variety of dithienopyrrole isomers.[34,35] Unfortunately, the failure to synthesize **5.1** made it impossible to attempt this reaction.

Subsequent efforts focused on preparation of protected dithienopyrroles that could then be deprotected to yield the desired product. The first method attempted was an adaptation of the Buchwald-Hartwig ring closure used to synthesize 3,5-didodecyl-4N-hexyldithieno[3,2-*b*:2',3'-*d*]pyrrole discussed in **Chapter 4**, with $Pd_2dba_3$ as the catalyst and BINAP as a ligand in the presence of $Na^tBuO$ in anhydrous toluene. It was hoped that performing this ring closure with a tert-butoxycarbonyl (BOC)-protected amine would allow removal of this protecting group using acidic conditions, thereby yielding the deprotected product. The envisaged synthetic route is shown in **Figure 5.2**.

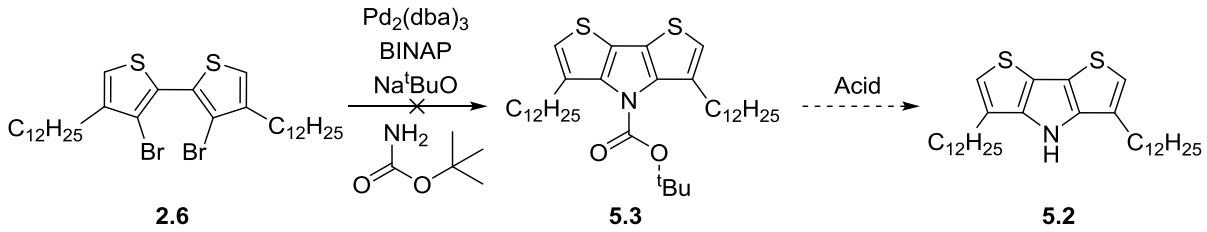



**Figure 5.2: Attempted synthesis of 3,5-didodecyl-4NH-dithieno[3,2-*b*:2',3'-*d*]pyrrole via the BOC-protected analogue**

Unfortunately, although the starting material was consumed in the reaction there was no final product produced, with the only identifiable product from the reaction being the secondary amine (3'-bromo-4,4'-didodecyl-*N*-(tert-butoxycarbonyl)-2,2'-bithiophene-3-amine). As a similar result was seen when attempting ring closure using 2-ethyl-1-hexylamine (see **Chapter 4**), it is believed that steric interference between the BOC group and the peripheral alkyl chains was responsible for the failure of this reaction.

### *5.2.1 – Synthesis of N-benzyldithienopyrroles*

In the light of the failure of the N-BOC reaction, it was decided that alternative amine-protecting groups should be investigated. In order to avoid the steric hindrance problems

encountered using N-BOC, the class of functional group chosen for study was the benzylamines, which can be removed using a variety of conditions.[36] Synthesis of the N-benzyl-protected dithienopyrroles was performed using the Buchwald-Hartwig coupling reaction described previously, using primary benzylamines under the reaction conditions shown in **Figure 5.3**. The two products of these reactions were 3,5-didodecyl-4N-benzyldithieno[3,2-*b*:2',3'-*d*]pyrrole (**5.4**) and 3,5-didodecyl-4N-(4-methoxy)-benzyl-dithieno[3,2-*b*:2',3'-*d*]pyrrole (**5.5**).

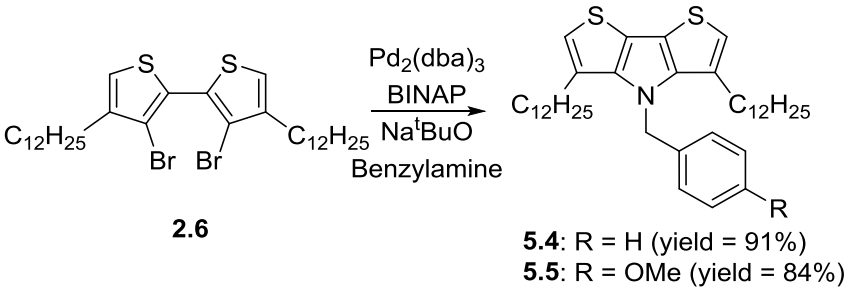



**Figure 5.3: Synthesis of 3,5-didodecyl-4N-benzyl-dithieno[3,2-*b*:2',3'-*d*]pyrroles via Buchwald-Hartwig coupling**

As before, both of these reactions used $Pd_2dba_3$ as a catalyst, BINAP as a ligand, and were performed in anhydrous toluene with $Na^tBuO$ as a base. After purification via column chromatography, the yield of **5.4** was 91% while that of **5.5** was 84%. In order to allow the use of the molecule for sensing applications, the next synthetic step attempted was removal of the protecting groups to leave the pyrrolic nitrogens as secondary amines, allowing deprotonation of the molecule in response to stimuli.

#### *5.2.1.1 – Attempted deprotection*

Two different deprotection reactions were investigated, with the first method considered being hydrogenolysis using palladium on carbon (Pd/C) and hydrogen gas, which is a common technique used for N-debenzylation.[36] However, exposing **5.4** to hydrogen gas in the presence of 10% Pd/C yielded no product, with the starting material being recovered in an almost quantitative yield. The most likely reason for this lack of reaction was poisoning of the catalyst, which is not uncommon for Pd catalysts in the presence of sulfur-containing systems such as thiophenes.[37,38]

The second method considered was based on the work of Haddach et al., who used potassium tert-butoxide ($K^tBuO$) in DMSO whilst bubbling $O_2$ through the reaction to perform N-debenzylation reactions on a wide variety of heterocycles, which included carbazole but no thiophene-based compounds.[39] Although the debenzylation appeared to work well on a test scale (<10 mg), attempts to replicate this early success with larger amounts of material proved largely unsuccessful, with the starting material being consumed but only around 20% of the product being observed by $^1H$ NMR. Changing the reaction conditions, for example by altering the temperature or using a stronger base such as potassium bis(trimethylsilyl) amide, had little to no positive impact on the yield. Furthermore, attempts to brominate the small amounts of product obtained failed due to degradation of the material, and as such the synthesis of **5.2** and its derivatives was abandoned in favour of the methodology discussed below.

### *5.3 – Coupling of N-benzyldithienopyrroles with bithiophene*

Due to the failure of the deprotection reactions and the functionalization of **5.2**, it was decided to couple the N-benzyldithienopyrroles with flanking aromatic rings in order to reduce the electron density of the dithienopyrrole system, in an attempt to improve the stability of the deprotected material. This approach had the additional advantage of removing the need to couple the dithienopyrrole after deprotection to increase light absorption in the visible spectrum. However, the vast majority of transition-metal catalysed coupling reactions require the use of functionalized materials to work: for example, Stille, Negishi, and Suzuki coupling involve cross-coupling of halogenated units with stannylated, organozinc, and borylated compounds, respectively. Fortunately, it is possible to form carbon-carbon bonds between halogenated aromatics and simple arenes using the coupling technique known as direct arylation.[40] The primary advantages of this technique revolve around avoidance of the pre-functionalization step, which often involves functionalizing simple arenes in low-yielding reactions using toxic metal compounds and results in the production of stoichiometric amounts of metal-containing waste during cross-coupling.[41] An additional advantage of avoiding pre-

functionalization is that it can enable chemists to synthesize cross-coupled compounds that are inaccessible via more traditional techniques due to the difficulty of attaching the required functional groups.[42] As such, direct heteroarylation was a technique that was of great interest to us for the extension of the dithienopyrrole ring system.

A number of different options were considered for the flanking groups, with several criteria requiring consideration before a decision could be made. In order to avoid the need to functionalize the ditheinopyrroles, it was necessary for the second substrate to take the form of a halogenated unit with a sufficiently labile C-X bond. Additionally, the flanking units had to alter the energy levels of the dithienopyrrole sufficiently to bring the absorption profile of the product into the visible region. Finally, the ideal candidate needed to have no particularly reactive C-H bonds that could compete with those of dithienopyrrole, as this would significantly lower the reaction yield. With these factors in mind, it was decided to investigate 5-bromo-5′-hexyl-2,2′-bithiophene (see **Figure 5.4**) as the flanking unit. The monobrominated nature of the material was expected to enable coupling to take place, with the hexyl group on the other end of the molecule preventing competition from the reactive C-H bond in the 5' position. Additionally, increasing the conjugation length by four thiophene rings (two on each side of the dithienopyrrole) was expected to substantially red shift the UV-visible spectrum of the material, which would be useful for colorimetric sensing applications.

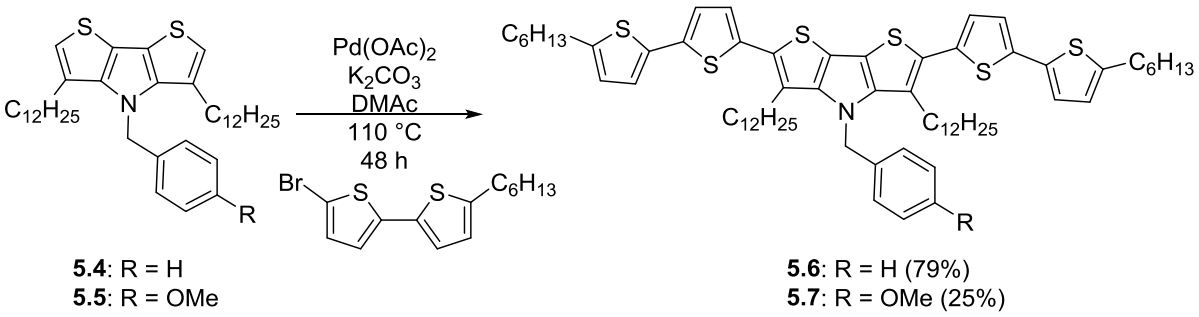



**Figure 5.4: Coupling of N-benzyl-dithienopyrroles (5.4/5.5) with 5-bromo-5′-hexyl-2,2′-bithiophene via direct arylation to yield 5.6 and 5.7**

Coupling of the N-benzyl-dithienopyrroles with 5-bromo-5′-hexyl-2,2′-bithiophene via direct arylation is shown in **Figure 5.4**. This involved the use of two equivalents of the

brominated flanking unit per dithienopyrrole, with the α C-H bonds of the dithienopyrrole being the most active in the reaction, resulting in the formation of new C-C bonds between the 2- and 6-positions of the dithienopyrrole and the 5-positions of the bithiophenes. Although there are a wide variety of different conditions used for direct arylations,[43,44] the use of the polar, aprotic solvent dimethylacetamide (DMAc) has been proven to be beneficial when using electron-rich thiophene systems,[45] and as such this solvent was selected for this reaction. Some conditions do not include the use of a base,[46,47] and their exact role in direct arylation is not fully known;[40] however, it has generally been found that the presence of a base helps to promote the reaction and neutralize the stoichiometric amounts of acid evolved (in this case, HBr).[48] One of the more common bases used is $K_2CO_3$, and as such this was employed here. Finally, $Pd(OAc)_2$ was used as the catalyst due to its proven success when used in reactions with similar conditions and substrates.[49] After heating to 110 °C for 48 h in the dark, the reactions were purified via column chromatography to yield the products as waxy orange solids in yields of 79% and 25% for **5.6** and **5.7**, respectively.

### *5.3.1 – Deprotection*

Having synthesized the extended dithienopyrroles, methods of removing the benzyl groups were investigated. Initially this focused on using the same technique that had been found to show some promise when used for the deprotection of **5.4**, including the use of K$^t$BuO in DMSO while bubbling oxygen through the solution. Unfortunately, this proved unsuccessful. During the exploration of the various options for removal of benzyl groups, the work of Knights and co-workers on the synthesis of carbazole-based dendrimers drew our attention.[50] In this paper, the group removed N-benzyl groups from second- and third-generation carbazole dendrons through exposure to aluminium chloride ($AlCl_3$) and anisole, yielding their secondary amines in yields over 50%.

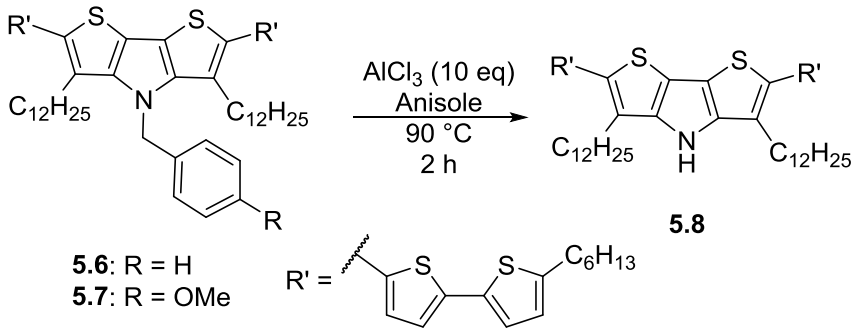



**Figure 5.5: Synthesis of 3,5-didodecyl-2,6-bis(5'-hexyl-2,2'-bithiophenyl)-4H-dithieno[3,2-*b*:2',3'-*d*]pyrrole from the benzylated analogues**

The application of a modified version of these reaction conditions to the extended N-benzyl-dithienopyrroles (as shown in **Figure 5.5**) was found to lead to deprotection in poor but not unacceptable yields of 20% and 45% when using **5.6** and **5.7** as starting materials, respectively. The product was purified by flushing it through a plug of basic alumina (eluent: hexane/ethyl acetate in a 93:7 ratio), then recrystallizing the resulting brown waxy material from THF and hexane to give the product as an orange solid. Comparing the NMR spectra of the starting materials and the product (**Figure 5.6**) clearly shows the loss of the benzylic and methoxy protons along with the appearance of a new peak at 10.63 ppm that is caused by the secondary amine, giving a clear indication that the reaction was a success. In addition, there was a slight red shift in the UV-vis absorption spectrum of the product compared to the starting material, with $\lambda_{max}$ shifting from 416 nm to 424 nm.

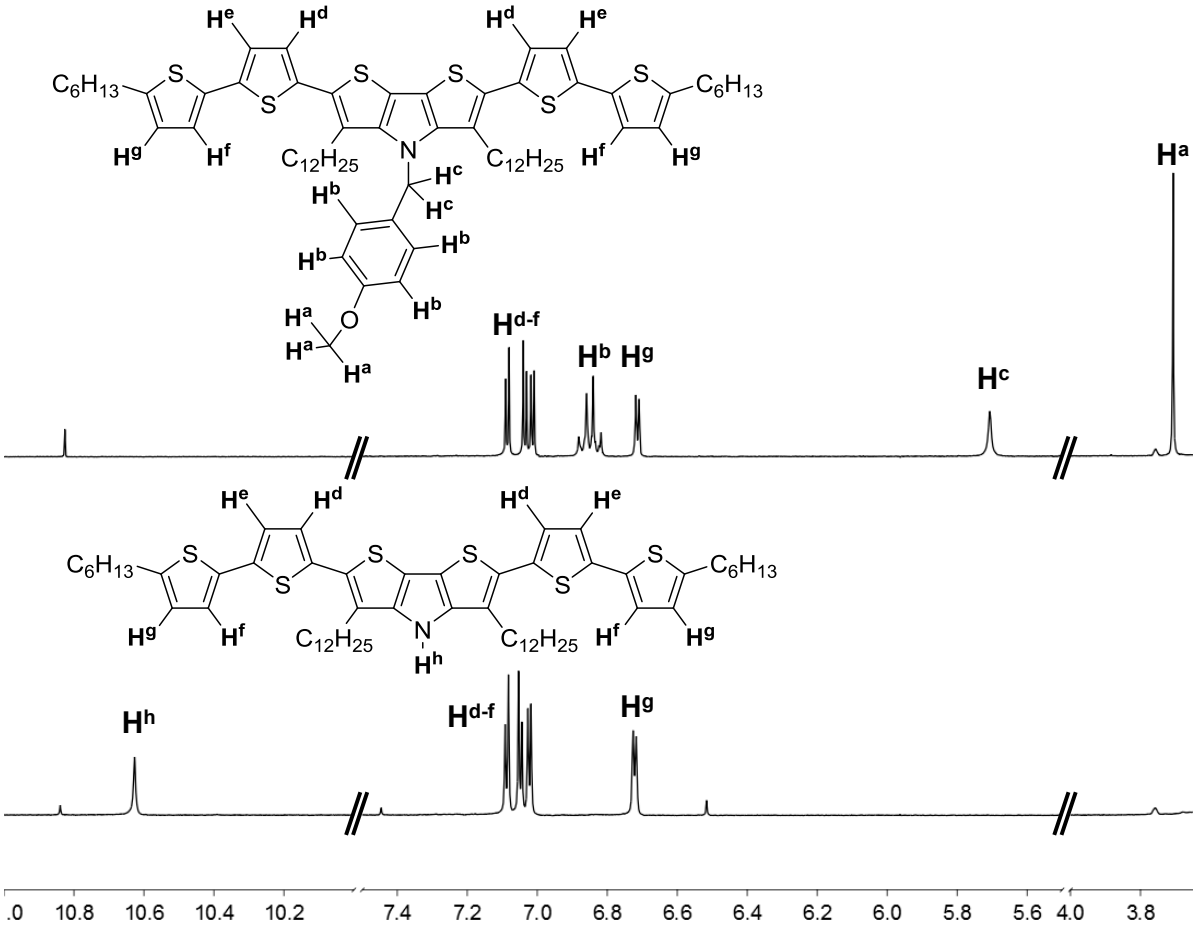



**Figure 5.6: Comparison of the $^1$H NMR spectra of 5.7 (top) and 5.8 (bottom) in THF-$d_8$ between 3.65–4.0, 5.5–7.5, and 10–11 ppm**

### *5.4 – Screening potential analytes*

With the deprotected material in hand, we began screening for potential materials that would interact with the secondary amine and cause a colour change, which would enable colorimetric detection of the analyte. Given the secondary amine functionality of **5.8**, it was decided to investigate common materials that had the potential to interact with this group. The chemicals used for the screening were 1,8-diazabicycloundec-7-ene (DBU, a non-nucleophilic base), trifluoroacetic acid (TFA, an organic acid), and TBAF (an organic base). The structures of these compounds and their impact on the absorption spectrum of **5.8** can be seen in **Figures 5.7a** and **b**, respectively.

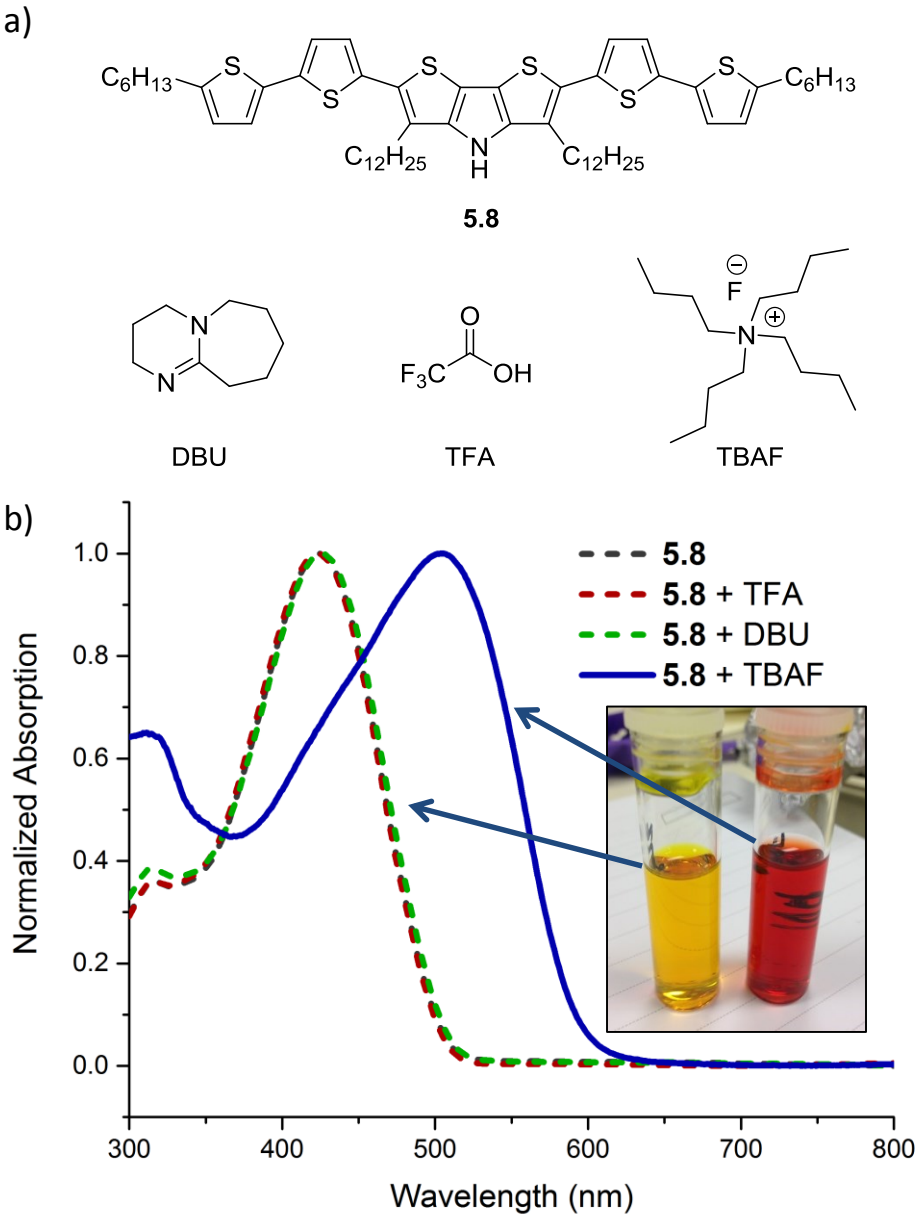



**Figure 5.7: (a) Structures of (clockwise from top) 3,5-didodecyl-2,6-bis(5'-hexyl-2,2'-bithiophen-5-yl)-4H-bisthieno[3,2-*b*:2',3'-*d*]pyrrole (5.8), TBAF, TFA, and DBU. (b) Normalized UV-vis absorption spectra of solutions of 5.8 with excesses of the three analytes in THF; inset – image of vials containing solutions of 5.8 (left) and 5.8 and TBAF (right)**

It can clearly be seen that the addition of TFA and DBU to **5.8** had no impact on its absorption spectrum, with $\lambda_{max}$ of all three being approximately 425 nm. However, it can be seen that addition of the organic base TBAF had a substantial impact, with $\lambda_{max}$ red shifting by over 80 nm to 506 nm. As a control experiment, the same tests were carried out using the benzylated analogue of the sensor (**5.6**), with the results showing no change in the absorption spectrum with any of the analytes.

### *5.5 – Method of action*

It was considered that the most likely reason for the change in colour of **5.8** on exposure to TBAF was deprotonation of the secondary amine by the analyte, similar to its action in assisting the N9-alkylation of purines and methylation of nucleobases via deprotonation of NH groups.[51,52] As evidence of this, the $^{1}$H NMR spectra of **5.8** before and after addition of TBAF are compared in **Figure 5.8**, along with the proposed reaction equilibrium in **Equation 5.1**.

$$\mathbf{5.8}(\mathrm{NH}) + \mathrm{F^-} \rightleftharpoons \mathbf{5.8}(\mathrm{N^-}) + \mathrm{HF} \qquad \textbf{Equation 5.1}$$

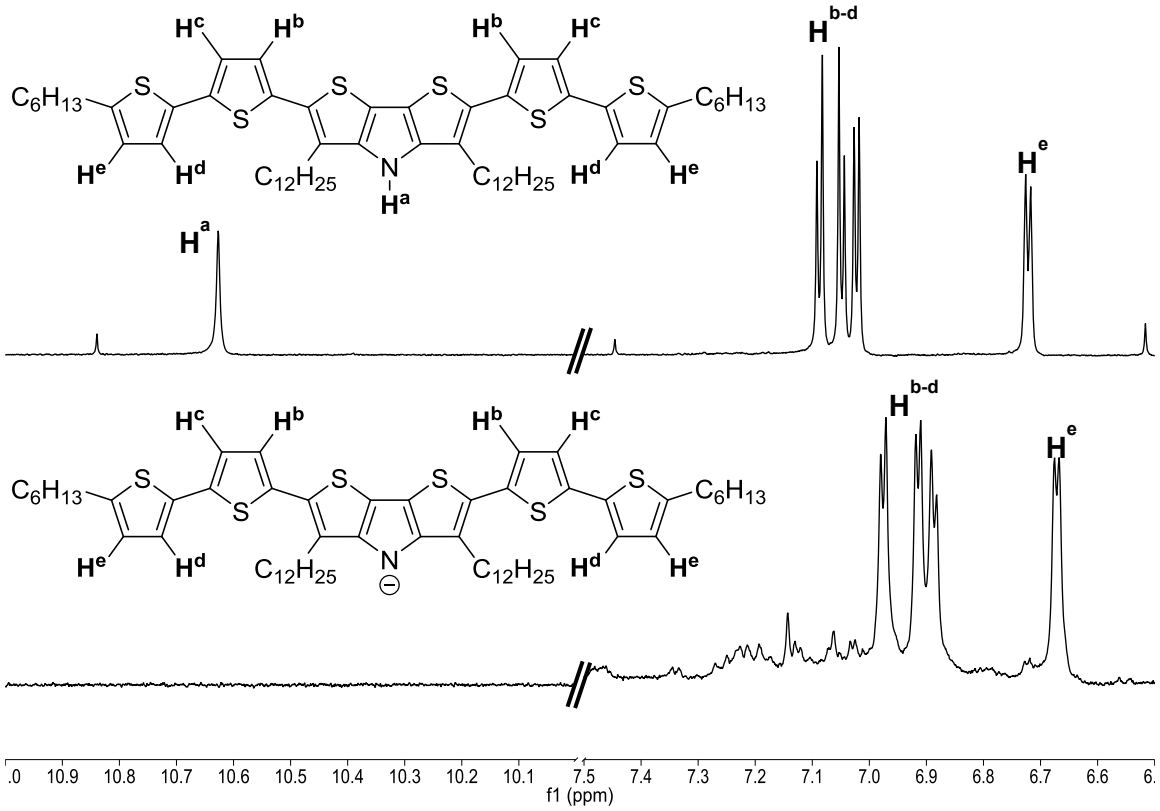



**Figure 5.8 – Comparison of the $^{1}$H NMR spectra of 5.8 in THF-$d_8$ before (top) and after addition of excess TBAF (bottom) between 6.5–7.5 and 10–11 ppm**

As can be seen, the addition of excess TBAF resulted in complete loss of the peak at 10.63 ppm, corresponding to the pyrrolic proton. In addition, the aromatic protons shifted upfield by between 0.05 and 0.15 ppm on deprotonation, likely due to the additional shielding conferred by the negative charge on the molecule. Although it would be expected that there would be a downfield shift in the signal of the α-protons on the dodecyl chains, these peaks

were obscured by one of the TBAF signals, meaning that this shift could not be verified, and so the figure focusses purely on the aromatic region.

Obtaining further evidence for the proposed method of action required examination of the UV-visible absorption spectra of a solution of **5.8** in THF as the concentration of TBAF was changed for the presence of an isosbestic point. These occur when the molar absorption coefficients of two chromophores are equal at a given wavelength, meaning that when using a set concentration of substrate (**5.8**), the absorbance at this wavelength should be identical at any point in the reaction equilibrium. Isosbestic points are common in reactions in which only a single reactant and product are observable in the region of interest, as would be expected for the hypothesized deprotonation reaction. Thus, the presence of an isosbestic point would be strong evidence that the colour change observed was a result of deprotonation of **5.8** to yield **5.8**($N^-$).

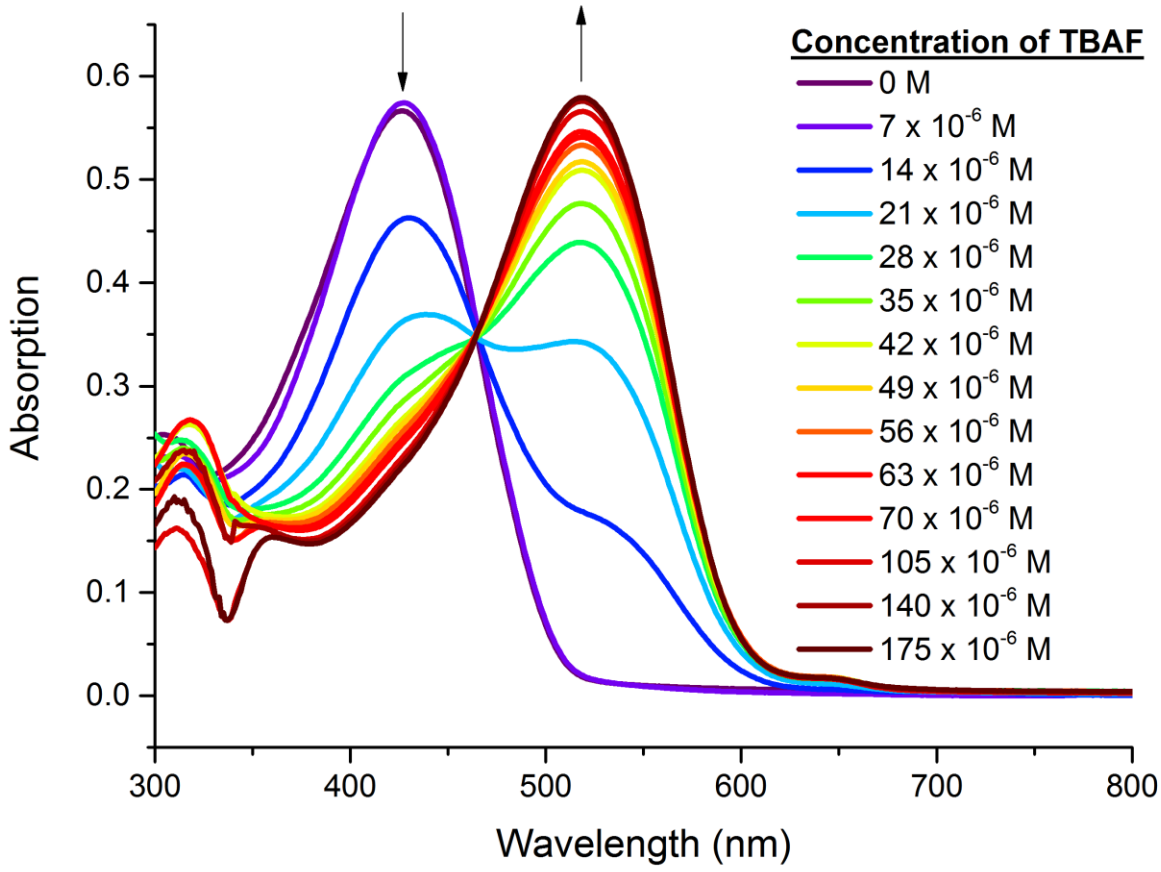



**Figure 5.9: Absorption spectra of 11.6 µM solutions of 5.8 in THF as the concentration of TBAF was increased from 0 to 1.75 × $10^{-4}$ M (all spectra measured at 25 °C)**

Monitoring the absorption of an 11.6 µM solution of **5.8** in anhydrous THF as the concentration of TBAF was increased from 0 to 175 µM resulted in **Figure 5.9**. The concentration of TBAF in the solution was first increased by increments of 7 µM between 0 and 70 µM, then by 35 µM between 70 and 175 µM. As the concentration of TBAF was increased, the intensity of the peak at 424 nm decreased, indicating a reduction in the amount of **5.8** in the solution. At the same time, the peak at 518 nm increased in intensity as a result of formation of the deprotonated species **5.8**($N^-$). As expected, an isosbestic point can be seen at 464 nm, providing evidence of a linear relationship between the stoichiometry of the reactant and the product. Furthermore, the reaction could be reversed by the addition of water to the system – indeed, if left undisturbed and open to air solutions of **5.8**($N^-$) returned to their original colour, likely due to diffusion of water into the solvent.

The results described to this point provide a good indication that the colour change is the result of deprotonation of **5.8**(NH) to give **5.8**($N^-$), as shown in **Equation 5.1**. It should therefore be possible to determine the concentration of **5.8**($N^-$) in an unknown sample by applying the Beer-Lambert law:

$$c = \frac{A}{\varepsilon l} \qquad \textbf{Equation 5.2}$$

Where $c$ is the concentration of the molecule of interest, $A$ is the absorbance at a given wavelength, $\varepsilon$ is the attenuation coefficient, and $l$ is the path length. However, using this equation first requires determination of the molar extinction coefficient of the product at its $\lambda_{max}$. This can be obtained by measuring the change in absorbance at the $\lambda_{max}$ of the material of interest as a solution is diluted to various known concentrations. Using this technique, the $\varepsilon_{max}$ of **5.8** was found to be 55301 $M^{-1}$ $cm^{-1}$, while that of the deprotonated product was 57189 $M^{-1}$ $cm^{-1}$. Unfortunately, these values (especially the latter) have a slight degree of error due to the nature of deprotonation reactions as equilibria, which means that driving the reaction towards complete deprotonation can be difficult. However, the equilibrium of the reaction was pushed as far as possible towards the product by using a substantial excess of TBAF and anhydrous solvent.

### *5.5.1 – Calculation of dissociation constant*

Utilizing $\varepsilon_{max}$ for the deprotonated product in **Equation 5.2** allowed the absorbance at $\lambda_{max}$ of the deprotonated product to be used to calculate the dissociation constant ($K_d$) of **5.8** as follows. The reaction equilibrium shown in **Equation 5.1** has an equilibrium constant, K:

$$\textbf{5.8}NH + F^- \overset{K}{\rightleftharpoons} \textbf{5.8}N^- + HF \qquad \textbf{Equation 5.3}$$

This equilibrium can be broken into two separate equilibria, each of which has its own equilibrium constant: the dissociation constant of **5.8**NH ($K_d$) and the association constant of $F^-$ ($K_a$).

$$\mathbf{5.8}(NH) \overset{K_d}{\rightleftharpoons} \mathbf{5.8}(N^-) + H^+ \qquad \textbf{Equation 5.4}$$

$$H^+ + F^- \overset{K_a}{\rightleftharpoons} HF \qquad \textbf{Equation 5.5}$$

$$K = K_d \times K_a \qquad \textbf{Equation 5.6}$$

Each of the equilibrium constants can be calculated using the following formula:

$$K_i = \frac{\Pi(Mole\ fractions\ of\ products)}{\Pi(Mole\ fractions\ of\ reactants)}$$

Such that when $x_i$ is the mole fraction of a component:

$$K_d = \frac{x_{\mathbf{5.8}N^-} \cdot x_{H^+}}{x_{\mathbf{5.8}NH}} \qquad \textbf{Equation 5.7}$$

$$K_a = \frac{x_{HF}}{x_{H^+} \cdot x_{F^-}} \qquad \textbf{Equation 5.8}$$

$$K = \frac{x_{\mathbf{5.8}N^-} \cdot x_{HF} \cdot x_{H^+}}{x_{\mathbf{5.8}NH} \cdot x_{F^-} \cdot x_{H^+}} = \frac{x_{\mathbf{5.8}N^-} \cdot x_{HF}}{x_{\mathbf{5.8}NH} \cdot x_{F^-}} \qquad \textbf{Equation 5.9}$$

If we assume that there are no moles of HF in the reaction except those that have been formed via reaction with **5.8**NH, and that $x_{5.8NH}$ and $x_{F^-}$ can be approximated by subtracting the moles of **5.8**($N^-$) formed from the total numbers of moles of **5.8** and TBAF added to the solution, respectively, then **Equation 5.9** can be converted to:

$$K = \frac{(x_{\mathbf{5.8}N^-})^2}{\left(\frac{\left(M_{\mathbf{5.8}(total)} - M_{\mathbf{5.8}N^-}\right)}{M_{total}} \times \frac{(M_{TBAF} - M_{\mathbf{5.8}N^-})}{M_{total}}\right)}$$ **Equation 5.10**

Where $M_i$ is the number of moles of a component. As mole fractions can be calculated by multiplying the concentration of a component by the volume of the solution and then dividing by the total number of moles, this means that K can be calculated by:

$$K = \frac{\left(\frac{[\mathbf{5.8}N^-] \cdot V}{M_{total}}\right)^2}{\left(\frac{\left(M_{\mathbf{5.8}(total)} - ([\mathbf{5.8}N^-] \cdot V)\right)}{M_{total}} \times \frac{(M_{TBAF} - ([\mathbf{5.8}N^-] \cdot V))}{M_{total}}\right)}$$ **Equation 5.11**

$$= \frac{\left(\frac{\left(\frac{A_{\lambda_{max}}}{\varepsilon_{\mathbf{5.8}N^-} \cdot l} \cdot V\right)}{M_{total}}\right)^2}{\left(\frac{\left(M_{\mathbf{5.8}(total)} - \left(\frac{A_{\lambda_{max}}}{\varepsilon_{\mathbf{5.8}N^-} \cdot l} \cdot V\right)\right)}{M_{total}} \times \frac{\left(M_{TBAF} - \left(\frac{A_{\lambda_{max}}}{\varepsilon_{\mathbf{5.8}N^-} \cdot l} \cdot V\right)\right)}{M_{total}}\right)}$$ **Equation 5.12**

All the parameters in **Equation 5.12** are known or can be calculated: $A_{\lambda max}$ is given by the UV-Vis spectrum, $\varepsilon_{5.8N^-}$ is the attenuation coefficient of the deprotonation product (57189 $M^{-1}$ $cm^{-1}$), $l$ is the path length (1 cm), $V$ is the volume of the cuvette (3 ml), $M_{total}$ is the total number of moles in the solution (reactants + products + solvent), $M_{5.8(total)}$ is the total number of moles of **5.8** in the solution, and $M_{TBAF}$ is the total number of moles of TBAF in the solution. By inserting these into the equation, it is possible to obtain a value for $K$. **Table 5.1** lists the values of $K$ obtained using the data shown in **Figure 5.9**.

**Table 5.1: Calculation of *K* from data used to produce Figure 5.9**

| $A_{\lambda max}$ | $M_{5.8N^-}$ | $M_{5.8(total)}$ | $M_{TBAF}$ | $M_{total}$ | $K$ |
|---|---|---|---|---|---|
| 0.4768 | $2.50\times10^{-8}$ | $1.16\times10^{-5}$ | $1.67\times10^{-4}$ | $3.70\times10^{-2}$ | $1.35\times10^{-1}$ |
| 0.5090 | $2.67\times10^{-8}$ | $1.16\times10^{-5}$ | $2.00\times10^{-4}$ | $3.70\times10^{-2}$ | $1.54\times10^{-1}$ |
| 0.5171 | $2.71\times10^{-8}$ | $1.16\times10^{-5}$ | $2.33\times10^{-4}$ | $3.70\times10^{-2}$ | $1.43\times10^{-1}$ |
| 0.5331 | $2.80\times10^{-8}$ | $1.16\times10^{-5}$ | $2.66\times10^{-4}$ | $3.70\times10^{-2}$ | $1.48\times10^{-1}$ |
| 0.5409 | $2.84\times10^{-8}$ | $1.16\times10^{-5}$ | $3.00\times10^{-4}$ | $3.70\times10^{-2}$ | $1.44\times10^{-1}$ |
| 0.5464 | $2.87\times10^{-8}$ | $1.16\times10^{-5}$ | $3.33\times10^{-4}$ | $3.70\times10^{-2}$ | $1.38\times10^{-1}$ |
| 0.5658 | $2.97\times10^{-8}$ | $1.16\times10^{-5}$ | $5.00\times10^{-4}$ | $3.70\times10^{-2}$ | $1.17\times10^{-1}$ |
| 0.5758 | $3.02\times10^{-8}$ | $1.16\times10^{-5}$ | $6.66\times10^{-4}$ | $3.70\times10^{-2}$ | $1.01\times10^{-1}$ |
| 0.5792 | $3.04\times10^{-8}$ | $1.16\times10^{-5}$ | $8.33\times10^{-4}$ | $3.70\times10^{-2}$ | $8.47\times10^{-2}$ |

The values of $K$ were calculated to be approximately 0.1, with the average of the values listed being 0.129. Returning to **Equation 5.5**, we can approximate the $K_a$ of HF in THF with the inverse of its acidity constant ($K_A$) in DMSO, which gives $1\times10^{15}$. This provides the following:

$$0.129 = K_d \times (1 \times 10^{15})$$

$$K_d = \frac{0.129}{1 \times 10^{15}}$$

$$K_d = 1.29 \times 10^{-16}$$

As $K_d$ of this equilibrium (its dissociation constant) is equal to the $K_A$ of **5.8,** using p$K_A$ = −log($K_A$) gives an approximate p$K_A$ for the pyrrolic proton in compound **5.8** of 15.9. Comparing this to the p$K_A$s of other pyrrolic protons (in DMSO), pyrrole has a p$K_A$ of 23.0, with the value decreasing on both extension of the ring system (e.g., indole = 20.95, carbazole = 17.09) and inclusion of other heteroatoms (e.g., triazole = 13.9).[53–55] Thus, it can be seen that this is a reasonable value due to the nature of the dithienopyrrole unit in combination with the extended π-conjugation conferred by the flanking bithiophene moieties.

Although there are several sources of inaccuracy in this calculation, beginning with the fact that the p$K_A$ of HF used is for solutions in DMSO rather than THF in addition to the non-ideality of the system, having an approximate value for the p$K_A$ of the pyrrolic proton provides a way of

explaining the behaviour of the sensor. For example, the p$K_A$ of the protonated form of DBU, the non-nucleophilic base that did not induce any change in the absorption spectrum of **5.8** (**Figure 5.7**), is estimated to be ~12 (in DMSO).[56] This means that DBU was not a strong enough base to deprotonate **5.8**, explaining why there was no colour change in this system. It can also help to explain why **5.8**($N^-$) is re-protonated when water is added to solutions deprotonated with TBAF. It is known that solvation of $F^-$ ions with polar protic solvents leads to a drastic decline in their basicity,[57–59] so it is likely that addition of water to the solution hydrates the TBAF, reducing its basicity and rendering it no longer capable of deprotonating **5.8**.

### *5.6 – Effects of varying analyte structure*

Having satisfactorily determined the method of action of the sensor, it was decided to investigate the effect of varying the analyte structure on the absorption spectrum of the material to determine whether the sensor could be used to identify materials colorimetrically.

#### *5.6.1 – Anion variation*

The first variation of the sensor system investigated involved changing the anion in the tetrabutylammonium salt to provide further evidence that the estimated p$K_A$ of **5.8** was plausible. Four 9.0 × $10^{-6}$ M solutions of **5.8** in THF were each exposed to one equivalent of a tetrabutylammonium salt (TBAF, TBABr, TBACl, or TBAOH) and their responses were monitored using UV-vis spectroscopy, as shown in **Figure 5.10**.

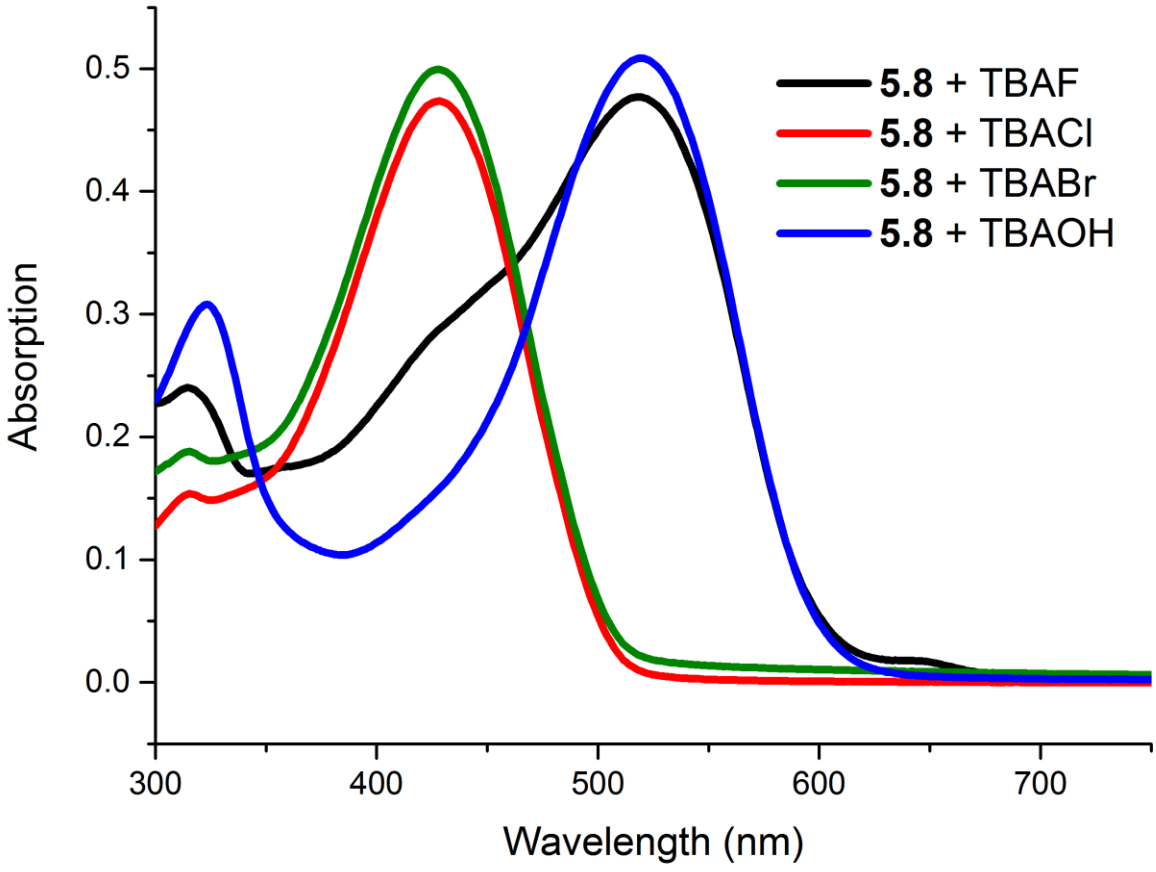



**Figure 5.10: UV-vis spectra of 9.0 × $10^{-6}$ M solutions of 5.8 in THF in the presence of one equivalent of various tetrabutylammonium salts**

It can be seen that changing the anion, which acted as the base in the deprotonation reaction, had a substantial impact on the amount of **5.8**($N^-$) formed but caused no measurable changes in the position of $\lambda_{max}$. These results directly agree with what would be expected from the findings above – as chloride and bromide ions are weaker bases than fluoride, with the p$K_A$s of HCl and HBr in DMSO being 1.8 and 0.9, respectively, they were unable to remove the pyrrolic proton from **5.8**.[53] On the other hand, $H_2O$ has a p$K_A$ of 32 in DMSO, making hydroxide a much stronger base than fluoride and thus explaining the increase in the amount of **5.8**($N^-$) formed in the presence of TBAOH.[53] Furthermore, there was no change in $\lambda_{max}$ as the anion was changed, which would be expected as the anion should not interact with the deprotonated species.

### *5.6.2 – Cation variation*

Having established that changing the anion influenced the extent of deprotonation but did not change the position of $\lambda_{max}$, the effect of altering the cation was then investigated. Solutions

of **5.8** in THF ($2.4 \times 10^{-6}$ M) were exposed to $1 \times 10^{-3}$ M of tetraalkylammonium hydroxides (TAAOHs) with alkyl chains between 2 and 10 carbon atoms in length. **Figure 5.11** shows the variation in $\lambda_{max}$ as the number of carbons increased.

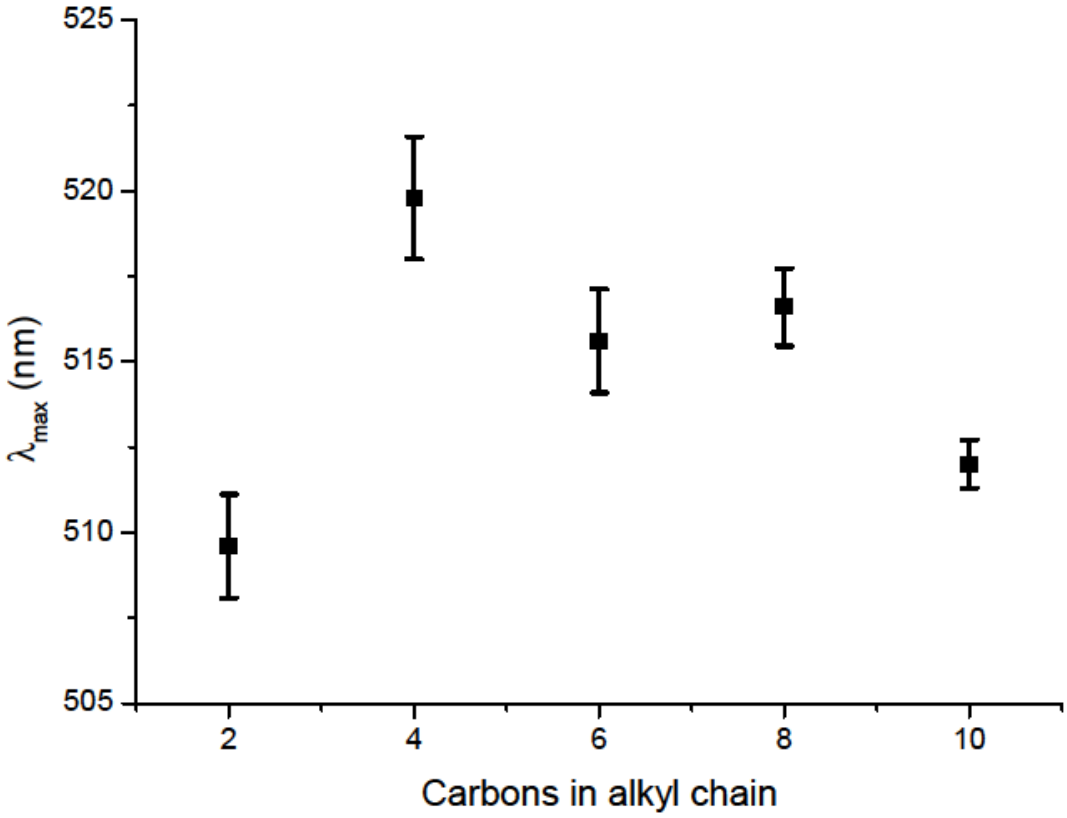



**Figure 5.11: $\lambda_{max}$ of UV-vis spectra of $2.4 \times 10^{-6}$ M solutions of 5.8 in THF after exposure to $1 \times 10^{-3}$ M of tetraalkylammonium hydroxides with between 2 and 10 carbons in their alkyl chains. Squares mark the averages of five measurements, while the error bars represent one standard deviation**

It can be seen that the number of carbons in the alkyl chains of the TAAOHs affected the position of $\lambda_{max}$, with the lowest value (and thus smallest red shift from the $\lambda_{max}$ of **5.8**(NH)) being observed with tetraethylammonium hydroxide, whilst the highest $\lambda_{max}$ was for tetrabutylammonium hydroxide, followed by a decrease with increasing chain length. This pattern can be explained by considering the twin effects of electrostatic interactions between the ions and the solvation of the TAA cation. The short alkyl chains on the tetraethylammonium cation make it the most charge-dense of the five materials investigated. This means that it is the

most strongly attracted to the negative charge on **5.8**($N^-$), allowing it to withdraw some electron density from the sensor molecule ring system and thus giving a smaller $\lambda_{max}$. On the other hand, the butyl chains on tetrabutylammonium effectively screen the charge on the cation, preventing it from fully interacting with the anion and thus giving a larger $\lambda_{max}$ as more of the electron density remains on the sensor molecule. Although it might be expected that this trend would continue, with longer alkyl chains causing larger red shifts, this was not observed. We speculate that this is related to the fact that longer alkyl chains allowed solvation of the TAA cations by the peripheral alkyl chains on **5.8**($N^-$), which was less likely for those with chains containing fewer than five carbons.[60] This solvation effect allowed cations with longer alkyl chains to be held closer to the anion, again withdrawing some electron density and so decreasing $\lambda_{max}$ of the solution from its maximum with the tetrabutylammonium cation.

The effect of electrostatic interactions between the **5.8**($N^-$) anion and the cation was further investigated by examining the impact of changing the analyte to one with a completely different cation, rather than a TAA group. As it has been proven that varying the anion does not affect the position of $\lambda_{max}$, we investigated the use of *n*-BuLi ($pK_A \sim 56$) and NaH ($pK_A \sim 34$) to deprotonate **5.8**, with the relevant cations for these materials being $Li^+$ and $Na^+$, respectively. For the results above, it would be expected that the lower electronegativities of these two elements when compared to nitrogen would lead to high polarization of the resulting ionic bonds with **5.8**($N^-$), and thus even larger red shifts than were seen for TBAOH. In addition, the increased charge screening provided by the 2s and 2p electrons in $Na^+$ should result in NaH giving a slightly lower red shift than *n*-BuLi.

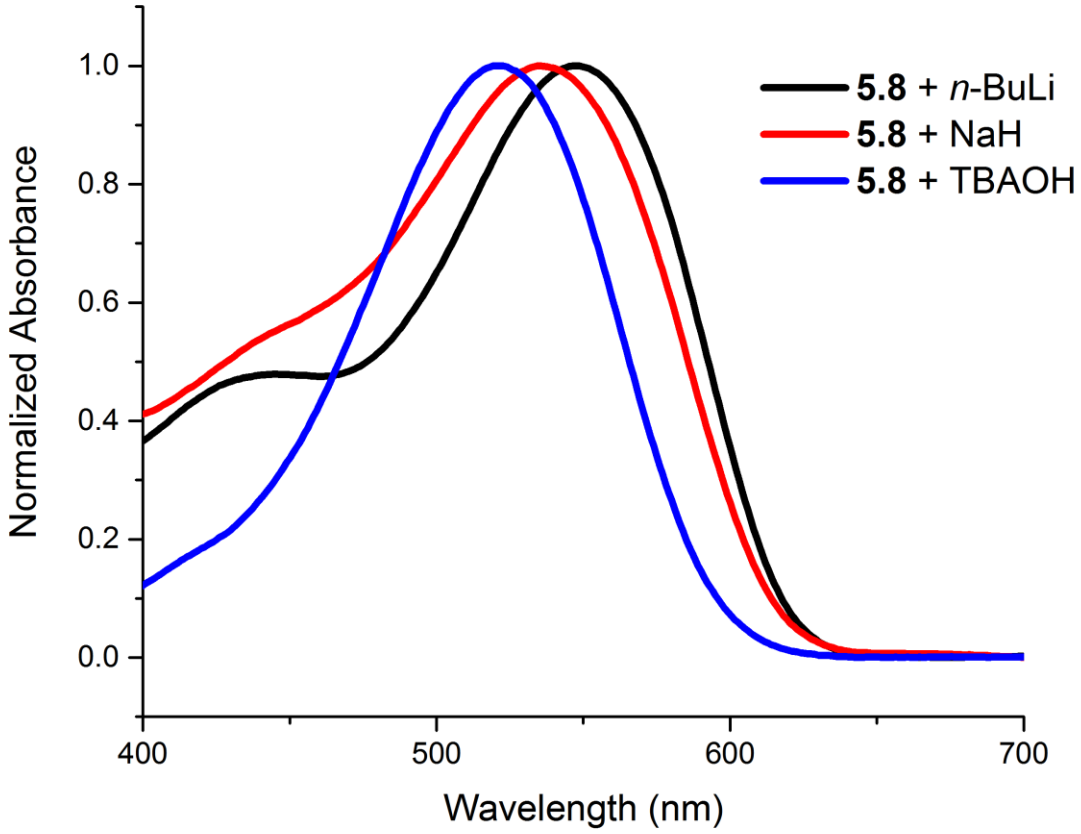



**Figure 5.12: UV-vis spectra of solutions of 5.8 in THF in the presence of different analytes**

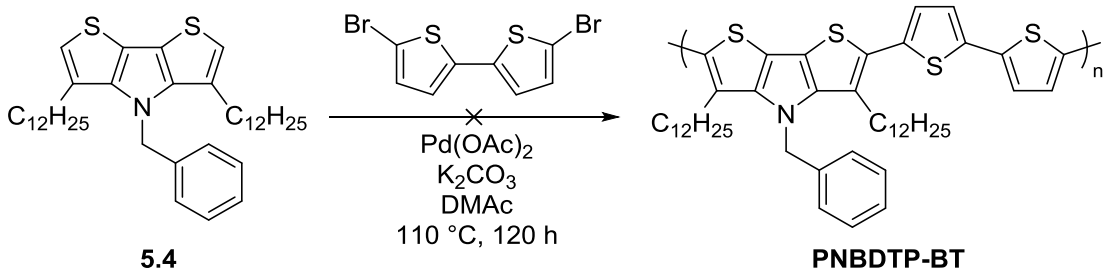
As can be seen in **Figure 5.12**, changing the analyte to NaH or *n*-BuLi had a significant impact on the position of $\lambda_{max}$, as predicted. The spectrum of **5.8**($N^-$)($TBA^+$) had an absorbance maximum at 520 nm, as described above, while changing the analyte to *n*-BuLi resulted in this value red shifting to 547 nm, with the use of NaH giving a slightly smaller red shift to 535 nm. These substantial changes were the result of large amounts of electron density remaining on the sensor due to the highly polarized nature of the $N^-$-$Li^+$ and $N^-$-$Na^+$ interactions.

Overall, it can be seen that compound **5.8** worked as an effective sensor for bases and could potentially be used to identify the presence of specific cations in organic solutions, with the position of $\lambda_{max}$ for **5.8**($N^-$) varying across almost 40 nm depending on the cations present in the specific analyte. Further changes to the structure of the sensor could be used to tune the colour of solutions to different wavelength or to alter the reactivity of the material, potentially enabling

more obvious determination of different analytes by increasing the differences between their red shifts.

### *5.7 – Polymer-based system*

With work on the small molecule dithienopyrrole sensor progressing, it was decided to investigate the potential of a polymer-based analogue of the system. Whilst the small molecule sensor has specific advantages, such as the colorimetric method of detection, polymer systems have positive characteristics of their own, with polymers that can be deprotonated potentially able to be used either as sensors or as n-doped materials in organic electronic devices.[27,28]



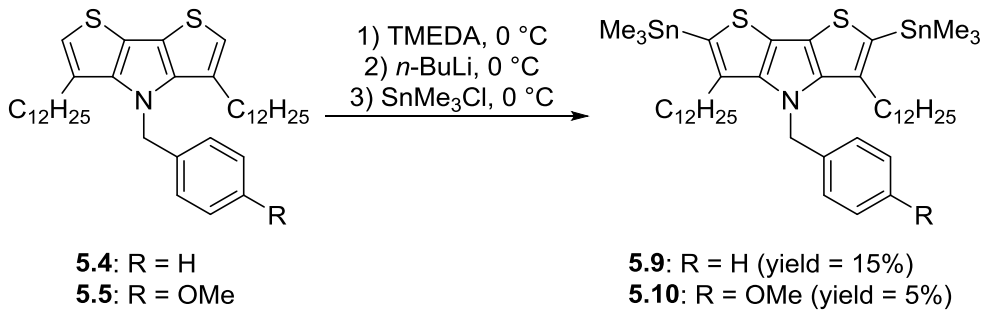

**5.4** **PNBDTP-BT**

**Figure 5.13: Attempted polymerization of 3,5-didodecyl-4N-benzyl-dithieno[3,2-*b*:2',3'-*d*]pyrroles with dibromobithiophene via direct heteroarylation**

The first method of polymerizing N-benzyldithienopyrrole attempted was a logical extension of the small molecule work, with the unfunctionalized material (**5.4**) being polymerized with dibromobithiophene via direct arylation under similar conditions to those used to synthesize **5.6** and **5.7**. However, it was found that this resulted in the formation of a polymer residue that was insoluble even in hot trichlorobenzene. The most likely reason for the formation of such material is competition between the C-H bonds leading to cross-linking of the material during polymerization, potentially at either the 3 or 4 positions of the bithiophene co-monomer or on the N-benzyl group. Unfortunately, due to the high insolubility of the cross-linked material further characterization was impractical, making the determination of the specific site at which cross-linking occurred impossible. Although it could be possible to prevent cross-linking by carefully tuning the reaction conditions (as mentioned in **Chapter 4**),[42,49] this was not attempted. Instead, the dithienopyrrole monomers were functionalized with stannyl

groups to allow Stille polymerization with dibromobithiophene, which would prevent cross-linking as C-C bonds would only form between the C-Sn and C-Br sites.

### *5.7.1 – Stannylation of N-benzyldithienopyrroles*



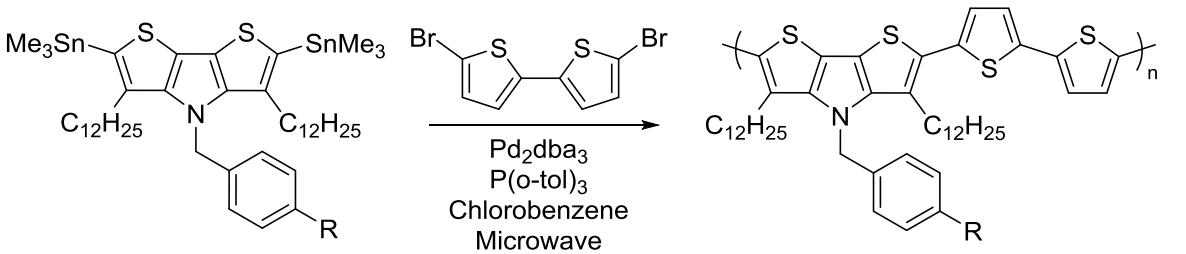

**5.4**: R = H
**5.5**: R = OMe

**5.9**: R = H (yield = 15%)
**5.10**: R = OMe (yield = 5%)

**Figure 5.14: Stannylation of 3,5-didodecyl-4N-benzyl-dithieno[3,2-*b*:2',3'-*d*]pyrroles**

Both **5.4** and **5.5** were functionalized with trimethylstannyl groups using the same methodology. First, the dithienopyrrole was dilithiated by sequential addition of TMEDA and *n*-BuLi at 0 °C, then quenched with trimethylstannylchloride. The resulting distannyl compounds were purified by recycling GPC (hexane, 40 °C) to remove mono- and nonstannylated material, resulting in yields of 15% and 5% for **5.9** and **5.10**, respectively.

### *5.7.2 – Polymerization*




**5.9**: R = H
**5.10**: R = OMe

**PNBDTPBT**: R = H (yield = 33%)
**PNOMeBDTPBT**: R = OMe (yield = 38%)

**Figure 5.15: Stille polymerization of 2,6-bis(trimethylstannyl)-3,5-didodecyl-4N-benzyl-dithieno[3,2-*b*:2',3'-*d*]pyrroles with 5,5'-dibromo-2,2'-bithiophene**

Having obtained the distannylated monomers, Stille polymerization was carried out using dibromobithiophene as the co-monomer in order to give a direct analogue of the small molecule sensor. The polymerizations were performed in a microwave reactor using $Pd_2dba_3$ as the catalyst and P(*o*-tol)$_3$ as a ligand. After cooling to room temperature, the polymers were

precipitated in methanol then purified by Soxhlet extraction with methanol, acetone, hexane, and chloroform in that order. The chloroform fractions were concentrated in vacuo and reprecipitated in methanol, yielding **PNBDTPBT** and **PNOMeBDTPBT** in yields of 33% and 38%, respectively. The molecular weight data, as determined by GPC in chlorobenzene at 80 °C against polystyrene standards, are shown in **Table 5.2**, and the structures of the polymers were confirmed by $^1$H NMR and elemental analysis.

**Table 5.2: Molecular weight information for PNBDTPBT and PNOMeBDTPBT**

| Polymer | $M_n$ (kg/mol) | $M_w$ (kg/mol) | Đ |
|---|---|---|---|
| **PNBDTPBT** | 7.1 | 10.4 | 1.46 |
| **PNOMeBDTPBT** | 11.8 | 17.3 | 1.47 |

### *5.7.3 – Deprotection*

After successful synthesis of the N-benzylated polymers via Stille coupling, deprotection was performed using the same methodology as was used for the removal of the benzyl groups from **5.6** and **5.7**. The polymers were dissolved in degassed anisole and exposed to $AlCl_3$ while heating to 90 °C for 2 h. A slightly smaller amount of $AlCl_3$ was used for deprotecting the polymers than was used for the small molecule (5 equivalents instead of 10) in order to lower the chances of degradation of the polymer backbone due to exposure to harsh conditions. After two hours, the reaction was quenched with water and washed with 3 M HCl, with the product being extracted in chloroform. The solvent was removed in vacuo, after which the polymer was redissolved in the minimum amount of hot chlorobenzene and reprecipiated in methanol to remove impurities. This final step was repeated twice to yield **PNHDTPBT-1** and **PNHDTPBT-2** from the benzylated and *o*-methoxybenzylated polymers, respectively.

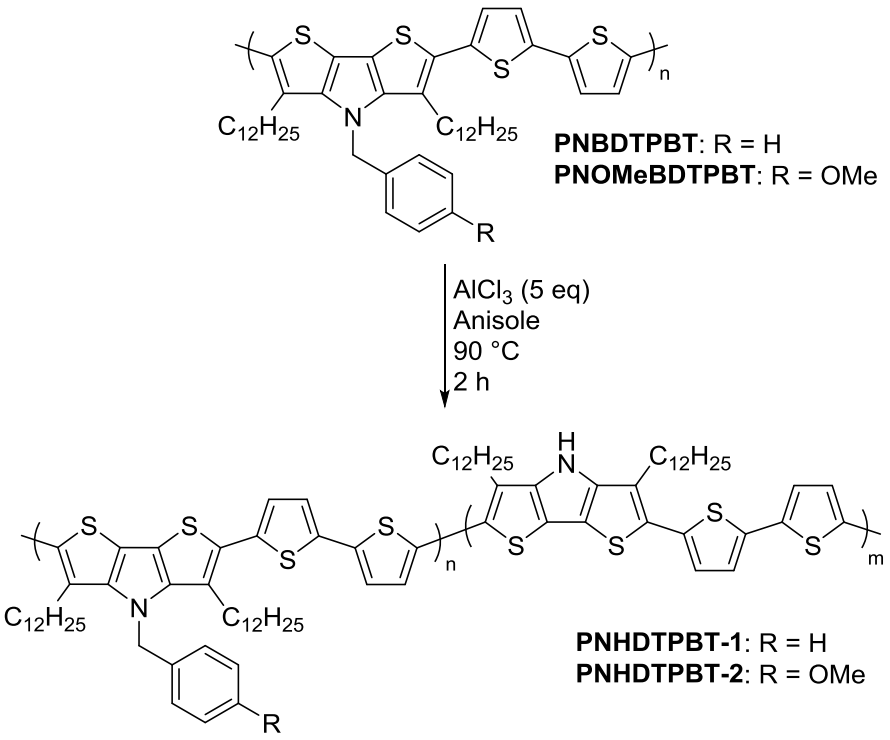



**Figure 5.16: Deprotection of N-benzylated polymers using $AlCl_3$ in anisole**

Unfortunately, the reactions did not go to completion and thus yields could not be calculated for these reactions as individual polymer chains likely included both benzylated and deprotected units, meaning that the two could not be separated. This also prevented characterization of the polymers by elemental analysis. Although pyrrolic protons could not be identified in the $^1$H NMR spectra of the polymers, a reduction in the relative intensities of the benzylic protons was observed, as well as a shift in the peaks relating the α-protons on the dodecyl chains, both of which provide strong indications that the desired products were formed.

### *5.8 – Sensing using polymer*

The sensing properties of the deprotected polymers were investigated in a similar manner to that used for the small molecule sensor. It was assumed that the polymeric material would act in the same manner as **5.8**, with deprotonation occurring in the presence of adequately strong bases, although the extension of the conjugation length in the polymer may result in a slight decrease in the strength of base required as it may lower the p$K_A$ of the pyrrolic proton.

### *5.8.1 – Optical properties*

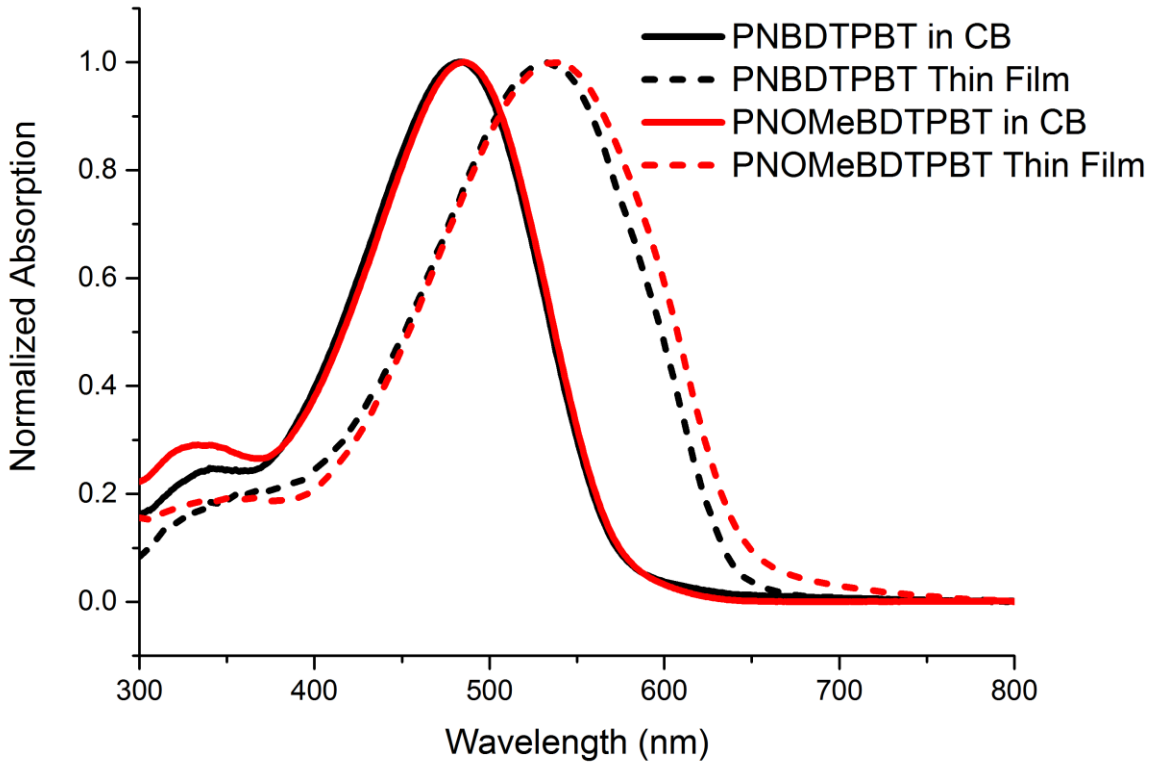



**Figure 5.17: UV-vis absorption spectra of N-benzylated polymers in chlorobenzene solution and as thin films**

The absorption spectra of the polymers were measured using UV-vis spectroscopy both in chlorobenzene solutions and as thin films, as can be seen in **Figure 5.17**. As would be expected from the similarities of the structures of these two polymers their absorption spectra were highly similar – indeed they were almost indistinguishable in solution, with $\lambda_{max}$ values of 483 and 485 nm for **PNBDTPBT** and **PNOMeDTPBT**, respectively. Although the red shift on film formation was 50 nm for both materials, the onset of absorption of the methoxybenzylated polymer occurred at a slightly longer wavelength than that of the benzylated polymer, likely due to the lower molecular weight of the latter material.

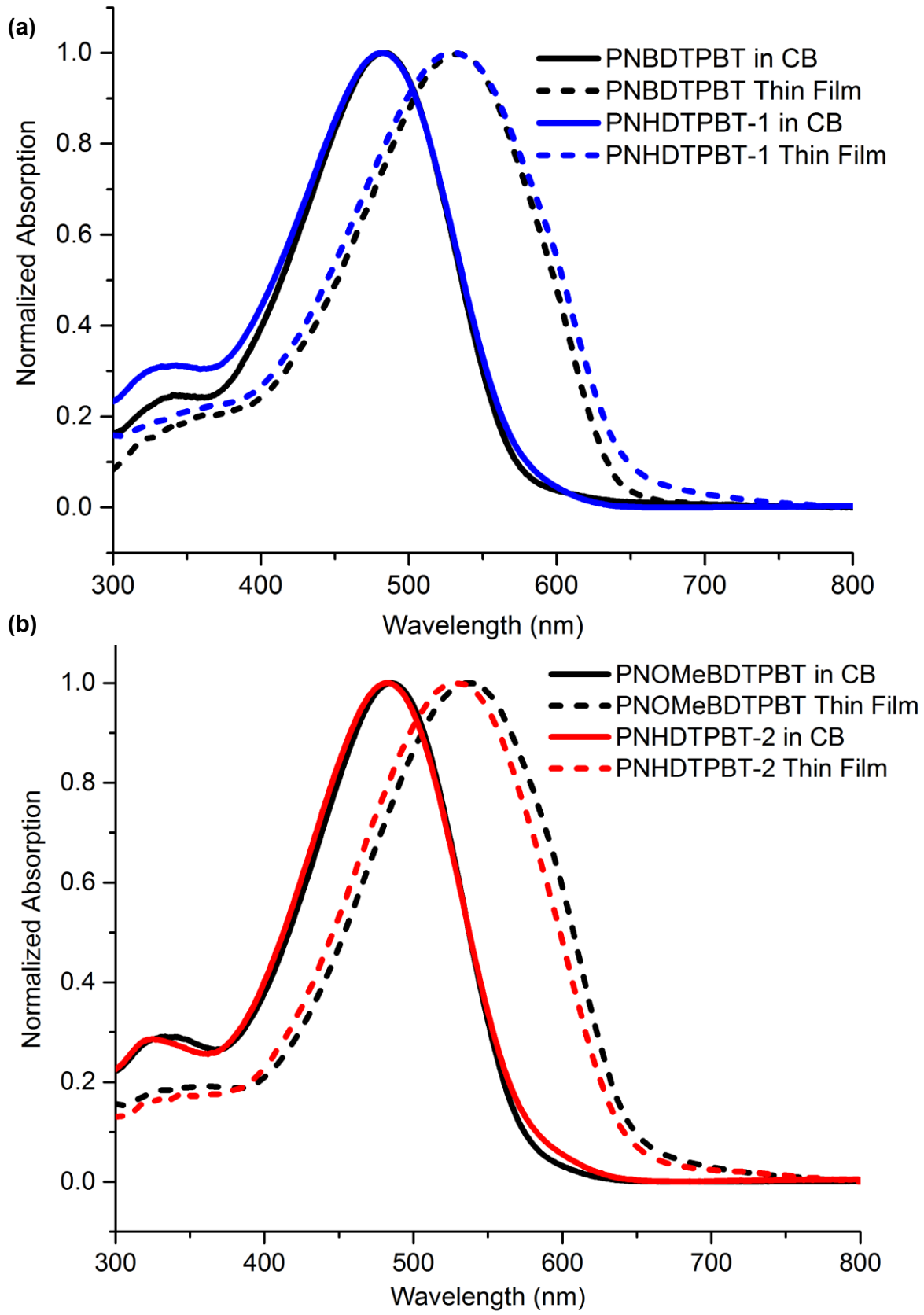



**Figure 5.18 – UV-vis absorption spectra of (a) PNBDTPBT and (b) PNOMeBDTPBT before and after deprotection, both in chlorobenzene solutions and as thin films**

As can be seen in **Figure 5.18**, removing the benzyl/methoxybenzyl groups from the polymers has very little impact on the UV-vis spectrum, with only a slight increase in the onset of the thin film absorption observed for the benzylated polymer and a slight decrease for the methoxybenzylated polymer. This was expected due to the minimal changes observed on deprotection of the small molecule sensor, which only resulted in an 8 nm redshift, as mentioned in **Section 5.3.1**. One might expect that partially removing the protecting groups would result in some morphological changes to the polymer thin film that could change the optical spectra. The minor changes observed suggest therefore that the polymers are relatively amorphous, both before and after the partial removal of the benzyl group. The similarity of spectra before and after benzyl removal suggests it does not influence the electron density on the bridging N significantly.

### *5.8.2 – Deprotonation with TBAF*

Having obtained the deprotected polymers **PNHDTPBT-1** and **-2**, we investigated the impact that deprotonation would have on their optical spectra. **Figure 5.19** shows the changes in the absorption spectrum of a 2.4 mM solution of **PNDTPBT-1** in THF as the concentration of TBAF was increased from 0 to 11.5 mM. The concentration of TBAF was increased by 0.46 mM per measurement between 0.23 and 2.3 mM, then by 2.3 mM per measurement up to 11.5 mM.

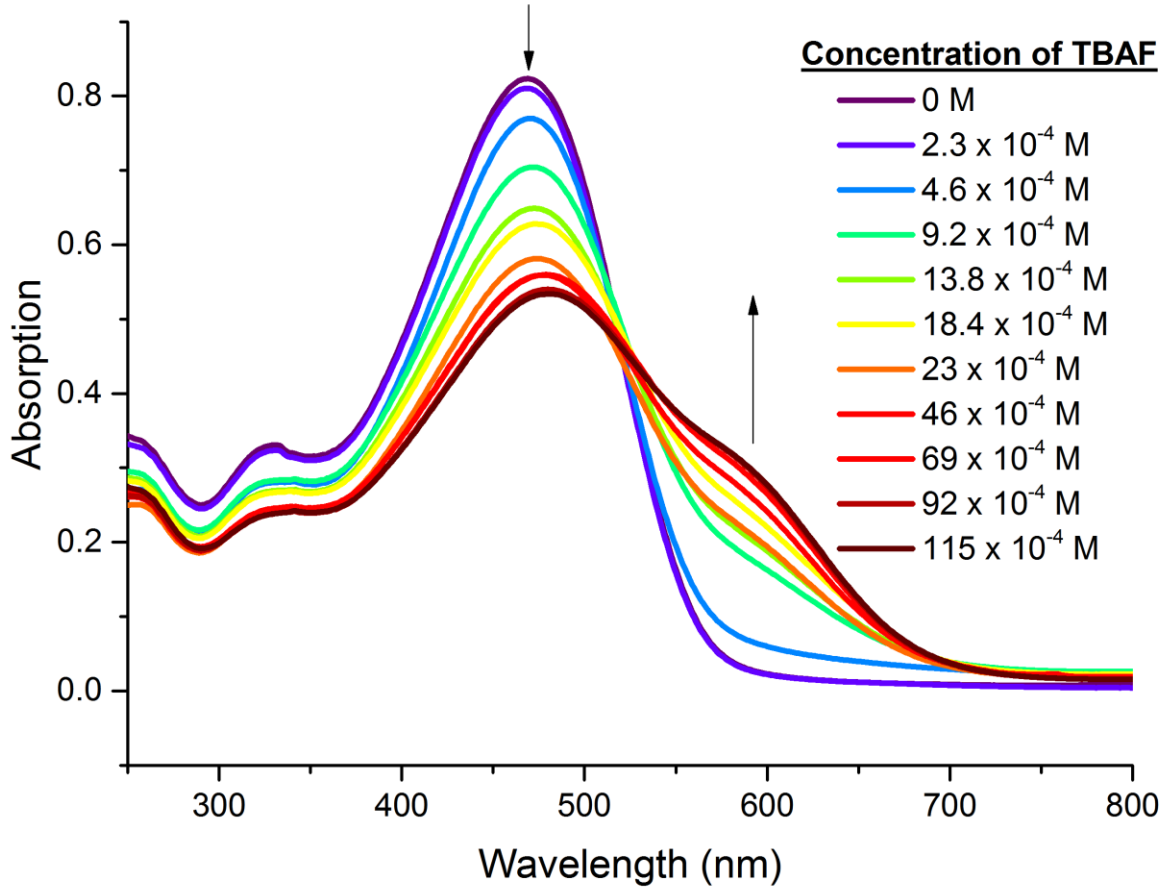



**Figure 5.19 – UV-vis absorption spectra of 2.4 mM solutions of PNHDTPBT-1 in THF as the concentration of TBAF was increased from 0 to 11.5 mM**

As would be expected, there was a decrease in the intensity at $\lambda_{max}$ (468 nm) as the concentration of TBAF was increased, related to the deprotonation of the NH group. Simultaneously, a shoulder appeared in the red-shifted region centred at ~590 nm, giving an approximate red shift of 122 nm. This was larger than that seen in the small molecule system (~80 nm), likely due to the larger impact that deprotonation would be expected to have on the delocalised backbone structure of the polymer. However, it should be noted that the intensity of the shoulder never exceeded that of the original peak, likely due to the high proportion of benzylated DTP still present on the polymer backbone. As benzylated DTP has a similar absorption maximum to protonated NHDTP, any benzylated material remaining would lead to both a reduction in the intensity of the $N^-$ peak and increased retention of the original peak. Solutions of **PNHBTPBT-2** showed highly similar results on exposure to excess TBAOH (**Figure 5.20**).

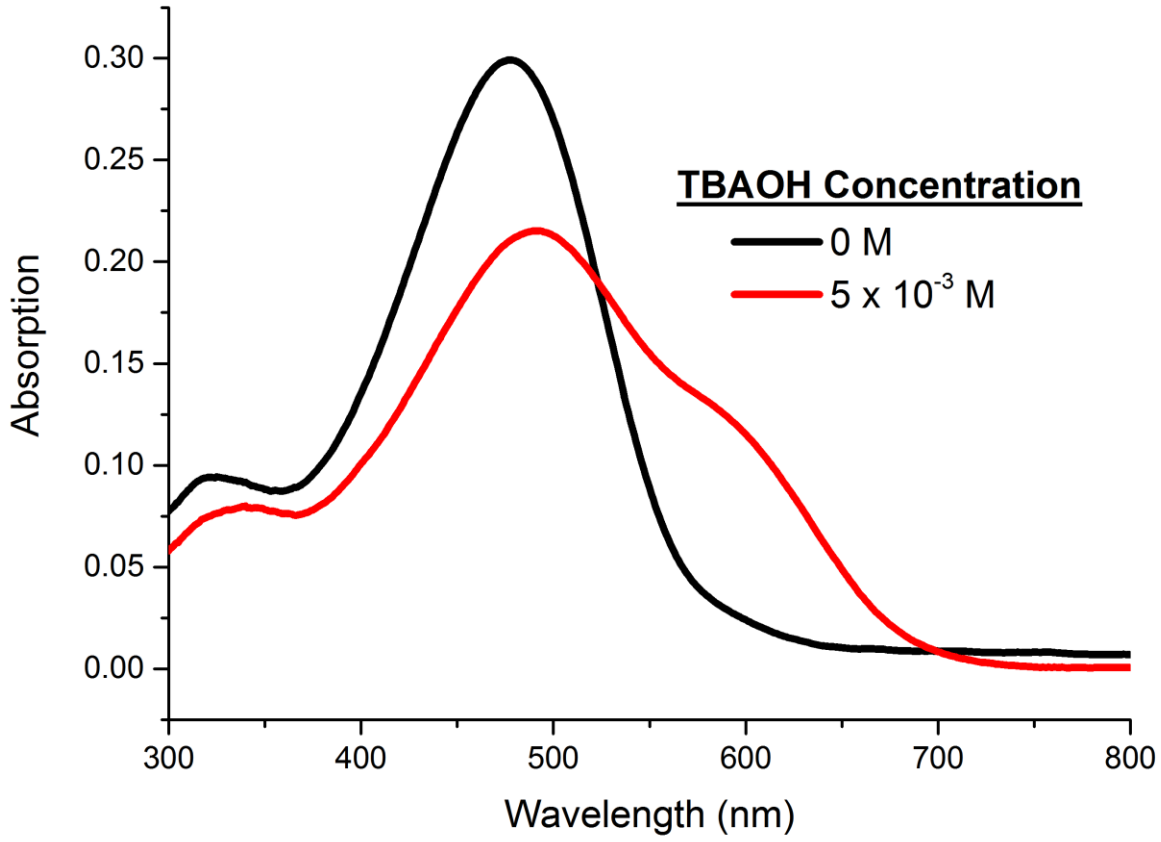



**Figure 5.20: UV-vis absorption spectra of PNHDTPBT-2 (2.6 × $10^{-5}$ M in THF) before and after addition of 5 × $10^{-3}$ M TBAOH**

This behaviour is potentially useful, as it could give a second method of controlling the degree of deprotonation on the polymer backbone in addition to the concentration of TBAF added. The number of benzyl groups removed from the backbone, which should be tuneable via alteration of the reaction conditions, would set an effective upper limit on the number of deprotonation sites available, while the amount of analyte/doping agent added would determine the relative degree of deprotonation of the NH groups on the backbone. Whilst for sensing applications it would likely be preferable to have as many deprotonatable sites as possible to give a wider range of activity, if these materials were to be used in organic electronic devices it may be necessary to reduce the number of NH sites in order to prevent excessive formation of traps during doping.

In order to investigate the potential for these materials to be used in doped OFET devices, we attempted to investigate the impact of adding TBAF to thin films of the polymers. However,

although the polymers themselves managed to form acceptable films on glass slides, it was found that the addition of TBAF led to almost instantaneous dewetting, preventing further analysis by either UV-vis absorption spectroscopy or cyclic voltammetry, both of which we were hoping to use to examine the optoelectronic impact of doping with TBAF. It is hoped that it will be possible for dewetting to be prevented under the right conditions: for example, annealing the polymer films could improve their adherence to the glass slide, using a different doping agent could reduce incentives for dewetting, and increasing the molecular weight of the polymers could improve the stability of the films. However, investigation of these possibilities is ongoing.

### *5.9 – Conclusions*

This chapter has detailed the synthesis and method of action of a colorimetric sensor for strong bases utilizing a peripherally alkylated dithienopyrrole (DTP) unit as the reactive moiety. A number of different synthetic routes were attempted to try to produce secondary amine-functionalised DTP that was capable of being deprotonated, with the eventual route using a benzyl-protected amine, followed by coupling of the DTP with flanking bithiophene systems via direct heteroarylation and deprotection of the amine using $AlCl_3$ and anisole. The resulting material was found to react with relatively strong bases such as tetralkylammonium salts, sodium hydride, and *n*-butyl lithium, and determination of the mechanism of action showed that this was indeed occurring through deprotonation of the secondary amine. Furthermore, the $pK_A$ of the sensor was determined to be ~15.9, a reasonable value given those of other pyrrolic-nitrogen-containing ring systems. Knowing the $pK_A$ explained a great deal of the behaviour of the sensor, such as its failure to be deprotonated by DBU. It was also found that varying the anion of the tetraalkylammonium salts had no effect on the $\lambda_{max}$ of the deprotonated material, although the degree of deprotonation was found to be dependent on the $pK_A$ of the anion. On the other hand, varying the cation by changing the length of the chains on the tetraalkylammonium group had a measurable impact on the position of $\lambda_{max}$, indicating that factors such as charge

density and screening could affect the response of the sensor. Similar results were seen when changing the analyte completely, for example to *n*-BuLi or NaH.

The DTP unit was also incorporated into analogous polymeric systems that have the potential to be used for either sensing or as n-doped materials in organic electronics. Although direct heteroarylation proved unsuccessful for this polymerisation reaction, functionalising the benzylated DTP with stannyl groups and performing Stille polymerisation allowed DTP-containing polymers to be obtained in reasonable yields. The polymers could be deprotected under the same conditions as the small molecule, albeit incompletely. As with the small molecule, the deprotected polymers reacted with tetrabutylammonium salts, showing that they could be used for sensing and/or doping applications.

### *5.10 – Experimental*

General experimental details can be found in **Section 2.9**, as can the synthesis of compound **2.6**. Solution UV spectra of sensors and analytes such as those shown in **Figure 5.9** were carried out at 25 °C and allowed to equalise for 5 min before measurement. The melting points of **5.6** and **5.7** were determined from the onset and completion of the melting peak as determined by DSC at 10 °C/min.

#### *5.10.1 – Synthesis of 3,5-didodecyl-4N-benzyldithieno[3,2-b:2',3'-d]pyrrole (5.4)*

Over 5 min, benzylamine (0.1 ml, 0.915 mmol) was added dropwise to a stirring solution of 3,3'-dibromo-4,4'-didodecyl-[2,2'-bithiophene] (**2.6**) (0.593 g, 0.897 mmol), $Pd_2dba_3$ (39 mg, 0.043 mmol), BINAP (0.105 g, 0.169 mmol), and sodium *t*-butoxide (0.427 g, 4.443 mmol) in degassed anhydrous toluene (15 ml). The resulting mixture was refluxed at 120 °C for 12 h in the absence of light. After completion, the reaction was quenched with water (5 ml) and the aqueous and organic layers separated. The aqueous layer was extracted with DCM (2 × 10 ml), and the combined organic layers were washed with water (3 × 5 ml). The resulting solution was dried over sodium sulfate and the solvent was removed in vacuo. The crude product was then

purified by column chromatography over silica (eluent: DCM/hexane in a 1:6 ratio) to give 3,5-didodecyl-4N-benzyldithieno[3,2-*b*:2',3'-*d*]pyrrole (**5.4**) as a yellow solid (0.496 g, 0.818 mmol, 91%, m.p. 70–71 °C). $^{1}$H NMR (400 MHz, $CDCl_3$) δ 7.30 – 7.16 (m, 4H), 6.94 – 6.87 (m, 2H), 6.69 (s, 2H), 5.65 (s, 2H), 2.64 – 2.58 (m, 4H), 1.63 – 1.50 (m, 4H), 1.35 – 1.16 (m, 36H), 0.88 (t, *J* = 6.7 Hz, 6H). $^{13}$C NMR (101 MHz, $CDCl_3$) δ 143.26 (2C), 139.57, 128.99 (2C), 128.24 (2C), 127.42 (2C), 125.18 (2C), 118.52 (2C), 116.44, 49.24, 32.08 (2C), 30.13 (2C), 29.80–29.53 (overlapping peaks, 14C), 28.75 (2C), 22.85 (2C), 14.29 (2C). HRMS (ES$^+$) calculated for $C_{39}H_{60}NS_2$ [M$^+$], 606.4167; found, 606.4180.

### *5.10.2 – Synthesis of 3,5-didodecyl-4N-(4-methoxy)-benzyldithieno[3,2-b:2',3'-d]pyrrole (5.5)*

The same methodology as described above was applied, using 4-methoxybenzylamine instead of benzylamine. This yielded 3,5-didodecyl-4N-(4-methoxy)-benzyldithieno[3,2-*b*:2',3'-*d*]pyrrole (**5.5**) as a yellow solid (1.680 g, 2.641 mmol, 84%, m.p. 58–59 °C). $^{1}$H NMR (400 MHz, $CDCl_3$) δ 6.86 – 6.75 (m, 4H), 6.69 (s, 2H), 5.58 (s, 2H), 3.74 (s, 3H), 2.65 – 2.59 (m, 4H), 1.65 – 1.51 (m, 4H), 1.34 – 1.17 (m, 36H), 0.88 (t, *J* = 6.7 Hz, 6H). $^{13}$C NMR (101 MHz, $CDCl_3$) δ 158.91 (2C), 143.25 (2C), 131.64 (2C), 128.27 (2C), 126.32 (2C), 118.46 (2C), 116.38 (2C), 114.34 (2C), 55.34, 48.71, 32.08 (2C), 30.14 (2C), 29.81–29.51 (overlapping peaks, 14C), 28.77 (2C), 22.85 (2C), 14.29 (2C). HRMS (ES$^+$) calculated for $C_{40}H_{62}NOS_2$ [M+H], 636.4273; found, 636.4281.

### *5.10.3 – Synthesis of 3,5-didodecyl-2,6-bis(5'-hexyl-2,2'-bithiophenyl)-4N-benzyldithieno[3,2-b:2',3'-d]pyrrole (5.6)*

A solution of 3,5-didodecyl-4N-benzyldithieno[3,2-*b*:2',3'-*d*]pyrrole (**5.4**, 1.00 g, 1.65 mmol), 5-bromo-5'-hexyl-2,2'-bithiophene (1.14 g, 3.47 mmol), palladium (II) acetate (15 mg, 0.066 mmol), and potassium carbonate (0.34 g, 2.48 mmol) in degassed anhydrous DMAc (13 ml) was heated to 110 °C in the dark for 48 h. After completion, the solution was concentrated in vacuo and purified by column chromatography over silica (eluent: hexane/ethyl acetate, 93:7 v/v) to yield 3,5-didodecyl-2,6-bis(5'-hexyl-2,2'-bithiophenyl)-4N-

benzyldithieno[3,2-*b*:2',3'-*d*]pyrrole (**5.6**) as a red-brown solid (1.45 g, 1.31 mmol, 79%, m.p. 90–94 °C). $^{1}$H NMR (400 MHz, TCE-$d_2$) δ 7.35 – 7.24 (m, 3H), 7.09 – 7.05 (m, 2H), 7.01 (dd, *J* = 5.1, 3.6 Hz, 4H), 6.96 (d, *J* = 7.6 Hz, 2H), 6.71 (d, *J* = 3.6 Hz, 2H), 5.67 (s, 2H), 2.87 – 2.72 (m, 8H), 1.74 – 1.52 (m, 8H), 1.45 – 1.05 (m, 48H), 0.90 (m, 12H). $^{13}$C NMR (101 MHz, $CDCl_3$) δ 145.64 (2C), 144.04, 139.19, 137.87, 135.76, 134.68, 129.84, 129.44, 129.17 (2C), 129.08, 128.75, 127.59, 126.47 (2C), 125.39, 124.97–124.93 (overlapping peaks, 6C), 123.32 (6C), 115.01, 48.79, 32.10 (2C), 31.72 (6C), 30.36 (2C), 29.84–29.67 (overlapping peaks, 10C), 29.54 (3C), 29.38 (2C), 28.92 (2C), 27.29, 22.87 (2C), 22.73 (2C), 14.29 (2C), 14.23 (2C). MS (MALDI-TOF) *m/z* = 1101.9 [$M^+$]. UV (THF): $\lambda_{max}$ = 416 nm.

### *5.10.4 – Synthesis of 3,5-didodecyl-2,6-bis(5'-hexyl-2,2'-bithiophenyl)-4N-(4-methoxy)-benzyldithieno[3,2-*b*:2',3'-*d*]pyrrole (5.7)*

The same methodology as described in **Section 5.10.3** was used, with **5.5** replacing **5.4** to yield 3,5-didodecyl-2,6-bis(5'-hexyl-2,2'-bithiophenyl)-4N-(4-methoxy)-benzyldithieno[3,2-*b*:2',3'-*d*]pyrrole (**5.7**) as a red-brown solid (0.170 g, 0.150 mmol, 25%, m.p. 68–80 °C). $^{1}$H NMR (400 MHz, $CDCl_3$) δ 7.05 – 7.02 (m, 2H), 7.01 – 6.96 (m, 4H), 6.86 – 6.79 (m, 4H), 6.69 – 6.67 (m, 2H), 5.60 (s, 2H), 3.75 (s, 3H), 2.78 (q, *J* = 7.2 Hz, 8H), 1.68 (p, *J* = 7.5 Hz, 4H), 1.44 – 1.15 (m, 52H), 0.89 (m, 12H). $^{1}$H NMR (400 MHz, THF-$d_8$) δ 7.09 (d, *J* = 3.7 Hz, 2H), 7.04 (d, *J* = 3.8 Hz, 2H), 7.01 (d, *J* = 3.5 Hz, 2H), 6.90 – 6.81 (m, 4H), 6.71 (m, 2H), 5.71 (s, 2H), 3.71 (s, 3H), 2.83 (m, 8H), 1.78 – 1.55 (m, 8H), 1.45 – 1.19 (m, 48H), 0.94 – 0.84 (m, 12H). $^{13}$C NMR (101 MHz, $CDCl_3$) δ 159.03, 145.64 (2C), 144.04 (2C), 137.84 (2C), 135.79 (2C), 134.69 (2C), 131.21 (2C), 129.37 (2C), 126.45 (2C), 126.11 (2C), 125.42, 124.93 (2C), 123.36–123.32 (overlapping peaks, 4C), 114.93, 114.53 (2C), 114.44, 55.35, 48.27, 32.10 (2C), 31.72 (6C), 30.36 (2C), 29.85–29.76 (overlapping peaks, 10C), 29.54 (3C), 29.42 (2C), 28.92 (2C), 27.28, 22.87 (2C), 22.73 (2C), 14.29 (2C), 14.24 (2C). MS (MALDI-TOF) *m/z* = 1132.1 [$M^+$] UV ($CHCl_3$): $\lambda_{max}$ = 418 nm.

### *5.10.5 – Synthesis of 3,5-didodecyl-2,6-bis(5'-hexyl-2,2'-bithiophenyl)-4H-dithieno[3,2-b:2',3'-d]pyrrole (5.8)*

Solutions of **5.6**/**5.7** (1 eq) and aluminium chloride (10 eq) in anhydrous anisole (4 ml per 100 mg) were heated to 90 °C for up to 2 h while monitoring via TLC (stationary phase: alumina; eluent: hexane/ethyl acetate, 93:7 v/v). Once the reactions were complete, they were cooled to room temperature and quenched with water (5 ml), after which ethyl acetate (25 ml) and 3M HCl (10 ml) were added. The layers were separated, after which the organic layer was washed with water (2 × 10 ml) and brine (1 × 5 ml), dried over sodium sulfate, and concentrated in vacuo. The material was then vacuum-filtered through a plug of basic alumina using a 93:7 v/v mixture of hexane and ethyl acetate as the eluent. After concentration via rotary evaporation, the resulting brown material was recrystallized by dissolving it in the minimum quantity of hot THF, adding hexane, and then boiling off the THF, leaving a solution of product in hot hexane. On cooling to room temperature, this gave 3,5-didodecyl-2,6-bis(5'-hexyl-2,2'-bithiophenyl)-4H-dithieno[3,2-*b*:2',3'-*d*]pyrrole as an orange solid that turned brown on prolonged exposure to air in yields of 21% and 42% from **5.6** and **5.7**, respectively. $^{1}$H NMR (400 MHz, THF-$d_8$) δ 10.63 (s, 1H), 7.09 (d, *J* = 3.8 Hz, 2H), 7.05 (d, *J* = 3.8 Hz, 2H), 7.02 (d, *J* = 3.6 Hz, 2H), 6.72 (d, *J* = 3.2 Hz, 2H), 3.04 – 2.97 (m, 4H), 2.81 (t, *J* = 7.6 Hz, 4H), 1.82 – 1.63 (m, 4H), 1.50 – 1.22 (m, 52H), 0.90 (m, 12H). $^{13}$C NMR (101 MHz, THF) δ 145.77 (2C), 145.39 (2C), 137.83 (2C), 136.89 (2C), 135.36 (2C), 129.01 (2C), 126.21 (2C), 125.66 (2C), 125.25 (2C), 123.83 (2C), 123.77 (2C), 114.61 (2C), 32.71 (2C), 32.39–32.36 (overlapping peaks, 4C), 30.65–30.39 (overlapping peaks, 10C), 30.15 (2C), 29.49 (2C), 27.85, 25.66 (2C), 25.46 (3C), 25.26 (2C), 23.39 (2C), 23.30 (2C), 14.27 (2C), 14.23 (2C). MS (MALDI-TOF) *m/z* = 1011.9 [$M^+$]. UV (THF): $\lambda_{max}$ = 424 nm.

### *5.10.6 – Synthesis of 2,6-bis(trimethylstannyl)-3,5-didodecyl-4N-benzyl-dithieno[3,2-b:2',3'-d]pyrrole (5.9)*

A solution of 3,5-didodecyl-4N-benzyldithieno[3,2-*b*:2',3'-*d*]pyrrole (**5.4**, 1.00 g, 1.65 mmol) and TMEDA (0.75 ml, 4.95 mmol, 3.0 eq) in anhydrous hexane (70 ml) was cooled to 0 °C, after

which *n*BuLi (2.5M in hexane, 1.98 ml, 4.95 mmol, 3.0 eq) was added dropwise via syringe over 10 min. The reaction was stirred at 0 °C for 0.5 h, after which $SnMe_3Cl$ (1 M in THF, 4.95 ml, 4.95 mmol, 3.0 eq) was added dropwise over 10 min. The reaction was allowed to warm to room temperature overnight, then was washed with water (2 × 10 ml), acetonitrile (1 × 5 ml), and extracted with hexane (2 × 20 ml). The product was then concentrated under reduced pressure and purified by recycling preparative GPC (40 °C, hexane) to yield 2,6-bis(trimethylstannyl)-3,5-didodecyl-4N-benzyl-dithieno[3,2-*b*:2',3'-*d*]pyrrole (**5.9**) as a pale yellow oil (0.222 g, 0.243 mmol, 15%). $^1$H NMR (400 MHz, $CDCl_3$) δ 7.31 – 7.16 (m, 3H), 6.92 – 6.86 (m, 2H), 5.62 (s, 2H), 2.60 – 2.53 (m, 4H), 1.53 – 1.41 (m, 4H), 1.36 – 1.15 (m, 36H), 0.90 (t, *J* = 6.7 Hz, 6H), 0.34 (s, 18H).

### *5.10.7 – Synthesis of 2,6-bis(trimethylstannyl)-3,5-didodecyl-4N-(4-methoxy)-benzyl-dithieno[3,2-b:2',3'-d]pyrrole (5.10)*

The same synthetic procedure as is described in **Section 5.10.6** was used, with **5.5** replacing **5.4** in order to give 2,6-bis(trimethylstannyl)-3,5-didodecyl-4N-(4-methoxy)-benzyl-dithieno[3,2-*b*:2',3'-*d*]pyrrole (**5.10**) as a pale yellow oil (40 mg, 0.004 mmol, 5%). $^1$H NMR (400 MHz, $CDCl_3$) δ 6.82 – 6.76 (m, 4H), 5.54 (s, 2H), 3.74 (s, 3H), 2.61 – 2.53 (m, 4H), 1.53 – 1.42 (m, 4H), 1.35 – 1.16 (m, 36H), 0.93 – 0.85 (m, 6H), 0.37 (s, 18H).

### *5.10.8 – Stille polymerization of 2,6-bis(trimethylstannyl)-3,5-didodecyl-4N-benzyl-dithieno[3,2-b:2',3'-d]pyrrole with 5,5'-dibromo-2,2'-bithiophene (PNBDTPBT)*

An oven-dried high-pressure microwave vial was charged with 2,6-bis(trimethylstannyl)-3,5-didodecyl-4N-benzyl-dithieno[3,2-*b*:2',3'-*d*]pyrrole (**5.9**, 222 mg, 0.243 mmol), 5,5'-dibromo-2,2'-bithiophene (79 mg, 0.243 mmol), $Pd_2dba_3$ (4.5 mg, 0.005 mmol), and P(*o*-tol)$_3$ (5.9 mg, 0.019 mmol). The tube was sealed and flushed with Ar, after which 1 ml of degassed chlorobenzene was added. The solution was thoroughly degassed with Ar, after which the inlet was removed. The vial was then placed in a microwave reactor and heated as follows: 2 min at 100, 120, 140, and 160 °C, 10 min at 180 °C, and 40 min at 200 °C. After cooling to room

temperature, the polymer was precipitated into methanol and filtered into a Soxhlet thimble. The polymer was purified by Soxhlet extraction with methanol, acetone, hexane, and chloroform in that order. The chloroform fraction was concentrated under reduced pressure, dissolved in a minimal amount of hot chlorobenzene, and collected by reprecipitation into methanol followed by vacuum filtration. After drying under vacuum, **PNBDTPBT** was obtained (61 mg, 33%). GPC (chlorobenzene): $M_n$ 7,100 g/mol, $M_w$ 10,400 g/mol, Đ 1.45. $^1$H NMR (400 MHz, 323 K, $CDCl_3$) δ 7.33 – 7.21 (m, 3H), 7.14 – 7.01 (m, 4H), 6.96 – 6.91 (m, 2H), 5.70 (broad s, 2H), 2.84 – 2.75 (broad m, 4H), 1.65 – 1.55 (broad m, 4H), 1.35 – 1.17 (broad m, 36H), 0.92 – 0.84 (broad m, 6H). Anal. Calcd. for $C_{47}H_{61}NS_4$: C,73.48; H, 8.00; N, 1.82. Found: C, 70.27; H, 6.98; N, 2.03.

### *5.10.9 – Stille polymerization of 2,6-bis(trimethylstannyl)-3,5-didodecyl-4N-(4-methoxy)-benzyl-dithieno[3,2-**b**:2',3'-**d**]pyrrole with 5,5'-dibromo-2,2'-bithiophene (PNOMeBDTPBT)*

An oven-dried high-pressure microwave vial was charged with 2,6-bis(trimethylstannyl)-3,5-didodecyl-4N-(4-methoxy)-benzyl-dithieno[3,2-*b*:2',3'-*d*]pyrrole (**5.10**, 39 mg, $4.08 \times 10^{-5}$ mmol), 5,5'-dibromo-2,2'-bithiophene (13 mg, $4.08 \times 10^{-5}$ mmol), $Pd_2dba_3$ (0.7 mg, $8.15 \times 10^{-7}$ mmol), and P(o-tol)$_3$ (1.0 mg, $3.26 \times 10^{-6}$ mmol). The tube was sealed and flushed with Ar, after which 1 ml of degassed *o*-xylene was added. The solution was thoroughly degassed with Ar, after which the inlet was removed. The vial was then placed in a microwave reactor and heated as follows: 2 min at 100, 120, 140, and 160 °C, 10 min at 180 °C, and 30 min at 200 °C. After cooling to room temperature, the polymer was precipitated into methanol and filtered into a Soxhlet thimble. The polymer was purified by Soxhlet extraction with methanol, acetone, hexane, and chloroform in that order. The chloroform fraction was concentrated under reduced pressure, dissolved in a minimal amount of hot chlorobenzene, and collected by reprecipitation into methanol followed by vacuum filtration. After drying under vacuum, **PNOMeBDTPBT** was obtained (12.3 mg, 39%). GPC (chlorobenzene): $M_n$ 11,800 g/mol, $M_w$ 17,300 g/mol, Đ 1.47. $^1$H NMR (400 MHz, $CDCl_3$) δ 7.16 – 7.06 (m, 2H), 7.05 – 6.98 (m, 2H),

6.90 – 6.78 (m, 4H), 5.62 (broad s, 2H), 3.75 (s, 3H), 2.87 – 2.70 (broad m, 4H), 1.40 – 1.08 (broad m, 40H), 0.96 – 0.78 (broad m, 6H).

### *5.10.10 – Deprotection of polymers*

Solutions of **PNBDTPBT/PNOMeBDTPBT** (1 eq) and aluminium chloride (5 eq) in anhydrous anisole (0.5 ml) were heated to 90 °C for 2 h. Once the reactions were complete, they were cooled to room temperature and quenched with water (5 ml), after which chloroform (25 ml) and 3M HCl (10 ml) were added. The layers were separated, after which the organic layers were washed with water (2 × 10 ml) and brine (1 × 5 ml), dried over sodium sulfate, and concentrated in vacuo. The materials were then dissolved in minimal volumes of hot chlorobenzene and precipitated into methanol to yield **PNHDTPBT-1** and **PNHDTPBT-2**. An NMR spectrum of **PNHDTPBT-1** can be found in **Appendix A**.

## *5.11 – References*


1. R. R. McCusker, H. Paget-Wilkes, C. W. Chronister, B. A. Goldberger, and M. A. ElSohly, *J. Anal. Toxicol.*, 1999, **23**, 301–305.
2. Y. Liu, X. Dong, and P. Chen, *Chem Soc Rev*, 2012, **41**, 2283–2307.
3. D. Jariwala, V. K. Sangwan, L. J. Lauhon, T. J. Marks, and M. C. Hersam, *Chem. Soc. Rev.*, 2013, **42**, 2824–60.
4. P. Konieczka, B. Zygmunt, and J. Namieśnik, *Bull. Environ. Contam. Toxicol.*, 2000, **64**, 794–803.
5. Y. Zhou, J. F. Zhang, and J. Yoon, *Chem. Rev.*, 2014, **114**, 5511–5571.
6. A. P. Demchenko, Ed., *Introduction to Fluorescence Sensing*, Springer Netherlands, Dordrecht, 2009.
7. H. N. Kim, W. X. Ren, J. S. Kim, and J. Yoon, *Chem. Soc. Rev.*, 2012, **41**, 3210–3244.
8. M. Schäferling, *Angew. Chemie Int. Ed.*, 2012, **51**, 3532–3554.
9. Y. Salinas, R. Martínez-Máñez, M. D. Marcos, F. Sancenón, A. M. Costero, M. Parra, and S. Gil, *Chem. Soc. Rev.*, 2012, **41**, 1261.
10. I. A. Buryakov, T. I. Buryakov, and V. T. Matsaev, *J. Anal. Chem.*, 2014, **69**, 616–631.
11. R. Sakai, *Polym. J.*, 2016, **48**, 59–65.

12. J. Hodgkinson and R. P. Tatam, *Meas. Sci. Technol.*, 2013, **24**, 12004.

13. M. Krausa and A. A. Reznev, Eds., *Vapour and Trace Detection of Explosives for Anti-Terrorism Purposes*, Springer Netherlands, Dordrecht, 2004.

14. P. Cachelin, J. P. Green, T. Peijs, M. Heeney, and C. W. M. Bastiaansen, *Adv. Opt. Mater.*, 2016, **4**, 592–596.

15. X. Chen, Y. Zhou, X. Peng, and J. Yoon, *Chem. Soc. Rev.*, 2010, **39**, 2120.

16. Z. Xu, X. Chen, H. N. Kim, and J. Yoon, *Chem. Soc. Rev.*, 2010, **39**, 127–137.

17. H. N. Kim, Z. Guo, W. Zhu, J. Yoon, and H. Tian, *Chem. Soc. Rev.*, 2011, **40**, 79–93.

18. J. C. Pickup, F. Khan, Z.-L. Zhi, J. Coulter, and D. J. S. Birch, *J. Diabetes Sci. Technol.*, 2013, **7**, 62–71.

19. O. Wakao, Y. Fujii, M. Maeki, A. Ishida, H. Tani, A. Hibara, and M. Tokeshi, *Anal. Chem.*, 2015, **87**, 9647–9652.

20. H. Szmacinski and J. R. Lakowicz, *Sensors Actuators B. Chem.*, 1995, **29**, 16–24.

21. J. Spadavecchia, A. Barras, J. Lyskawa, P. Woisel, W. Laure, C. M. Pradier, R. Boukherroub, and S. Szunerits, *Anal. Chem.*, 2013, **85**, 3288–3296.

22. W.-C. Lin, S.-K. Fang, J.-W. Hu, H.-Y. Tsai, and K.-Y. Chen, *Anal. Chem.*, 2014, **86**, 4648–52.

23. A. P. Demchenko, in *Advanced Fluorescence Reporters in Chemistry and Biology II*, 2010, vol. 9, pp. 3–24.

24. T. H. El-Assaad, S. B. Shiring, Y. A. Getmanenko, K. M. Hallal, J.-L. Brédas, S. R. Marder, M. H. Al-Sayah, and B. R. Kaafarani, *RSC Adv.*, 2015, **5**, 43303–43311.

25. C. K. Chiang, C. R. Fincher, Y. W. Park, A. J. Heeger, H. Shirakawa, E. J. Louis, S. C. Gau, and A. G. MacDiarmid, *Phys. Rev. Lett.*, 1977, **39**, 1098–1101.

26. B. Lüssem, M. Riede, and K. Leo, *Phys. Status Solidi*, 2013, **210**, 9–43.

27. K. Walzer, B. Maennig, M. Pfeiffer, and K. Leo, *Chem. Rev.*, 2007, **107**, 1233–1271.

28. F. Ghani, A. Opitz, P. Pingel, G. Heimel, I. Salzmann, J. Frisch, D. Neher, A. Tsami, U. Scherf, and N. Koch, *J. Polym. Sci. Part B Polym. Phys.*, 2015, **53**, 58–63.

29. S. Rossbauer, C. Müller, and T. D. Anthopoulos, *Adv. Funct. Mater.*, 2014, **24**, 7116–7124.

30. C. Z. Li, C. C. Chueh, F. Ding, H. L. Yip, P. W. Liang, X. Li, and A. K. Y. Jen, *Adv. Mater.*, 2013, **25**, 4425–4430.

31. C. D. Weber, C. Bradley, and M. C. Lonergan, *J. Mater. Chem.*, 2014, **2**, 303.

32. Z. Fei, X. Gao, J. Smith, P. Pattanasattayavong, E. Buchaca Domingo, N. Stingelin, S. E. Watkins, T. D. Anthopoulos, R. J. Kline, and M. Heeney, *Chem. Mater.*, 2013, **25**, 59–68.

33. P. Spagnolo, P. Zanirato, and S. Gronowitz, *J. Org. Chem.*, 1982, **47**, 3177–3180.

34. P. A. S. Smith, J. M. Clegg, and J. H. Hall, *J. Org. Chem.*, 1958, **23**, 524–529.

35. P. Zanirato, P. Spagnolo, and G. Zanardi, *J. Chem. Soc. Perkin Trans. 1*, 1983, **3263**, 2551.

36. P. G. M. Wuts and T. W. Greene, in *Greene's Protective Groups in Organic Synthesis*, John Wiley & Sons, Inc., Hoboken, NJ, USA, 2006, pp. 696–926.

37. P. Albers, J. Pietsch, and S. F. Parker, *J. Mol. Catal. A Chem.*, 2001, **173**, 275–286.

38. X. L. Seoane, P. C. L'Argentiere, N. S. Fígoli, and A. Arcoya, *Catal. Letters*, 1992, **16**, 137–148.

39. A. A. Haddach, A. Kelleman, and M. V. Deaton-Rewolinski, *Tetrahedron Lett.*, 2002, **43**, 399–402.

40. D. Alberico, M. E. Scott, and M. Lautens, *Chem. Rev.*, 2007, **107**, 174–238.

41. L.-C. Campeau and K. Fagnou, *Chem. Commun.*, 2006, 1253.

42. K. Okamoto, J. Zhang, J. B. Housekeeper, S. R. Marder, and C. K. Luscombe, *Macromolecules*, 2013, **46**, 8059–8078.

43. T. Satoh and M. Miura, *Chem. Lett.*, 2007, **36**, 200–205.

44. F. Bellina and R. Rossi, *Tetrahedron*, 2009, **65**, 10269–10310.

45. J. Kuwabara, K. Yamazaki, T. Yamagata, W. Tsuchida, and T. Kanbara, *Polym. Chem.*, 2015, **6**, 891–895.

46. F. Bellina, S. Cauteruccio, and R. Rossi, *European J. Org. Chem.*, 2006, **2006**, 1379–1382.

47. F. Bellina, C. Calandri, S. Cauteruccio, and R. Rossi, *Tetrahedron*, 2007, **63**, 1970–1980.

48. L. G. Mercier and M. Leclerc, *Acc. Chem. Res.*, 2013, **46**, 1597–1605.

49. S. W. Chang, H. Waters, J. Kettle, Z. R. Kuo, C. H. Li, C. Y. Yu, and M. Horie, *Macromol. Rapid Commun.*, 2012, **33**, 1927–1932.

50. K. A. Knights, S. G. Stevenson, C. P. Shipley, S.-C. Lo, S. Olsen, R. E. Harding, S. Gambino, P. L. Burn, and I. D. W. Samuel, *J. Mater. Chem.*, 2008, **18**, 2121.

51. A. Brik, C. Y. Wu, M. D. Best, and C. H. Wong, *Bioorganic Med. Chem.*, 2005, **13**, 4622–4626.

52. K. K. Ogilvie, S. L. Beaucage, and M. F. Gillen, *Tetrahedron Lett.*, 1978, **19**, 1663–1666.

53. F. G. Bordwell, *Acc. Chem. Res.*, 1988, **21**, 456–463.

54. F. G. Bordwell, G. E. Drucker, and H. E. Fried, *J. Org. Chem.*, 1981, **46**, 632–635.

55. T. Eicher, S. Hauptmann, and A. Speicher, *The Chemistry of Heterocycles: Structures, Reactions, Synthesis, and Applications*, John Wiley & Sons, 3rd edn., 2013.

56. M. A. Blanchette, W. Choy, J. T. Davis, A. P. Essenfeld, S. Masamune, W. R. Roush, and T. Sakai, *Tetrahedron Lett.*, 1984, **25**, 2183–2186.

57. T. Liang, C. N. Neumann, and T. Ritter, *Angew. Chemie Int. Ed.*, 2013, **52**, 8214–8264.

58. D. Albanese, D. Landini, and M. Penso, *Synthesis*, 1998, **63**, 9587–9589.

59. D. Landini, A. Maia, and A. Rampoldi, *J. Org. Chem.*, 1989, **54**, 328–332.

60. R. A. Minear and L. H. Keith, *Water Analysis Volume II: Inorganic Species, Part 2*, Academic Press Inc., London, 1984, vol. 2.

# *Chapter 6*

# *Conclusions*

This thesis has covered a wide range of topics, primarily focusing on the use of a variety of dithienometallole-containing materials with different bridging heteroatoms in plastic electronics applications. The results shown in **Chapter 2** documented the synthesis and characterisation of the first dithienoarsole-containing conjugated polymers, and explored their use in OFET devices. The copolymer of dithienoarsole and vinylene (**PDTAsV**) showed a promising charge carrier mobility of around 0.08 $cm^2\ V^{-1}\ s^{-1}$, and good overall performance in top gate, bottom contact OFET devices. Whilst copolymers with bithiophene and benzodithiophene (**PDTAsBT** and **PDTAsBDT**, respectively) showed lower device performances, they still showed some promise, with mobilities of $5–6 \times 10^{-3}\ cm^2\ V^{-1}\ s^{-1}$. Comparing **PDTAsBT** with its phosphole-containing analogue indicated that switching phosphorus for arsenic improved device performance whilst maintaining the interesting properties of **PDTPhBT**. Further work showed that the arsenic lone pair could be modified using a variety of different reagents including oxygen, gold, and palladium. A related heterocycle, dithiazoloarsole, was prepared for the first time and its structure examined by X-ray crystallography. The results indicated that the compound was less aromatic than its phosphole analogue, in line with theoretical predictions.

The usefulness of arsole as a donor co-monomer in the development of low band gap polymer for organic photovoltaic devices was further explored in the first half of **Chapter 3**. Using **PDTAsBDT** in an active layer blend with PCBM proved disappointing, with a PCE of only 0.42% being obtained, however replacing alkyl side chains on the BDT units with pendant alkylthienyl groups led to significant improvements in efficiency, with PCEs of 2.73 and 4.04% being achieved for **PDTAsBDT-TBO** and **PDTAsBDT-TEH**, respectively. Despite this improvement, the PCEs of these polymers were still below that obtained by the Park group, who have investigated a phosphole-oxide-containing analogue of the 2D-PDTAsBDT polymers and achieved a maximum PCE of 6.10%. The reasons for this difference are unclear, although some speculations were made regarding the oxidation state of the pnictogen and the morphology of

the active layer. However, further studies and a more direct comparison would be needed to confirm either of these theories.

The second half of **Chapter 3** investigated novel donor-acceptor polymers utilizing the aforementioned 2-D BDT monomers as electron donors and 4,7-bis(thiophen-2-yl)-5,6-dicyano-2H-benzo[*d*][1,2,3]triazole as an electron acceptor. It was found that longer butyloctyl side chains were required to ensure polymer solubility, and the impact of various device configurations on performance was investigated, with the highest PCE obtained being 6.93% for **PDCBTzBDT-TBO** with a PEDOT:PSS hole transporting layer.

The effect of changing the bridging heteroatom of dithienometallole systems on the optoelectronic properties of polymers was studied in **Chapter 4**. A dithieno[3,2-*b*;2',3'-*d*]pyrrole molecule was synthesised and polymerised with thieno[3,2-*b*]thiophene, and the resulting material (**PDTP-TT**) was compared with analogous materials with silyl, germyl, and carbonyl bridging groups. Despite the molecular weights of the materials showing some variation, it was found that their optoelectronic properties were significantly affected by the bridged group, and the results were rationalised using DFT calculations. When used in OFET devices, it was found that the more planar polymers (which also had higher molecular weights) outperformed the more twisted materials with shorter chains, with **PDTP-TT** not producing any useable data at all.

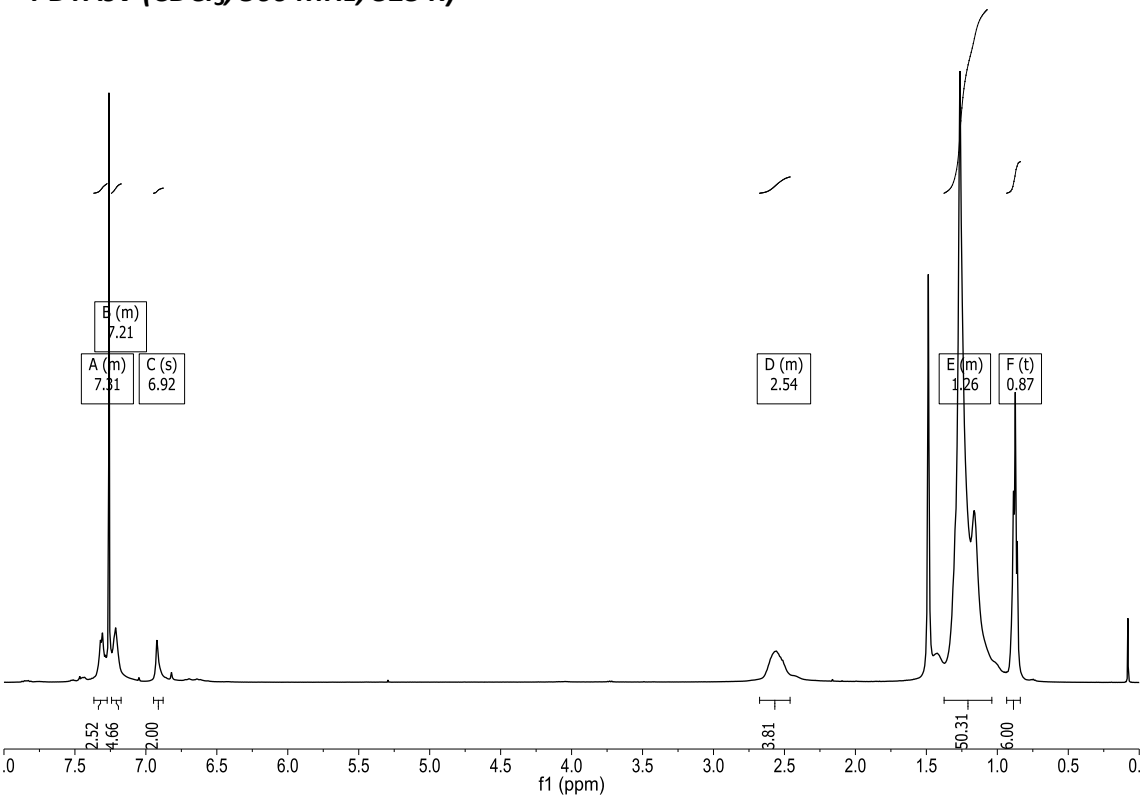
The final experimental chapter described the synthesis and method of action of a dithienopyrrole-based colorimetric sensor for strong bases such as tetralkylammonium salts, sodium hydride, and *n*-butyl lithium. These analytes could deprotonate the secondary amine that bridged the dithienopyrrole system, resulting in a red shift in $\lambda_{max}$ of over 80 nm. It was found that the $pK_A$ of the sensor was approximately 15.9, which is in agreement with the reported $pK_A$s of related pyrrolic-nitrogen-containing ring systems. The behaviour of the sensor with respect to other analytes was rationalised on the basis of the acidity of the pyrrolic nitrogen – for example, it explains the lack of deprotonation in the presence of DBU. Although

the degree of deprotonation was found to be dependent on the $pK_A$ of the anion of the tetraalkylammonium salt, varying the anion had no effect on the position of $\lambda_{max}$, while varying the cation had a measurable impact on the position of $\lambda_{max}$, indicating that charge density and charge screening could have an impact on the response of the sensor. The peripherally alkylated dithienopyrrole unit was also included in polymeric systems that showed potential for use either as a sensor or as an n-dopable material for organic electronics applications. As with the small molecule, the deprotected polymers reacted with tetrabutylammonium salts, resulting in the appearance of a new peak in the UV-vis absorption spectrum. Future work will be required to establish whether the mechanism of action is similar to the small molecule, and to determine what impact the reaction with tetrabutylammonium salts has on the electronic properties of the material.

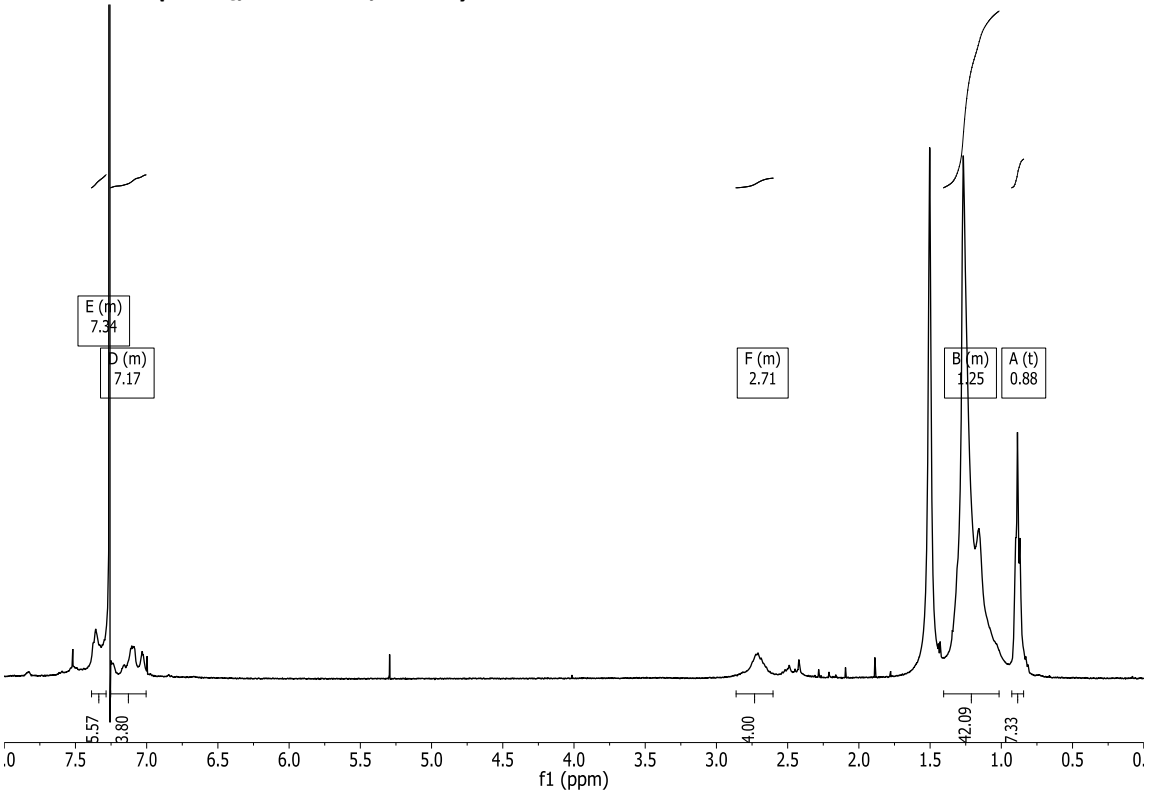
Overall, the results presented give a good overview of the versatility of the dithienometallole ring system, and show that its properties can be influenced by changing the heteroatom. The highly novel dithienoarsole moiety represents a new class of material for use in organic electronics, with the potential to combine the interesting properties of the phosphole analogue with increased air stability and potentially more selective alteration of the lone pair. Whilst peripherally alkylated dithienopyrroles were less promising candidates for OFET device, they still showed some interesting trends when compared with silyl, germyl, and carbonyl analogues. In addition, dithienopyrroles with secondary amine bridging groups were capable of acting as sensors for a variety of strong bases, both in small molecules and in polymeric systems.

## *Appendix A – Polymer $^{1}H$ NMR spectra*

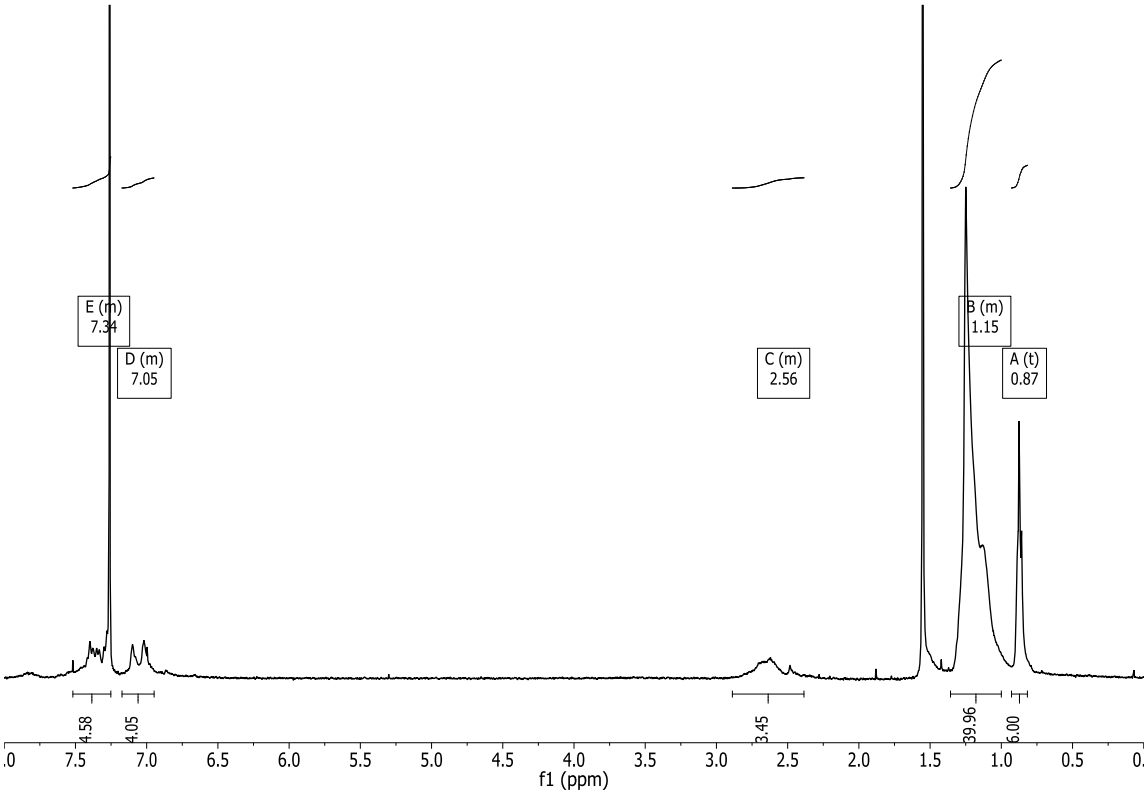
### *PDTAsV ($CDCl_3$, 500 MHz, 323 K)*



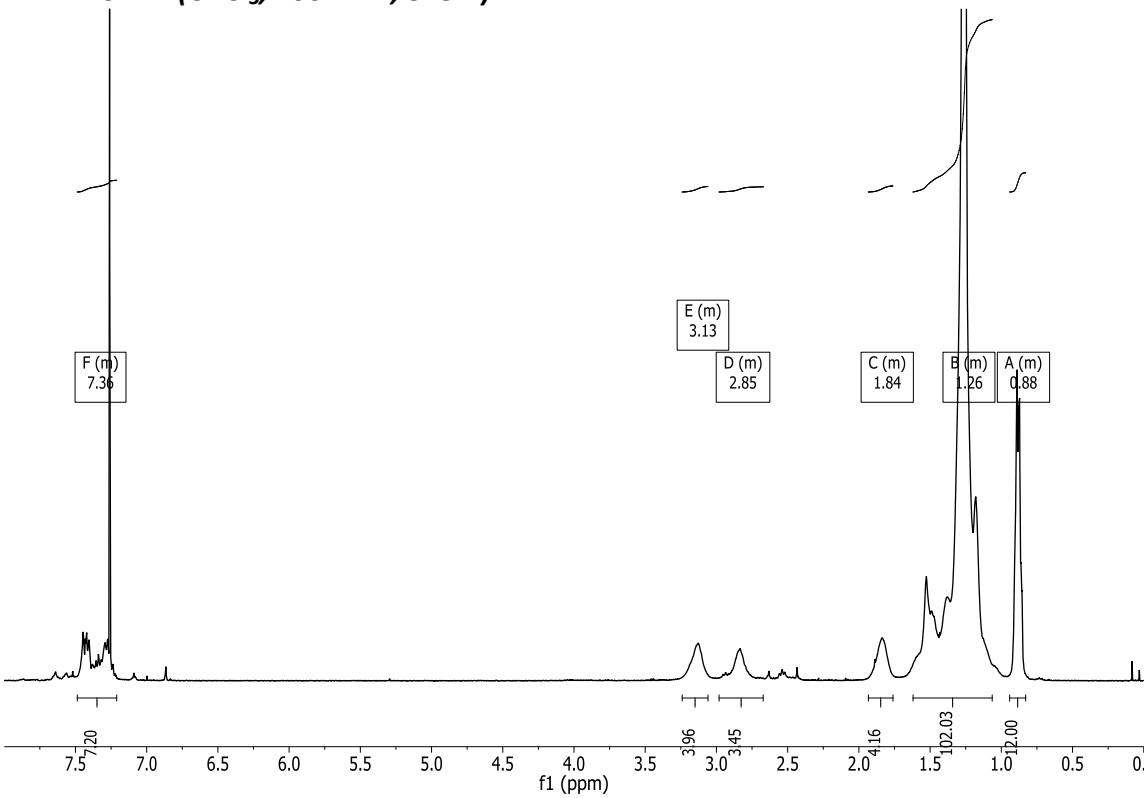

### *PDTAsBT ($CHCl_3$, 400 MHz, 323 K)*



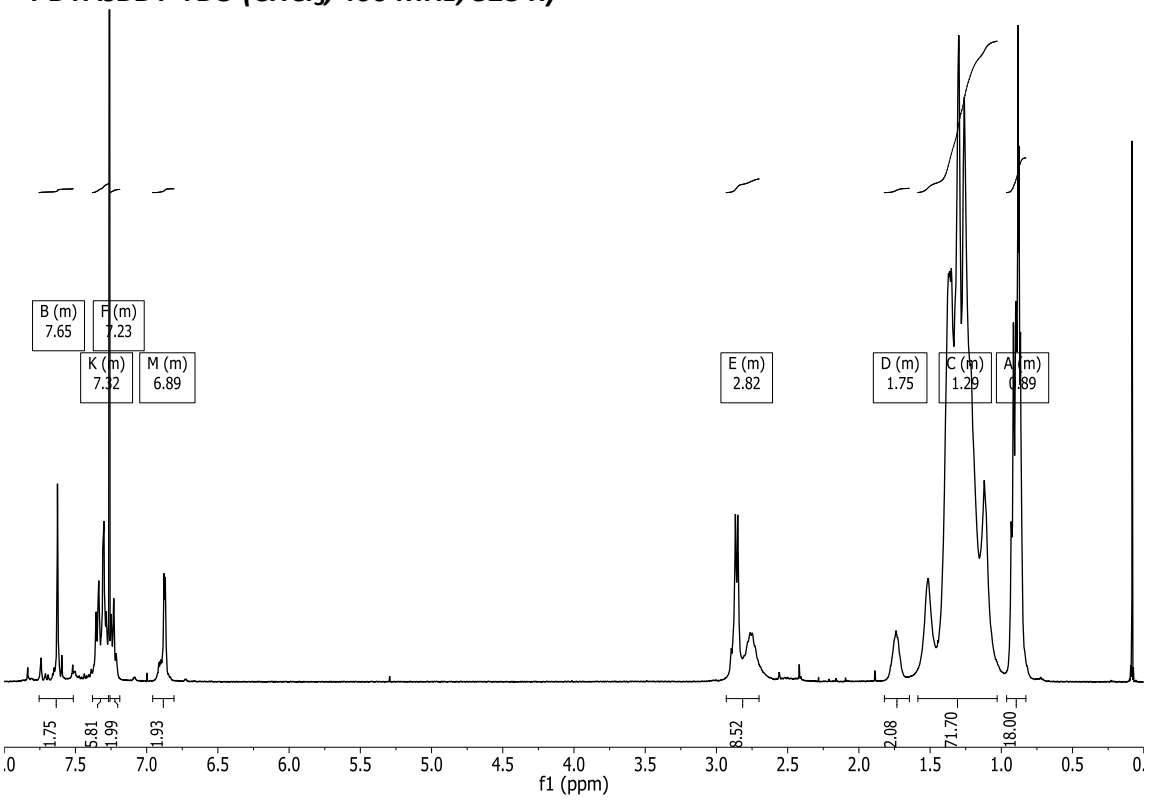
***PDTPhBT ($CHCl_3$, 400 MHz)***



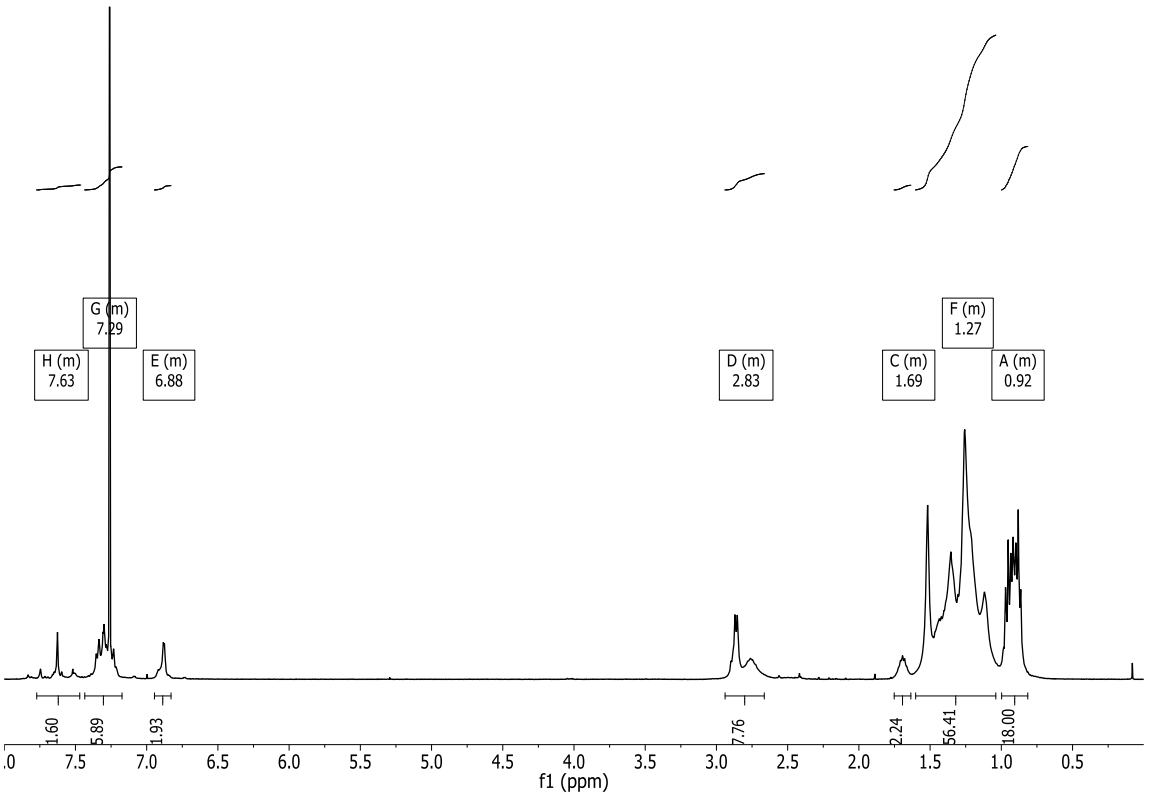

***PDTAsBDT ($CHCl_3$, 400 MHz, 323 K)***



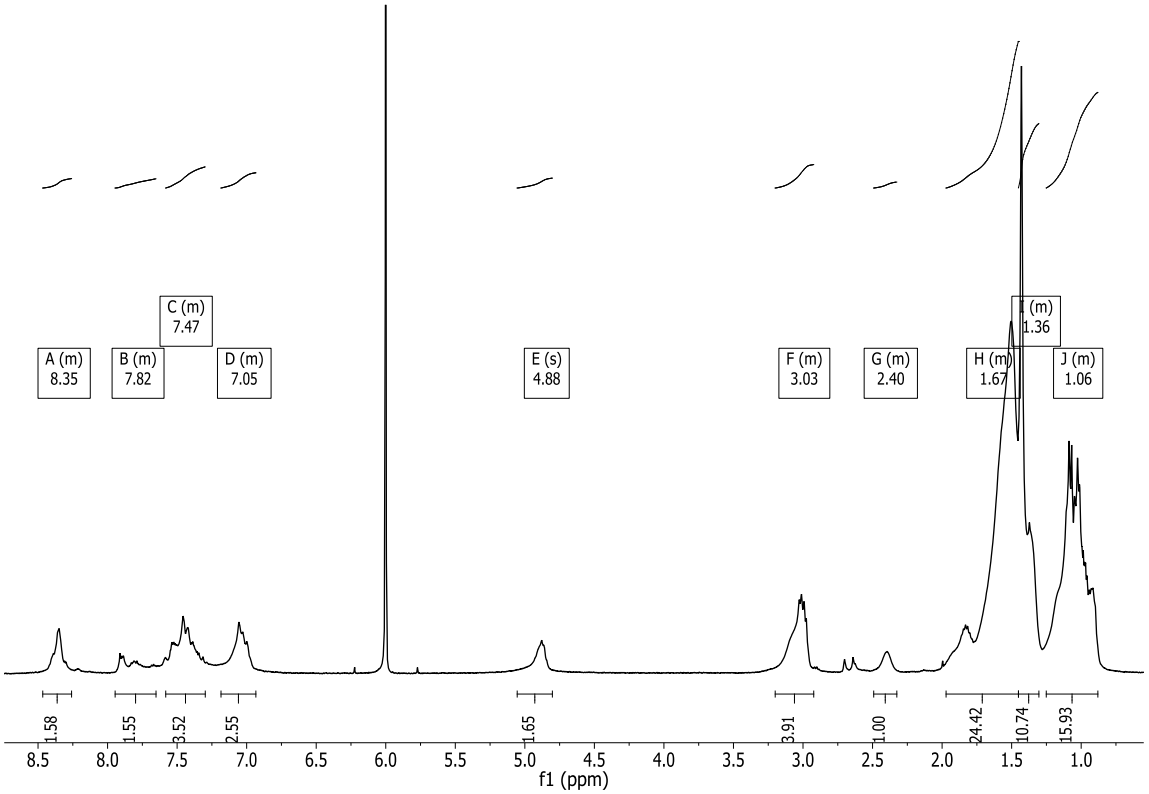
***PDTAsBDT-TBO ($CHCl_3$, 400 MHz, 323 K)***



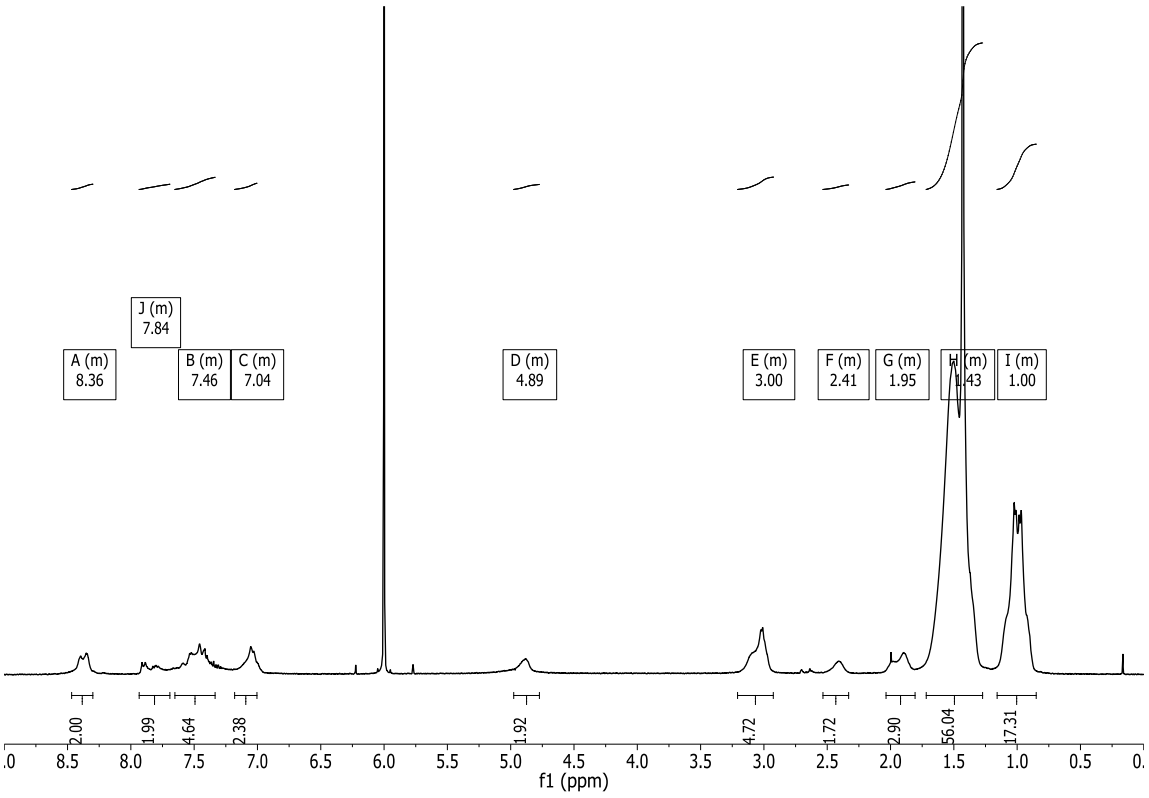

***PDTAsBDT-TEH ($CHCl_3$, 400 MHz, 323 K)***



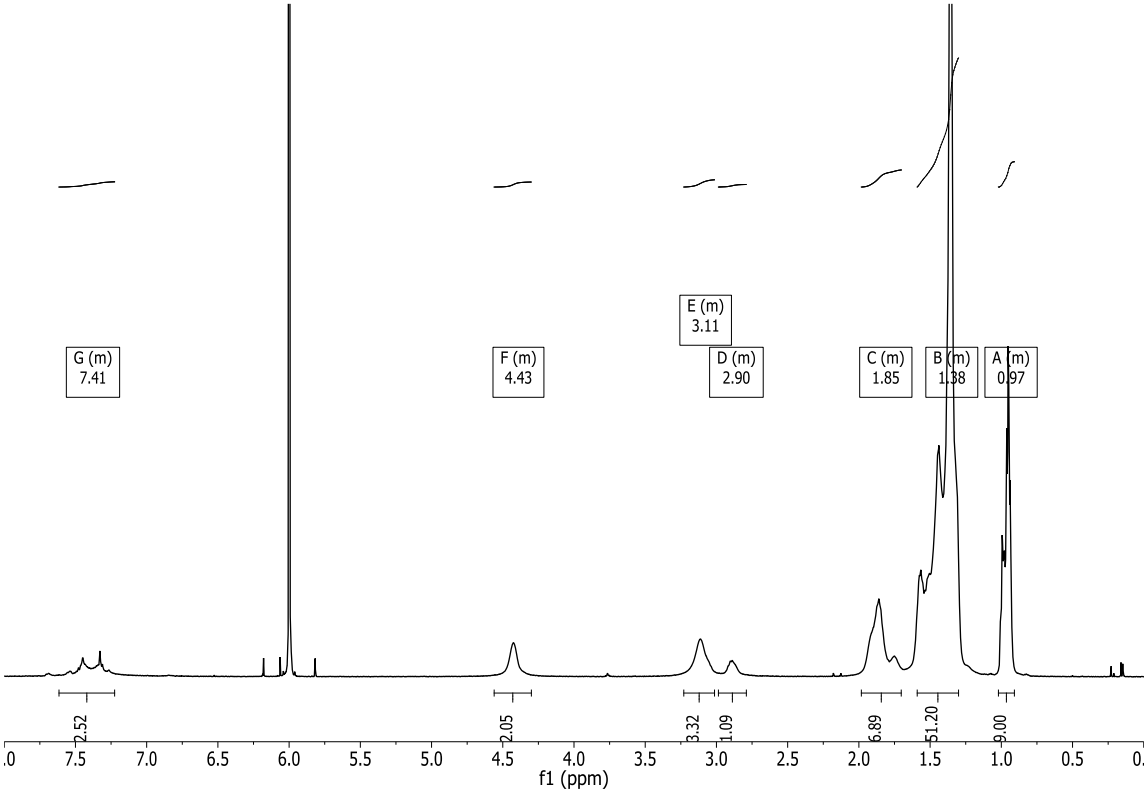
***PDCBTzBDT-TEH (400 MHz, TCE-$d_2$, 403 K)***



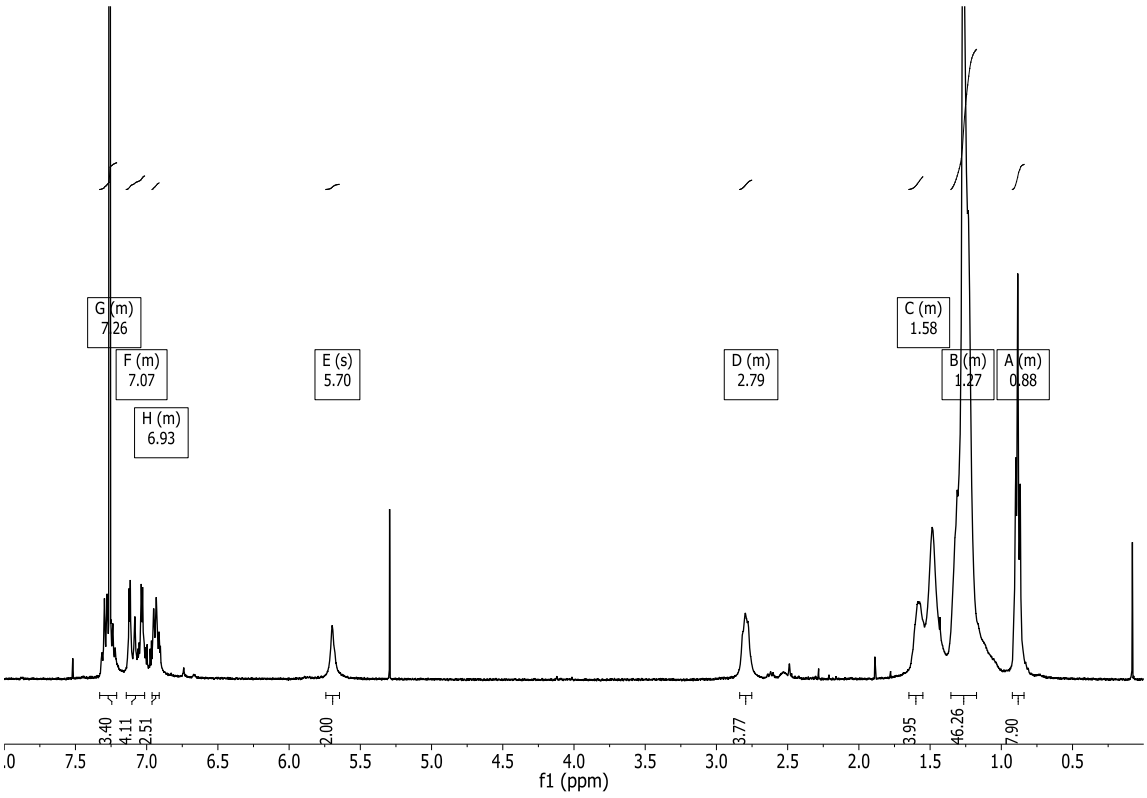

***PDCBTzBDT-TBO (400 MHz, TCE-$d_2$, 403 K)***



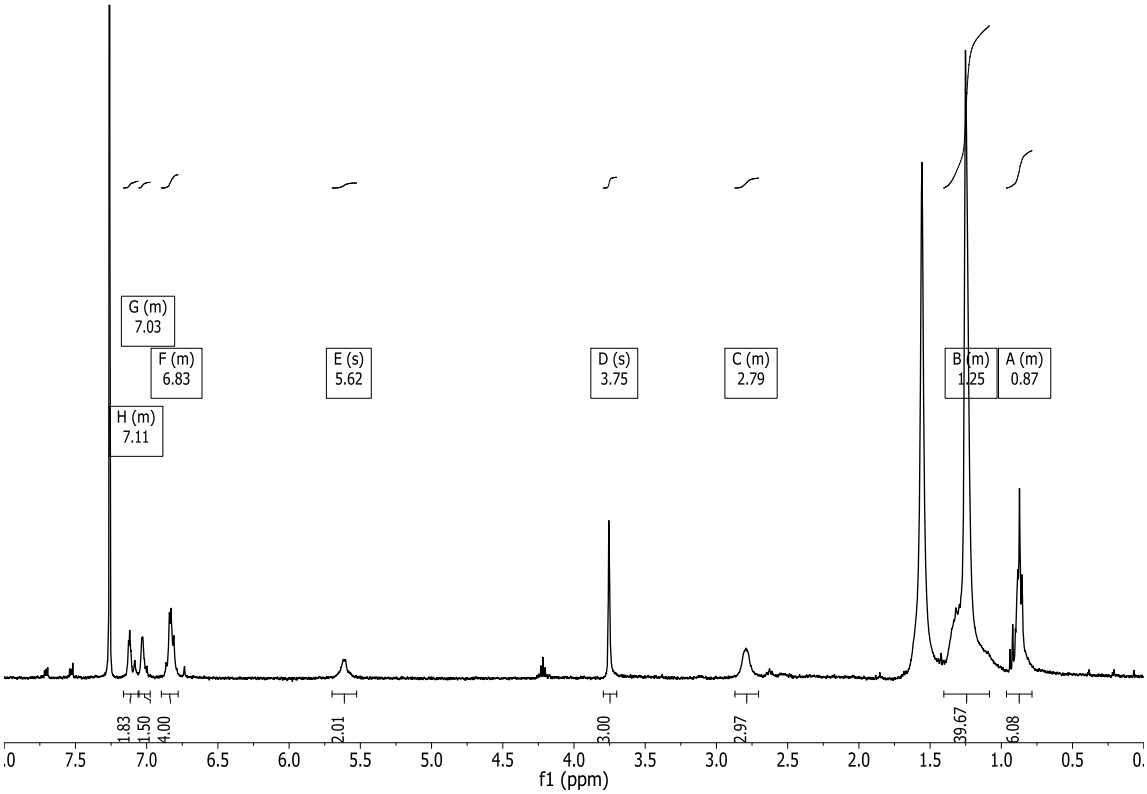
***PDTP-TT (500 MHz, TCE-$d_2$, 373 K)***



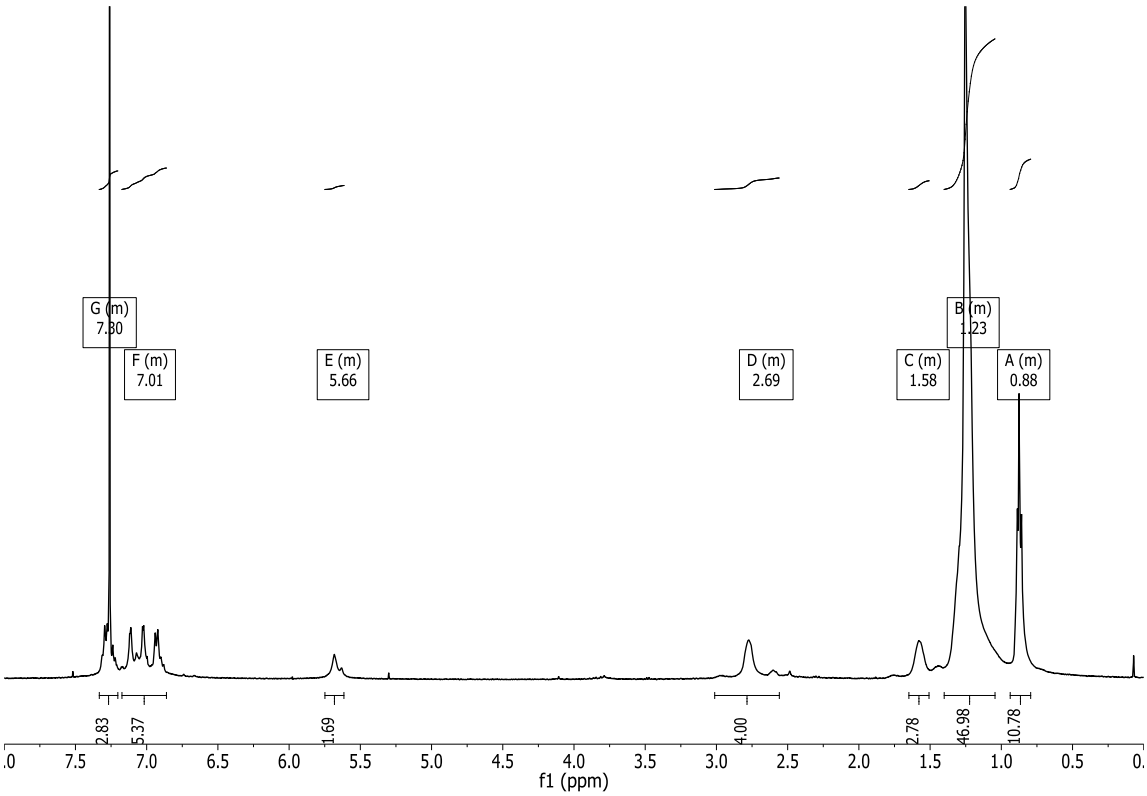

***PNBDTPBT (400 MHz, $CDCl_3$, 323 K)***



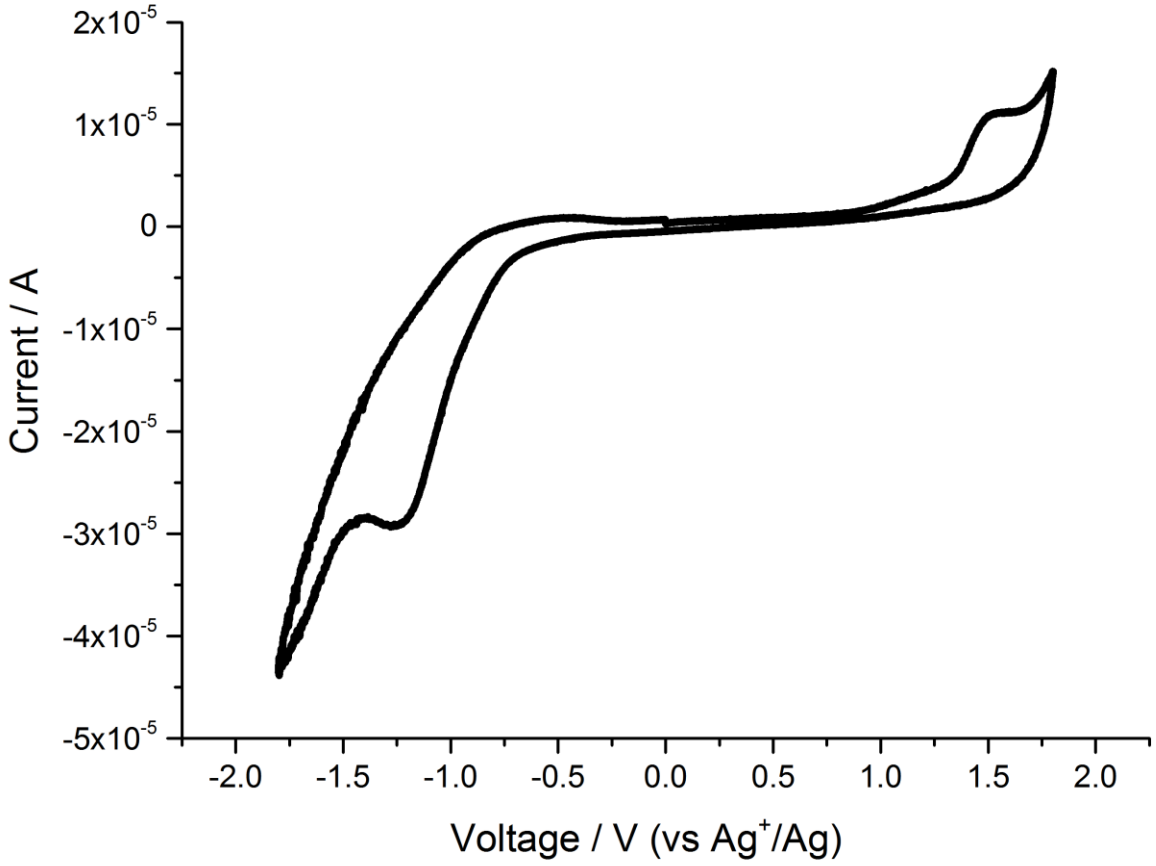
***PNOMeBDTPBT (400 MHz, $CDCl_3$)***




***PNHDTPBT-1***



***Appendix B – CV of blank FTO-coated glass***




**Cyclic voltammogram of blank FTO-coated glass slides in a 0.1 M $[Bu_4N][PF_6]$ acetonitrile solution at a scan rate of 50 mV $s^{-1}$. Oxidation and reduction peaks were each measured using pristine slides.**

## *Appendix C – Cystallographic data*

### *X-ray crystal structure data for 2.21*

Table 1. Crystal data and structure refinement for 2.21

| | |
|---|---|
| Formula | C12 H7 As N2 S2 |
| Formula weight | 318.24 |
| Temperature | 173(2) K |
| Diffractometer, wavelength | Agilent Xcalibur 3 E, 0.71073 Å |
| Crystal system, space group | Orthorhombic, Pbca |
| Unit cell dimensions | a = 7.43156(17) Å α = 90° |
| | b = 17.1951(5) Å β = 90° |
| | c = 18.4840(5) Å γ = 90° |
| Volume, Z | 2362.01(11) $Å^3$, 8 |
| Density (calculated) | 1.790 $Mg/m^3$ |
| Absorption coefficient | 3.206 $mm^{-1}$ |
| F(000) | 1264 |
| Crystal colour / morphology | Green blocks |
| Crystal size | 0.57 x 0.48 x 0.30 $mm^3$ |
| θ range for data collection | 2.613 to 28.188° |
| Index ranges | -8<=h<=9, -11<=k<=21, -23<=l<=15 |
| Reflns collected / unique | 5387 / 2389 [R(int) = 0.0168] |
| Reflns observed [F>4σ(F)] | 2039 |
| Absorption correction | Analytical |
| Max. and min. transmission | 0.456 and 0.332 |
| Refinement method | Full-matrix least-squares on $F^2$ |
| Data / restraints / parameters | 2389 / 0 / 155 |
| Goodness-of-fit on $F^2$ | 1.043 |
| Final R indices [F>4σ(F)] | R1 = 0.0253, wR2 = 0.0525 |
| R indices (all data) | R1 = 0.0338, wR2 = 0.0558 |
| Largest diff. peak, hole | 0.356, -0.349 $eÅ^{-3}$ |
| Mean and maximum shift/error | 0.000 and 0.002 |

Table 2. Bond lengths [Å] and angles [°] for 2.21

| | |
|---|---|
| As(1)-C(12) | 1.954(2) |
| As(1)-C(2) | 1.955(2) |
| As(1)-C(11) | 1.960(2) |
| C(2)-C(6) | 1.368(3) |
| C(2)-N(3) | 1.369(3) |
| N(3)-C(4) | 1.300(3) |
| C(4)-S(5) | 1.728(3) |
| S(5)-C(6) | 1.710(2) |
| C(6)-C(7) | 1.443(3) |
| C(7)-C(11) | 1.370(3) |
| C(7)-S(8) | 1.706(2) |
| S(8)-C(9) | 1.725(2) |
| C(9)-N(10) | 1.306(3) |
| N(10)-C(11) | 1.370(3) |
| C(12)-C(13) | 1.386(3) |
| C(12)-C(17) | 1.389(3) |
| C(13)-C(14) | 1.383(3) |
| C(14)-C(15) | 1.378(3) |
| C(15)-C(16) | 1.378(4) |
| C(16)-C(17) | 1.387(3) |

| | |
|---|---|
| C(12)-As(1)-C(2) | 99.91(9) |
| C(12)-As(1)-C(11) | 97.89(9) |
| C(2)-As(1)-C(11) | 83.85(9) |
| C(6)-C(2)-N(3) | 115.8(2) |
| C(6)-C(2)-As(1) | 112.65(16) |
| N(3)-C(2)-As(1) | 131.44(17) |
| C(4)-N(3)-C(2) | 109.4(2) |
| N(3)-C(4)-S(5) | 116.25(18) |
| C(6)-S(5)-C(4) | 88.34(11) |
| C(2)-C(6)-C(7) | 115.4(2) |
| C(2)-C(6)-S(5) | 110.25(17) |
| C(7)-C(6)-S(5) | 134.37(18) |
| C(11)-C(7)-C(6) | 115.3(2) |
| C(11)-C(7)-S(8) | 110.08(16) |
| C(6)-C(7)-S(8) | 134.55(18) |
| C(7)-S(8)-C(9) | 88.48(11) |
| N(10)-C(9)-S(8) | 116.54(17) |
| C(9)-N(10)-C(11) | 108.7(2) |
| N(10)-C(11)-C(7) | 116.2(2) |
| N(10)-C(11)-As(1) | 131.29(17) |
| C(7)-C(11)-As(1) | 112.47(16) |
| C(13)-C(12)-C(17) | 119.2(2) |
| C(13)-C(12)-As(1) | 117.39(16) |
| C(17)-C(12)-As(1) | 123.45(18) |
| C(14)-C(13)-C(12) | 120.4(2) |
| C(15)-C(14)-C(13) | 120.3(2) |
| C(16)-C(15)-C(14) | 119.7(2) |
| C(15)-C(16)-C(17) | 120.4(2) |
| C(16)-C(17)-C(12) | 120.0(2) |

***Structures used to calculate C=As bond lengths***

| Cambridge Crystallographic Data Centre Reference Number | C=As Bond Length (Å) |
|---|---|
| CADMID | 1.822 |
| HELPOD | 1.842 |
| JUXBAF | 1.816 |
| LOSHOQ | 1.847 |
| RUNWEC | 1.899 |
| RUQGUF | 1.807 |
| TOGQIP | 1.857 |
| WADCOT | 1.921 |
| XIQBII | 1.790 |
| YINJEK | 1.867 |

***Structures used to calculate C=P bond lengths***

| Cambridge Crystallographic Data Centre Reference Number | C=P Bond Length (Å) |
|---|---|
| ABINOP | 1.674 |
| ABINUV | 1.673 |
| ANUMAS | 1.708 |
| ANUQEH | 1.715 |
| BETPUN | 1.743 |
| BETQAU | 1.734 |
| BIBMEF | 1.623 |
| BOGLIU | 1.678 |
| BUPRAG | 1.687 |
| CALLIM | 1.703 |
| CECKON | 1.73 |
| CENGEH | 1.691 |
| COQYOY | 1.691 |
| COQYUE | 1.688 |
| DAKTUF | 1.643 |
| DAVFOW | 1.701 |
| DIJVIC | 1.74 |
| DOTJON | 1.719 |
| DOTKEE | 1.729 |

VIP Polymers Very Important Paper

International Edition: DOI: 10.1002/anie.201602491
German Edition: DOI: 10.1002/ange.201602491

# An Air-Stable Semiconducting Polymer Containing Dithieno[3,2-*b*:2′,3′-*d*]arsole

*Joshua P. Green, Yang Han, Rebecca Kilmurray, Martyn A. McLachlan, Thomas D. Anthopoulos, and Martin Heeney**

***Abstract:*** *Arsole-containing conjugated polymers are a practically unexplored class of materials despite the high interest in their phosphole analogues. Herein we report the synthesis of the first dithieno[3,2-b;2′,3′-d]arsole derivative, and demonstrate that it is stable to ambient oxidation in its +3 oxidation state. A soluble copolymer is obtained by a palladium-catalyzed Stille polymerization and demonstrated to be a p-type semiconductor with promising hole mobility, which was evaluated by field-effect transistor measurements.*

Since the first reports of the metallic behavior of conjugated polymers (CPs), the development of new materials has been at the forefront of research in plastic electronics.[1,2] The enormous scope to tune their optoelectronic characteristics and device performance by the copolymerization of different monomeric units is appealing for many applications.[3] In recent years, there has been a growing interest in the incorporation of heavier elements—silicon and germanium in Group 14, phosphorus in Group 15, selenium and tellurium in Group 16—as replacements for lighter elements, such as carbon, nitrogen, and sulfur, in CPs.[4–7] Their use has been shown to have a significant impact on the polymer band gap and energy levels, as well as the solid-state packing.[8] The inclusion of heavy atoms can also facilitate intersystem crossing, leading to the rapid conversion of singlet excitons into triplets, and can lead to solid-state phosphorescence.[9,10]

Among the CPs containing Group 15 elements, those incorporating a dithienometallole (Figure 1) have garnered much attention. For example, dithieno[3,2-*b*:2′,3′-*d*]pyrrole (X = N) and dithieno[3,2-*b*:2′,3′-*d*]phosphole (X = P, DTP) have seen application in all major areas of plastic electronics.[11–13] The interest in DTPs partially arises from their high electron affinity, which results from the σ–π hyperconjugation exhibited by the phosphole ring, whereby the σ* orbital of the exocyclic P–C bond is able to interact with the π* orbitals of the fused heterocycle.[14] Furthermore, modification of the P lone pair, through reactions with either Lewis acids or oxidizing agents, can further tune the energy levels.[15] However, as phosphole derivatives are prone to uncontrolled oxidation in ambient atmosphere, the phosphole oxide is often deliberately formed to prevent uncontrolled aging.[16] As such, the properties of the unoxidized phospholes are rarely reported.

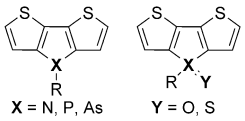



***Figure 1.*** Structures of pnictogen-containing dithienometalloles.

Inspired by the fascinating properties of DTP, we were interested in preparing the heavier analogue containing a bridging arsenic atom. Of particular interest was the fact that arsenic-containing compounds are typically more difficult to oxidize to the +5 oxidation state than their P analogues.[17–19] This is related to the poor shielding of the filled 3d orbitals in As, such that the s electrons are relatively tightly bound compared to those in the corresponding phosphorus-based compounds. Therefore, arsole-containing polymers may be intrinsically more resistant to ambient oxidation than their phosphole equivalents, allowing the properties of the heterocycle in the +3 oxidation state to be explored. As far as we are aware, there have been no reports of the use of arsole-containing materials in organic electronics and only limited examples of conjugated polymers containing arsenic in the backbone, mostly related to poly(vinylene arsine)s.[20–22]

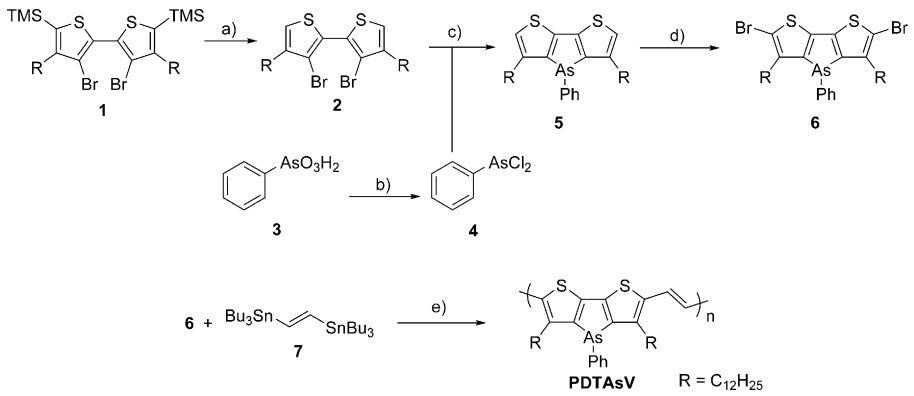
Herein, we present the first synthesis of a dithienoarsole (DTAs) monomer and demonstrate that it is stable to oxidation under ambient conditions. Significantly, we show that it is possible to directly polymerize the DTAs derivative in its +3 oxidation state by a palladium-catalyzed Stille polymerization. To the best of our knowledge, the equivalent Pd-catalyzed polymerizations with DTP derivatives have only been reported for the +5 oxidation state (commonly DTP oxides).[16] To demonstrate the utility of the DTAs building block, we synthesized the vinylene copolymer PDTAsV (see Scheme 1), in which the vinylene comonomer plays an important role in allowing the backbone to planarize, thereby leading to a promising organic field effect transistor (OFET) performance.[23,24]

[*] J. P. Green, Dr. Y. Han, Prof. M. Heeney
Department of Chemistry and Centre for Plastic Electronics
Imperial College London
London, SW7 2AZ (UK)
E-mail: m.heeney@imperial.ac.uk
Dr. Y. Han, Prof. T. D. Anthopoulos
Department of Physics and Centre for Plastic Electronics
Imperial College London (UK)
R. Kilmurray, Prof. M. A. McLachlan
Department of Materials and Centre for Plastic Electronics
Imperial College London (UK)

Supporting information and the ORCID identification number(s) for the author(s) of this article can be found under http://dx.doi.org/10.1002/anie.201602491. Additional data can be found under doi.org/10.6084/m9.figshare.3171586.

 © 2016 Wiley-VCH Verlag GmbH & Co. KGaA, Weinheim 

One issue in planning a synthetic route to DTAs is the toxicity of many arsenic-containing precursors. We therefore utilized dichlorophenylarsine as the arsenic building block as its synthesis from a readily available precursor in one step is well established.[25] Although it is a strong lachrymator and vesicant, it has a history of safe use in synthetic chemistry.[26] However, one potential drawback of dichlorophenylarsine is that the resulting 4-phenyldithieno[3,2-*b*;2′,3′-*d*]arsole (DTAs) would only have a phenyl substituent as the solubilizing sidechain, possibly resulting in polymers with limited solubility. As such, we incorporated additional dodecyl sidechains into the peripheral positions of the DTAs to ensure good polymer solubility and processability.




***Scheme 1.*** Synthesis and polymerization of the dithienoarsole monomer. Reaction conditions: a) tetrabutylammonium fluoride (TBAF), THF, 0 °C; b) HCl, $SO_2$, 55 °C; c) *n*-BuLi (2.2 equiv), −78 °C→RT; d) lithium diisopropylamide (LDA), −78 to −30 to −78 °C, $CBr_4$; e) $Pd(PPh_3)_4$, chlorobenzene, microwave reactor.

The synthesis of the DTAs monomer is shown in Scheme 1. Compound **1**[27] was desilylated with TBAF, and the resulting compound **2** was reacted with *n*-BuLi at −78 °C, followed by quenching of the resulting dianion with dichlorophenylarsine to afford dithienoarsole **5** in 57 % yield. Attempts to brominate **5** under electrophilic conditions (NBS) resulted in some competing oxidization of the arsole ring to the arsole oxide. However, **5** could be cleanly brominated in 60 % yield by dilithiation with LDA at low temperature, followed by the addition of carbon tetrabromide as a non-oxidizing halogen source.

With monomer **6** in hand, we investigated its oxidation to the arsole oxide, initially using hydrogen peroxide, which gives almost quantitative yields when used to oxidize dithienophosphole.[13] However, the reaction was found to be low-yielding when DTAs was used, with around 60 % of the unoxidized material being recovered. Using *meta*-chloroperoxybenzoic acid as a stronger oxidant resulted in an improved yield of the oxide of **6**, although starting material still remained even with excess *m*-CPBA. The oxidation was readily monitored by $^1$H NMR spectroscopy, with the phenyl resonances shifting downfield and splitting upon oxidation (Figure 2). In agreement with the reduced reactivity of the monomer compared to DTP, samples of **6** stored under ambient conditions displayed no signs of oxidation after six months. The reluctance of the DTAs to oxidize is in agreement with the poor shielding ability of the filled 3d orbitals, and is in stark contrast to the DTP analogue. We note that 2,5-diarylarsoles were very recently be reported to be more air-stable than their phosphole analogues.[28]

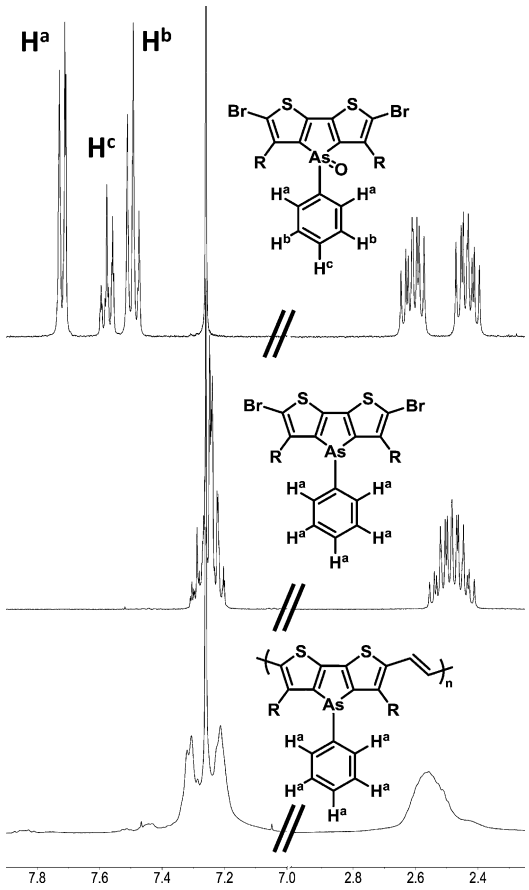



***Figure 2.*** Comparison of the $^1$H NMR spectra of **6** (middle), the oxide of **6** (top), and PDTAsV (bottom) between 7.10–7.90 ppm.

Stille polymerization of **6** with *trans*-1,2-bis(tributylstannyl)ethene using catalytic $Pd(PPh_3)_4$ was performed in a microwave reactor to yield PDTAsV (Scheme 1). Gratifyingly, the presence of the arsenic atom, a possible site for binding to the Pd catalyst, did not seem to have any detrimental effects. This finding is in line with the weaker donicity of triphenylarsine versus triphenylphosphine as ligands for palladium.[29] After precipitation and work-up, PDTAsV was obtained as a dark blue polymer of reasonable molecular weight ($M_n$ = 12.3 kDa, Đ = 1.9 by size exclusion chromatography).

The chemical structure of the polymer was confirmed by a combination of elemental analysis and $^1$H NMR spectroscopy. Although the $^1$H NMR resonances were significantly

 © 2016 Wiley-VCH Verlag GmbH & Co. KGaA, Weinheim 

These are not the final page numbers!

broadened in comparison to the monomer material, no signals attributable to uncontrolled oxidation to the arsole oxide were observed (Figure 2). Together with the matching elemental analysis, these results provide good evidence for the stability of the polymer under the polymerization conditions.

The absorption spectra of PDTAsV in chlorobenzene solution and as a thin film are shown in Figure 3a. In solution,

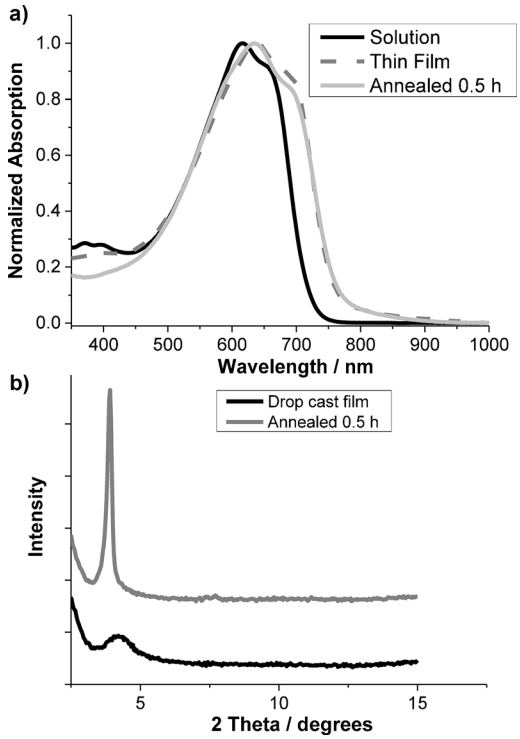



***Figure 3.*** a) UV/Vis absorption spectra of PDTAsV in chlorobenzene solution (black), as a thin film on a glass slide (dashed), and after annealing at 200 °C for 30 min (gray). b) XRD patterns of PDTAsV films drop-cast onto silicon wafers, as-cast (black) and after annealing at 200 °C for 30 min (gray). Traces offset for clarity.

PDTAsV shows an absorption maximum ($\lambda_{max}$) at 616 nm with a pronounced shoulder ($\lambda_{sh}$) at 652 nm. Upon film formation, the $\lambda_{max}$ value of PDTAsV was red-shifted to 638 nm, whereas $\lambda_{sh}$ was shifted to 682 nm. The red shift is suggestive of enhanced molecular ordering compared to the solution state. Further evidence of solid-state ordering was obtained by X-ray diffraction (XRD) of drop-cast films before and after thermal annealing for 30 min at 200 °C (Figure 3b). The as-cast sample displayed a broad, low-intensity peak with a *d*-spacing of 21.0 Å. Upon annealing, this peak became sharper and significantly enhanced in intensity, which is indicative of an increase in molecular ordering. The *d*-spacing increased to 22.6 Å, which is very similar to the value observed for other bridged bithiophene–vinylene co-polymers with dodecyl sidechains, and attributed to the distance between conjugated backbones in a lamellar-type arrangement.[30]

The XRD data and UV/Vis spectra suggest that the polymer is able to planarize and crystallize in the solid state. To further probe the monomer and polymer geometries, DFT calculations were performed at the B3LYP level of theory with the 6-311G(d,p) basis set. Initially considering the monomer, the calculations predicted the bridged bithiophene to be perfectly co-planar whilst the phenyl group attached to the bridging arsenic atom is twisted orthogonally to the fused-ring structure, and is almost perpendicular to the molecular plane (Figure 4a). The predicted frontier molecular orbitals

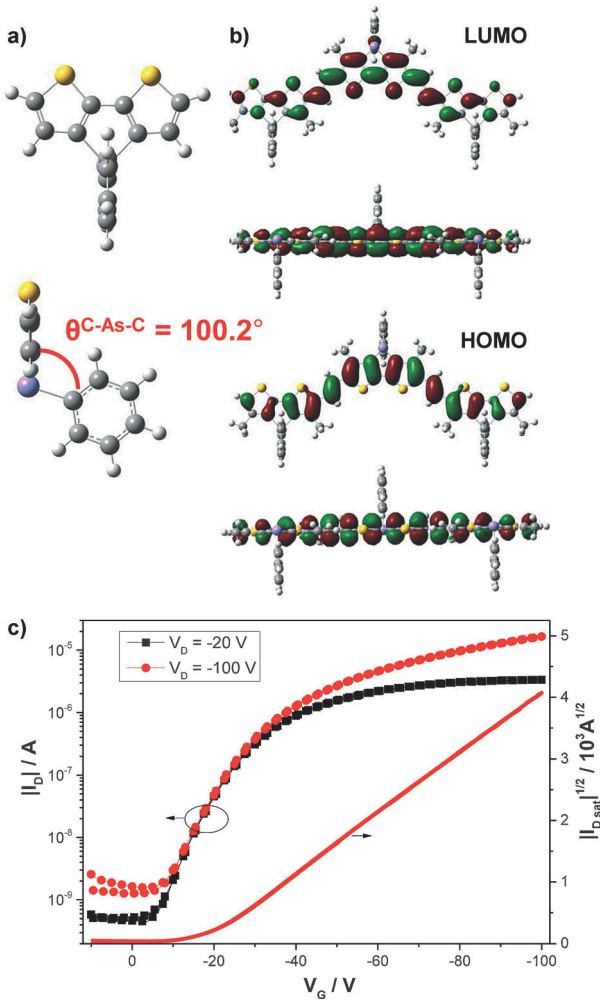



***Figure 4.*** a) Predicted geometry of the dithienoarsole monomer and b) frontier molecular orbitals of PDTAsV, as calculated by DFT [B3LYP, 6-311G(d,p)]. c) Representative transfer characteristics measured with a top-gate/bottom-contact architecture in nitrogen atmosphere at room temperature.

(Supporting Information, Figure S11) show that the highest occupied molecular orbital (HOMO) has a nodal plane through the arsenic atom whereas the lowest unoccupied molecular orbital (LUMO) has some contribution from the σ* orbital of the As–Ph bond.

Moving to the polymeric system, minimum energy models of the trimer predict a highly planar backbone with twists of $<1°$ between the DTAs and adjacent double bonds (Figure 4b). The insertion of the double bond between the head-to-head dodecyl sidechains clearly reduces any undesirable torsional twisting between the DTAs units. Furthermore, the


© 2016 Wiley-VCH Verlag GmbH & Co. KGaA, Weinheim

side-on view clearly shows that the phenyl rings protrude perpendicularly to the conjugated backbone. Note that in the minimum-energy conformer shown, the phenyl groups are predicted to alternate above and below the plane of the backbone, but there is no energy difference between trimers with alternative arrangements, and we therefore expect a random arrangement in the actual polymer. It is also worth noting that the barrier to inversion of the phenyl group in arsole has been predicted to be large owing to the limited p character of the lone pair,[31] and we would expect similar in DTAs. Finally, the frontier molecular orbital calculations (Figure 4b) show that whereas both the HOMO and LUMO are extensively delocalized over the polymer backbone, only the LUMO has a significant contribution on the As bridge, similar to the monomer.

Finally, we tested the electrical performance of PDTAsV in a top-gate/bottom-contact transistor geometry. The PDTAsV was annealed at 200 °C for 30 min prior to deposition of the gate dielectric (Cytop™). As can be seen in Figure 4c, the devices displayed p-type behavior, with negligible hysteresis between the forward and reverse sweeps. The polymer exhibited promising average hole mobilities, measured in saturation, of 0.08 $cm^2 V^{-1} s^{-1}$, with a current on/off ratio of approximately $10^4$. Importantly, the hole mobility was relatively independent of the gate voltage, and did not display the peak observed at low gate voltage for some materials (Figure S12). To the best of our knowledge, this is the only report of an arsole-containing compound exhibiting macroscopic charge transport in an electronic device. The promising performance suggests that the presence of the arsenic bridging group with the phenyl substituent does not inhibit the close overlap of the conjugated backbones needed for charge transport.

In conclusion, we have reported the synthesis of the first dithienoarsole heterocycle and shown that unlike the analogous dithienophosphole, it is stable to oxidation in the presence of ambient air. We incorporated the dithienoarsole into a soluble conjugated polymer backbone, which can aggregate and crystallize in the solid state and demonstrates promising charge-carrier mobility in OFET devices. We believe that these results show that dithienoarsole is an interesting building block for organic electronics. In particular, the opportunity to tune the oxidation state of the bridging arsenic atom may offer interesting opportunities for the utilization of these materials in sensing applications.

## Acknowledgements

We thank the UK's Engineering and Physical Sciences Research Council (EPSRC) for financial support through the Doctoral Training Centre in Plastic Electronics (EP/G037515/1).

**Keywords:** arsenic · conjugated polymers · field-effect transistors · molecular electronics · semiconductors

[1] L. Lu, T. Zheng, Q. Wu, A. M. Schneider, D. Zhao, L. Yu, *Chem. Rev.* **2015**, *115*, 12666.
[2] C. B. Nielsen, I. McCulloch, *Prog. Polym. Sci.* **2013**, *38*, 2053.
[3] X. Guo, M. Baumgarten, K. Müllen, *Prog. Polym. Sci.* **2013**, *38*, 1832.
[4] J. Crassous, R. Réau, *Dalton Trans.* **2008**, 6865.
[5] A. M. Priegert, B. W. Rawe, S. C. Serin, D. P. Gates, *Chem. Soc. Rev.* **2016**, *45*, 922.
[6] E. I. Carrera, D. S. Seferos, *Macromolecules* **2015**, *48*, 297.
[7] M. Jeffries-El, B. M. Kobilka, B. J. Hale, *Macromolecules* **2014**, *47*, 7253.
[8] X. He, T. Baumgartner, *RSC Adv.* **2013**, *3*, 11334.
[9] R. D. Pensack, Y. Song, T. M. McCormick, A. Jahnke, J. Hollinger, D. S. Seferos, G. D. Scholes, *J. Phys. Chem. B* **2014**, *118*, 2589.
[10] G. He et al., *Chem. Commun.* **2015**, *51*, 5444.
[11] T. Baumgartner, R. Réau, *Chem. Rev.* **2006**, *106*, 4681.
[12] S. C. Rasmussen, S. J. Evenson, *Prog. Polym. Sci.* **2013**, *38*, 1773.
[13] T. Baumgartner, T. Neumann, B. Wirges, *Angew. Chem. Int. Ed.* **2004**, *43*, 6197; *Angew. Chem.* **2004**, *116*, 6323.
[14] Y. Ren, T. Baumgartner, *Dalton Trans.* **2012**, *41*, 7792.
[15] Y. Dienes, S. Durben, T. Kárpáti, T. Neumann, U. Englert, L. Nyulászi, T. Baumgartner, *Chem. Eur. J.* **2007**, *13*, 7487.
[16] C. Romero-Nieto, T. Baumgartner, *Synlett* **2013**, 920.
[17] A. M. Gregson, S. M. Wales, S. J. Bailey, P. A. Keller, *J. Organomet. Chem.* **2015**, *785*, 77.
[18] A. M. Gregson, S. M. Wales, S. J. Bailey, A. C. Willis, P. A. Keller, *J. Org. Chem.* **2015**, *80*, 9774.
[19] C. J. O'Brien, Z. S. Nixon, A. J. Holohan, S. R. Kunkel, J. L. Tellez, B. J. Doonan, E. E. Coyle, F. Lavigne, L. J. Kang, K. C. Przeworski, *Chem. Eur. J.* **2013**, *19*, 15281.
[20] K. Naka, T. Umeyama, Y. Chujo, *J. Am. Chem. Soc.* **2002**, *124*, 6600.
[21] T. Umeyama, K. Naka, Y. Chujo, *Macromolecules* **2004**, *37*, 5952.
[22] K. Naka, *Polym. J.* **2008**, *40*, 1031.
[23] S.-Y. Jang et al., *Chem. Mater.* **2014**, *26*, 6907.
[24] Z. Fei, P. Pattanasattayavong, Y. Han, B. C. Schroeder, F. Yan, R. J. Kline, T. D. Anthopoulos, M. Heeney, *J. Am. Chem. Soc.* **2014**, *136*, 15154.
[25] R. Betz, M. M. Reichvilser, E. Schumi, C. Miller, P. Klüfers, *Z. Anorg. Allg. Chem.* **2009**, *635*, 1204.
[26] V. Matuska, A. M. Z. Slawin, J. D. Woollins, *Inorg. Chem.* **2010**, *49*, 3064.
[27] Z. Fei, Y. Kim, J. Smith, E. B. Domingo, N. Stingelin, M. A. McLachlan, K. Song, T. D. Anthopoulos, M. Heeney, *Macromolecules* **2012**, *45*, 735.
[28] M. Ishidoshiro, Y. Matsumura, H. Imoto, Y. Irie, T. Kato, S. Watase, K. Matsukawa, S. Inagi, I. Tomita, K. Naka, *Org. Lett.* **2015**, *17*, 4854.
[29] V. Farina, B. Krishnan, *J. Am. Chem. Soc.* **1991**, *113*, 9585.
[30] Z. Fei, X. Gao, J. Smith, P. Pattanasattayavong, E. Buchaca Domingo, N. Stingelin, S. E. Watkins, T. D. Anthopoulos, R. J. Kline, M. Heeney, *Chem. Mater.* **2013**, *25*, 59.
[31] S. Pelzer, K. Wichmann, R. Wesendrup, P. Schwerdtfeger, *J. Phys. Chem. A* **2002**, *106*, 6387.

Received: March 10, 2016
Published online: ■■ ■■, ■■■■

 © 2016 Wiley-VCH Verlag GmbH & Co. KGaA, Weinheim 

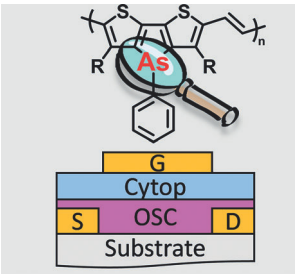
These are not the final page numbers!

# Communications

**Polymers**

J. P. Green, Y. Han, R. Kilmurray, M. A. McLachlan, T. D. Anthopoulos, M. Heeney* ——— ■■■■–■■■■

An Air-Stable Semiconducting Polymer Containing Dithieno[3,2-*b*:2′,3′-*d*]arsole




**Arsenic-containing** conjugated polymers were obtained by copolymerization of the first dithieno[3,2-*b*;2′,3′-*d*]arsole derivative. These polymers are stable under ambient conditions in their +3 oxidation state and display p-type semiconductivity with promising hole mobility in field-effect transistors.


© 2016 Wiley-VCH Verlag GmbH & Co. KGaA, Weinheim

DOI: 10.1002/((please add manuscript number))
**Article type: Full Paper**

# Optical Acetone Vapor Sensors Based on Chiral Nematic Liquid Crystals and Reactive Chiral Dopants

*Pascal Cachelin, Joshua P. Green, Ton Peijs, Martin Heeney and Cees W. M. Bastiaansen**

P. Cachelin, Prof. C.W.M. Bastiaansen, Prof. T Peijs
Queen Mary University of London, Mile End Road, E1 4NS, United Kingdom

J. P. Green, Prof. M. Heeney
Imperial College London, Exhibition Road, SW7 2AZ, United Kingdom

Prof. C.W.M. Bastiaansen
Technische Universiteit Eindhoven, Den Dolech 2, 5612, the Netherlands
C.W.M.Bastiaansen@tue.nl

Keywords: **Chiral Nematic Liquid Crystals, Sensors, Acetone Vapor, Chemosensors**

Accurate monitoring of exposure to organic vapors, such as acetone, is an important part of maintaining a safe working environment and adhering to long- and short-term exposure limits. Here, a novel acetone vapor detection system is described based on the use of a reactive chiral dopant in a nematic liquid crystal thin film, which can accurately monitor the total exposure over a given timeframe through changes in the reflection band of the film. It was found that films exposed to 1000 parts per million by volume (ppmv) of acetone vapor for two hours exhibited a shift in reflection band of 12 nm, with smaller shifts observed at lower concentrations of acetone. Such sensors have potential applications in industrial hygiene.

## 1. Introduction

Recently, much attention has been paid towards the development of optical sensors, particularly for personal safety applications.[1] These sensors are attractive as they can allow for analysis without requiring access to analytical facilities. Optical sensors based on liquid crystals (LCs) have been investigated extensively in the past. For instance, a broad range of

optical sensors was developed previously which are based on interfacial changes that influence the alignment of liquid crystals in response to analytes such as light,[2] gasses,[3–6] biomolecules[7–9] and aerosols[5] which is covered in an excellent recent review by Carlton *et al*.[10] In these sensors, chemically functionalized self-assembled monolayers are employed which react with analytes that act as an alignment layer for liquid crystals. The change in birefringence is monitored upon exposure to an analyte via transmission measurements between crossed linear polarizers.

Optical sensors based on the chiral nematic phase were also explored in the past. Typically, these sensors operate on a change in the reflection band of the chiral nematic liquid crystal, which allows for optical monitoring without the need for polarizers. In most cases, these sensors operate by the absorption of the analyte causing swelling which in turn alters the cholesteric pitch. Such sensors have been previously described for alcohols,[11] amines,[12,13] VOCs[14–16] and gases like oxygen and carbon dioxide.[17] These optical sensors can have a high sensitivity but are often also cross-sensitive to similar molecules. These sensors act as real-time sensors, and measure the level of analyte that is present. This is in contrast to time-integrating sensors, which can effectively act as a chemical dosimeters by measuring the total exposure to an analyte over a given time frame.

To date, only one time-integrating sensors based on chiral nematic liquid crystals has been reported.[18] This sensor operated on the basis of a reactive chiral dopant in a nematic LC matrix that irreversibly reacted with water vapor, resulting in a change in the reflection band of the chiral nematic liquid crystals which was attributed to a change in the helical twisting power (HTP) of the dopant.

Detection of acetone vapor with a time-integrating sensor requires the use of a chiral dopant system capable of irreversibly reacting with acetone. TADDOLs (TetraAryl-1,3-Dioxolane-

4,5-DimethanOLs) are a group of compounds traditionally used in catalysis as chiral auxiliaries.[19] A secondary use is as chiral dopants in chiral-nematic liquid crystals, where they act as dopants with exceptionally high HTP.[20] Previous work by Han et al[17] has demonstrated that *R,R*-TADDOLs can be complexed with amines to produce a reactive dopant complex capable for the real-time detecting of $CO_2$.

In this study, a new chiral nematic reactive dopant is reported and their use in time-integrating sensors for acetone is explored. This dopant consists of R,R-TADDOL complexes with phenylhydrazine to generate reactive and irreversible systems with a high sensitivity to acetone and low cross sensitivity.

## 2. Results and discussion

### 2. Complex formation and testing

In this study, R,R-TADDOLs are again used as chiral auxiliaries.[18] Phenylhydrazine (PH), which is capable of hydrogen-bonding to the TADDOL, is expected to have a high reactivity and selectivity towards ketones. The specific TADDOL-PH complex chosen is shown in **Figure 1**, and consists of (4*R*,5*R*)-2,2-Dimethyl-α,α,α′,α′-tetra(2-naphthyl)dioxolane-4,5-dimethanol complexed to PH.

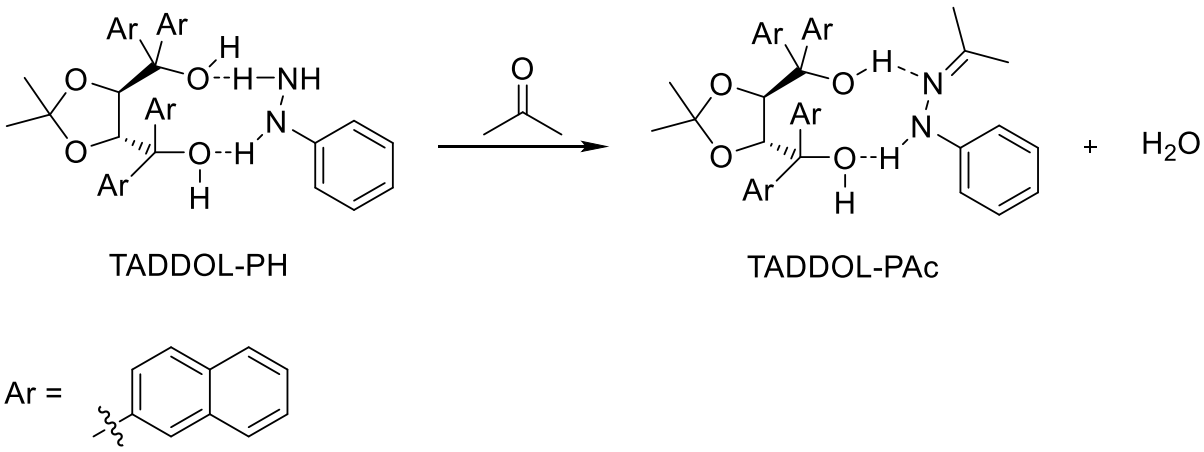



**Figure 1.** The TADDOL-Phenylhydrazine (TADDOL-PH) complex, and the imine product of the reaction with acetone (TADDOL-PAc)

The formation of this complex was confirmed by $^{1}$H NMR (**Figure S1**). The $^{1}$H NMR spectrum of a 1:1 molar ratio mixture of the TADDOL-PH complex shows several important changes in comparison to those of samples of pure PH and TADDOL. The majority of the aromatic peaks in both TADDOL and PH are largely unaffected by complexation, with changes in chemical shifts of less than 0.02 ppm seen for all peaks except those corresponding to the protons in *ortho* positions of phenylhydrazine, which shift upfield from around 6.83 ppm to 6.74 ppm in the presence of TADDOL. This is expected as the naphthyl protons on TADDOL are molecularly distant from the predicted complexation site, whilst the *ortho* position of PH is directly attached to the hydrazine functional group. The -CH protons on the TADDOL dioxolane ring show slight shielding from 4.97 ppm to 4.94 ppm, whilst the methyl groups show no change from their original position. By far the largest shifts are seen for the protons corresponding to the functional groups (hydroxyl for TADDOL and hydrazinyl for PH). The protons of the latter shift upfield from 5.17 to 5.05 ppm and 3.58 to 3.52 ppm for the -NH- and -NH2 protons respectively, with the hydroxyl protons shifted downfield from 4.24 ppm to 4.62 ppm. The fact that the hydrazinyl protons shift upfield and the hydroxyl protons downfield indicates that hydrogen bonds form between the two molecules with -NH/-NH2 acting as hydrogen bond donors and the -OH groups acting as hydrogen bond acceptors.

In order to determine the maximum shift in the reflection band resulting from full conversion of the hydrazine to imine product, it was first necessary to create the expected product of the reaction between TADDOL-PH and acetone (TADDOL-PAc, Figure 1). A reaction of PH with saturated acetone vapor was carried out. We found that the resultant product (PAc) was obtained quantitatively with and without the use of an acid catalyst (**Figure S2**). This was then combined with TADDOL to produce a TADDOL-PAc complex.

In order to determine the suitability of the TADDOL-PH system as a reactive dopant, reference experiments were performed to measure the HTP of the TADDOL complexes before and after reaction with acetone. LC/dopant mixtures were formulated and processed by spin-coating onto a rubbed polyimide alignment layer. The prepared samples yielded brightly colored films and optical microscopy revealed that the films exhibited a so-called fingerprint texture when viewed between crossed polarizers (**Figure 2**), indicating splay alignment at the LC-air interface.[21] The films exhibit a reflection band at 493.5 nm for TADDOL, 499.5 nm for TADDOL-PH and 514.5 nm for TADDOL-Pac respectively. From this, the pitch and the HTP were calculated using enantiomeric excess ($e_e$) and weight fraction ($c_w$) of the dopant, as well as the average refractive index of the nematic liquid crystalline host ($\bar{n}$) (Equations 1, 2). This information is summarized in Table 1.

$$p = \frac{\lambda}{\bar{n}} \quad [1]$$

$$HTP = (pe_e c_w)^{-1} \quad [2]$$

The difference in the HTP values of TADDOL and TADDOL-PH provide a strong indication that the TADDOL-PH complex is formed, and the difference in the HTP values of TADDOL-PH and TADDOL-PAc indicates the reaction with acetone produces the TADDOL-PAc compound.

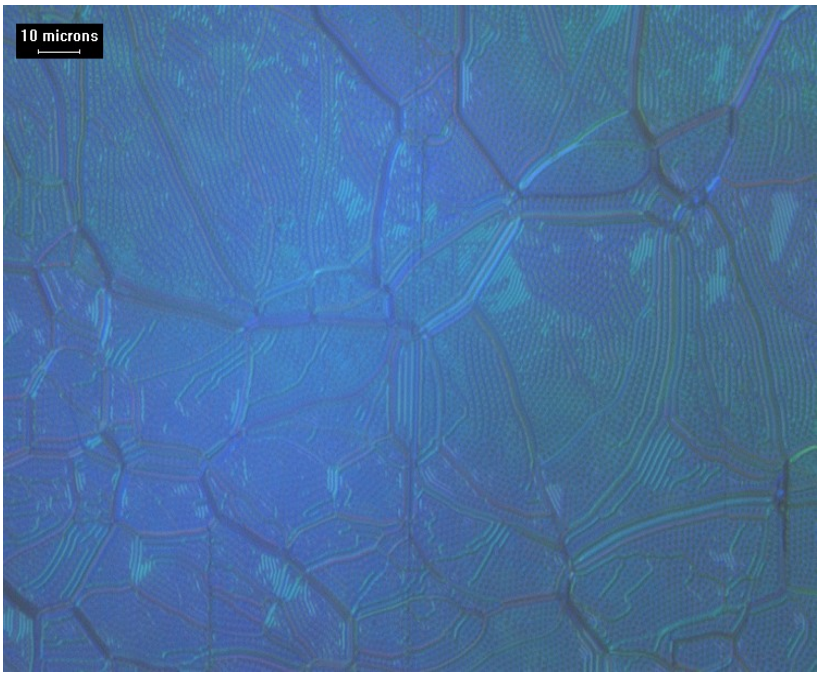
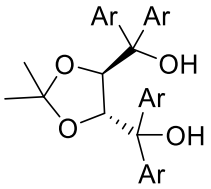
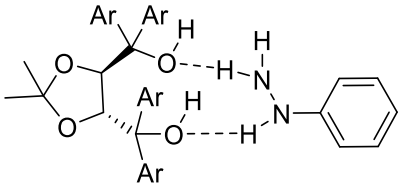
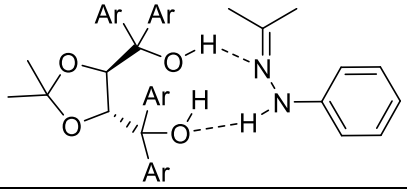



**Figure 2.** Optical Microscopy image between crossed polarizers showing the fingerprint texture. Scale bar = 10 μm

**Table 1.** Film compositions and resultant helical twisting powers.

| Dopant | Concentration (wt. %) | Reflection maximum (nm) | Pitch (nm) | HTP ($\mu m^{-1}$) |
|---|---|---|---|---|
|  | 3.44 | 493.5 | 324 | 90.62 |
|  | 4.00 | 499.5 | 328 | 76.79 |
|  | 4.01 | 514.5 | 338 | 74.71 |

As indicated in Equation 3 the pitch, and therefore the wavelength of the reflection band, is dependent on the doping concentration used.

In order to determine a suitable exposure time for this reaction, GCMS analysis of the bulk phase reaction of $PhNNH_2$/*R*,*R*-TADDOL and 1000 p.p.m.v. acetone vapor in E7 solvent was carried out. It was found that the reaction proceeded to 60% conversion over 120 minutes, after which it plateaued (**Figure S3**). Extended exposure (>24 hours) did not lead to any increase in conversion. The time frame of 2 hours was therefore used as the basis for subsequent experiments.

2.2. Sensitivity to acetone vapor

To test the sensitivity of the sensor, chiral nematic films were prepared containing 4 % of chiral dopant. It was reported previously that exposure to saturated acetone results in complete dissolution of the LC[22] and therefore this study is limited to low acetone levels such as encountered in industrial hygiene.

CNLC films manufactured with the TADDOL-PH showed an irreversible red-shift of 12 nm in absorption maximum compared to before acetone exposure (**Figure 3c)**, while those of control films made with TADDOL-PAc and pure TADDOL showed no change in absorption (**Figure 3a,b**) compared to before acetone exposure. This indicates that the change observed for the films made with TADDOL-PH is due to a reaction between the dopant and the analyte, and not due to a swelling of the nematic host. As shown in Table 1, full conversion of PH to PAc would give a red-shift in absorption maximum of 14 nm, with the observed 12 nm shift equating to an 85% conversion.

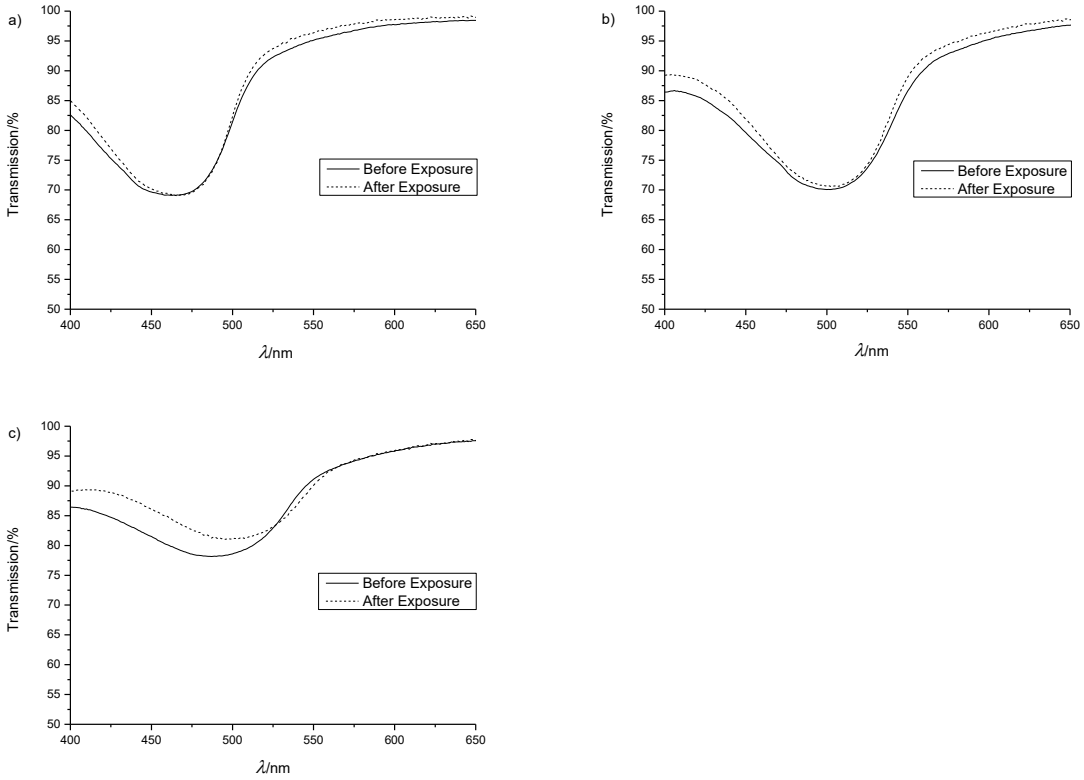



**Figure 3**. The UV/Vis absorption spectra of **a)** TADDOL, **b)** TADDOL-PAc and **c)** TADDOL-PH before and after exposure to acetone vapor.

A series of experiments consisting of exposing CNLC films to a variety of acetone concentrations was carried out. It was found that the operational range of the detector is in the 100 –1000 ppmv range of acetone vapor over a time frame of two hours with the absorption maximum exhibiting a close to linear relationship in with acetone concentration up to approximately 1000 ppmv (**Figure 4**).

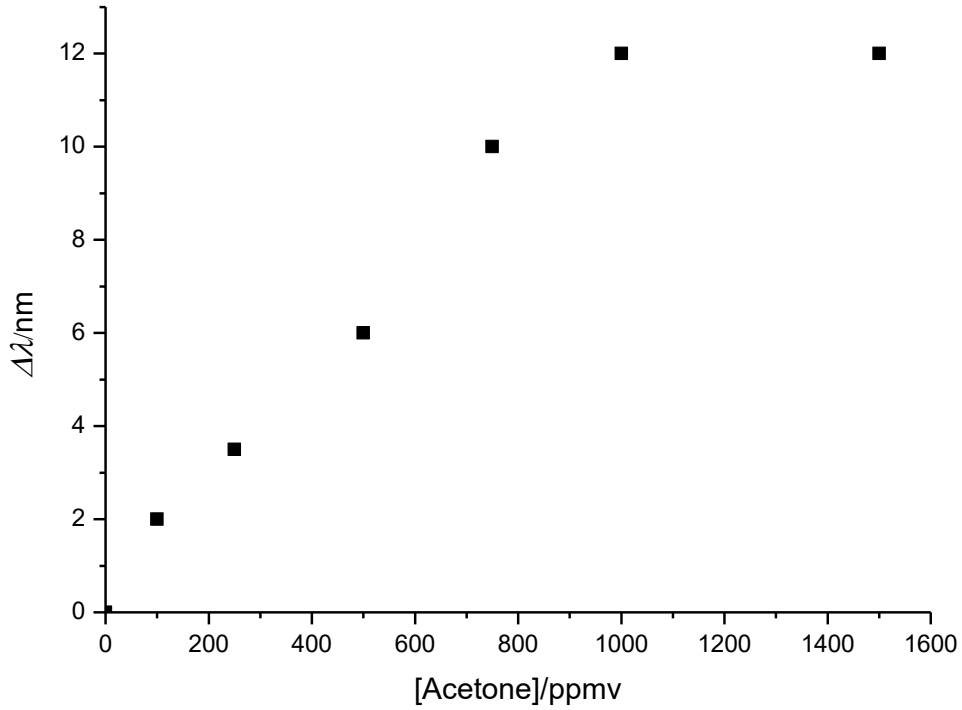



**Figure 4.** Change in absorption maximum (Δλ) of CNLC sensors exposed acetone vapor.

As shown in Figure 4, concentrations above 1,000 ppmv did not result in any change in the reflection band of the sample, indicating saturation of the sensor. Similarly, concentrations below 100 ppmv did not produce a measurable shift. The sensitivity of the sensor in the intermediate region was calculated from the slope and was 0.0012 nm/ppmv.

2.3 Cross-sensitivity

A key requirement for any sensor is a low cross-sensitivity to other components of a potential analyte mixture. In order to quantify this cross-sensitivity, experiments were performed to test the response of the sensor to an atmosphere of 10,000 ppmv of other industrial chemicals, such as isopropyl alcohol, ethanol, and water vapor, for a 24 hours. It was found that there was no change in absorption maximum after exposure to ethanol or water, although a 4 nm redshift was seen after exposure to isopropyl alcohol vapor.

## 3. Discussion

Acetone is a widely used industrial solvent, with many varied applications in different industries. Although relatively harmless at low concentrations for short times, chronic exposure to acetone vapor can lead to a progression of symptoms from irritation of mucous membranes to headaches, nausea, loss of coordination, central nervous system depression and finally, at sufficiently high exposure levels, cardiorespiratory failure.[23–27] Exposure to levels as low as 250 ppmv for 4 hours has been shown to lead to neurobehavioral effects, including increased aggression in males.[28] As such, monitoring exposure to acetone vapor and ensuring that it falls within safety guidelines is an important aspect of industrial hygiene.

The industrial guidance issued by the American Conference of Governmental Industrial Hygienists on acetone vapor gives a maximum time weighted average (TWA) of 750 ppmv and a short term exposure limit (STEL) of 1000 ppmv, while the Workplace Exposure Limit set by the UK Health and Safety Executive is 500 ppmv for the TWA and 1500 ppmv for the STEL. The sensor developed in this work is capable of monitoring the TWA for both these standards over a time frame of two hours, although maximum change in the reflection band of 12 nm is too small to be monitored visually, and currently requires spectrometric analysis.

Another potential application for acetone sensors is monitoring blood-glucose levels in the case of type 1 diabetes by using breath acetone level as a proxy,[29,30] although significant debate remains over the validity of breath acetone as a suitable proxy.[31,32] If acetone is shown to be a reliable biomarker then acetone sensors have the potential for diagnostic and monitoring applications in diabetes management. Such a sensor would need to be able to detect very low concentrations of acetone vapor, typically in the range of 0.1-10 ppmv. This is significantly below the capability of the sensors developed here.

## 4. Conclusions

A chiral nematic sensor for acetone was developed that exhibits a low sensitivity (0.0012 nm/ppmv) and a low cross-sensitivity. The sensor was based on a TADDOL hydrazine complex as a reactive chiral dopant within a nematic LC that irreversibly reacts with acetone, resulting in a change in the reflection band of the sensor. It is shown that this sensor is potentially useful for industrial hygiene applicants and not for the detection of diabetes via breath analysis which is related to the high sensitivity that is needed.

## 5. Experimental Section

*Materials and sample preparation:* All materials were used as received. Glass slides (Fischer Scientific) were washed with isopropyl alcohol and $N_2$ dried prior to spin coating with polyimide precursor AL1051 (JSR Micro). The substrates were thermally cured (200 °C for two hours). The coated glass slides were then uniaxially rubbed with a velvet cloth in order to induce a planar alignment layer.

The PAc imine product was formed by exposing phenylhydrazine (Alfa Aesar) to a saturated acetone vapor under argon for 24 hours. The PAc was obtained quantitatively and used without further purification.

CNLC mixtures were formed by dissolving *R*,*R*-TADDOL (Sigma-Aldrich) and phenylhydrazine in E7 (Synthon Chemicals). The resultant mixture was diluted 1:1 w/w with *p*-xylene (Sigma-Aldrich) in order to decrease the viscosity ahead of spin-coating.

*GCMS experiment:* $PhNNH_2$ was dissolved in E7 and exposed to 1000 p.p.m.v. acetone in an argon atmosphere for the lengths of time shown in the graph. Samples were then removed

from the reaction vessel, dissolved in dichloromethane and submitted for GCMS analysis. Peaks corresponding to $PhNNH_2$ and PhNNAc (as determined by the presence of ions at m/z = 108 and m/z = 148 respectively) were integrated using Origin Pro software, and the relative areas plotted as a function of reaction time.

*Formation of thin films by spin-coating:* The CLC mixtures were spin-coated onto the coated glass slides. After spin-coating the samples were briefly heated to just above the clearing point of the mixture (65 °C) in order to aid evaporation of any residual xylene solvent.

*Solvent vapor exposure testing:* Samples were placed inside a 2 L 3-necked-flask and the necks were sealed with Suba-Seal septa. The flask was flushed with nitrogen gas to remove any residual solvent vapor, and then acetone, ethanol, isopropyl alcohol (Sigma-Aldrich) or deionized water was injected through the septa using a microsyringe. Unless otherwise stated, samples were exposed for 2 hours before characterization, after which they were briefly heated above the isotropic point in order to remove any residual solvent.

*Characterization:* UV spectra were taken using a Lambda 950 UV spectrometer (Perkin Elmer) using non-polarized light. GCMS data were obtained using Agilent Technologies 7890A gas chromatograph connected to an Agilent 5975C detector. $^{1}H$ and $^{13}C$ NMR spectra were recorded using Bruker AV-400 spectrometers ($^{1}H$ = 400 MHz, $^{13}C$ = 101 MHz) at 298 K.

**Supporting Information**

Supporting Information is available from the Wiley Online Library or from the author.

Acknowledgements

We thank the UK's Engineering and Physical Sciences Research Council (EPSRC) for financial support via the Doctoral Training Centre in Plastic Electronics EP/G037515/1. We gratefully acknowledge Dr. Olivier Picot for advice and helpful discussions.

Received: ((will be filled in by the editorial staff))
Revised: ((will be filled in by the editorial staff))
Published online: ((will be filled in by the editorial staff))

[1] A. Lobnik, *Intelligent Textiles for Personal Protection and Safety*, IOS Press, Amsterdam, **2006**.

[2] H. Knobloch, H. Orendi, M. Buchel, T. Seki, S. Ito, W. Knoll, *J. Appl. Phys.* **1995**, *77*, 481.

[3] J. L. Adgate, A. Barteková, P. C. Raynor, J. G. Griggs, A. D. Ryan, B. R. Acharya, C. J. Volkmann, D. D. Most, S. Lai, M. D. Bonds, *J. Environ. Monit.* **2009**, *11*, 49.

[4] R. Nandi, S. K. Singh, H. K. Singh, B. Singh, R. K. Singh, *Chem. Phys. Lett.* **2014**, *614*, 62.

[5] K. D. Cadwell, N. a. Lockwood, B. a. Nellis, M. E. Alf, C. R. Willis, N. L. Abbott, *Sensors Actuators, B Chem.* **2007**, *128*, 91.

[6] R. R. Shah, N. L. Abbott, *Langmuir* **2003**, *19*, 275.

[7] S. R. Kim, N. L. Abbott, *Adv. Mater.* **2001**, *13*, 1445.

[8] S. Zhong, C.-H. Jang, *Biosens. Bioelectron.* **2014**, *59*, 293.

[9] H. Tan, S. Yang, G. Shen, R. Yu, Z. Wu, *Angew. Chemie - Int. Ed.* **2010**, *49*, 8608.

[10] R. J. Carlton, J. T. Hunter, D. S. Miller, R. Abbasi, P. C. Mushenheim, L. N. Tan, N. L. Abbott, *Liq. Cryst. Rev.* **2013**, *1*, 29.

[11] C.-K. Chang, C. W. M. Bastiaansen, D. J. Broer, H.-L. Kuo, *Macromolecules* **2012**, *45*, 4550.

[12] N. Kirchner, L. Zedler, T. G. Mayerhöfer, G. J. Mohr, *Chem. Commun. (Camb).* **2006**, 1512.

[13] L. Sutarlie, H. Qin, K.-L. Yang, *Analyst* **2010**, *135*, 1691.

[14] D. A. Winterbottom, R. Narayanaswamy, I. M. Raimundo, *Sensors Actuators, B Chem.* **2003**, *90*, 52.

[15] F. Dickert, A. Haunschild, P. Hofmann, *Fresenius. J. Anal. Chem.* **1994**, 577.

[16] A. Mujahid, H. Stathopulos, P. A. Lieberzeit, F. L. Dickert, *Sensors* **2010**, *10*, 4887.

[17] Y. Han, K. Pacheco, C. W. M. Bastiaansen, D. J. Broer, R. P. Sijbesma, *J. Am. Chem. Soc.* **2010**, *132*, 2961.

[18] A. Saha, Y. Tanaka, Y. Han, C. M. W. Bastiaansen, D. J. Broer, R. P. Sijbesma, *Chem. Commun. (Camb).* **2012**, *48*, 4579.

[19] D. Seebach, A. K. Beck, A. Heckel, *Angew. Chem. Int. Ed. Engl.* **2001**, *40*, 92.

[20] R. Eelkema, B. L. Feringa, *Org. Biomol. Chem.* **2006**, *4*, 3729.

[21] P. J. Collings, *Liquid Crystals*, Adam Hilger, Bristol, **1990**.

[22] C. K. Chang, S. W. Chiu, H. L. Kuo, K. T. Tang, *Appl. Phys. Lett.* **2012**, *100*, 2013.

[23] J. H. E. Arts, J. Mojet, L. J. van Gemert, H. H. Emmen, J. H. C. M. Lammers, J. Marquart, R. a Woutersen, V. J. Feron, *Crit. Rev. Toxicol.* **2002**, *32*, 43.

[24] G. E. Ziem, B. I. Castleman, *J. Occup. Med.* **1989**, *31*, 910.

[25] A. Fujino, T. Satoh, T. Takebayashi, H. Nakashima, H. Sakurai, T. Higashi, H. Matumura, H. Minaguchi, T. Kawai, *Br. J. Ind. Med.* **1992**, *49*, 654.

[26] E. Wigaeus, S. Holm, I. Åstrand, *Scand. J. Work. Environ. Health* **1981**, *7*, 84.

[27] S. Kumagai, I. Matsunaga, T. Tabuchi, *Am. Ind. Hyg. Assoc. J.* **1998**, *59*, 242.

[28] R. B. Dick, J. V Setzer, B. J. Taylor, R. Shukla, *Br. J. Ind. Med.* **1989**, *46*, 111.

[29] A. Manolis, *Clin. Chem.* **1983**, *29*, 5.

[30] K.-H. Kim, S. A. Jahan, E. Kabir, *TrAC Trends Anal. Chem.* **2012**, *33*, 1.

[31] P. Spaněl, K. Dryahina, A. Rejšková, T. W. E. Chippendale, D. Smith, *Physiol. Meas.* **2011**, *32*, N23.

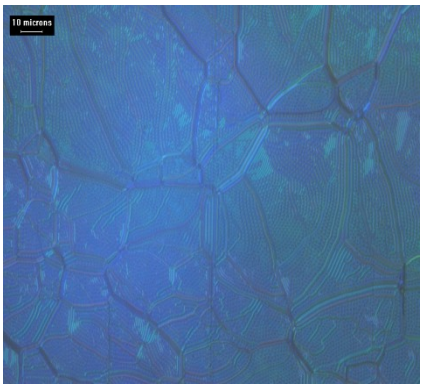
[32] P. Spaněl, D. Smith, *Curr. Opin. Clin. Nutr. Metab. Care* **2011**, *14*, 455.

**A novel sensor based on a chiral nematic liquid crystal doped with a reactive dopant is fabricated and investigated.** It is found that the sensor acts as a real-time integrator, responding to total acetone dose by changing the wavelength of the reflection maximum of the chiral nematic liquid crystal. The sensitivity and cross sensitivity of the sensor are investigated.

**Keyword: Chiral Nematic Liquid Crystals, Sensors, Acetone Vapor, Chemosensors**

*Pascal Cachelin, Joshua P. Green, Ton Peijs, Martin Heeney and Cees W. M. Bastiaansen**

**Optical Acetone Vapor Sensors Based on Chiral Nematic Liquid Crystals and Reactive Chiral Dopants**



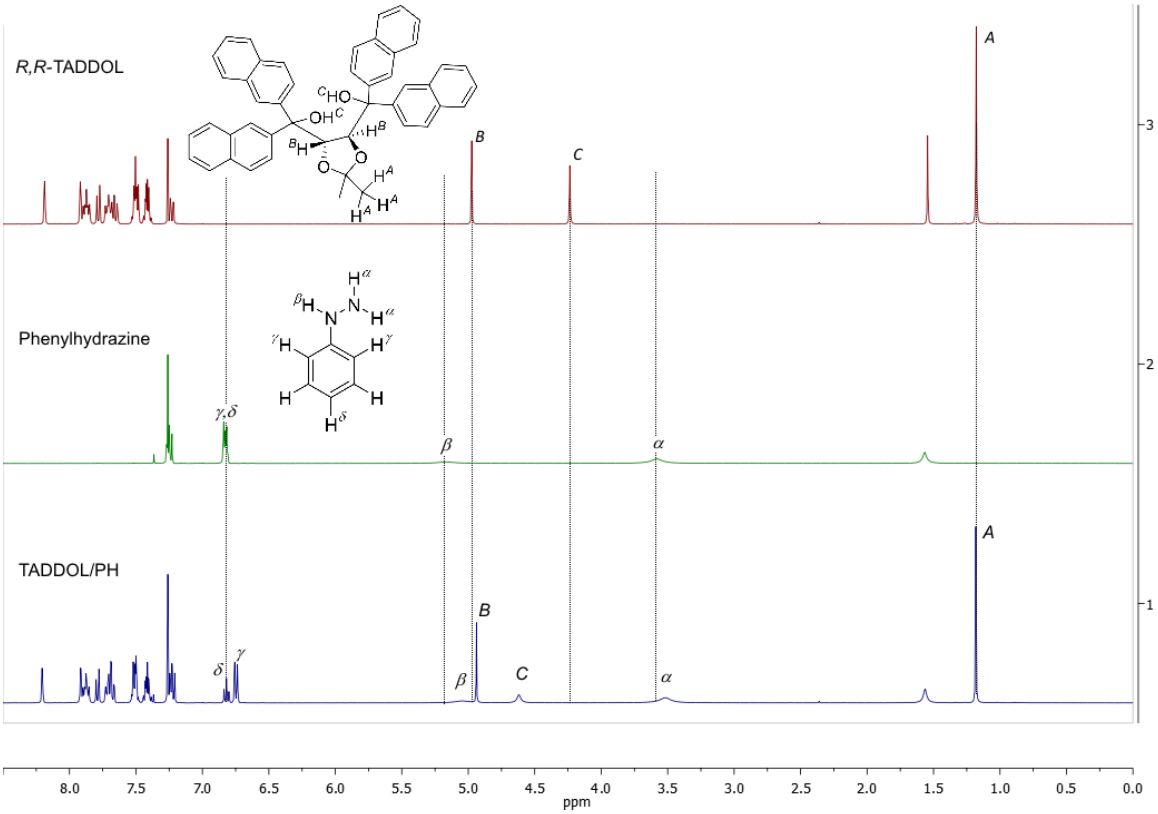

Copyright WILEY-VCH Verlag GmbH & Co. KGaA, 69469 Weinheim, Germany, 2013.

# Supporting Information

**Optical Acetone Vapor Sensors Based on Chiral Nematic Liquid Crystals Thin Films Using Reactive Chiral Dopants**

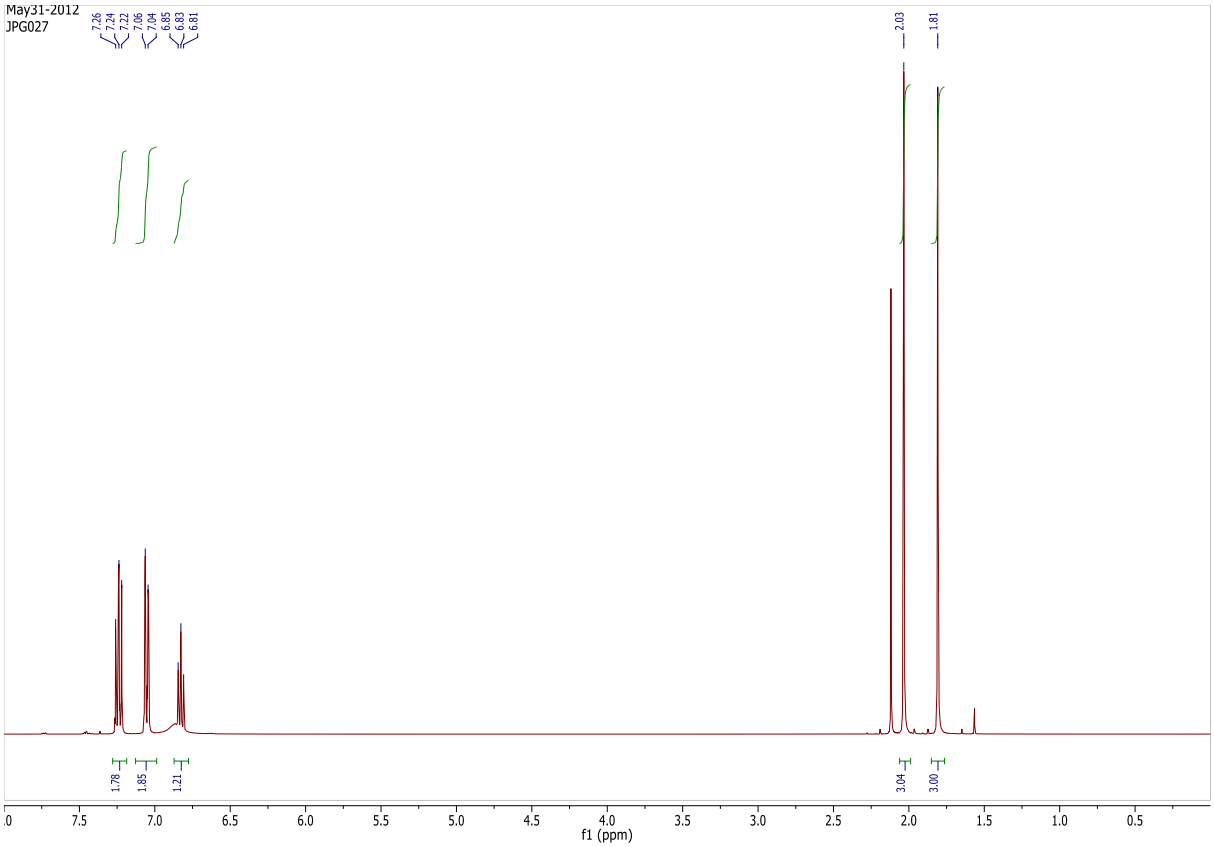
*Pascal Cachelin, Joshua Green, Dr. Martin Heeney and Prof. Cees Bastiaansen*

**Figure S1. $^{1}$H NMR spectra of TADDOL, PH, and the TADDOL-PH complex**




Spectra are $^{1}H$ NMR of TADDOL, PH, and complex of the two at 1:1 molar equivalents, displayed in order from top to bottom. All spectra taken in $CDCl_3$. Peaks relevant to the discussion are highlighted with dotted lines. The peaks at 7.26 ppm and 1.56 ppm are assigned to residual solvent ($CDCl_3$) and water respectively.

**Figure S2. $^{1}H$ NMR of PAc**




$^{1}$H NMR of PAc. The sample was prepared by exposing PH to saturated acetone vapor under argon for 24 hours, with no additional purification steps. The unassigned peak corresponds to unreacted acetone.

**Figure S3. GCMS analysis of the reaction between PH and acetone.**

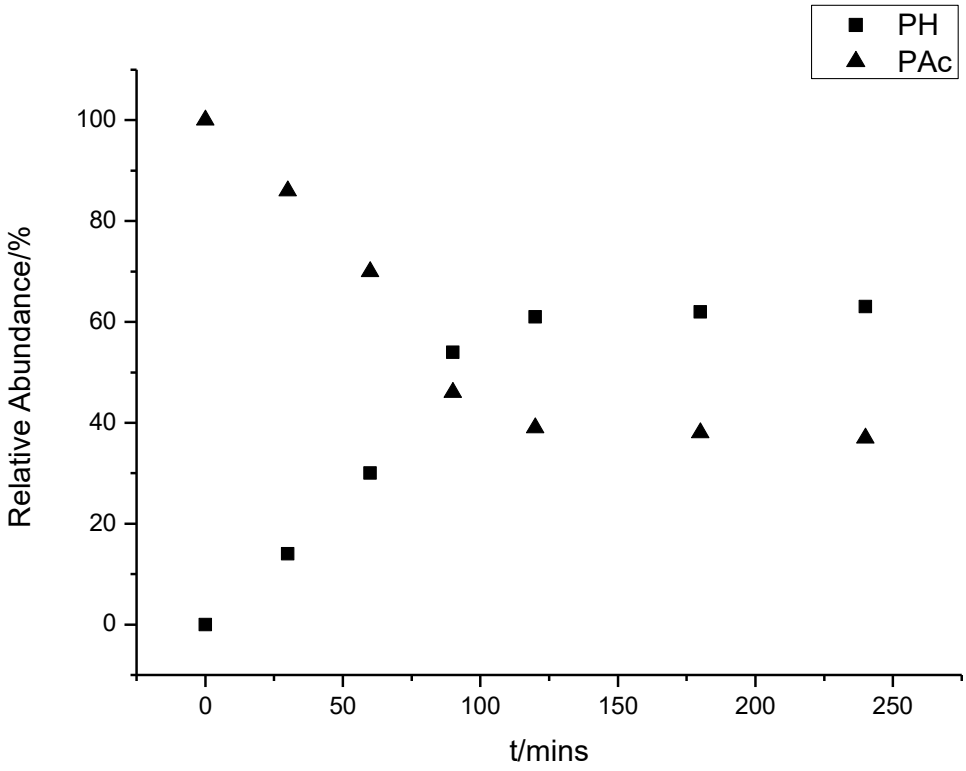



Figure S3 depicts the change in relative amounts of $PhNNH_2$ and PhNNAc over the course of four hours as measured by GCMS.